Structure and Reactivity of Terrestrial and Extraterrestrial Pyrrhotite

Von der Fakultät für Biologie, Chemie und Geowissenschaften
der Universität Bayreuth

zur Erlangung der Würde eines
Doktors der Naturwissenschaften
− Dr. rer. nat. −

genehmigte
Dissertation

Vorgelegt durch

Dennis Harries, Dipl.-Geow.
aus Seesen am Harz

Bayreuth 2012

Die vorliegende Arbeit wurde in der Zeit von September 2008 bis Januar 2012 in Bayreuth am Bayerischen Geoinstitut unter Betreuung von Herrn Prof. Dr. Falko Langenhorst und Dr. Kilian Pollok angefertigt.

Vollständiger Abdruck der von der Fakultät für Biologie, Chemie und Geowissenschaften der Universität Bayreuth genehmigten Dissertation zur Erlangung des akademischen Grades eines Doktors der Naturwissenschaften (Dr. rer. nat.).

Dissertation eingereicht: 12. Januar 2012
Zulassung durch die Promotionskommission: 18. Januar 2012
Tag des wissenschaftlichen Kolloquiums: 30. April 2012

Amtierender Dekan:
Prof. Dr. Beate Lohnert

Prüfungsausschuss:
Prof. Dr. Falko Langenhorst (Erstgutachter)
Prof. Dr. Herbert Palme (Zweitgutachter)
Prof. Dr. Stefan Peiffer (Vorsitz)
Prof. Dr. Tomoo Katsura
Prof. Dr. Leonid Dubrovinsky

Abstract

Pyrrhotite ($Fe_{1-x}S$) is a non-stoichiometric iron monosulfide common in terrestrial rocks, ore deposits, and many extraterrestrial materials. The non-stoichiometry due to metal vacancies relates to a variety of composition-dependent crystallographic superstructures, but little of the existing structural and microstructural complexity has been explored yet. This thesis investigates the occurrences and nature of pyrrhotite superstructures, examines the related nano- and microstructural phenomena, and explores their effects on chemical reactivity. The goal is to comprehend the relations of the nanoscale real structure of pyrrhotite to its physicochemical properties. A central tool in these studies is analytical transmission electron microscopy (TEM), which has been extensively used to study terrestrial and extraterrestrial samples. In three studies, published or submitted as scientific research articles, it is shown that structural complexity of pyrrhotites is a widespread feature in terrestrial and extraterrestrial materials and is strongly interrelated with its physicochemical properties and environments of formation and alteration. A new model based on translation interface modulation is being introduced to provide a realistic description of the structural state of natural NC-pyrrhotites. Novel insights into the thermodynamically stable phase assemblages in the Fe-S system at ambient temperatures are presented and the crystallography and connected thermochemistry of pyrrhotites are deployed to reach new conclusions about the petrogenetic history of chondritic meteorites and the alteration processes they were involved in. Finally, an experimental alteration study reveals for the fist time quantitatively that the vacancy superstructures and anisotropy of pyrrhotites have tremendous effects on their kinetic behaviors during dissolution under acidic and oxidizing conditions. Intrinsic reactivity differences between 4C- and NC-pyrrhotite are clearly resolved and discusses in the framework of the newly established structure model.

Zusammenfassung

Pyrrhotin ($Fe_{1-x}S$) ist ein in terrestrischen Gesteinen, Erzlagerstätten und vielen extraterrestrischen Materialien verbreitetes, nichtstöchiometrisches Eisenmonosulfid. Die Nichtstöchiometrie durch Metallleerstellen steht in Verbindung zu einer Vielzahl kristallographischer Überstrukturen, die von der Zusammensetzung abhängig sind, jedoch hinsichtlich ihrer strukturellen und mikrostrukturellen Komplexität bislang wenig erforscht worden sind. Diese Arbeit untersucht die Vorkommen und Eigenschaften der Pyrrhotinüberstrukturen, behandelt die in Beziehung stehenden nano- und mikrostrukturellen Phänomene und erforscht ihre Effekte auf die chemische Reaktivität. Das Ziel ist, zu verstehen, in welchem Verhältnis die nanoskaligen Realstrukturen des Pyrrhotins zu seinen physikochemischen Eigenschaften stehen. Im Rahmen der Studien wurde vor allem analytische Transmissionselektronenmikroskopie (TEM) als wichtigste Methode verwendet, um terrestrische und extraterrestrische Pyrrhotine detailliert zu untersuchen. In drei Arbeiten, die als wissenschaftliche Forschungsartikel entweder eingereicht oder schon publiziert wurden, wird gezeigt, dass die strukturelle Komplexität der Pyrrhotins ein weit verbreitetes Merkmal in terrestrischen und extraterrestrischen Materialien ist und in engem Zusammenhang mit seinen physikochemischen Eigenschaften und den Bildungs- und Alterationsbedingungen steht. Es wird ein neues Modell eingeführt, welches basierend auf Translationsgrenzflächenmodulation eine realistische Beschreibung des strukturellen Zustandes natürlicher NC-Pyrrhotine ermöglicht. Neue Einsichten zu den thermodynamisch stabilen Phasenbeziehungen im Fe-S System bei Umgebungstemperatur werden präsentiert, und die Kristallographie und die damit verbundene Thermochemie der Pyrrhotine werden genutzt, um neue Erkenntnisse über die petrogenetische Entwicklung chondritischer Meteorite und ihrer Alterationsprozesses zu gewinnen. Zum Abschluss wird in einer experimentellen Studie zu ersten Mal quantitativ gezeigt, dass die Leerstellenüberstrukturen und die Anisotropie der Pyrrhotine einen enormen Einfluss auf das kinetische Verhalten während oxidativer Auflösung unter sauren pH-Bedingungen ausüben. Die intrinsischen Reaktivitätsunterschiede zwischen 4C- und NC-Pyrrhotin werden eindeutig aufgelöst und im Rahmen des neu eingeführten Strukturmodells diskutiert.

Acknowledgements

I am grateful to Prof. Dr. Falko Langenhorst and Dr. Kilian Pollok for providing the chance to work on this project with great latitude for my own ideas, as well as for their guidance and support. Work in the cordial and highly professional environment of the Bayerisches Geoinstitut was a great pleasure and I cordially thank all of its present and past members for sustaining it. Particular thanks go to Hubert Schulze and Uwe Dittmann for their excellent sample preparation, to Heinz Fischer and Stefan Übelhack for swift and precise machining of all the bits and pieces needed in my research, and to Julia Huber, Gertrud Gollner, Petra Buchert, Lydia Kison-Herzing, Detlef Krausse and Dr. Stefan Keyssner for their help and support. Dr. Nobuyoshi Miyajima is specially thanked for his kind help and maintenance of BGI's TEM laboratory. Drs. Tiziana Boffa Ballaran and Florian Heidelbach are thanked for their support in the X-ray diffraction and SEM laboratories, respectively. I thank Prof. Dr. Herbert Palme for his willingness and time to provide the second evaluation of this thesis.

My office mates and fellow colleagues are cordially thanked for their support, friendship, and many barbecue parties. Particular thanks go to Linda Lerchbaumer, Vincenzo Stagno, Konstantin Glazyrin, Geertje Ganskow, Antje Vogel, Martha Pamato, and Mattia Giannini.

Samples used in this work were provided by the Mineralogical Collection and Museum of the University of Jena, and the Japanese National Institute of Polar Research.

This research was funded by the GEOTECHNOLOGIEN R&D program grant (03G0718A to K.P.), which itself is funded by the German Ministry of Education and Research (BMBF) and German Research Foundation (DFG). It was financially supported by the DFG Leibniz program (LA 830/14-1 to F.L.) and the ENB program "Structure, Reactivity and Properties of Oxide Materials" of the Bavarian State Ministry of Sciences, Research and the Arts. I particularly thank the latter for providing travel funding and support of student seminars and short courses. Travel funds and awards were granted to me by the Meteoritical Society and the Deutsche Mineralogische Gesellschaft, and I gratefully acknowledge these.

Last but not least I would like to thank my parents Gabriele Harries and Otmar Harries for their constant support.

TABLE OF CONTENTS

LIST OF FIGURES

CHAPTER 1

CHAPTER 2

CHAPTER 3

CHAPTER 4

LIST OF TABLES

CHAPTER 1

NO TABLES

CHAPTER 2

CHAPTER 3

CHAPTER 4

CHAPTER 1 Introduction

1.1. Motivation and Background

1.1.1. Motivation

Sulfide minerals have always been of keen interest to mineralogists due to their economic value as ores of metals. After mineralogy had emerged from a qualitative and descriptive discipline to a quantitative natural science in the 18th and 19th century, the knowledge on the great diversity and complexity of sulfide minerals vastly increased and likely culminated in the comprehensive work 'The Ore Minerals and Their Intergrowths' by Paul Ramdohr (1st ed. 1950). This milestone resulted from the introduction and skilful application of the petrographic microscope. When in the following decades the electron microprobe and the transmission electron microscope (TEM) were introduced to mineralogical research, the quantitative understanding of minerals and their role in geological, environmental, and planetary processes became even more intensely amplified. Because the behaviour of minerals in natural and anthropogenically influenced systems is primarily governed by their chemical and physical properties at atomic level, the high spatial resolution of TEM provided and provides significant insight into the real crystal structures of minerals and the processes on the nanoscopic scale (e.g., Wenk 1976; Drits 1987; Buseck 1992). As pointed out by Pósfai and Buseck (1997), sulfides received rather less attention than rock-forming silicates and oxides, but their review illustrates well the nonetheless extensive inventory of nanoscale phenomena in seemingly simple, binary sulfide minerals.

One of these minerals is pyrrhotite, a non-stoichiometric iron monosulfide in the compositional range between FeS and $Fe_{0.875}S$. Key points as to why the motivation for the study of the nano- and microscale mineralogy of pyrrhotite arose can be summarized by the following: (i) Pyrrhotite comprises many recognized structural varieties (often referred to as polytypes, but see Chapter 3), but still only little is known about their crystal structures and thermodynamically stable phase relationships, particularly at low (< 320 °C) or ambient temperatures (e.g., Wang and Salveson 2005). (ii) Pyrrhotite occurs abundantly in nature (section 1.1.3) and during formation at elevated temperatures above about 320 °C its degree of non-stoichiometry is governed by relatively simple physicochemical relations (Toulmin and Barton 1964; Rau 1976). Upon cooling, the imposed non-stoichiometry governs the crystal and microstructures and, hence, structural-chemical information might contribute valuably to the reconstruction of geodynamical and

planetological processes. (iii) Pyrrhotite shows very variable physical (particularly magnetic) and chemical properties, despite its structural variants are very closely related and compositions are often barely distinguishable. Surprisingly, virtually no quantitative and comparative data on chemical reactivity of pyrrhotite varieties existed, despite differential etching by various reagents is known since Ramdohr's time (e.g., Ramdohr 1950; Arnold 1966).

1.1.2. Modular vs. Modulated Structures in Mineralogy

Rather than treating the crystallography and mineralchemistry of pyrrhotite here in details, which are instead covered in the introductory sections of Chapters 2 and 3, I would like to point out a few basic concepts applicable to the structural mineralogy of pyrrhotite and brief the reader for the discussion of Chapter 2.

A basic and general notion is that many crystal structures have variable modular architectures characterized by recurrent slabs of certain structural motifs or modules. This is referred to as polysomatism (e.g., Veblen 1991). Polysomatism is most typically related to the stacking of layer units, as for example seen in many phyllosilicates, such as clays, serpentines, and micas (e.g., Dódony 1997; Nespolo et al. 1997). The stacking can be variable in terms of the internal make-up of modules and their relative sequences. If modules are identical (or nearly identical) in composition and internal structure and only variations in sequence occur, the resulting structures are referred to as polytypes (Guinier et al. 1984). Polytypisms is hence a special case of both polysomatism and polymorphism (Veblen 1991). A classical example from the realm of sulfide minerals is polytypism/polymorphism in zinc sulfide (ZnS), being responsible for the minerals sphalerite (cubic) and wurtzite (hexagonal). Figure 1-1 illustrates that both structures can be considered as stacked sheets of zinc atoms tetrahedrally coordinated by sulfur. Depending on the stacking scheme, either hexagonal or cubic close-packing of sulfur atoms results while the overall stoichiometry of ZnS is not changed. Likewise, many other stacking combinations are possible (Fig. 1-1b) and some indeed occur in synthetic or natural ZnS (Pósfai and Buseck 1997).

In case of pyrrhotite, the situation may be perceived similarly and, because the definition of polytypism allows for some (arbitrarily defined) deviations from uniform composition, structural diversity of pyrrhotites has often been associated with polytypism (e.g., Marusak and Mulay 1980; Kuban 1985).

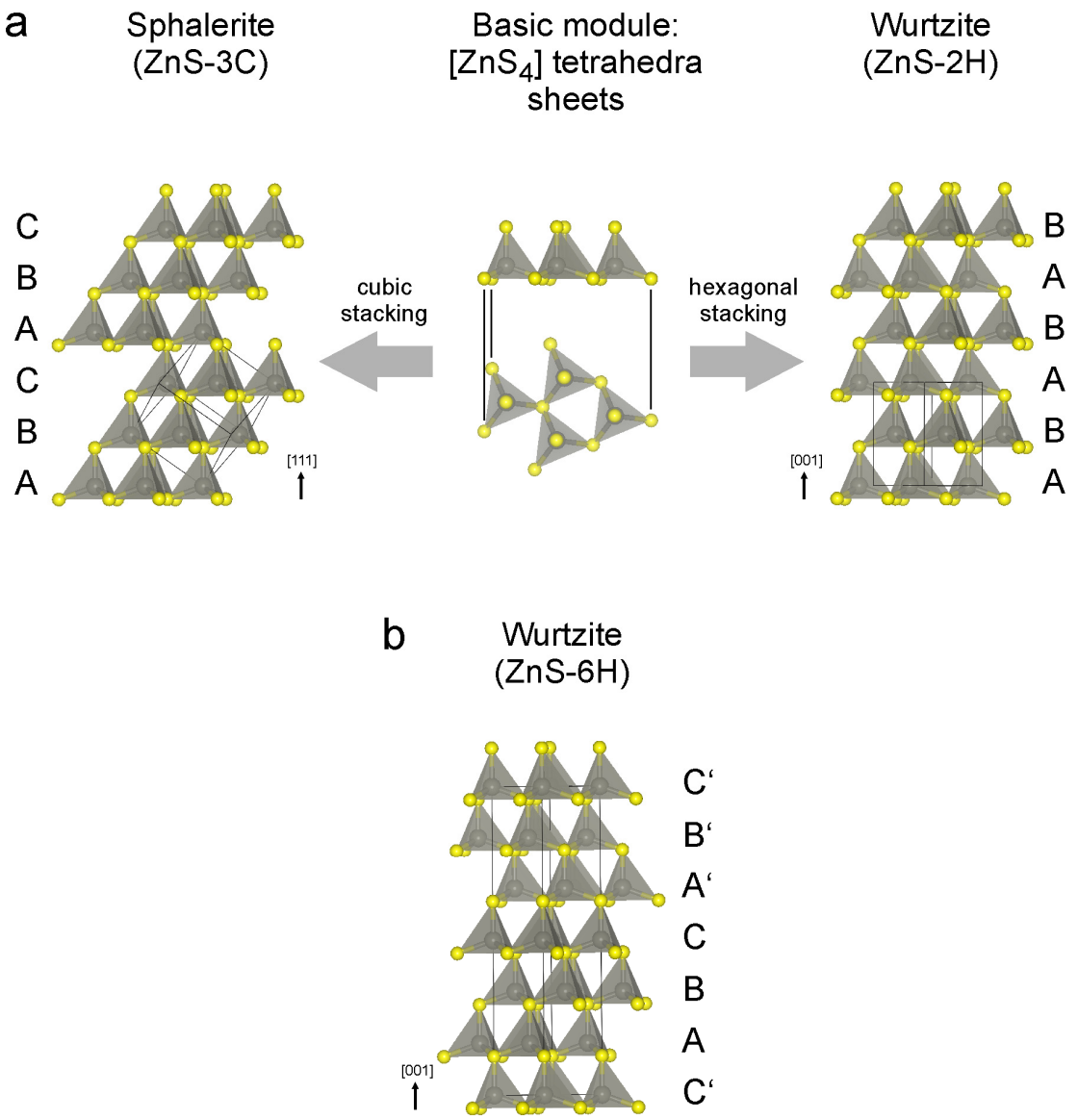

FIGURE 1-1. Polytypes of zinc sulfide (after Pósfai and Buseck 1997), sulfur atoms are yellow, zinc atoms are gray. (**a**) Sphalerite (ZnS-3C) has cubic stacking with a periodicity of 3 basic modules. Wurtzite (ZnS-2H) has hexagonal stacking with a periodicity of 2 basic modules. (**b**) Besides the simple hexagonal ZnS-2H structure, other hexagonal polytypes of wurtzite are possible, in which the stacking periodicity is larger, e.g., ZnS-6H.

The basic modules in pyrrhotite are layers of iron atoms octahedrally coordinated by sulfur (Fig. 1-2). There are two principle types of layers, one with completely filled octahedral Fe positions and one with some Fe positions being vacant (details in Chapter 2). Unlike the case of ZnS, all observed stacking variants of pyrrhotite involve hexagonal-close packing of sulfur atoms and the suggested polytypism in pyrrhotite rests upon stacking of filled layers with four geometrically different vacancy-bearing layers.

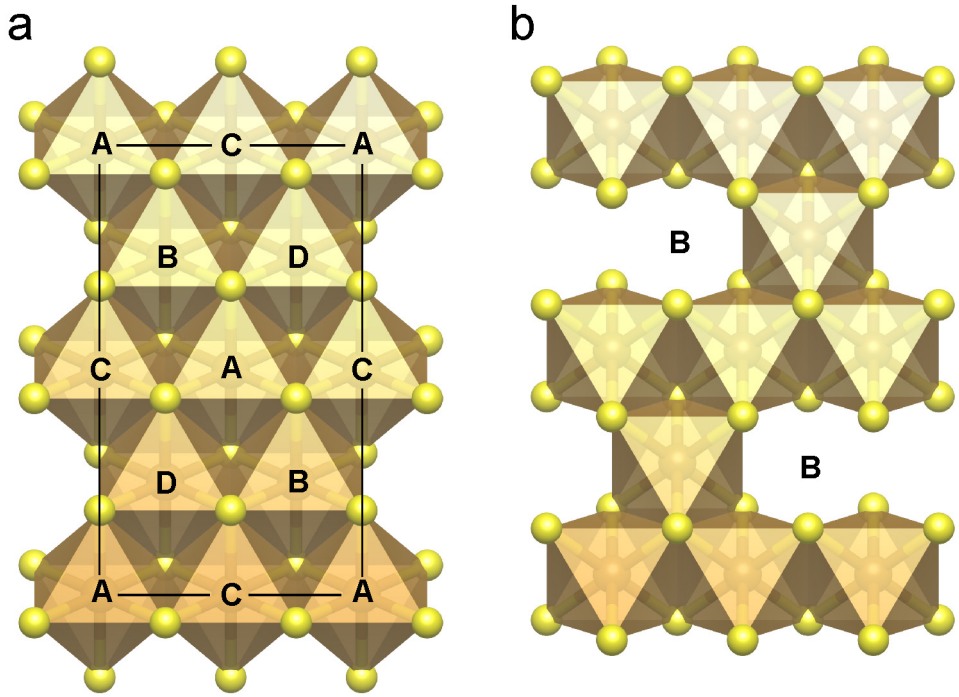

FIGURE 1-2. Basic building modules of pyrrhotite in the polytype model. Sulfur atoms are yellow, iron atoms are brown. (**a**) Iron is sixfold coordinated by sulfur and forms sheets of edge-sharing octahedra. Four different iron positions (A to D) are distinguished in the model. (**b**) One of four layers bearing iron-site vacancies, here the B position is shown vacant. The layer is the next unit to be stacked on the layer shown in (a). The stacking direction is out of the paper plane and stacking results in face-sharing of the octahedra.

In principle, the available five types of layers in pyrrhotite offer infinite stacking combinations, both periodic and aperiodic ones. Although the latter may appear on first sight incompatible with the classical definition of a crystal as a "solid composed of atoms arranged in a pattern periodic in three dimensions" (Cullity 1956), some aperiodic stacking sequences would indeed posses "quasiperiodic" properties that allow the solid to produce well defined Bragg diffraction (Burrows and Sulston 1991) in accordance with the modern definition of a crystal as a "solid having an essentially discrete diffraction diagram" (IUCr 1992). Such quasiperiodic sequences are non-repeating, but follow strict, deterministic patterns and have long-range order (as opposed to stochastic arrangements, which would have missing or streaky diffraction along the reciprocal stacking direction). In fact, the so-called non-integral NC-pyrrhotites are at odds with classical crystallography, because their sharp diffraction patterns cannot be readily indexed by assuming three-dimensional periodicity since the apparent repeat distances imply non-integral or even irrational multiples of the basic stacking units/layers (Morimoto and Nakazawa 1968; Nakazawa and Morimoto 1970).

A mathematically elegant way to reconcile long-range order and aperiodicity in a descriptive model applicable to many quasiperiodic solids is the "superspace modulation" approach of de Wolf, Janner and Janssen (de Wolf et al. 1981 and ref. therein; Chapuis 2003; van Smaalen 2004). This approach describes three-dimensional crystal structures with one aperiodic direction as slices out of fully periodic, four-dimensional structure representations (analogous to a two-dimensional cross-section obtained by slicing a three-dimensional object). In this (3+1)-superspace individual atomic positions within the unit cell are no longer zero-dimensional points but one-dimensional (line-)objects with an assigned modulation function, which specifies displacement or occupancy of an atomic site as a function of position along the direction of the extra dimension. The location of the three-dimensional intersection with the modulation function determines the real atomic displacements and occupancies, and whether the resulting structures are periodic or aperiodic. The structure is said to be one-dimensionally modulated. The necessity to describe one-dimensionally modulated, aperiodic structures in (3+1)-dimensional unit cells becomes apparent from the geometry of diffraction patterns, because they need four integers to be indexed properly (sometimes even macroscopic crystal forms need four integers to be indexed, e.g., Chapuis 2003).

A first application of the superspace approach to pyrrhotite was published by Yamamoto and Nakazawa (1982) and was supplemented by the model of Izaola et al. (2007). Both models use modulation functions to define the occupancy of Fe sites, but the Izaola model uses discrete occupancies (i.e., an atom is either present or not) instead of statistical representations (probability of an atom being present). This facilitates an elegant representation of many possible layer stacking combinations (periodic and aperiodic) in one concise model. However, like conventional crystallographic models, also the superspace approach represent averaged and idealized structures "condensed" into a unit cell and does not particularly specify the nature of stochastically occurring faults or defects that may contribute to the real structural makeup.

As mentioned before, the layer stacking in pyrrhotite is always hexagonal with respect to the sulfur atoms, and hence the many possible stacking variants are basically different arrangements of the Fe site vacancies within the octahedral framework of the fixed sulfur lattice. This is a fundamental difference to the ZnS polytypes, where the structural diversity is contributed by stacking variations and faults of the sulfur layers (i.e., singular or repeated switching between cubic and hexagonal stacking). Suggestions have been

made to describe pyrrhotite structures by invoking planar crystallographic defects known as anti-phase boundaries (APBs; Pierce and Buseck 1974; Nakazawa et al. 1975; Koto and Kitamura 1981), which result from translational displacements of Fe site vacancies within the sulfur lattice (hence, they are translation interfaces as opposed to rotational twins, cf. Fig. 2-2 in Chapter 2). These defects introduce some degree of disorder to the pyrrhotite structure, because, unlike the very static stacking faults in the sulfur lattice, they can move quite freely through the crystal by jumping of Fe atoms between filled and vacant lattice positions, which effectively shifts the vacancies and requires relatively little activation energy (compared to shifting sulfur atoms, Condit et al. 1974).

In principle, there are three states of disorder to be recognized: (i) Vacancies are completely disordered without any short-range interaction. APBs cannot exist and the structure is purely stochastic. (ii) Vacancies and APBs are perfectly long-range ordered. This is analogous to idealistic layer stacking models, and APBs are intrinsic structural elements and not defects *sensu strico*. (iii) In-between the two cases vacancies are ordered, but APBs are not strictly confined and cause variable degrees of disorder by being irregular on mesoscopic length scales much larger than the interatomic distances (e.g., by being wavy). In Chapter 2 we present evidence for the latter case in pyrrhotite.

1.1.3. Pyrrhotite in Earth and Planetary Materials

Magmatic pyrrhotite is a primary phase in unaltered basaltic rocks (Hall 1986) and often occurs closely associated with Ni- and Cu-bearing Fe sulfides. Down to temperatures of about 260 to 300 °C a complete solid solution series exists between metal-deficient $Fe_{1-x}S$ and $Ni_{1-x}S$ and is known as monosulfide solid solution (MSS; Craig 1973; Misra and Fleet 1973). Pentlandite, $(Fe,Ni)_9S_8$, precipitates from MSS below 610 °C (Kullerud 1963; Naldrett et al. 1967), but may also form through inversion of a high temperature pentlandite form (Sugaki and Kitakaze 1998). The addition of Cu to the system adds further complexities (Fleet and Pan 1994; Fleet 2006). Consequently, the mineral parageneses formed in high-temperature magmatic sulfide deposits and sulfide droplets in gabbros and basalts, can be rather rich assortments of sulfide minerals, although pyrrhotite and pentlandite usually dominate (e.g., Prichard et al. 2004). Mostly simpler pyrrhotite-bearing assemblages are frequently found in many silicic magmatic rocks (e.g., Whitney 1984).

Hydrothermally formed pyrrhotite occurs, although mostly subordinate to pyrite (FeS_2),

in polymetallic volcanic-hosted massive sulfide (VMS) and shale-hosted/ sedimentary exhalative (SEDEX) deposits, where it formed from hot, metal-laden solutions in submarine environments (e.g., Ohmoto 1996; Saéz et al. 2011). Its modern precipitation and deposition as µm-sized crystals from the black plumes of deep sea 'black smoker' vents is well documented (Converse et al. 1984; Herzig and Hannington 1995). In epigenetic hydrothermal systems and metasomatic ore deposits pyrrhotite can occur locally in abundance, but only if conditions are sufficiently reducing to prevent formation of pyrite or oxidized sulfur species (Hall 1986).

Pyrrhotite occurs in sedimentary environments, but its often proposed formation during early diagenesis has been challenged and most pyrrhotite is likely of detrital origin (Horng and Roberts 2006). From a physicochemical point of view pyrrhotite formation in low-temperature, reduced sedimentary environments is unlikely even under the most favorable conditions (Hall 1986; Horng and Roberts 2006). Instead, pyrite and other monosulfide phases such as mackinawite (tetragonal FeS), greigite (Fe_3S_4), and possibly smyhite (Fe_9S_{11}) form (Rickard and Luther 2007).

In metamorphic rocks, the stability of pyrrhotite relative to pyrite is primarily determined by temperature and the redox state, namely by the fugacities of oxygen (fO_2) and sulfur (fS_2), which are themselves controlled by fluid transport (i.e., H_2S removal), buffering mineral assemblages, and the content of carbonaceous matter (Hall 1986). Pyrrhotite and MSS are known from a variety of rocks from Earth's upper mantle, which are accessible as xenoliths in basaltic and kimberlitic/lamproitic volcanic rocks (e.g., de Waal and Calk 1975; Tsai et al. 1979; Shaw 1997). The very redox-sensitive thermochemistry of pyrrhotite/MSS has been used to infer fO_2 and fS_2 of the lithospheric mantle using the equilibrium with fayalite and ferrosilite components in coexisting olivine and orthopyroxene (Eggler and Lorand 1993; Fig. 1-3). Pyrrhotite as part of exsolved MSS frequently occurs as inclusions in mantle-derived diamonds (Sharp 1966; Taylor and Liu 2009) and could be used as a physical geobarometer based on its pressure-dependent magnetic properties (Clement et al. 2008; Gilder et al. 2011).

In extraterrestrial materials, troilite (stoichiometric FeS) occurs extensively in almost all classes of meteorites (Rubin 1997). Non-stoichiometric pyrrhotite (+pentlandite) is present several chondritic meteorite groups, particularly in the carbonaceous CI, CM, and CK chondrites and the Rumuruti group (Kerridge 1976; Kerridge et al. 1979a,b;

Kallemeyn et al. 1991; Geiger and Bischoff 1995; Rubin and Kallemeyn 1989; Schulze et al. 1994), in interplanetary dust particles (IDPs; Zolensky and Thomas 1995; Dai and Bradley 2001), and in samples of comet 81P/Wild 2 returned by NASA's Stardust mission (Berger et al. 2011).

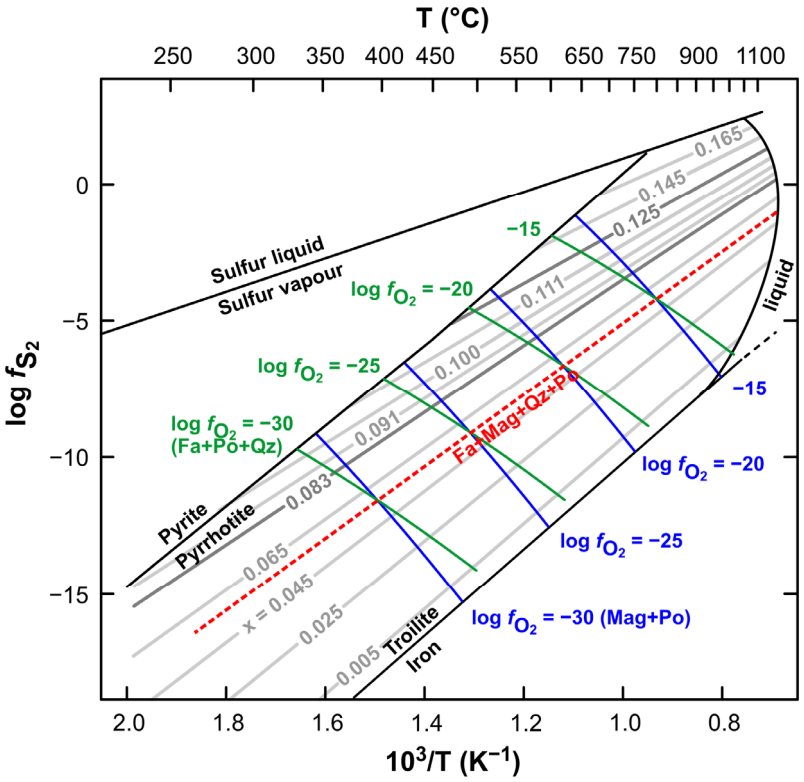

FIGURE 1-3. Thermochemistry of pyrrhotite (at 1bar). The composition of pyrrhotite at high temperatures depends on fS_2 and T, shown as isopleths of x values in $Fe_{1-x}S$ (gray, Toulmin and Barton 1964; Rau 1976). The pyrrhotite stability field is bounded by reactions forming iron (low fS_2) and pyrite (high fS_2). Pyrrhotite can undergo reactions with oxides and these can be used to formulate fS_2 buffers, exemplarily shown for the fayalite-magnetite-quartz-pyrrhotite (Fa+Mag+Qz+Po) buffer (red dashed line, after Eggler and Lorand 1993). The buffer curve results from the intersection of equivalent fO_2 isobars that relate to two basic reactions: Fe_2O_3 (Mag) + S_2 ↔ 2FeS (Po) + 1.5O_2 (blue isobars) and Fe_2SiO_4 (Fa) + S_2 ↔ 2FeS (Po) + SiO_2 (Qz) + O_2 (green isobars). The isobars are derived by relating the activity of FeS in $Fe_{1-x}S$ for given reaction, temperature, and fO_2 to the x value and fS_2 using the relations of Toulmin and Barton (1964) and Rau (1976).

These materials date back to the early Solar System about 4.56 Ga ago when the collapse of an interstellar molecular cloud (i.e., a vast region of enhanced gas and dust density) led to the formation of the proto-Sun and an envelope and later encompassing disk-like body of dense gas and dust, known as the solar nebula or protoplanetary disk (Alexander et al. 2001; Boss 2003). Their primary components formed by evaporation and condensation of dust in exchange with a gas phase of approximate solar composition and

were processed in the complexly evolving disk environment, which experienced multiple heating events and extensive transport and mixing of debated origin (e.g., Krot et al. 2009). These processes led to the formation of coarse-grained, up to mm-sized objects (e.g., Mg,Fe silicate spherules or 'chondrules', the namesakes for 'chondrites') that accreted to form planetesimal bodies (Chiang and Youdin 2010). The materials named above are considered 'primitive', because they have never been subjected to melting and differentiation in their parent planetesimal bodies. However, many of these bodies experienced secondary effects by hydrothermal alteration (Brearley 2006), sub-solidus thermal metamorphism (Huss et al. 2006), or impact-related shock metamorphism and brecciation (Bischoff and Stöffler 1992). Distinguishing fingerprints for these processes are difficult to constrain and Chapter 3 goes into detail about these problems.

Pyrrhotite appears to be relatively rare in meteorites that formed as products or residues of partial melting and melt segregation ('achondrites', lacking chondrules). However, pyrrhotite is well documented in achondrites of the shergottite-nakhlite-chassignite (SNC) group (Rochette et al. 2001; Lorand et al. 2005; Chevrier et al. 2011), which bear resemblance to terrestrial basalts and ultramafic rocks and originated on Mars (Treiman et al. 2000). The possibly widespread distribution of pyrrhotite on the surface of Mars might relate to observed magnetic anomalies (Rochette et al. 2001), and some evidence suggests that pyrrhotite and silicates were subjected to alteration or weathering processes while still residing on Mars (Treiman 2005; Chevrier et al. 2011).

1.1.4. Oxidation and Dissolution of Pyrrhotite

Albeit pyrrhotite occurs occasionally abundantly in many ore deposits, its own economic value is practically nil and commonly its associated phases, like pentlandite, are the main focus of mining and mineral processing (e.g, Becker et al. 2010). In order to reduce environmentally detrimental SO_2 emission from smelting processes, mineral processing aims at enhancing the valuable phases and reducing the pyrrhotite content in the ore concentrates. Because the magnetic behavior of pyrrhotite varies extensively (e.g., Schwarz and Vaughan 1972) magnetic separation is difficult to apply and commonly flotation is the method of choice in processing of pyrrhotite bearing ores. Flotation exploits the intrinsic or induced hydrophobic surface properties of minerals to separate them in streams of air bubbles passing through a mineral suspension in water (e.g., Fuerstenau et al. 2007). Pyrrhotite can have self-induced or intrinsically hydrophobic

surfaces (Buckley and Riley 1991) and, in principle, could be separated from hydrophilic minerals with reduced application of expensive and environmentally problematic surfactants ('collectors') used modify the grain's surface properties. However, oxidation of pyrrhotite surfaces and the formation of hydrophilic Fe oxyhydroxide layers can significantly impair the efficiency of flotation and studies have shown that different types of pyrrhotite have distinct susceptibilities to surface oxidation during processing (Ekmekçi et al. 2010; Becker et al. 2010).

Once economically barren sulfides have been separated from the ore, they are usually stored in tailings repositories or used to refill mine workings. Similarly, pyrite- and pyrrhotite-bearing waste rock from mining activity is dumped or used as backfill. Both in surface and underground settings, sulfides exposed to oxygen-containing surface waters start to oxidize. As detailed in Chapter 4 for pyrrhotite, the weathering process can lead to the production of acid and the consequential decreases of the pH of effluent mine waters. This problem is known as 'acid mine drainage' (AMD) or 'acid rock drainage' (ARD; if unrelated to mining) and has stimulated intensive research in the recent years (e.g., Jambor et al. 2003; Hudson-Edwards et al. 2011), because such waters can have tremendous environmental and economic impacts by disrupting riverine ecosystems (e.g., Gray 1997; Gray and Delaney 2010) and transporting toxic metals and semi-metals (e.g., Ni, Cu, As) in their mobile, dissolved state (e.g., Cheng 2008 et al; Nordstrom 2011), capable of endangering human health.

Research has focused both on the generation of AMD and the mitigation and remediation of its effects (e.g., Johnson and Hallberg 2005; Lottermoser 2011) and thereby much attention has concentrated on the weathering of pyrite, undoubtedly the most common source of AMD. However, the contribution of pyrrhotite to AMD can be significant (e.g., Belzile et al. 2004; Moncur et al. 2009; Jamieson 2011), and it is known that the rates of oxidation and dissolution of pyrrhotite can exceed those of pyrite by factors of 20 to 100 (Nicholson and Scharer 1994). Research of the past decades has also shown that microbiological interactions play a significant role in enhancing the weathering rates of Fe sulfides (e.g., Johnson and Hallberg 2003; Hallberg 2010). Hence, the knowledge of the intrinsic physicochemical properties of pyrrhotites, as detailed in Chapter 4, is important to predict the mineral's behavior in mining environments and mineral processing and serves as important benchmark for the evaluation of how microorganisms affect weathering processes. Aside from mining environments this

understanding is of general interest in the light of growing recognition of Earth's 'critical zone', where rocks interact with the atmosphere, hydrosphere, and biosphere (e.g., Anderson et al. 2007). The occurrence of pyrrhotite not only in terrestrial rocks but also in chondrites and particularly on the surface of Mars (section 1.1.3) renders pyrrhotite's alteration behavior interesting for the understanding of water-rock interactions in asteroidal (or cometary) bodies and the evolution of the 'critical zone' on planetary surfaces.

1.2. Novel and Specialized Methods

This section serves to explain some of the newer or more unusual techniques deployed in the research presented in this dissertation. Operation details on these and the conventional methods used are provided in the respective chapters.

1.2.1. Focused Ion Beam Preparation

In the recent years focused ion beam (FIB) microscopes have become widely available in material sciences (Volkert and Minor 2007) and find increasing application in Earth and planetary sciences (e.g., Heaney et al. 2001; Lee et al. 2003; Zega et al. 2007). The working principle of a FIB microscope is comparable to a conventional scanning electron microscope (SEM). Instead of an electron source, a liquid metal ion source (LMIS) is used, which commonly invokes gallium due to its low melting point (~30 °C) and low vapor pressure (Volkert and Minor 2007). Within the LMIS, gallium forms a thin film on a sharp metal tip and Ga^+ ions are extracted from this by field emission through application of a high extraction voltage. The ions are then accelerated (typically to 2−30 keV) and focused by electrostatic lenses into a narrow beam, which scans the sample surface analogously to an SEM. Similarly to a high energy electron beam, the impact of ion produces secondary electrons that can be detected to form images. In modern FIB microscopes the physically limited lateral image resolution can reach about 10 nm (Volkert and Minor 2007).

Unlike SEM, FIB microscopy is inherently damaging to the sample, because the large size and momentum of impacting ions leads to ejection ('sputtering') of the sample's atoms. However, this effect has been made advantageous use of by combining the high resolution, controllability, and sputtering efficiency of FIBs to do microscale machining on sample surfaces. One particularly important development is the capability of preparing

<100 nm thin lamellae for TEM studies with very high spatial selectivity. TEM samples can be obtained from regions as small as 10×10 µm without damaging the surrounding material (Fig. 1-4). This is particularly useful to target scarce or locally very confined features that would be nearly impossible to prepare by conventional methods (e.g., ion milling, ultramicrotomy).

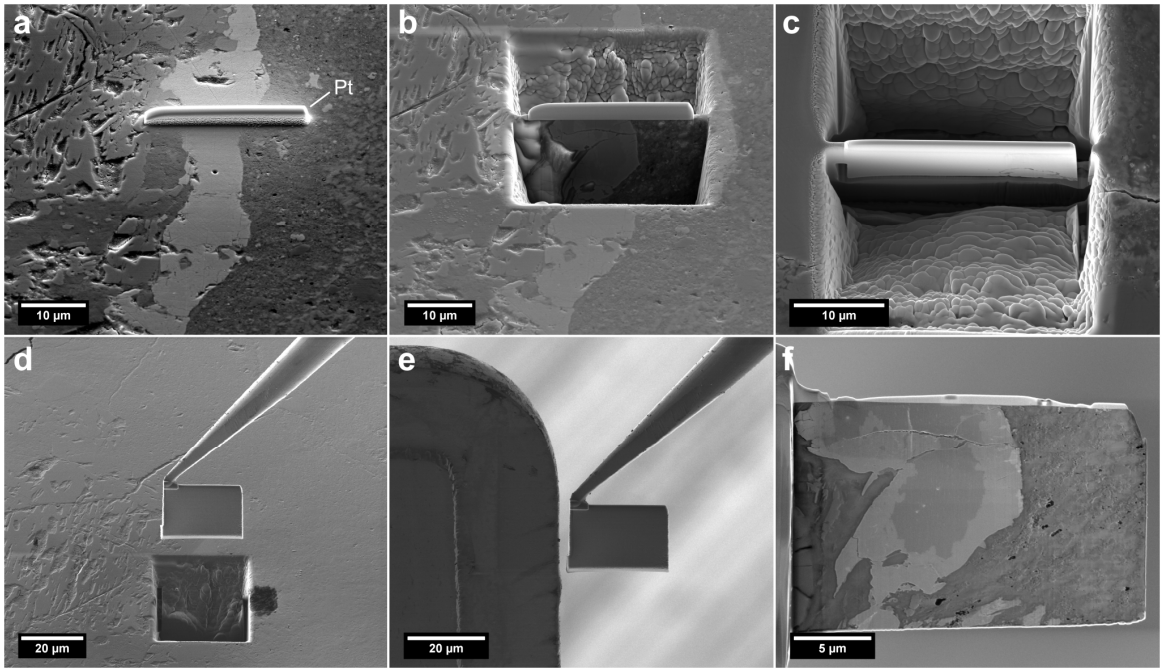

FIGURE 1-4. FIB sample preparation for TEM (SEM secondary electron images). (**a**) A platinum strip is deposited on the site of interest. (**b**) The surrounding material on either side of the intended TEM lamella is sputtered away by the ion beam. (**c**) The lamella is reduced in thickness (~ 0.5 µm), cleaned, and cut free by the ion beam. Only one attaching point remains (left side). (**d**) A tungsten needle micromanipulator is welded to the lamella by platinum deposition. The remaining attaching point is sputtered away and the lamella is extracted. (**e**) The lamella is attached to the post of a TEM grid by platinum deposition and the tip of tungsten needle is cut off. (**f**) The lamella is then thinned to final, electron-transparent thickness (< 100 nm ideally) by use of the ion beam.

Commonly, modern FIB systems consist of a 'dual beam' arrangement, which combines an SEM column with an inclined FIB column and allows monitoring the sample non-destructively by electrons while performing micromachining by ions. Notably, modern FIB preparation is not only capable of removing material, but also provides addition of material via ion-beam-assisted chemical vapor deposition, which serves to provide protection and 'glue' to the prepared sample. Mostly deployed is the deposition of platinum through injection of an organo-metallic gas into the vacuum that adsorbs to the sample surface and is dissociated by the secondary electrons produced by the ion beam (e.g., Puretz and Swanson 1992). Careful beam current control allows achieving net

growth of material instead of sputtering, and, in principal, deposition can be accommodated also by the electron beam in order to further reduce damage (albeit at much slower deposition rate).

1.2.2. TEM Superstructure Dark-Field Imaging

TEM dark-field imaging is a powerful method to study structural details, particularly defects, in crystals. In brief (based on Williams and Carter 2009), the functioning principle of a TEM rests upon an electron beam interacting with the sample's atoms through elastic and coherent scattering. The incident beam can be equally described as a plane wave front, which interacts with the (quasi-)periodically arranged electrostatic atomic potentials of the thin specimen to form an interference or diffraction pattern in the back-focal plane of the objective lens (Fig. 1-5).

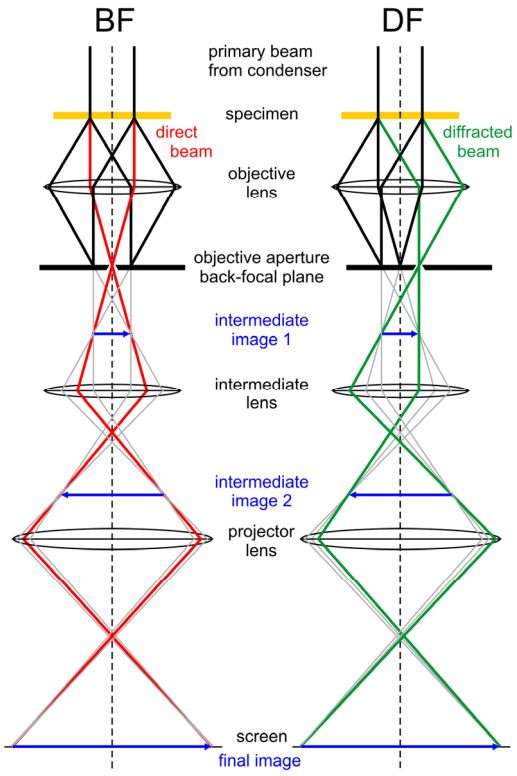

FIGURE 1-5. Principles of bright-field (BF) and dark-field (DF) TEM imaging (after Williams and Carter 2009). In BF mode, the direct beam contributes primarily to the image. In DF mode, the image is formed from a diffracted beam. Both images show the same region of the sample, but the contrast of the images differs.

Diffraction patterns represent sections through the reciprocal crystal lattice (basically related to its Fourier-transformed electron density) and can be either projected on a screen or recombined into real images. In this process, each interference maximum, corresponding to a Bragg reflection or diffracted beam, contributes partial information to the final image, and commonly TEM employs apertures of variable sizes placed in the objective's back-focal plane to control the specific contributions.

In bright-field (BF) mode the image is formed from the direct beam (passing straight through the sample without diffraction) and optionally some of the diffracted beams. In dark-field (DF) mode the image is formed from one or (rarely) few diffracted beams. Because each beam carries distinct partial information of the sample's image, the DF images obtained from different beams show distinct details. Such details can be for

example dislocations (linear defects due to displaced atoms), which cause local anomalies in lattice spacings and appear prominently in DF images when the selected diffracted beam corresponds to the disturbed lattice periodicity.

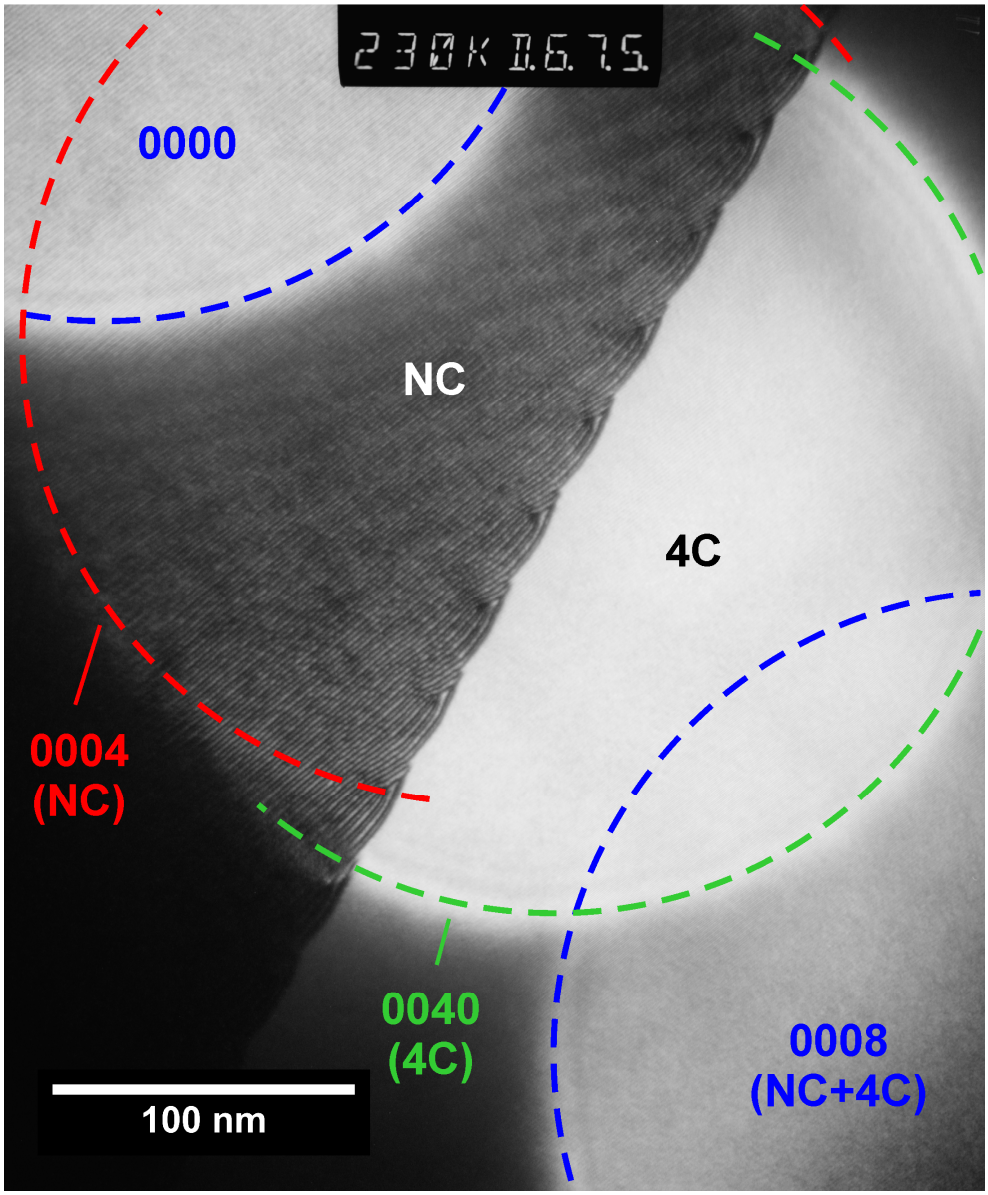

FIGURE 1-6. Explanatory example of TEM-SDF imaging. Shown is a coherent interface between 4C- and NC-pyrrhotite under non-parallel illumination conditions. Because the incoming electron beam is convergent, several disks of diffracted beams are seen, despite a small objective aperture is used. The dark stripes and node structures are APBs in the NC structure (cf. Chapter 2). They are not (or only very weakly) visible in the direct 0000 beam (corresponding to a BF image). The 0008 beam is a fundamental reflection common to both structures and APBs would be invisible as well, if the beam originated from the NC region. The 0004 and 0040 beams are related superstructure reflections of the NC and 4C structures, respectively, and form SDF images. For better image quality the convergence of the incoming beam would be reduced to obtain close-to parallel illumination. The 0000 and 0008 beam images would then out of the image frame.

Structural features of particular interest in Chapter 2 are translation interfaces, which, in this case, are anti-phase boundaries (APBs; cf. Fig. 2-2). Such interfaces separate crystal domains, which have relative phase differences of their periodic atomic potentials. These phase differences become imposed on the interfering electron wave (e.g., Amelinckx 1972) and result in dark fringes along the domain boundaries in DF images of certain diffracted beams (Fig 1-6). Because APBs only occur in materials that display ordering phenomena (superstructures) superposed on more simple, fundamental crystal structures, APBs are only visible (clearly) in DF images obtained with diffracted beams that relate to the superposed (quasi-)periodicity (e.g., Amelinckx 1972). In Chapter 2 DF images are obtained from such superstructure diffraction, and hence the technique is referred to as TEM superstructure dark-field (TEM-SDF) imaging.

1.2.3. Quantitative 3D Topometry

Quantitative 3D topometry aims at obtaining a 3-dimensional surface representation of an object in order to quantify processes, particularly mass losses or gains, occurring at that surface. On microscopic scales there are three major techniques employed for this purpose: i) atomic force microscopy (AFM) ii) interferometric microscopy, and iii) confocal microscopy.

While AFM is intrinsically most suitable to topographies in the sub-µm range, interferometric and confocal microscopy can capture wider ranges of surface heights up to the µm range and provide larger fields of view (e.g., Conroy and Armstrong 2005). In the study outlined in Chapter 4 a vertical scanning confocal microscope with Nipkow disk was used. The principle of confocal light microscopy bases on a µm-sized pinhole aperture in front of the detector, which permits only those beams to pass that originated in the focal plane of the objective lens (Fig. 1-7). Light coming from the defocused region of the specimen is therefore suppressed. Owing to the fact that the confocal principle works basically only with point light sources and point detectors, a multi-pinhole or Nipkow disk, replacing the single pinhole aperture, is inserted into the beam path in order to obtain confocal images. The rapidly rotating disk contains pinholes in a spiral arrangement and therefore acts as a scanning point light source and provides at the same time detector pinholes for the pixels of a conventional CCD detector (Conroy and Armstrong 2005).

3D representations of surfaces are obtained by moving the objective, and hence its focal plane, in steps of 5 to 100 nm vertically relative to the specimen through use of very

accurate, piezo-driven actuators. At each step a confocal image is obtained. Because objectives of high numerical aperture are used, which result in very narrow depths of focus, only very narrow height regions of the sample are imaged in each step (similar to contour lines on topographic maps). Software is then used to reconstruct the surface topography from the obtained image stack.

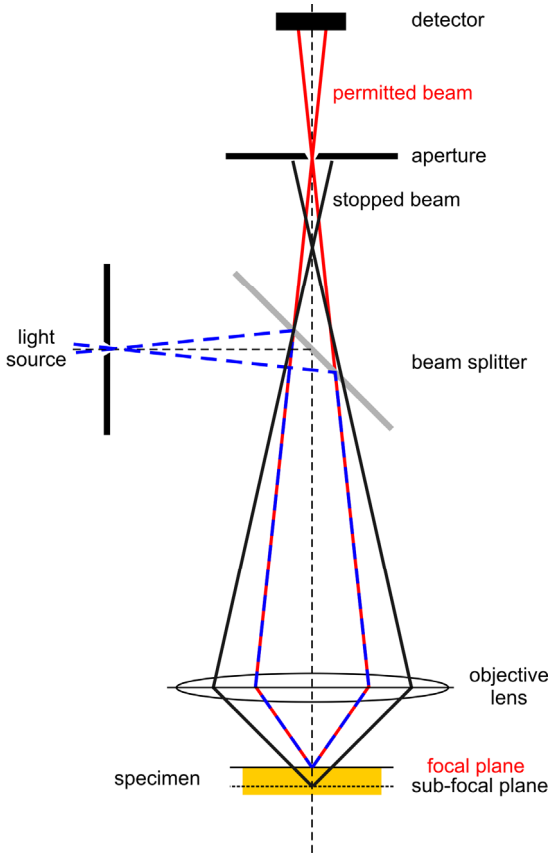

FIGURE 1-7. Principle of confocal light microscopy (after Conroy and Armstrong 2005). A pinhole aperture in front of the detector only permits light to pass that originated in the focal plane of the objective lens. Light from out-of-focus regions is blocked.

1.3. Detailed Summary and Linkage of Research Studies

The overall focus of this cumulative dissertation is to comprehend the relations of the nanoscale real structure of pyrrhotite to its physicochemical properties. It investigates the occurrences and nature of pyrrhotite superstructures, examines the related nano- and microstructural phenomena, and explores their effects on chemical reactivity. The goals are to shed light on the structural complexity of natural pyrrhotites, both terrestrial and extraterrestrial, and understand the effects of this complexity on its behavior in cosmochemical and geochemical processes, particularly related to alteration processes by physical and chemical environments, in which pyrrhotite is thermodynamically unstable.

Besides this introduction, the dissertation consists of three research articles written by me as first author and submitted to or accepted by major journals in the field. These articles constitute the Chapters 2, 3, and 4. Initially, the nanoscale complexity of natural, terrestrial pyrrhotites is investigated in three detailed studies (Chapter 2). Building upon this, two case studies follow, which investigate two very different alteration environments. One focuses on a phenomenological study of pyrrhotite in extraterrestrial materials, which experienced aqueous and thermal alteration (Chapter 3), the other focuses on an experimental study of oxidative dissolution applicable to terrestrial mining environments (Chapter 4).

Chapter 2 (published in the *American Mineralogist*) lays out and refines the fundamental concept of how to understand the crystallographic real structures of natural pyrrhotites by using transmission electron microscopy techniques. It presents a new conceptual model that reconciles the complex diffraction patterns and nanoscale structures of pyrrhotites and bridges between defect structure models (e.g., Pierce and Buseck 1974) and idealized superstructure representations (Izaola et al. 2007). Moreover, the observations put constraints on low-temperature stable phase relations that have not been detailed before.

The results show that complex and variable NC-type pyrrhotites can be crystallographically described in a novel way as a continuum of aperiodically modulated structures, in which the modulating entities are anti-phase domain boundaries (APBs) related to the ordering of Fe-site vacancies. Based on the geometry of electron diffraction patterns and structural considerations it is for the first time shown that APBs are chemically non-conservative and change the composition of the host pyrrhotite crystal

structure toward more Fe-rich compositions. Hence, the density and regular (modulated) arrangement of APBs is found to be the key to understand the correlation between superstructure and Fe/S ratio of pyrrhotite. The new model challenges the previous concept of polytypism and modular structural hierarchy in pyrrhotites, because APBs can, and by evidence do, introduce much more dynamical structural variation than a rigid modular model could account for. In three terrestrial samples investigated, exsolved assemblages of 4C-pyrrhotite and NC-pyrrhotite occur. In these assemblages, the N value of the NC phase (characterizing the superstructure) varies between 4.78 and 4.92 and common mesoscopic self-organization of APBs into narrow node structures at phase interfaces suggest that these phases are in equilibrium. A terrestrial example of troilite exsolution in NC-pyrrhotite with N between 5.12 and 5.52 shows indications for incomplete phase equilibration. (*Note*: In Chapter 2 we speak of N_c values, these are equivalent to the N values discussed elsewhere. The reason to specify N_c and $N_{[uv0]}$ is due to the discussion of diffraction features, which are of specific interest in Chapter 2 but in general rarely observed, see Fig. 2-5)

Chapter 3 (submitted to *Meteoritics and Planetary Science*) builds upon Chapter 2 by exploring the nanoscale mineralogy of extraterrestrial pyrrhotites in a case study invoking novel FIB sampling technology. The unique samples not only corroborate the phase relationships by Nakazawa and Morimoto (1970), but also show resolvable differences that imply distinct low-temperature histories over time spans unattained by any terrestrial pyrrhotite. A key aspect in the study of petrogenetic processes is the linkage between pyrrhotite's superstructure crystallography and its composition, which was formulated in the model of Izaola et al. (2007) and confirmed and refined in Chapter 2.

Pyrrhotite has received relatively little attention in meteorite studies, mostly due to its similarity to stoichiometric and more abundant troilite. This study clearly demonstrates, that extraterrestrial pyrrhotite in carbonaceous chondrites displays the same structural complexity as its terrestrial counter parts. In compact sulfide grains of CM2 chondrites the pyrrhotite is NC-pyrrhotite with N values between 5.63 and 6.01 and occurs in exsolution association with troilite and pentlandite. This association is close to the 6C-pyrrhotite-troilite assemblage proposed to be in equilibrium at room temperature (Nakazawa and Morimoto 1970). A comparison of a pristine and a mildly metamorphosed CM2 chondrite suggest that slower cooling rates led to N values closer to 6 in accordance with the

suggested gradual evolution of N values toward the 6C structure (Nakazawa and Morimoto 1970). The additional, novel finding of polycrystalline 4C-pyrrhotite and the observation of dissolution features indicates complex physicochemical formation and transformation conditions of Fe sulfides in these meteorites. In anomalous, strongly thermally metamorphosed carbonaceous chondrites related to the CM and CI groups, pyrrhotite converted to troilite and metallic iron, indicating very reducing conditions connected to low sulfur fugacity Detailed TEM observations however show that the outermost portions of troilite grains converted back to vacancy-bearing pyrrhotite and provide for the first time evidence for a retrograde metamorphic episode. The interpretation of physicochemical conditions of sulfide formation and metamorphosis in this work relies strongly on the relationships between the vacancy content of pyrrhotite, temperature, and sulfur and oxygen fugacities. These relationships set the preconditions for the complex evolution of pyrrhotite's superstructures and low temperature phase assemblages upon cooling, and hence their understanding requires consideration of how crystallographic structures relate to chemical composition and physicochemical environments. Chapter 3 demonstrates this in unprecedented detail.

Chapter 4 (submitted to *Geochimica et Cosmochimica Acta*) treats the physicochemical properties of pyrrhotite surfaces and, for the first time, reveals clearly the influence of pyrrhotite's vacancy superstructures and anisotropy on its kinetic behavior during oxidative dissolution (cf. Belzile et al. 2004). The experimental study primarily bases on a natural sample characterized in depth in Chapter 2, and the interpretation of results extensively employs the structural model established therein. In Chapter 3 evidence for aqueous dissolution of chondritic pyrrhotite is presented, and, although fluid conditions were like very different to those studied experimentally, the yet little facilitated experimental approach of Chapter 4 could be utilized for future studies of these and similar processes.

In a novel approach, the study subjected structurally coherent assemblages of terrestrial 4C- and NC-pyrrhotite (N ≈ 4.8 to 4.9) to oxidizing, acidic solutions and dissolution rates were derived by quantitative, confocal 3D topometry. Transmission and scanning electron microscopy in conjunction with focused ion beam preparation have been used to correlate textural and mineralogical observations with the dissolution data. The results show that the surface dissolution kinetics and interface morphologies are strongly controlled by

crystallographic anisotropy and surface charge. A strong change in kinetic behavior occurs at a pH value of 2.70 at 35 °C, which most likely corresponds to the isoelectric point of pyrrhotite surfaces. The abundant formation of elemental sulfur at pH values below this transition points to incomplete oxidation of sulfide and strengthens the interpretation that the availability of iron on the exposed surfaces of pyrrhotite is the main controlling factor on rates of oxidative dissolution. Above the transition, no elemental sulfur precipitates and reaction rates on previously reactive surfaces drop sharply by almost two orders of magnitude. Most remarkably, very pronounced, intrinsic reactivity differences of +80 to −50 % (depending on pH) exist among 4C- and NC-pyrrhotite. Because their Fe/S ratios differ only marginally, this is clear evidence that APBs originating from vacancy ordering exert strong control on chemical processes at the mineral surface. A key aspect in the understanding of the reactivity differences appear to be chains of face-sharing FeS_6 octahedra, which occur in the pyrrhotite structure and exhibit strong axial electronic interactions. These chains are truncated by Fe-site vacancies, but are longer in case of NC-pyrrhotites, where non-conservative APBs add additional Fe atoms to the structure. This might increase the reactivity NC-pyrrhotite compared to 4C-pyrrhotite due to easier interaction between oxidant species and the Fe electronic system. In accordance with the discussion in Chapter 2, these ideas again exemplify that the rigid and modular layer model of pyrrhotites may be inappropriate to describe realistic pyrrhotite structures and their bearing on physicochemical properties.

In conclusion, the combination of evidence from the three research studies demonstrates that the complex and variable crystallographic real structures of pyrrhotite correlate with its physicochemical properties and behaviors. The structural diversity of pyrrhotite is a key aspect to understand the petrogenetic histories of pyrrhotite-bearing rocks as well as natural and anthropogenically induced weathering processes. Particularly, future studies of the complex magnetic properties of pyrrhotite and pyrrhotite-bearing rocks and of the yet poorly understood structure modifications of pyrrhotite at intermediate temperatures between about 200 to 320 °C could benefit from the evidence and models presented in this thesis.

1.4. Author Contributions

In Chapters 2 and 4, Dr. Kilian Pollok (K.P.) and Prof. Dr. Falko Langenhorst are co-authors of the published or submitted research articles. In Chapter 3 F.L. is co-author of the submitted article. K.P. conceived and proposed the project to study the influence of microstructures on the weathering behavior of monosulfides and conduct basic research on the real structures of natural pyrrhotites. F.L. suggested to study microstructures and alteration processes in meteoritic pyrrhotites. Both supported the research and contributed valuable expertise, particularly in TEM work. I selected all samples, carried out all analytical characterization, and processed and evaluated the analytical data. I conceived and designed the experiments of Chapter 4, acquired the experimental and analytical data, and processed and evaluated them. I interpreted the data and developed the ideas and concepts presented in Chapters 2, 3, and 4. I wrote the manuscripts reproduced therein and created all figures. The manuscripts incorporate valuable comments and suggestions by K.P. and F.L. Chapter 2 incorporates suggestions from reviews by Prof. Dr. Allan Pring and an anonymous reviewer. In summary, I contributed at least 90 % to the work and concepts presented in Chapters 2, 3, and 4.

1.5. Publications Connected to This Dissertation and Related Work

Articles, Peer Reviewed and Published

Harries D., Pollok K., and Langenhorst F. (2011) Translation interface modulation in NC-pyrrhotites: Direct imaging by TEM and a model toward understanding partially disordered structural states. *American Mineralogist* **96**, p. 716−731 (**Chapter 2**).

Articles, Submitted and in Review

Harries D. and Langenhorst F. (2012) The Nanoscale Mineralogy of Fe,Ni Sulfides in Pristine and Metamorphosed CM- and CM/CI-like Chondrites: Attempting to Tap a Petrogenetic Record. Submitted to *Meteoritics and Planetary Science* on December 12, 2011. (**Chapter 3**).

Harries D., Pollok K., and Langenhorst F. (2012) Oxidative dissolution of 4C- and NC-pyrrhotite: Intrinsic reactivity differences, pH dependence, and the effect of anisotropy. Submitted to *Geochimica et Cosmochimica Acta* on January 9, 2012. (**Chapter 4**).

Conference Contributions

Harries D., Berg T., Palme H., and Langenhorst F. (2011) The fate of metals in the solar nebula: From condensation to oxidation, sulfidation, and nitridation. Workshop on Formation of the First Solids in the Solar System (Kaua'i, USA), abstract 9071. (Poster presentation).

Harries D., Pollok K., and Langenhorst F. (2011) Pyrrhotite oxidative dissolution: Crystallographic and microstructural controls observed by FIB-TEM and 3D topometry. Joint Meeting of DGK, DMG and ÖMG (Salzburg, Austria), abstract 145.

Harries D., Pollok K., and Langenhorst F. (2011) Pyrrhotite oxidative dissolution: A microstructural perspective by FIB-TEM and surface topometry. 21st Annual V. M. Goldschmidt Conference (Prague, Czech Republic). *Mineralogical Magazine* **75**, p. 980.

Harries D. and Langenhorst F. (2011) Nanocrystalline P-bearing pentlandite and chromium nitrides from CM2 chondrites Y-791198 and Y-793321. 74th Annual Meteoritical Society Meeting 2011 (Greenwich, United Kingdom), abstract 5165.

Harries D. and Langenhorst F. (2011) Sulfides in CM and CM/CI-like chondrites and their record of thermal metamorphism: A FIB-TEM study. 74th Annual Meteoritical Society Meeting 2011 (Greenwich, United Kingdom), abstract 5166.

Harries D., Fabian K., Pollok K., and McEnroe S.A. (2011) Correlation of microstructures and exsolution lamellae in natural pyrrhotites and magnetic properties. EGU General Assembly 2011 (Vienna, Austria), abstract 12987.

Harries D., Berg T., Palme H., and Langenhorst F. (2011) The structure of refractory metal alloys, condensates from the early solar nebula. 42nd Lunar and Planetary Science Conference (The Woodlands, USA), abstract 1837.

Mang Ch., Kontny A.M., Harries D., Langenhorst F., and Reimold, U. (2010) Shock deformation and nucleation of magnetic minerals in suevites of the Chesapeake Bay impact crater, USA. AGU Fall Meeting 2010 (San Francisco, USA), abstract

GP43B-1056.

Pollok K., Harries D., Hopf J., Etzel K., Chust T., Hochella M.F., Hellige K., Peiffer S., and Langenhorst F. (2010) Microstructural controls on monosulfide weathering and heavy metal release (MIMOS). Geotechnologien Science Report No. 16, Status Seminar 2010 (Mainz, Germany), p. 182-197.

Harries D. and Langenhorst F. (2010) A FIB-TEM study of sulfide mineralogies in CM chondrites. Paneth Kolloqium 2010 (Nördlingen, Germany), abstract volume.

Harries D., Pollok K., and Langenhorst F. (2010) Translation interface modulation in pyrrhotite: Structural self-organisation observed by transmission electron microscopy. 88th Annual Meeting of the DMG (Münster, Germany), abstract volume.

Pollok K., Chust T., and Harries D. (2010) From surface morphology to rates: An automated routine to evaluate converged roughness parameters of heterogeneous surfaces. 88th Annual Meeting of the DMG (Münster, Germany), abstract volume.

Harries D., Pollok K., and Langenhorst F. (2010) Self-organisation in the modulated structure of pyrrhotite: Direct observations by TEM. 20th General Meeting of the IMA, (Budapest, Hungary), abstract volume p. 740.

Pollok K., Hopf J., Harries D., Chust T., Hochella M.F., and Langenhorst F. (2010) Microbially enhanced dissolution of pyrrhotite polytypes: Surface roughness, reactivity and rates. 20th General Meeting of the IMA (Budapest, Hungary), abstract volume, p. 381.

Harries D., Pollok K., and Langenhorst F. (2009) Nanometer-wide magnetite lamellae in mixed 4C/NC-type pyrrhotite from Bodenmais (Bavaria, Germany) – alteration or exsolution? 87th Annual Meeting of the DMG (Halle, Germany). *Hallesches Jahrbuch für Geowissenschaften* **31**, p. 94.

Harries D., Pollok K., and Langenhorst F. (2009) Pyrrhotite, polytypes and pH: A TEM study on structural complexity and its effects at the mineral-fluid interface. MAPT meeting 2009 (Edinburgh, United Kingdom), abstract volume.

Harries D., Pollok K., Etzel K., and Langenhorst F. (2009) Structural Complexity in Pyrrhotites: What are the implications for mineral water interactions? 19th Annual V. M. Goldschmidt Conference (Davos, Switzerland). *Geochimica et Cosmochimica Acta* **73**, Suppl. 1, abstract A495.

Pollok K., Hellige K., Harries D., and Peiffer S. (2009) Redox Processes at the Nanoscale: A TEM Perspective of Iron Sulfide-Iron (Oxyhydr)oxide Reactions. 19th Annual V. M. Goldschmidt Conference (Davos, Switzerland) *Geochimica et Cosmochimica Acta* **73**, Suppl. 1, abstract A1039.

CHAPTER 2 Translation Interface Modulation in NC-Pyrrhotite: Direct Imaging by TEM and a Model toward Understanding Partially Disordered Structural States

by Dennis Harries*, Kilian Pollok, and Falko Langenhorst[#]

Bayerisches Geoinstitut, University of Bayreuth, D-95440 Bayreuth, Germany. [#]Present address: Institut für Geowissenschaften, Friedrich-Schiller-Universität Jena, Burgweg 11, D-07749 Jena, Germany.
*Corresponding author. Email: dennis.harries@uni-bayreuth.de

2.1. Abstract

The crystallographic complexity of 'hexagonal' or 'intermediate' pyrrhotites ($Fe_{1-x}S$ with $0.125 > x > 0.080$) is a long-standing and challenging problem. Integral (e.g., 5C) and non-integral NC type structures found within this group at ambient temperatures are characterized by sharp but complicated electron diffraction patterns, which were found to be interpretable in terms of a translation interface modulation (TIM) superstructure. Transmission electron microscopy (TEM) dark-field images obtained using superstructure reflections show dense arrangements of stripes which can be interpreted as arrays of closely spaced anti-phase domain boundaries (APB). The displacement vector at the interface is **R** = 1/8[001] of a metrically hexagonal 4C superstructure cell and the involved translations are solely confined to the Fe sublattice. The vacancy arrangement of the APB-free monoclinic 4C-pyrrhotite serves as a base of the TIM superstructure and therefore NC structures can be regarded as two super-imposed ordering phenomena relating to the arrangements of individual vacancies and APBs, respectively. APBs are chemically non-conservative and govern the higher Fe/S ratios of intermediate NC-pyrrhotites. If oriented strictly parallel to (001) the APBs can be regarded as completely filled Fe double layers within the 4C stacking sequence. However, direct imaging of APBs shows waviness and variable disorder on mesoscopic scales, yielding essentially aperiodic structures. A high degree of self-organization among APBs has been observed within apparent diffusion profiles around exsolved troilite lamellae and along interfaces with 4C-pyrrhotite, where complicated eight-fold node arrangements occur. Our TEM observations indicate that all NC-type pyrrhotites can be treated by the TIM approach and that the concepts of polytypism and polysomatism in pyrrhotite are not fully capable in representing the observed structural complexities.

2.2. Introduction

Pyrrhotite comes a close second after pyrite among the most abundant iron sulfides in ore deposits and crustal rocks. Its NiAs-derivative structure contains sequences of hexagonal close-packed S atom layers stacked in alternation with layers of Fe atoms in octahedral coordination. Non-stoichiometric compositions arise from the presence of vacancies within Fe layers and span the range in-between ~47 to 50 at% Fe (Fe_7S_8 to FeS), whereas most structural complexity occurs in the narrow compositional range between 47 to 48 at% Fe. At temperatures below 300°C various superstructures are observed in this range due to vacancy ordering among and within Fe layers, resulting in a rather complicated subsolidus phase diagram (Desborough and Carpenter 1965; Kissin and Scott, 1972; Kissin and Scott 1982; Nakazawa and Morimoto 1970). A recent review on structural and magnetic phase transitions is given by Wang and Salveson (2005). At ambient temperatures there are three members of the pyrrhotite family being found in nature: troilite (2C-pyrrhotite, FeS, antiferromagnetic), 4C-pyrrhotite (Fe_7S_8, ferrimagnetic) and NC-pyrrhotite (in-between FeS and Fe_7S_8, antiferromagnetic). Here pyrrhotite prefixes indicate the superstructure lattice repeat along the axis of layer stacking relative to the *c*-axis periodicity of the NiAs substructure (Morimoto et al., 1970) and the latter two types correspond to the more traditional 'monoclinic' and 'hexagonal' (or 'intermediate') pyrrhotite designations, respectively. Unlike the well known 2C and 4C structures the NC-type pyrrhotites form a structurally diverse group with widely variable N_c values among which the special cases Fe_9S_{10} (5C), $Fe_{11}S_{12}$ (6C), and $Fe_{10}S_{11}$ (11C or 5.5C without considering sulfur layer stacking) have been proposed as stable phases at room temperature (Morimoto et al. 1970; Nakazawa and Morimoto 1970). Besides these integral NC-pyrrhotites it is established that NC-pyrrhotites exist, in which the apparent superstructure periodicity is related to the *c*-axis repeat of the NiAs substructure in a non-integral manner. Reported N_c values range between 4.2 to 6.6 (Morimoto et al. 1975a; Morimoto et al. 1975b; Pósfai et al. 2000; Yamamoto and Nakazawa 1982). Over the last decades the stability relations of integral and non-integral superstructures have been a matter of debate, although it seems that studies preferentially focussed on the structural and physical properties of the integral types. Alongside conceptual problems regarding the crystallographic description of non-integral superstructures, observations on synthetic and natural pyrrhotites at ambient temperatures face difficulties due to slow ordering kinetics, pronounced phase heterogeneity, and a high, but often subtle, variability of diffraction

data, demanding careful evaluation. Pyrrhotite shows excessively variable magnetic and physicochemical properties (Wang and Salveson 2005) and occurs widespread in rocks and ore deposits. Realistic structural models are required to conceive the nature of magnetic properties and phase transitions and are crucial to understand processes on mineral surfaces. A prominent example is flotation processing, where drastic differences in efficiency have been demonstrated for magnetic and non-magnetic pyrrhotites (Becker et al. 2010).

The monoclinic 4C-pyrrhotite is without doubt the best characterized and understood pyrrhotite superstructure (Bertaut 1953; Tokonami et al. 1972; Powell et al. 2004). Based on a NiAs-type structure of FeS, the 4C structure is derived by removing 1/4 of Fe atoms from every second Fe layer, leading to the composition Fe_7S_8. Within vacancy-bearing layers the Fe atoms arrange in planar kagome lattices, of which four variants (V_A, V_B, V_C, V_D; Fig. 2-1a) are mutually discernible in the stacked arrangement. The kagome arrangement governs equal spacings between neighboring vacancies while avoiding direct neighborship by surrounding each vacancy by six Fe atoms. The resulting sequence of partially vacant (V) and filled (F) Fe layers is $V_AFV_BFV_CFV_DF$; it is characterized by strict alternation of V and F layers. The spacing between V layers of the same type is strictly four times the c-axis repeat of the NiAs substructure (or eight Fe layers; the possible permutations of the ABCD sequence are equivalent and relate to different choices of the reference frame/coordinate system).

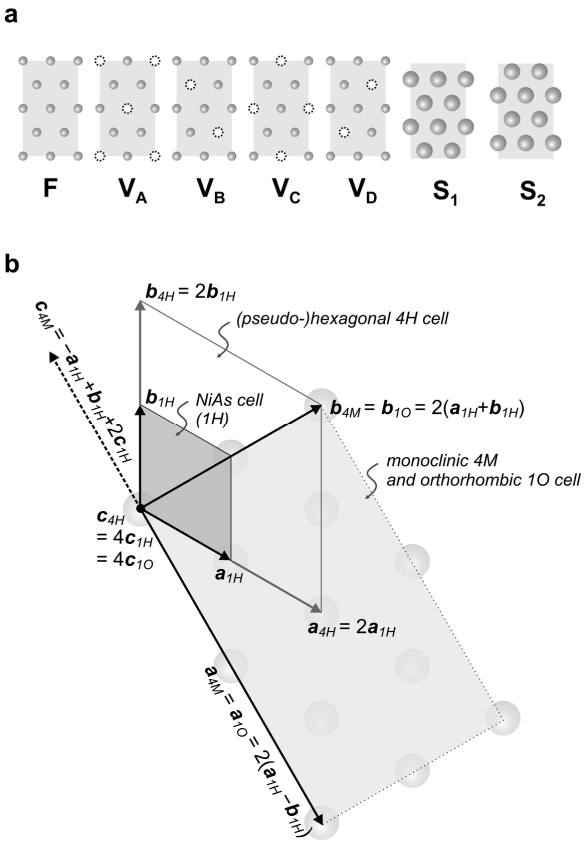

FIGURE 2-1. (**a**) Schematic representation of the principal layer types in the ideal structures of 4C- and NC-pyrrhotites. F: filled Fe layer, V: partially vacant Fe layer in four mutually different settings (VA, VB, VC, VD), S: sulfur layers in two mutually different settings (S1, S2) of the hcp stacking. (**b**) Basal view of different pyrrhotite unit-cell settings (1H, 1O, 4M, 4H) with indications of Fe site positions. Note that the original 4M cell of 4C-pyrrhotite as described by Bertaut (1953) is for reasons of centering shifted with respect to the Fe positions.

Structural descriptions of integral NC-pyrrhotite structures can be roughly divided into two approaches using either discrete (zero or one) or partial Fe site occupancies. The former relates to an idealized extension of the 4C stacking scheme by introducing additional F layers or stacking of certain building blocks, which increases both the periodicities of the superstructures as well as the Fe/S ratios (Corlett 1968; Dódony and Pósfai 1990; Pósfai and Dódony 1990; Vaughan 1971). These concepts can be viewed in terms of a polytypic or polysomatic series. The additional introduction of partial (i.e., statistical) site occupancies implies a considerable disorder of Fe vacancies (de Villiers and Liles 2010; de Villiers et al. 2009; Elliot 2010; Koto et al. 1975), whereas the nature of this disorder is usually not addressed.

The problem of non-integral pyrrhotites was first addressed by Pierce and Buseck (1974) who suggested a disordered arrangement of anti-phase domains ranging in size between one to three unit cells of the substructure. Despite being able to closely reproduce experimental diffraction patterns, only few details on the nature and ordering of domains were given and the relationship to compositional variations was not addressed. Koto and Kitamura (1981) proposed a somewhat similar model involving a formalism of two 'out-of-step' vectors lying in the **ab**-plane.

In contrast to these defect-related models Yamamoto and Nakazawa (1982) developed a superstructure description for an $N_c = 5.54$ pyrrhotite based on a continuous modulation of (partial) Fe site occupancies. In this model of an aperiodic crystal structure the probability of finding a Fe atom at a given lattice site is governed by a continuous, sinusoid-like modulation function embedded in a four-dimensional superspace formalism. Aperiodicity results from the occupation modulation being incommensurately related to the substructure periodicity. Based on this work Izaola et al. (2007) introduced a generalized superspace approach by replacing the continuous occupancy modulation with a step-like function governing discrete site occupancies. By virtue of a 'closeness' condition, the model strictly obeys the sequence of ABCD layering as well as the rule that two V layers must not follow consecutively without an interjacent F layer, resulting in the fixed relation $1/N_c = 2x$ between superstructure N_c value and composition expressed as x in $Fe_{1-x}S$. Depending on the N_c value being rational or irrational the model will either produce periodic/commensurate structures, including 4C and integral NC, or yield aperiodic/incommensurate layer sequences, respectively. These can be understood as uniform stacks of V and F layers in which certain patterns recur but are faulted by

deterministic, yet non-periodic insertions of extra layers. Because such uniform structures are expected to yield sharp Bragg diffraction maxima (Amelinckx and van Dyck 1993), they can be considered as being quasi-periodic (Burrows and Sulston 1991).

A primary motivation for this study was that the reported electron diffraction patterns of non-integral NC-pyrrhotites strongly resemble those seen in certain modulated binary alloys (Amelinckx and van Dyck 1993; Broddin et al. 1990). In these alloy systems primary integral superstructures arise in stoichiometric compounds (e.g., Au_3Zn) from ordering atoms on certain sites of the fcc lattice. Non-stoichiometric compositions (e.g., $Au_{3+x}Zn_{1-x}$) and secondary superstructures are related to additional ordering phenomena which can be described as regular arrangement of 2-dimensional defects or interfaces within the simple primary superstructures. This regular arrangement is a structural modulation. Specifically, non-conservative ('composition-changing') anti-phase boundary (APB) interfaces can be made responsible for a close coupling between the resulting secondary superstructures and concurrent non-stoichiometry. In these cases of APB modulated secondary superstructures, diffraction patterns are characterized by replacement (or splitting) of the primary superstructure reflections with arrays of satellite spots. In analogy, the NC diffraction pattern could be regarded as representative of a primary NiAs based superstructure, which is modulated by non-conservative APBs that lead to increased Fe/S ratios and the splitting of 4C reflections into the arrays of satellite spots seen in the NC diffraction patterns. Figure 2-2 serves to illustrate the differences in 2-dimensional defects, namely stacking faults, APBs, and twin boundaries, in a pyrrhotite-like material. Stacking faults and APBs are characterized by breaking the translation symmetry of a crystal and result in a phase shift along the, so called, translation interface. In contrast, twin boundaries are characterized by a rotation instead of a translation. APBs are well known to be very dynamical defects that can relatively easily move through crystals and arrange in complex patterns (e.g., Van Tendeloo et al. 1974).

A successful approach towards the rationalization of modulation by interfaces has been introduced by Fujiwara (1957) and has later been extended to the concepts of crystallographic shear (CS) structures and translation interface modulation (TIM) by van Landuyt et al. (1970) and van Dyck et al. (1987). The CS concept was successfully applied to many non-stoichiometric transition metal oxides (Andersson and Wadsley 1966) and is closely related to TIM because CS planes (or Wadsley defects) can be regarded as non-conservative APBs (van Landuyt 1974).

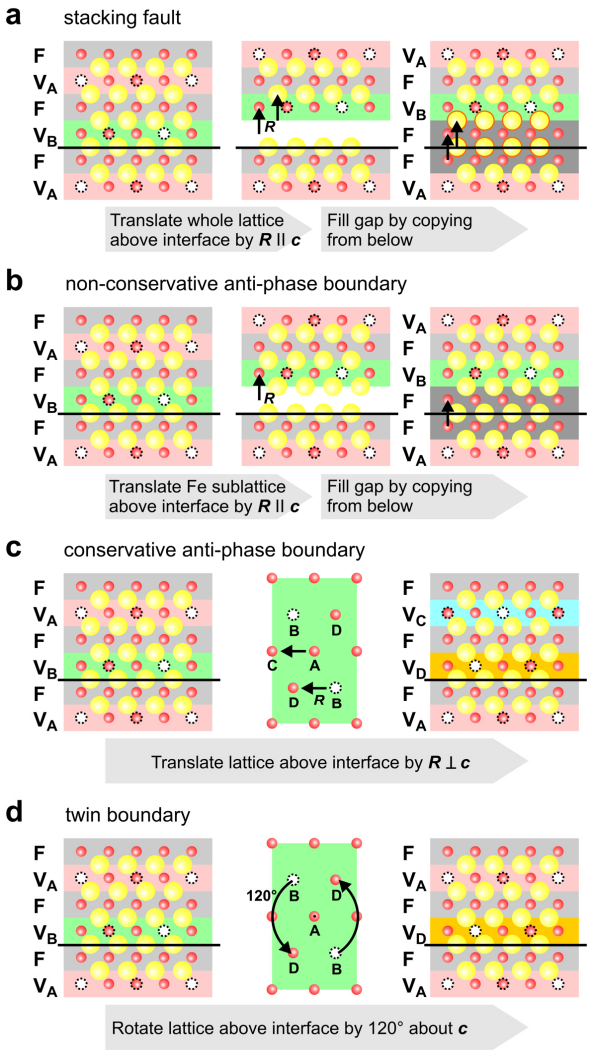

FIGURE 2-2. Types of defect interfaces perpendicular to c in a pyrrhotite-like material (note that only a simplified layer stacking and energetically favorable configurations are shown). (**a**) Stacking fault: The whole lattice is translated perpendicular to the interface by the displacement vector R and the gap is filled. A Fe double layer and a fault in the sulfur layer stacking sequence results. The Fe/S ratio is changed. (**b**) Non-conservative anti-phase boundary: Only the Fe sublattice is translated by R perpendicular to the interface. A Fe double layer results but the sulfur sublattice is left intact. The Fe/S ratio is changed. (**c**) Conservative anti-phase boundary: The whole lattice is translated by R parallel to the interface. All vacancy layer types change and the sulfur sublattice is left intact. The Fe/S ratio is preserved. (**d**) Twin boundary: The whole lattice is rotated about an axis parallel to c. The vacancy layer types change, but the one on which the rotation axis is centered remains the same. Depending on the angle the sulfur sublattice is left intact (120°, shown) or faulted (60°). The Fe/S ratio remains unchanged.

The different structural models discussed so far (polytypic/polysomatic layer stacking, superspace embedment, TIM) do not necessarily represent different structural states of pyrrhotites but are rather different descriptive approaches, which vary in their capabilities of representing the real structures. The TIM approach used in this study appears particularly useful to reconcile the theoretical treatment of diffraction patterns and the

conceptual understanding of mesoscopic scale phenomena and defects seen in direct space by TEM imaging as demonstrated in many cases of alloys and transition metal oxides. Our study aims at a realistic crystallographic description of natural, non-integral NC-pyrrhotites by utilizing TEM dark-field imaging as well as highly resolved electron diffraction in order to evaluate the structural states of these enigmatic, but geologically very significant phases.

2.3. Samples and Experimental Methods

We studied three natural pyrrhotite samples from geologically different locations. Sample EUL was obtained from the Sta. Eulalia mining district in Chihuahua, Mexico, and is an idiomorphic crystal of 30 mm largest dimension, associated with quartz and calcite. Sample NYS originated from the Nyseter mining area near Grua, Norway (ex coll. University of Jena HG12148), and consists of massive ore with mm-sized pyrrhotite grains and minor admixtures of chalcopyrite and galena. Sample TYS was collected from the dumps of pegmatite quartz mining at Drag in the Tysfjord region, Norway, and is a polycrystalline mass with grain sizes around 1 cm. For TEM double polished thin sections of ~30 μm thickness were prepared and subsequently epoxy mounted on 3 mm Cu or Ti TEM grids or slot apertures. Ar-ion thinning was accomplished by means of a Gatan Model 600 DuoMill (14° tilt, 4.5 keV ion energy) operating with liquid nitrogen cooling or a Gatan PIPS system thinning at low angles and ion energies (< 5°, < 3.5 keV). In order to check for preparation artefacts, powdered and ultramicrotomed samples were prepared as well, but no systematic differences in SAED pattern could be detected.

A Philips CM20FEG TEM operating at 200 kV was used for microstructural observations. Images and SAED patterns were recorded on conventional electron imaging films, leading to exposure times in the range of 3 to 5 s for SAED patterns obtained by using a selected area aperture of 4 μm diameter in the image plane. The determination of N_c values from SAED patterns involved manual measuring of 30-90 distances from which statistically significant N_c values with uncertainties of typically ±0.01 (2s) could be obtained. TEM-SDF was accomplished by placing an objective aperture of 2.3 nm^{-1} diameter on strong satellite reflections. HR-TEM bright field imaging of non-integral NC-pyrrhotites was attempted, but mostly unsuccessful, because observable structures disappeared within seconds after irradiation at high magnifications (>230.000 x) due to high current densities. Only in few instances after quick exposure the resulting HR images

showed fast Fourier transform (FFT) derived periodicity patterns that were comparable to real SAED patterns obtained at the same sites; only these images were considered in this study. No deterioration of SAED patterns could be detected even for irradiation times of up to 20 minutes (under these conditions the sampled area is large and the current density low due to spreading of the electron beam). Structures in SDF observed at moderate magnifications (50.000 to 200.000 x) were stable for several minutes before slowly fading out of contrast, allowing photographic documentation with exposure time of 10-20 s.

For EPMA and SEM-BSE imaging a JEOL JXA-8200 equipped with five wavelength dispersive spectrometers was used and operated at 15 kV acceleration voltage, 20 nA beam current and focussed probe size (counting 30s on peak, 15s on background). Reference material for Fe and S calibration was Ni-free Dalnegorsk pyrrhotite, which was shown by TEM-SAED to have a 4C superstructure and by inference the composition Fe_7S_8; it was tested against troilite coexisting with metallic iron and deviations from stoichiometry were found to be less than 0.005 in terms of Fe/S ratio. For Ni and Co pure metals were used for calibration. Matrix corrections were applied by use of the JEOL CITZAF implementation in $\phi(\rho z)$ mode, but could be reduced to a minimum by using pyrrhotite as reference material.

2.4. Results

2.4.1. EPMA/SEM-BSE

SEM-BSE imaging of EUL and NYS shows abundant exsolution lamellae in both samples (Fig. 2-3a,b). In sections the lamellae form two sets of lens shaped or sigmoidal bodies inclined towards the [001] direction of host pyrrhotite. Lamellae typically measure <200 μm in length and up to 30 μm in width and are darker in BSE images, indicating a lower average atomic number and thus a lower Fe/S ratio as the host pyrrhotites. Quantitative analyses given in Tab. 2-1 show the lamellae to have compositions near $Fe_{0.875}S$ (or Fe_7S_8) indicative of 4C-pyrrhotite, while the host pyrrhotites' Fe contents are slightly below $Fe_{0.900}S$ (or Fe_9S_{10}) as indicated by x values of 0.106±0.001 (EUL) and 0.102±0.001 (NYS). Exsolution of 4C-pyrrhotite from NC-pyrrhotite appears to be quite abundant in nature and is well documented by petrographic methods (e.g., Lianxing and Vokes 1996).

In contrast to EUL and NYS, BSE images of the TYS sample reveal a dense population of 1-3 μm wide exsolution lamellae reaching lengths of up to 500 μm and more (Fig. 2-

3c). The lamellae all share a common orientation parallel to (001) and reach densities of approx. 50-75 mm^{-1} along the [001] direction. They appear brighter compared to the host indicating a higher Fe/S ratio, which is confirmed by quantitative analyses (Tab. 2-1) placing them close to stoichiometric FeS. The host pyrrhotite shows an average x value of 0.096±0.001, indicating a composition between Fe_9S_{10} and $Fe_{10}S_{11}$. A slight deficiency of Fe in the lamellae is very likely due to a contribution of the matrix pyrrhotite, as the width of lamellae is close to the dimension of the X-ray excitation volume. EUL and TYS show no detectable amounts of Ni, while NYS contains about 500 to 1000 µg/g Ni, which appears to partition preferentially into the host NC-pyrrhotite.

TABLE 1-1. N_c values and chemical compositions of investigated pyrrhotite samples.

Sample	**EUL**		**NYS**		**TYS**	
Phase	**NC (host)**	**4C (lamellae)**	**NC (host)**	**4C (lamellae)**	**NC (host)**	**Troilite (lamellae)**
			SAED pattern			
N_c range	4.81 – 4.87	4	4.78 – 4.96	4	5.12 – 5.52	n.a.
			EPMA % m/m (1σ std uncertainty of mean)			
n	30	25	25	19	20	16
Fe	60.84(2)	60.26(3)	61.26(8)	60.50(4)	61.09(4)	63.19(3)
Ni	<0.02	<0.02	0.108(3)	0.050(4)	<0.02	<0.02
Co	<0.02	<0.02	<0.02	<0.02	<0.02	<0.02
S	39.07(3)	39.64(2)	39.24(3)	39.66(5)	38.81(3)	36.73(3)
Total	99.91(3)	99.90(4)	100.61(10)	100.21(7)	99.90(4)	99.91(4)
			Formula per 1 S (1σ std uncertainty of mean)			
Fe	0.894(1)	0.873(1)	0.896(1)	0.876(1)	0.904(1)	0.988(1)*
Ni	b.d.	b.d.	0.00151(3)	0.00069(5)	b.d.	b.d.
Co	b.d.	b.d.	b.d.	b.d.	b.d.	b.d.
***x* in $Fe_{1-x}S$**	0.106(1)	0.127(1)	0.102(1)	0.124(1)	0.096(1)	0.012(1)*
1/(2*x*)	4.71(3)	3.93(2)	4.89(5)	4.04(3)	5.19(5)	n.a.

Note: *Fe contents likely too low due to slight convolution with neighboring NC-pyrrhotite.
b.d.: below detection limit, n.a.: not available

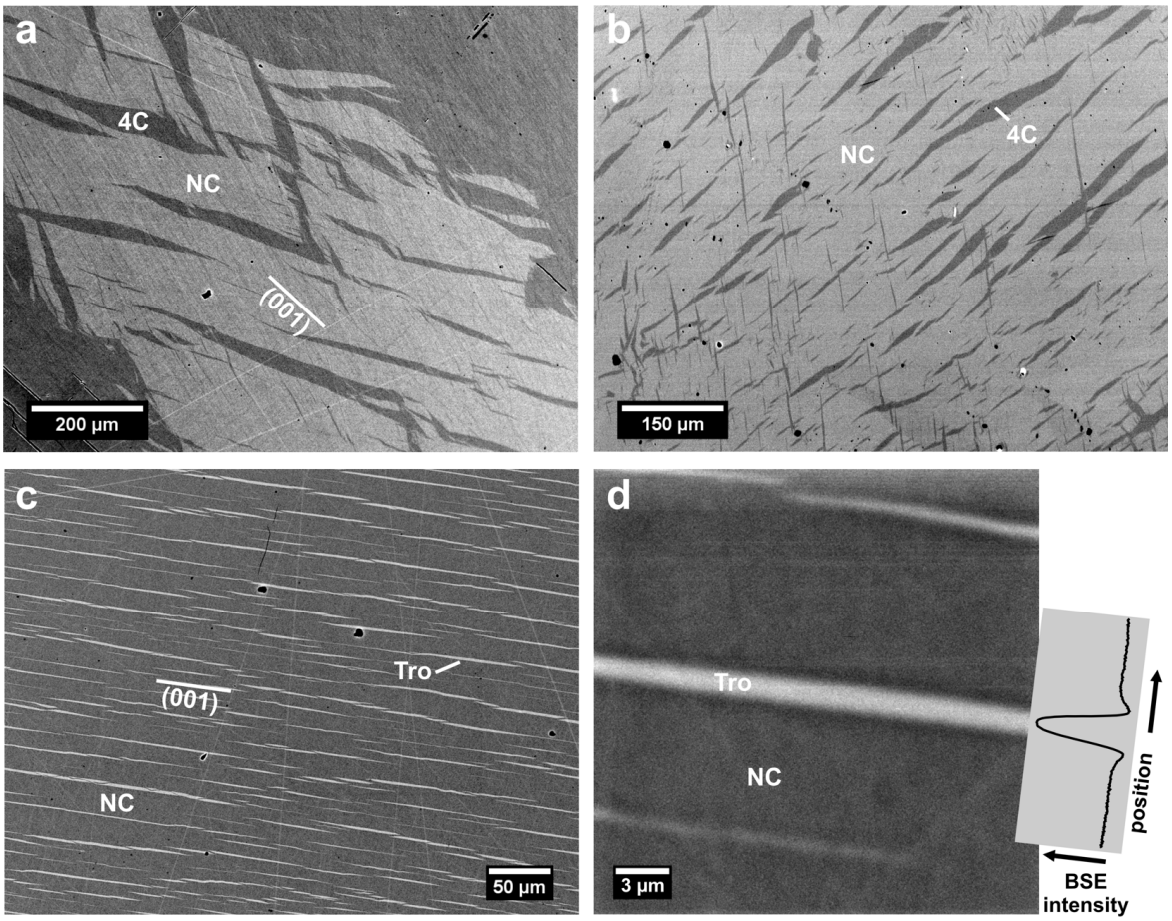

FIGURE 2-3. SEM-BSE images of the studied pyrrhotites. (**a**) Sta. Eulalia (EUL) showing two sets of dark exsolution lamellae of 4C-pyrrhotite in a matrix of NC-pyrrhotite. Adjacent dark areas are also 4C-pyrrhotite. (**b**) Nyseter (NYS) displaying two sets of dark 4C-pyrrhotite exsolution lamellae in NC matrix. (**c**) Tysfjord (TYS) displaying a single set of bright troilite (2C-pyrrhotite) exsolution lamellae parallel to (001). Faint lines and striations in (a–c) are artifacts from polishing and high detector gain. (**d**) Accumulated BSE image of TYS and extracted intensity profile showing dark haloes around troilite lamellae. Although the spatial extent of the BSE generating region causes a considerable convolution of the image, a clear low in backscattered intensity is visible around the lamella, pointing to an approximately 1 µm wide Fe depleted diffusion zone.

A detailed study of lamellae in TYS by accumulated BSE images (Fig. 2-3d) reveals dark haloes along the lamellae boundaries. Back-scatter electron coefficients are basically related to the average atomic number and the crystal orientation relative to the detector. TEM results (see below) have shown that lamellae and host share the same orientation and therefore the observed dark halos have to be due to a lowered Fe/S ratio along the lamellae margins. Unfortunately the X-ray generating region of the electron interaction volume is too large to allow for reliable quantitative analysis of these features. Because the source region of back-scatter electrons is much smaller than the X-ray generating region and the back-scatter factor is sufficiently sensitive to variations in the Fe/S ratio (as atomic

numbers are quite different), it appears possible to relate the observed haloes to Fe-deficient stranded diffusion profiles formed by growth of FeS lamellae from the NC host at relatively low temperatures (< 150 °C, see Wang and Salveson 2005).

2.4.2. TEM-SAED

2.4.2.1. Choice of Supercell and Determination of Structure Parameters

The structural diversity among pyrrhotites creates the problem of clearly defining crystallographic settings as the many possible superstructures are expected to have different symmetries and unit cells, which in turn are in most cases unknown. The superstructure reflections of NC-pyrrhotites can be described as satellites of multiple orders around the substructure reflections and thus an *ad hoc* indexing can be done based on the NiAs-type subcell (here abbreviated '1H'). However, doing so is rather inconvenient and similarly to Yamamoto and Nakazawa (1982) we preferred to use a supercell giving a more clear representation of the structure and systematically absent satellites. However, contrary to their orthorhombic cell (denoted '1O') we based our considerations on a hexagonal metric ('4H') with $\mathbf{a}_{4H} = 2\mathbf{a}_{1H}$, $\mathbf{b}_{4H} = 2\mathbf{b}_{1H}$ and $\mathbf{c}_{4H} = 4\mathbf{c}_{1H}$, which is a pseudo-hexagonal representation of the monoclinic 4C cell ('4M') of Bertaut (1953). Relations of all four cells are shown in Figure 2-1b. We have chosen this specific reference cell with four-fold extended *c*-dimension because the 4H cell is the most general representation of the suggested 4C primary superstructure as outlined above. We note that apparently all pyrrhotite structures, including those investigated by us, show small angular deviations in the order of ~0.5° from the ideal NiAs-derived metrics. For the sake of simplicity we did not include these distortions in our considerations of idealized structures.

The actual indexing of superstructure satellite reflections, shown in Figure 2-4, is done by applying a (3+1)-dimensional (*hklm*) scheme analogous to the one adopted by Yamamoto and Nakazawa (1982) and commonly used for the description of one-dimensionally modulated structures. A diffraction vector **g** is thus (with $\mathbf{a} = \mathbf{a}_{4H}$ etc.):

$$\mathbf{g} = h\,\mathbf{a}^* + k\,\mathbf{b}^* + l\,\mathbf{c}^* + m\,\mathbf{q}$$

m is the satellite order of a superstructure reflection and **q** is the modulation vector relating each satellite to a (*hkl*) substructure reflection. **q** is generally parallel or subparallel to **c***

and can be decomposed into components $\mathbf{q}_c$ and $\mathbf{q}_{[uv0]}$ being parallel to **c*** and the **ab**-plane, respectively. The component $\mathbf{q}_{[uv0]}$ is in most cases zero or hardly detectable by SAED, but occasionally modifies diffraction patterns significantly (Fig. 2-5a,b). The N value, or more precisely the N_c value of a superstructure is obtained as the ratio c_{1H}^*/q_c with c_{1H}^* referring to the NiAs-type subcell ($c_{1H}^* \approx 1.72$ nm^{-1}). Similarly, a $N_{[uv0]}$ value can be defined.

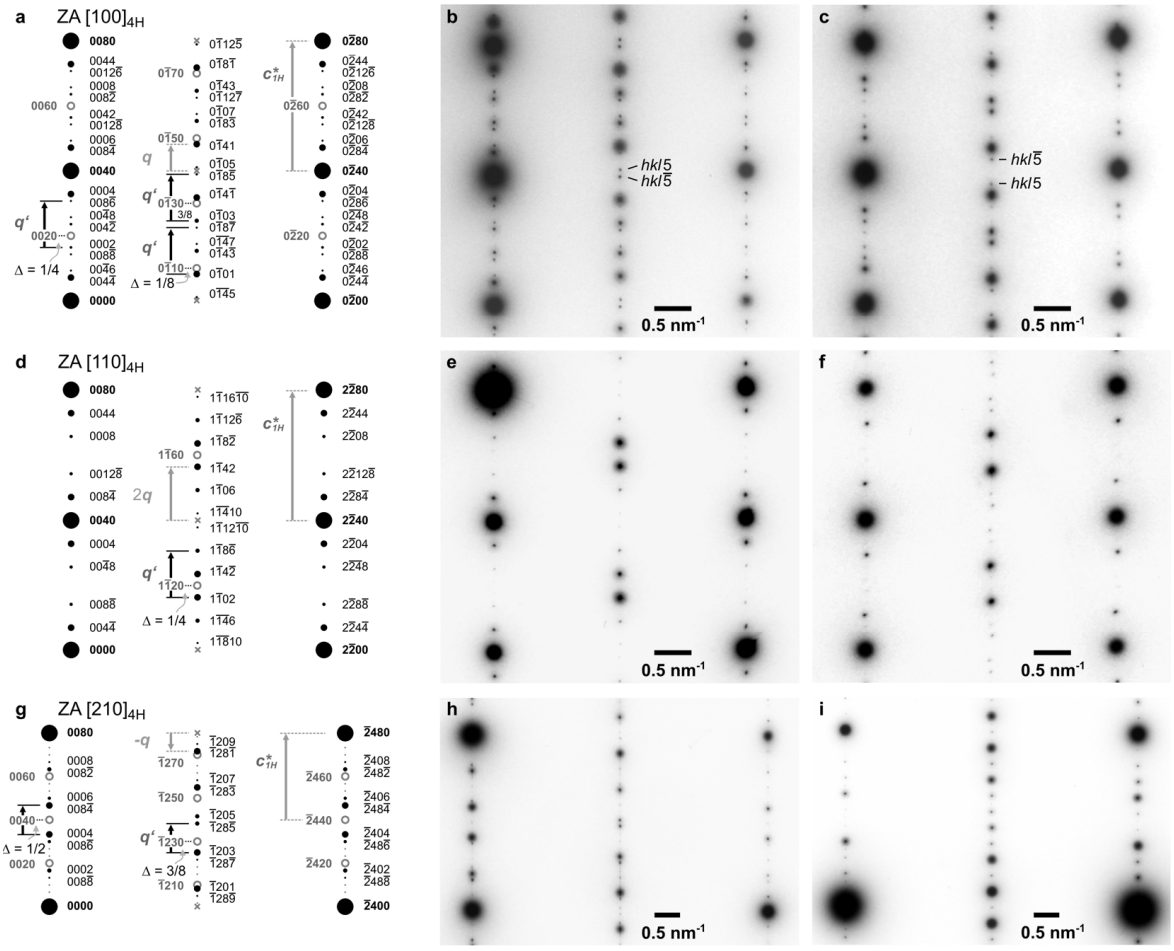

FIGURE 2-4. TEM-SAED patterns of non-integral NC-pyrrhotites together with schematic representations of pattern geometries and indexing based on the 4H cell (intensities are approximately adapted from the experimental patterns). Filled circles are NC diffraction spots, open circles are 4C diffraction spots, and crosses represent 4C diffraction spots, which are systematically absent but used as base for indexing the NC satellites. (**a**) Zone axis (ZA) $[100]_{4H}$ corresponding to $[110]_{4M}$ of the conventional monoclinic cell of 4C-pyrrhotite, drawn for N_c = 4.87. (**b**) $[100]_{4H}$ SAED pattern of NYS with N_c = 4.87±0.01. (**c**) $[100]_{4H}$ SAED pattern of TYS with N_c = 5.52±0.02. Note that at N_c = 5, the (*hkl*5) and ($hkl\bar{5}$) satellites coincide with the (absent) (*hk*40) reflection and change places for $N_c > 5$. (**d**) ZA $[110]_{4H}$ corresponding to $[010]_{4M}$, drawn for N_c = 4.87. (**e**) $[110]_{4H}$ SAED pattern of EUL with N_c = 4.87±0.01. (**f**) $[110]_{4H}$ SAED pattern of TYS with N_c = 5.48±0.01. (**g**) ZA $[210]_{4H}$ corresponding to $[130]_{4M}$, drawn for N_c = 4.85. (**h**) $[210]_{4H}$ SAED pattern of NYS with N_c = 4.84±0.01. Some weak streaky diffraction along the **c*** direction can be seen. (**i**) $[210]_{4H}$ SAED pattern of TYS with N_c = 5.49±0.02.

2.4.2.2. Geometrical Analysis of Diffraction Patterns

TEM-SAED patterns obtained from lamellae in NYS and EUL match the diffraction pattern of 4C-pyrrhotite and clearly confirm the presence of this phase as exsolution product in accordance with measured compositions. Lamellae in the TYS sample give sharp and unambiguous diffraction patterns of troilite, being also compatible with the measured compositions. Both 4C-pyrrhotite and troilite are in crystallographic continuity with their respective hosts, which are shown by SAED to be of the non-integral NC type in all cases (Fig. 2-4). This places them between 4C-pyrrhotite and troilite in agreement with measured compositions. By comparison of diffraction patterns (Fig. 2-4) and derived N_c values (Tab. 2-1), it becomes apparent that NYS and EUL share besides very similar Fe/S ratios also very similar structural parameters with N_c being mostly in the range of 4.8 to 4.9. Unlike EUL, NYS occasionally shows streaks and diffuse satellite diffraction maxima along the ***c**** direction. The latter correspond to N_c values being somewhat lower than 4.8, but quantification in these cases is difficult due to convolution of different diffuse satellites. The host NC-pyrrhotite in TYS appears more heterogeneous with N_c values in the range of 5.12 to 5.52, whereas most values scatter closely around 5.5 when troilite lamellae are present nearby. Observed orders *m* of satellite reflections generally reach very high, up to 8 or 10, and together with mostly sharp diffraction spots indicate well ordered structures. Occasionally lateral shifts of reflections can be observed as shown in Figure 2-5a (also weakly in Fig. 2-4f) and such diffraction patterns can be indexed by

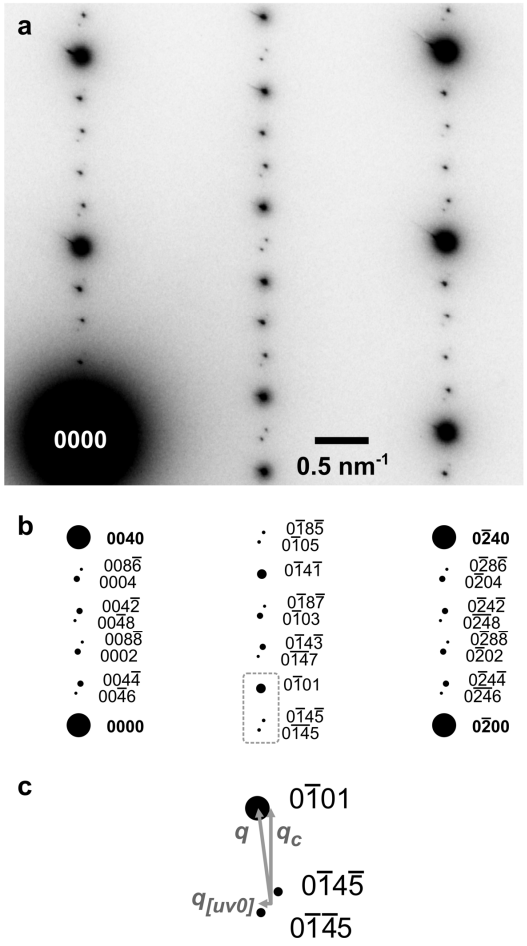

FIGURE 2-5. (**a**) TEM-SAED pattern in ZA $[100]_{4H}$ depicting an orientation anomaly in the TYS sample with N_c = 5.13±0.01 and $N_{[120]}$ approximately 6 to 800, relating to superstructure reflections being shifted laterally from their ideal positions. (**b**) Schematic representation of the SAED pattern. (**c**) Detail of (b) showing the relation of **q**, $\mathbf{q}_c$, and $\mathbf{q}_{[uv0]}$, which in this case is oriented toward $[120]_{4H}$.

allowing non-zero $\mathbf{q}_{[uv0]}$ components of **q** (Fig. 2-5b). These observations suggest that in close analogy to the Au-Zn system the NC type superstructures in pyrrhotite arise from modulated APBs modifying the primary 4C superstructure formed from vacancy ordering in the NiAs substructure – the NC structures are therefore analogous to non-stoichiometric $Au_{3+x}Zn_{1-x}$ TIM superstructures which are superposed on a primary superstructure due to simple ordering of Au and Zn in the fcc base lattice. Such an insertion of non-conservative APBs and formation of a TIM superstructure is capable of producing both integral and non-integral NC types depending on the density and arrangements of APBs. Lateral displacements of reflections via non-zero $\mathbf{q}_{[uv0]}$ components are hallmarks of TIM structures due to small systematic inclinations of APBs with respect to the host lattice and known as orientation anomalies in alloy systems (Amelinckx and van Dyck 1993).

Inspecting the schematic diffraction patterns in Figures 2-4a,d,g show that in general satellite reflections only occur for substructure reflections with *l* being a multiple of 4. For $h + l$ = even only satellites with m = even, and conversely for $h + l$ = odd only satellites with m = odd occur. As seen in Figure 2-4d the indexing of superstructure reflections in the $(0\,\bar{1}\,l)$ lattice row is facilitated by relating them as satellites to the $(0\,\bar{1}\,l)$ reflections with l = 0,4,8,... by m times **q**. These, generally absent, substructure reflections (marked by crosses) cannot be indexed based on the conventional monoclinic 4M cell of 4C-pyrrhotite, thus necessitating a (pseudo-)hexagonal cell. The proper 4C-pyrrhotite reflections (open circles in Fig. 2-4a,d,g) can be related to the satellites by a splitting vector (or distance) **q'**. For example, inspection of Figure 2-4g shows that in zone axis $[210]_{4H}$ the (0040) reflection of 4C-pyrrhotite is symmetrically split into the satellites $(008\bar{4})$ and (0004), the distance between them being *q'*. For the $(\bar{1}\,230)$ reflection of 4C-pyrrhotite an asymmetric splitting into the $(\bar{1}\,28\bar{5})$ and $(\bar{1}\,230)$ satellites occurs. The way how reflections are split or how **q'** is related to the split reflections can be described by a fractional shift Δ which is a multiple of 1/8. For Δ = 0, **q'** starts at the split reflection (i.e., satellite occurs at distance *q'*) and for Δ = 1/2 splitting is symmetric. The principle is applicable to all other $[uv0]_{4H}$ zone axes as shown in Figure 2-4, although splitting is not as obvious, because it produces interlocking arrays of many satellites with high orders. The significance of **q'** and fractional shifts stems from the fact that in a TIM structure the inverse length of **q'** directly relates to the average spacing of APBs and fractional shifts can be used to determine their displacement vector **R** (Amelinckx and Van Dyck 1993;

van Dyck et al. 1987). Based on the pattern geometries, we find that for pyrrhotite **q'** (describing orientation and spacing of APBs) and **q** (used for indexing satellites) can be related through the equation

$$\mathbf{q'} = 2\mathbf{c}_{1H}^{*} - 8\mathbf{q}.$$

For typical N_c ranges in our samples of 4.80 to 4.90 (EUL/NYS) and 5.45 to 5.55 (TYS) we therefore would theoretically expect average APB spacings along the *c* direction of 1.74 to 1.58 nm and 1.09 to 0.96 nm, respectively. The relation of **R** and Δ is such that for a given substructure reflection **g** (here those of the 4C structure) $\mathbf{g}\cdot\mathbf{R} = \Delta$ has to agree with the observed fractional shifts Δ. Using experimentally determined Δ, as indicated in Figure 2-4, it can be shown that only the vector

$$\mathbf{R} = 1/8[001]_{4H} = 1/2[001]_{1H}$$

is consistent with our observed diffraction pattern geometries. This vector, if applied to a filled Fe layer of the 4C structure, produces a chemically non-conservative APB being equivalent to two consecutively filled Fe layers. The converse case of forming two consecutive vacancy layers appears highly unfavorable due to strong repulsion between the neighboring vacancies. In general $\mathbf{R} = 1/8[001]_{4H}$ is a valid APB displacement vector only with respect to the Fe sublattice – if it is applied to an S layer a stacking fault in the hcp sublattice would result, which is not observed by TEM imaging, as we shall see. However, the separate treatment of the Fe sublattice is legitimate because superstructures solely arise from the ordering of Fe vacancies.

2.4.3. Superstructure Dark-Field Imaging (SDF-TEM)

In order to obtain SDF-TEM images from electron beams diffracted by the superstructure, it was found to be most effective to place the objective aperture on the (0004) and $(008\bar{4})$ satellite reflections accessed from near the $[210]_{4H}$ zone axis (Fig. 2-6). The sample foil was tilted such that in the ideal case only diffracted beams in the (00*lm*) reciprocal lattice row were excited.

In the NC portions of both the EUL and NYS samples, SDF images reveal dense arrays of dark stripes being aligned parallel to the (001) planes (Fig. 2-7a,b) and solely visible in

dark-field images using strong superstructure reflections. In EUL the stripes appear slightly wavy on scales of a few tens of nm along their course. In comparison, the stripes in NYS show much more wiggles and irregularities. Further, in NYS the configuration of stripes appears to change along certain domain boundaries where the thin stripes, as seen in EUL, change into thicker stripes (arrows in Fig. 2-7b,d). The latter dominate the SDF images of the NYS sample and are likely doublets of two stripes being too close to be resolved under the SDF imaging conditions.

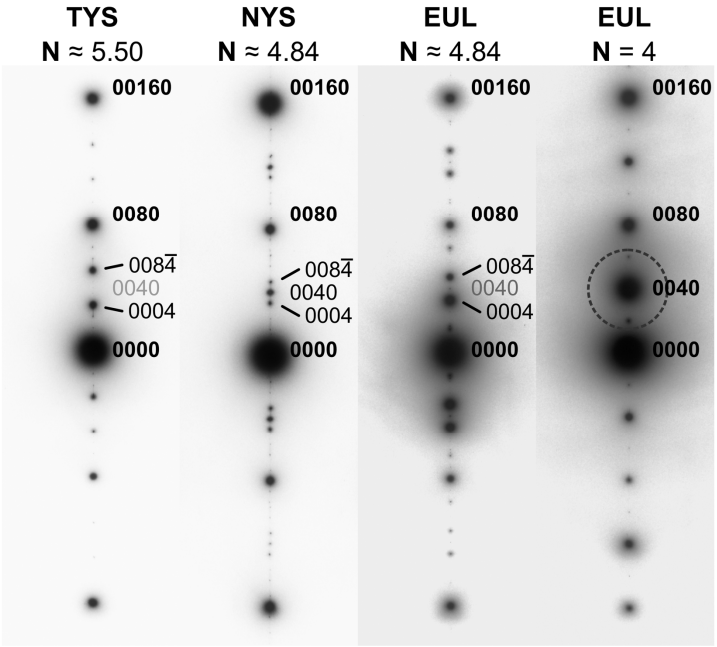

FIGURE 2-6. Diffraction conditions for SDF-TEM imaging as applied to the Nyseter (NYS), Sta. Eulalia (EUL), and Tysfjord (TYS) samples. The specimens are tilted from the $[210]_{4H}$ zone axis such that diffracted intensity is in the (00*l*) lattice row. The dashed circle represents the diameter of the objective aperture used for imaging, centered on the $(0040)_{4H}$ reflection of the substructure. In non-integral NC-pyrrhotites this reflection is weak or extinct, but occasionally occurs due to 4C domains within the diffracting volume.

The average spacing of stripes in EUL is 1.63±0.05 nm and the observed (half-)width of a single stripe is approx. 0.80 nm. We measured the distances by dividing measured intervals by the number of stripes occurring in them (intervals usually 45–60 nm). The average was obtained from 16 measurements on eight independent images. An alternative determination by FFT treatment of a 400×400 nm^2 area yielded a periodicity of 1.65±0.01, which is in very good agreement. Assuming the thick stripes in NYS to be non-resolvable doublets, the average spacing between individual stripes is 1.94±0.10 nm (n = 15, six images). A value of 1.97±0.03 nm was obtained from a 125×125 nm^2 area of thin stripes via FFT analysis and also agrees very well.

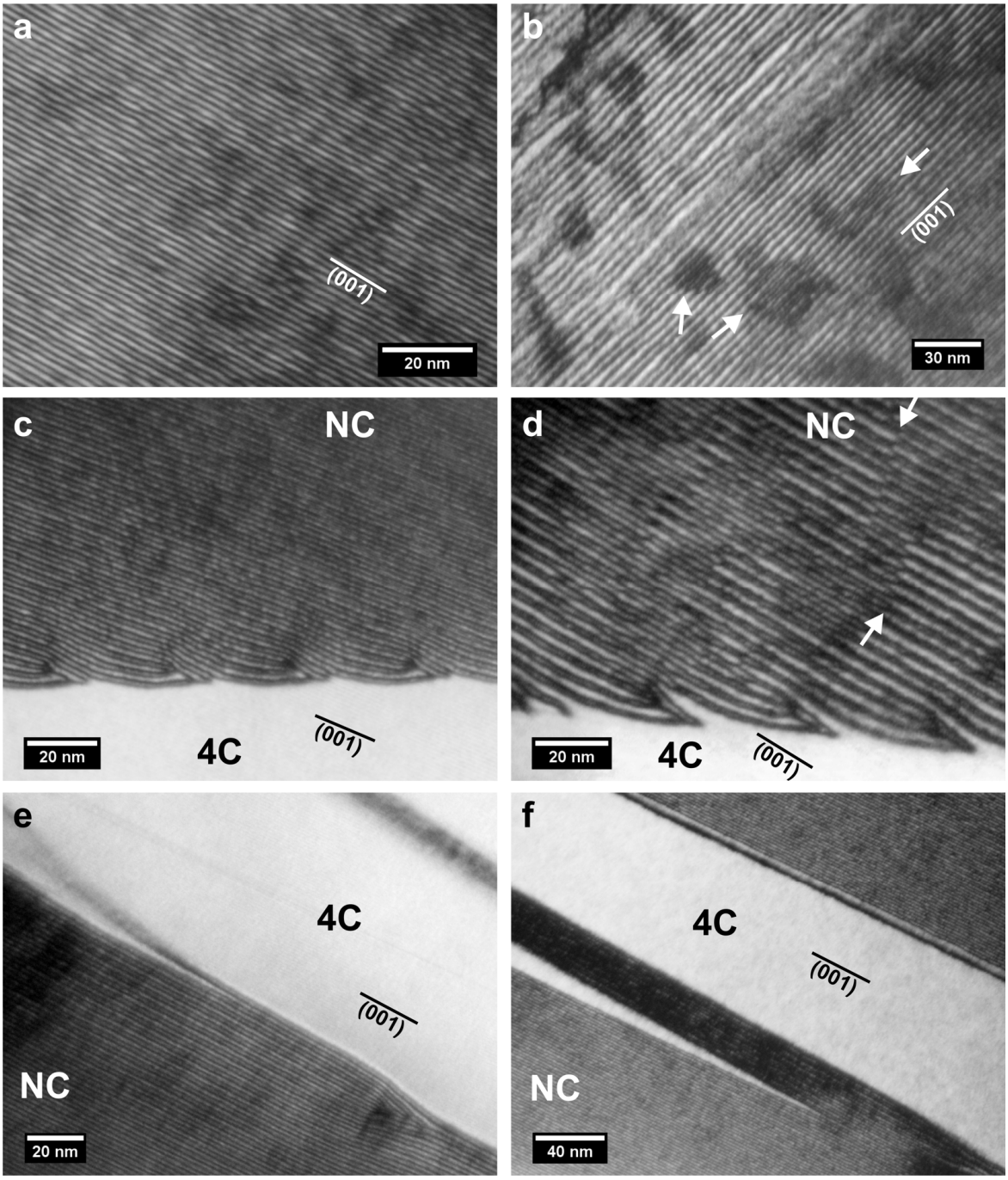

FIGURE 2-7. SDF-TEM images obtained using the diffraction conditions shown in Fig. 2-6. (**a**) Sample EUL showing parallel and slightly undulating APBs imaged as dark stripes. (**b**) Sample NYS showing thicker dark stripes that are irresolvable doublets of two APBs. Arrows indicate areas in which stripe configuration is analogous to (a). Disorder of APB spacings and orientations is higher than in EUL. (**c**) Sample EUL. Interface between NC- and 4C-pyrrhotite showing termination of APBs in eightfold node structures. The behavior of APBs as doublets is apparent. (**d**) Sample NYS. Interface between NC- and 4C-pyrrhotite showing the same type of node structures as seen in EUL. Arrows indicate changes in configuration of APB doublets. (**e**) Sample EUL. Interface between NC- and 4C-pyrrhotite subparallel to (001). An eightfold node structure is seen within the APB stripes and the outermost APB doublet tilts away into the adjacent 4C-pyrrhotite. (**f**) Sample EUL. 4C lamella parallel to (001) with a large block of APBs tilting away from adjacent NC-pyrrhotite.

The average distance for EUL compares very well with the expected APB spacing as obtained from the SAED pattern geometries and we therefore interpret the dark stripes to be APBs. The obtained SDF images strikingly resemble ordered APBs observed in Ni_3Mo by van Tendeloo et. al (1974). Based on contrast in dark-field images we can exclude the stripes to be stacking faults or twin boundaries, as the former would be seen with substructure reflections as well and the latter would show intensity differences of domains on either site of the boundary. The larger average spacing in NYS, despite very similar N_c values, is likely due to the higher disorder with larger and more irregular spacings between stripes, which bias the mean distance to higher values. Notably, the average of 1.94-1.97 nm corresponds to an N_c value of approx. 4.7, which is compatible with diffuse satellite reflections seen in SAED patterns obtained at the imaging sites. This may imply some locally increased disorder close to the exsolution lamellae which were targeted for imaging. Well defined SAED patterns which were considered for the calculation of expected average spacing were obtained rather far away from 4C lamellae and showed no contribution of 4C reflections.

Most striking features in SDF images of EUL and NYS are the phase boundaries between 4C- and NC-pyrrhotite where the stripes form complicated but remarkably similar node structures in which the stripes terminate (Fig. 2-7c,d). When the phase interface is oriented mostly parallel to the stripes, no nodes occur directly at the interface, but occasionally appear nearby within the NC phase (Fig. 2-7e), often associated with dislocations having the apparent Burgers vector $\mathbf{b} = [001]_{1H}$. In all cases of node structures we observed eight stripes to terminate in a single node. Occasionally stripes continue into the 4C phase and tilt away from the 'edge-on' view and blur out to some extent (Fig. 2-7e,f). Stripes in the 4C portion have been observed as singles, pairs, or larger blocks of multiple stripes (e.g., Fig. 2-7f), but it appears that there is a strong tendency of stripes to form doublet pairs as can be seen also in the bulk NC phases where the stripes are not equally spaced.

The behavior of stripes in the observed node structures and adjacent 4C-pyrrhotite strongly endorses our interpretation of them being non-conservative APBs of the 4C structure. Their orientation is fully compatible with the inferred displacement vector $\mathbf{R} = 1/8[001]_{4H}$ which creates double layers of completely filled Fe positions as opposed to single layers being present in the 4C structure. This is strictly true if the APBs are exactly normal to the displacement vector, i.e., parallel to (001). When the APBs are wavy or

inclined to the (001) plane the Fe excess associated with them will be somewhat less, depending of the angle of inclination. In cases where the APBs are parallel to **R**, and thus perpendicular to the pyrrhotite layer stacking, no Fe excess will occur as the structure is just sheared by the length of **R** along the APB 'fault' plane. APBs with small but systematic inclinations to the (001) planes are very likely the explanation of observed orientation anomalies (Fig. 2-5) analogous to anomalies seen in alloy systems (Amelinckx and van Dyck, 1993). Also the observed nodes find their analogs in these alloy systems where they are known as 'discommensuration nodes' or 'hairpin structures' (Schryvers et al., 1985; also well illustrated in van Tendeloo et al., 1974). In our case the eight-fold nodes facilitate the reconstruction of the 4C phases from the APB modulated NC phase and directly support the proposed displacement vector $1/8[001]_{4H}$ as its eight-fold multiple will be the *c* dimension of the 4C unit cell (see discussion section). Apparently the highly similar node configurations represent a self-organization towards an energetically optimal phase interface.

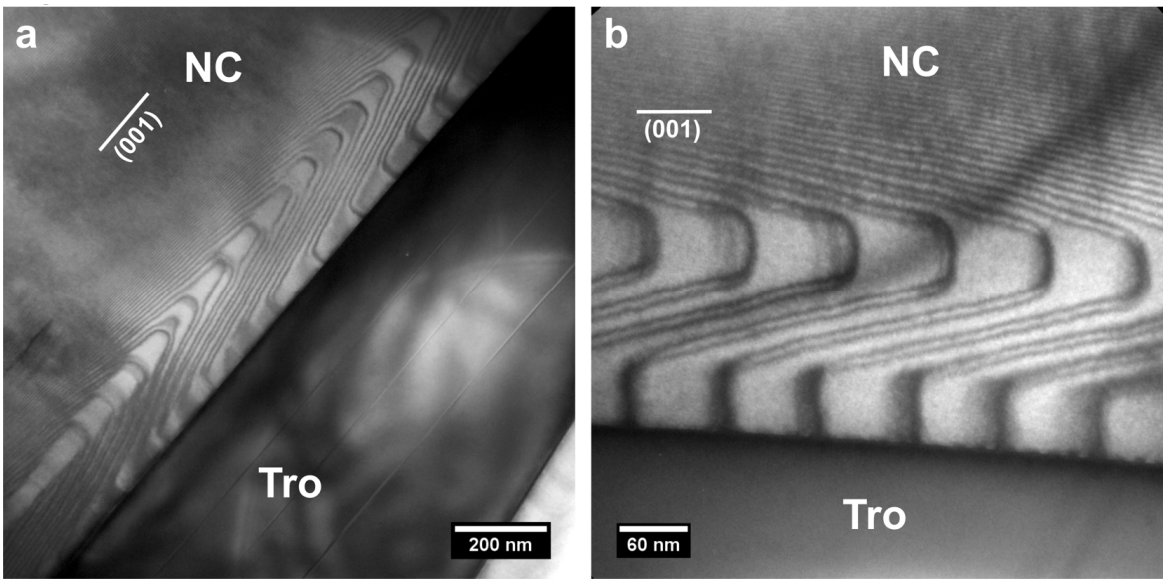

FIGURE 2-8. SDF-TEM images of APB configurations adjacent to troilite (Tro) exsolution lamellae in TYS pyrrhotite. Diffraction conditions as given in Fig. 2-6. (**a**) "Paper clip"-like APB arrangements within a Fe-depleted stranded diffusion profile along the NC-Tro interface. In orientations perpendicular to (001) APBs tilt away from edge-on view and stripes appear blurred. (**b**) Detailed view of APBs at the NC-Tro interface. With increasing distance APB stripes become more and more parallel to (001) and spacings narrow down.

Upon approaching the interfaces of the troilite exsolution lamellae in the TYS sample we were able to image stripes within the NC phase displaying bent configurations and gradually increasing spacings towards the phase boundaries (Fig. 2-8). Similar to EUL and NYS the stripes show a strong tendency to behave as pairs. SDF imaging of the pure NC

portion of the TYS sample could not reveal clearly visible stripes, which, however, appears to be a problem of imaging resolution as the expected APB spacings for N_c around 5.5 come close to our resolution limit of approx. 0.8 nm. We interpret the behavior of APBs close to the phase boundary to be a consequence of a compositional gradient in the Fe/S ratio as possibly indicated by SEM-BSE imaging. Because Fe deficiency of the APB modulated NC structure can be accomplished by either increasing the spacings of non-conservative APBs or changing their orientation towards the (001) planes (or a combination of both), the observed behavior is compatible with our APB modulation model and the inferred presence of stranded diffusion profiles arising from exsolution of troilite from the host pyrrhotite. As expected, SAED patterns obtained from the NC/troilite interface reveal diffuse NC satellite reflection, but the corresponding N_c values of the reflections fall in the range of approx. 5.7 to 6.1. Such high values are usually indicative of high Fe/S ratios and high densities of APBs, contrary to what we observe in the interface regions. However, the relations between N_c, composition and APB density are strictly applicable only when the APBs are distributed evenly or in the most ideal case uniformly, that is when the average spacing on any interval is as close as possible to a certain value (Amelinckx and van Dyck, 1993), which is in our case the inverse of *q*'. Within the observed structural gradient this condition is not fulfilled as distances between APBs gradually change. More importantly, the clear tendency of APBs to occur in pairs with relatively large spacings in-between them is expected to increase the apparent periodicity and N_c value of the structure, because repeat distances become longer compared to more equally spaced arrangements.

2.4.4. High Resolution Imaging (HR-TEM)

As mentioned, HR imaging faces difficulties when NC-pyrrhotite is subjected to high electron current densities. The HR image of the NC portion of EUL shown in Figure 2-9 was obtained on a previously non-irradiated area by adjusting the beam at the foil edge followed by quick movement of the specimen and immediate exposure (5 seconds). Its accompanying FFT pattern reproduces well the unaltered NC SAED pattern obtained from a much larger area at the imaged site (Fig. 2-9b,c). In this particular case we are confident that the obtained phase contrast in the HR image indeed represents the original state of the specimen. Based on image simulation (JEMS, Stadelmann 2008) of a constructed 5C-pyrrhotite structure with planar DSDS stacking (see below) the bright rows can be

identified as vacancy bearing Fe layers (note that even under ideal conditions the four possible V layer types cannot be distinguished unambiguously due to projection issues).

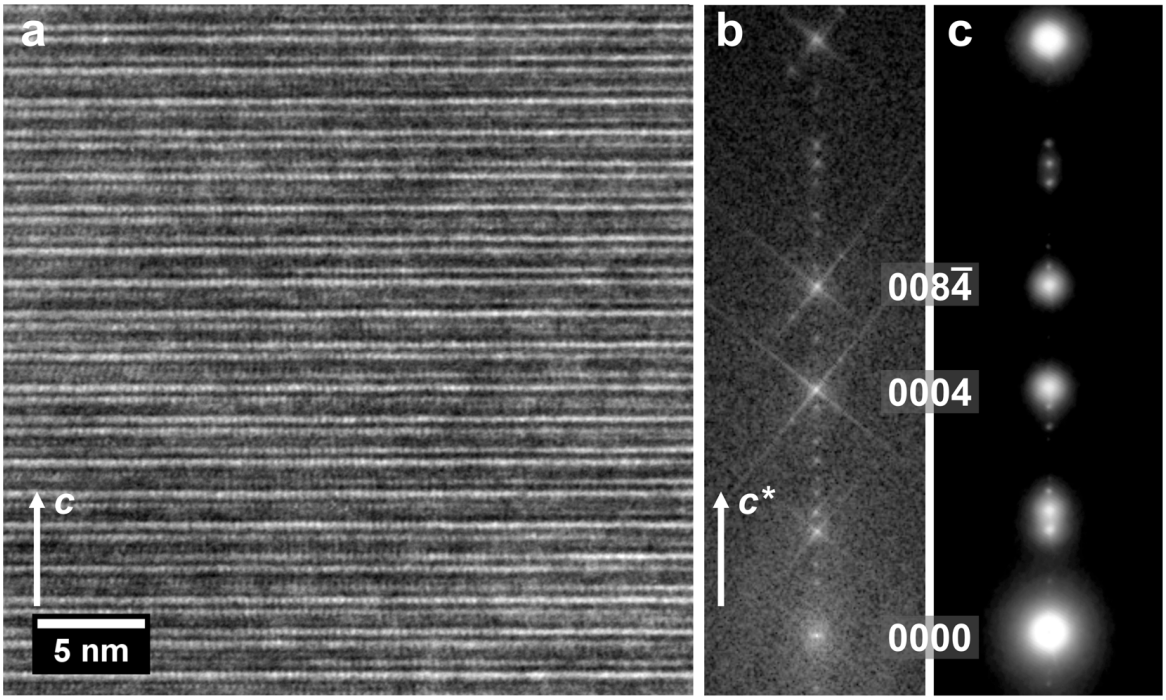

FIGURE 2-9. (**a**) HR-TEM image of NC-pyrrhotite in EUL. Alternating layer types stacked along the c direction are clearly visible and close inspection shows that some layers laterally change contrast, indicating undulation of APBs. (**b**) Central row of the FFT pattern derived from the HR image in a. For FFT sampling the images was rotated 45° to avoid streak artifacts overlapping the frequency maxima. (**c**) Central row of the NC SAED pattern obtained at the imaged site. The FFT and SAED pattern match very well, indicating that the imaged structure in (a) indeed represents the structural state of NC-pyrrhotites.

Closer inspection of the image shows that some vacancy layers extend over the width of the image while others gradually change their contrasts. This behavior is interpreted to be the result of waviness of APBs which is observed in SDF images of EUL (Fig 2-7a). This waviness can be explained as local jumps of APBs between adjacent (001) lattice planes of the base structure. This ultimately leads to transitions between vacant and filled layer types within the same layer plane. Because the HR image integrates over a relatively large specimen thickness of approximately 20 nm (compare to the width of Fig. 2-9a being 30 nm), the irregular jumps will result in gradual contrast changes. Also the typical scale of waviness of tens of nm as seen in Fig. 2-7a is well consistent with what is seen in the HR image.

2.5. Discussion

2.5.1 A Translation Interface Modulation Model for NC-Pyrrhotites

Based on our TEM observations we find that there is compelling evidence that the structural diversity observed in SAED patterns and SDF images of non-integral NC-pyrrhotites can be explained in terms of a TIM structure model. The translation interfaces are APBs formed by ordering of Fe vacancies in the Fe sublattice of the NiAs-type base structure. The resulting NC structures can be seen as superposition of two modulations: First, an occupation modulation of the NiAs-type base structure forming the 4C superstructure by a relatively simple vacancy ordering scheme. Second, a translation interface modulation by regular arrangement of APBs related to the primary 4C structure. This model bears resemblance to previously suggested 'out-of-step' and anti-phase defect models (Pierce and Buseck 1974) but is more precise on the actual nature of the involved translation interfaces and flexible enough to explain the variability of NC-pyrrhotite structures and compositions. On the other hand, the superspace approach of Izaola et al. (2007) is a single step occupancy modulation, but in principle fully compatible with our TIM model, which we see as a viable extension towards understanding the real structure of modulated pyrrhotites.

In order to explain why a two step modulation model provides a better description the real structure, we will discuss the idealized layer stacking. In essence, the superspace model of Izaola et al. (2007) produces discretely modulated superstructures by inserting additional F layers into the basic 4C layer sequence, producing either periodic or aperiodic (but uniform) stacking sequences parallel to (001). Because the so produced double F layers carry an Fe excess, the resulting phases will have higher Fe/S ratios than 4C-pyrrhotite and follow strictly the relation $2x = 1/N_c$ as spacings between double layers are evenly distributed (here $1/N_c$ corresponds to the modulation parameter γ of Izaola et al., 2007). A simple model of how more complicated structures can be gradually derived by insertion of extra F layers is shown in Figure 2-10a. Starting from the 4C structure the addition of one extra F layer results in a 4.5C structure in which one double F layer ("D" as opposed to single F layers designated "S") exists. Basically only one unique insertion option exists as the actual sequence of vacant layers V is solely dependent on how the origin is chosen (as outlined above) and hence there are four fully equivalent realizations (DSSS, SDSS, SSDS, SSSD). Adding another F layer to form a 5C structure now faces three options as there are three distinct sites for insertion into the DSSS structure: the D

layer, the two equivalent S layers next to it, and the isolated S layer. The resulting unique configurations are DSDS, DDSS and TSSS, whereas the latter contains a triple F layer ("T"). Further insertions lead to 5.5C and 6C structures with four and eight unique configurations, respectively, although in each case only one exists that has layers not larger than D, i.e., DDDS for 5.5C and DDDD for 6C.

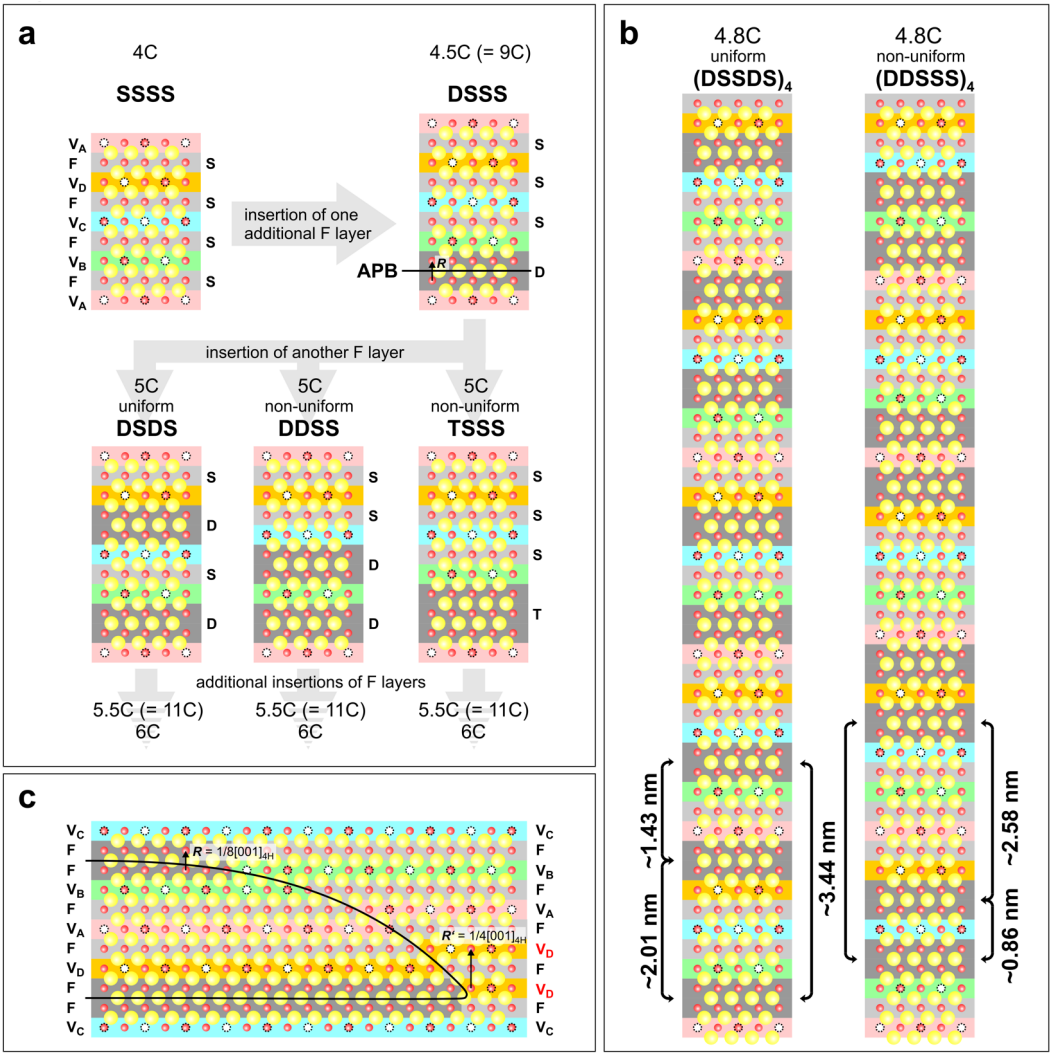

FIGURE 2-10. Representations of idealized stacking schemes and defect structures in NC-pyrrhotites. Yellow spheres = sulfur, red spheres = iron, dashed/white circles = vacancies (also in projection). (**a**) Structural evolution of 4C-pyrrhotite to NC-pyrrhotites by insertion of additional fully occupied Fe layers (F) forming double (D) and triple (T) layers. A double layer is equivalent to an APB with the displacement vector **R** = $1/8[001]_{4H}$. (**b**) Two periodic stacking sequences for N = 4.8. $(DSSDS)_4$ has an uniform distribution of D layers/APBs and can be considered as a very idealized representation of what is seen in sample EUL. $(DDSSS)_4$ is slightly less ordered and closer to the APB configuration seen in most of the NYS sample. (**c**) Schematic concept of the termination of two APBs leaving a fault in the vacancy layers sequence of 4C-pyrrhotite (here: two consecutive V_D layers). The sequence fault has a displacement of **R'** = $1/4[001]_{4H}$ = $[001]_{1H}$ and therefore eight APBs (four doublets) have to terminate, or two ABPs have to end in an edge dislocation with **b** = $[001]_{1H}$, to reconstruct the proper 4C sequence.

In principle all non-integral NC stacking sequences can be derived by combining blocks of these simple NC sequences. This leads to a vast amount of possible combinatorial variations, which are enhanced by the fact that equivalent sequences (e.g., DSDS vs. SDSD) loose their equivalency when heterogeneously stacked with each other or other blocks. Inspection of the three 5C layer configurations in Figure 2-10a shows that DSDS has the most evenly distributed D layers – in fact it is a uniform distribution, because on each arbitrary interval the average spacing of F layers is as close as possible to the average F layer spacing of the unit cell. The somewhat clustered F layers in the DDSS and TSSS sequences do not fulfill this condition as intervals can be found on which the averaged F spacings are not as close as possible to the unit cell average. In general, the uniform sequence out of a set of possible stacking variations is the one with the highest degree of order and corresponding lowest conditional entropy, which can be calculated using the method of Burrows and Sulston (1991). In this context it can be seen that the superspace approach of Izaola et al. (2007) yields in any case the uniform and most ordered sequence for a given N as both the widths and spacings of atomic domains are constant throughout the superspace cell.

For an idealized structure with $N_c = 4.8$, which is a simple representation for the host NC-pyrrhotite in our EUL and NYS samples, it is possible to derive two well ordered stacking schemes shown in Figure 2-10b. The $(DSSDS)_4$ sequence can be derived via the superspace model of Izaola et al. (2007) and is uniform, while the $(DDSSS)_4$ sequence cannot be obtained from the model and has less equally spaced D layers, leading to slightly less order while maintaining the same average vacancy-vacancy distance. We propose that the observed D layer or APB arrangements in EUL are alike the well ordered $(DSSDS)_4$ sequence, while in NYS domains relating to both stacking schemes coexist as indicated by the changes in stripe configuration (Fig. 2-7b,d). Here the domains containing the thicker, non-resolvable stripes correspond to the $(DDSSS)_4$ stacking in which the closest spacing between D layers or APBs is approx. 0.86 nm and thus more or less equal to the half-width of a single stripe as observed in EUL. The average ~1.72 nm D layers spacing of the idealized $(DSSDS)_4$ sequence compares well with the average stripe and APB spacings in EUL as obtained from SDF images and SAED patterns, respectively, and consistently reproduces the observed slightly non-equal spacings in the bulk NC phase. It appears reasonable to assume that in case of NYS the energetic difference between both arrangements of D layers in the $(DSSDS)_4$ and $(DDSSS)_4$ stacking variants are very small

and either the structure is observed on a transition to a more ordered state as in EUL or the elevated Ni content exerts some control on vacancy arrangements.

As pointed out, the discussion so far focused on an idealized layer stacking involving parallel layer arrangements. SDF and HR images clearly shows that this ideal situation is virtually never fulfilled in our samples as APBs are wavy, corrugated and often non-parallel. It therefore appears suitable to resolve the idealized layer stacking (or one step occupancy modulation) into a structural hierarchy: a 4C base structure and a superimposed TIM formed by quasi-periodically arranged APBs. We would like to emphasize that the sole cause of NC superstructures and APBs is still the arrangement of vacancies but in a rather complex manner.

Changes in stacking schemes at given N values as well as disorder introduced by wavy APBs will not immediately show strong effects in SAED patterns as long as the average APBs spacings stay constant. The $(DSSDS)_4$ and $(DDSSS)_4$ stacking schemes have exactly the same average APB spacing and the diffraction pattern geometries will be the same with only moderate differences in spot intensities, likely being hidden by dynamical diffraction effects. Increasing mesoscopic scale disorder of APBs will first lead to vanishing higher order satellite reflections and gradually lead to streaky diffraction along the **c*** direction when a quasi-periodicity is no longer maintained. Direct SDF imaging clearly can add a significant amount of additional information to this complex situation. While a D layer in the ideal layer model is always an APB of the Fe sublattice the converse is not strictly true as isolated APBs are capable of moving more or less freely through the crystal and can have even in the confinement of a modulated structure a much more dynamical behavior as represented by a static layer model. The waviness of APBs can be envisaged as the short range jumping of the boundary between lattice planes adjacent to its mean plane. Within a given Fe layer (defined by its position within the sulfur sublattice), these local jumps cause lateral transitions of the layer type from V to F or vice versa and result in a mixed state with patches of V and F types measuring tens of nm. The importance of recongnizing these structural details is exemplified by the fact, that the concept of stochastic waviness of APBs in TIM structures is well established in materials sciences (e.g., Jehanno and Perio 1964; Guymont et al. 1980). Guymont (1991) showed by entropy considerations that in TIM modulated alloys at elevated temperatures wavy APBs are thermodynamically preferred over straight APBs. The author postulates that the wavy APB configuration (structures of the second kind) cannot be stable down to

0 K and structural changes to planar APB arrangements (structures of the first kind) will take place below a certain transition temperature. In this context, our observations suggest that at ambient temperature the studied NC-pyrrhotites still exist in a wavy APB state of the second kind, implying that the minimization of defect energies by straightening out the APBs, and hence reducing the interface areas, is counterbalanced by entropy contributions.

2.5.2. Structural Organization at Phase Interfaces

The need of a more dynamical model clearly becomes apparent when trying to understand the node structures observed at NC/4C phase interfaces. The termination of eight stripes equivalent to eight APBs in a single node is necessary to reconstruct the 4C structure from an NC structure with well ordered V layer stacking. Figure 2-10c schematically illustrates the termination of two APBs in a simple node. Because the stacking of V layers on the left side strictly obeys the ABCD sequence, the termination creates a sequence fault on the right side, where two V_D layers follow in succession. Such a situation is energetically very unfavorable as the two close vacancies strongly repel each other. However, changing the V layer type at the termination by introducing another APB vector lying parallel to the (001) plane does not change this problem significantly as the most favorable ABCD stacking sequence cannot be regained by this. To achieve this, two APBs have to terminate either at a perfect dislocation with $\mathbf{b} = [001]_{1H} = 1/4[001]_{4H}$, which removes a pair of VF layers, or 4 pairs of APBs have to terminate close-by such that the eight $1/8[001]_{4H}$ displacement vectors add up to the 4C lattice repeat.

Both variants and combinations thereof are seen in our samples and we suggest that the observed node configurations in Figure 2-7c,d facilitate an energetically most favorable state when there are no or few dislocations involved. Also the very dynamical behavior of APBs in the inferred diffusion profiles surrounding the troilite exsolution lamellae in TYS requires our proposed TIM model. Apparently the arrangement and especially the tilting of APBs relative to the crystallographic axes facilitate energetically favorable states in conjunction with local Fe concentrations and gradients. However, currently it is not known whether formation of the diffusion profiles preceded the vacancy ordering and formation of APBs or whether the APBs actively played a role in the diffusion process. The latter implies interesting consequences for atomic transport in pyrrhotite as Fe diffusion would occur as collective movement of Fe atoms along the movement of APBs (being the

carriers of local Fe excess). The relatively large bright areas seen in-between the dark APB stripes within the diffusion region likely represent nm-sized domains of 4C-pyrrhotite which should show ferrimagnetic behavior in the otherwise antiferromagnetic NC-troilite mixture. Also the interface configurations seen in NC-4C mixture may bear effects on magnetic properties, but require more detailed understanding of the structure within the nodes.

2.5.3. Implications and Outlook

The omnipresent contribution of stochastic disorder in APB spacings and orientations renders the concept of a regular polytypism or polysomatism in pyrrhotites rather problematic. Despite the definition of polytypism is wide and also allows for minor variations in stoichiometry (Guinier et al. 1984), the most typical polytypic compounds, such as SiC or ZnS, show highly planar building layers. In such materials the interfaces of the building layers are usually stacking faults and, alternatively, polytypes could be viewed as stacking fault modulated crystals (van Landuyt et al. 1985). As shown, the modulating interfaces in pyrrhotite are not stacking faults but APBs. Moreover, the modulating APBs are not strictly planar, a consequence that likely results from smaller defect energies compared to stacking faults and the additional contribution of entropy. Conceiving APB modulated pyrrhotites as polytypes might be correct by definition, but potentially misleading when it comes to recognizing the structural variability on the scale of tens of nm. The concept of polysomatism is related to polytypism and discussed in detail by Veblen (1991). The author compares polysomatism to the alternative model of crystallographic shear structures, which is much alike our TIM approach, and concludes that both views are equally valid but have different strong points. While a regular stacking of building units or layers can be appropriate in the description of idealized crystallographic structures, it has its weakness in representing the real structures of NC-pyrrhotites. The TIM approach can at the same time rationalize observed diffraction pattern and conceptually explain the varied behavior of modulating interfaces. This appears to us essential in order to understand structural organization and eventually the bulk physical properties resulting from it.

The magnetism of pyrrhotites is likely the bulk property being most susceptible to structural changes. 4C-pyrrhotite is well known to be ferrimagnetic due to unbalanced antiferromagnetic coupling between internally ferromagnetic V and F layers

(experimentally shown, e.g., by Powell et al. 2004). The same principle of coupling has been applied to antiferromagnetic NC-pyrrhotites in order explain the absence of a significant net magnetic moment for structures with integral N_c values (e.g., Li and Franzen 1996). However, the full compensation of antiparallel moments of Fe layers works only for some of the many possible layer stacking sequences such as the integral ones – for others nonzero net moments result. It remains an open question whether such hypothetically ferrimagnetic NC-pyrrhotites are thermodynamically unstable with respect to their antiferromagnetic pendants or nonexistent due to the stochastic waviness of APBs and the concomitant lateral changes of Fe layer types. The latter could result in an averaging effect that may equalize the magnetic moments of the individual Fe layers and lead to a zero net moment of the bulk structure. These possibilities need careful testing by theoretical modeling and detailed magnetic studies of samples that are well characterized in terms of structure (N_c value), phase assemblage, and exsolution texture.

Based on the TIM model and the Izaola et al. (2007) superspace approach we suggest that there is no significant difference between integral and non-integral NC-pyrrhotites and both types can be understood as part of a continuum of structures in-between Fe_7S_8 and (at least) $Fe_{11}S_{12}$, in which variable Fe/S ratios are related to changes in densities and ordering states of APBs. This implies that X-ray crystallographic models of integral pyrrhotites involving partial occupancies of Fe sites likely reflect mesoscopic scale disorder of APBs by averaging over larger volumes of material in which APBs are not arranged in strictly parallel or uniform manner. Any completly uncorrelated disorder on atomic scales (i.e., the independent behavior of vacancies) seems unreasonable because such purely stochastic structures would not allow the formation of APBs. While to some extent partial occupancy models may be statistically correct representations, it must be cautioned that a general assumption of integral cell multiplicities (or crystallographic periodicity in general) may not be appropriate as these are only special cases within the continuum of possible modulated structures and many structural variants can coexist on and even below the grain size scale (e.g., Morimoto et al. 1975b; our observations).

Based on the presented data and preliminary data on other natural pyrrhotite samples we currently do not see evidence for preferred stability of integral NC-pyrrhotites, maybe with the exception of 11C (N_c = 5.5) as observed in our TYS sample. The true phase relations may be obscured by slow diffusion kinetics below 220 °C, where NC-pyrrhotites first appear (Nakazawa and Morimoto, 1970). However, unlike the situation observed in

the TYS sample, the very sharp compositional gradients at the 4C/NC interfaces in our EUL and NYS samples point to well equilibrated assemblages (basically the Fe/S gradient is confined to the size of the observed node structures, i.e., <20 nm). Therefore, the association of $N_c \approx 4.85$ pyrrhotite with exsolved 4C-pyrrhotite in two of our samples, as well as the coexistence of $N_c = 4.88$ pyrrhotite and 4C-pyrrhotite observed by Morimoto et al. (1975b), points to a favored stability of NC-pyrrhotites within the range of $N_c = 4.8$ to 4.9 – at least with regards to typical temperatures of the uppermost crust, where the samples resided for geological timescales. For pyrrhotites having $N_c > 5$ the situation appears somewhat more complicated as the range of realized N_c values seems to be much broader as shown by our TYS sample and the X-ray results of Morimoto et al. (1975b), who found a wide range of N_c values as well as coexisting troilite within a single sample. These findings may suggest that the association of $N_c \approx 5.5$ pyrrhotite and exsolved troilite is another phase assemblage stable at low temperatures of <150°C, where troilite becomes stable. Clearly, more observations on naturally occurring exsolution assemblages are required in order to derive reliable phase relations.

Obviously, APBs form by ordering of vacancies upon the transition from one of the high temperature structural variants of pyrrhotite (e.g., the disordered 1C-pyrrhotite or the poorly characterized, maybe partially disordered NA-pyrrhotite). However, at present it remains unknown what driving forces are responsible for structural organization in interface modulated pyrrhotites and what energetic contributions stabilize them with respect to the more simple structured end-members 4C-pyrrhotite and troilite. Generally, modulated structures arise from the competition of interactions imposing different structural periods when considered on their own (Amelinckx et al., 1989). For example, in case of a charge density wave modulated structures atoms are slightly shifted out of their ideal positions due to the existence of a modulation in electron density having a period different from the repeat of the crystal structure. The accompanying increase of elastic energy is overcompensated by a decrease of electronic energy due to modifications of the Fermi surface and thus allows for the formation of a stable displacement modulation. On the other hand, in cases of occupancy or interface modulated structures other phenomena like competing nearest and next nearest neighbor electrostatic or magnetic interactions may play significant roles and appear especially in case of pyrrhotite worth considering due to the increased mobility of Fe in the presence of vacancies (Condit et al., 1974). The understanding of mechanisms and driving forces behind structural organization in

modulated pyrrhotites promises interesting and significant implications for many fields of mineral and materials sciences due to the ubiquitous occurrence of this mineral and its highly variable magnetic and physicochemical properties.

2.6. Acknowledgements

This is publication no. GEOTECH-1526 of the R&D program GEOTECHNOLOGIEN funded by the German Ministry of Education and Research (BMBF) and German Research Foundation (DFG), grant 03G0718A. We also acknowledge financial support provided by the DFG Leibniz program (LA 830/14-1 to FL). The authors are grateful to R. Caracas for the discussion of modulated structures and N. Miyajima for assistance with TEM work. Reviews by A. Pring and an anonymous reviewer helped to improve the manuscript and are gratefully acknowledged.

CHAPTER 3 The Nanoscale Mineralogy of Fe,Ni Sulfides in Pristine and Metamorphosed CM- and CM/CI-like Chondrites: Attempting to Tap a Petrogenetic Record

by Dennis Harries[1,2]* and Falko Langenhorst[2]

[1]Bayerisches Geoinstitut, University of Bayreuth, D-95440 Bayreuth, Germany. [2]Institut für Geowissenschaften, Friedrich-Schiller-Universität Jena, Carl-Zeiss-Promendae 10, D-07745 Jena, Germany.
*Corresponding author. Email: dennis.harries@uni-bayreuth.de

3.1. Abstract

We have sampled sulfide grains from one pristine CM2 chondrite (Yamato [Y-] 791198), one thermally metamorphosed CM2 chondrite (Y-793321), and two anomalous, metamorphosed CM/CI-like chondrites (Y-86720 and Belgica [B-] 7904) by the focused ion beam (FIB) technique and studied them by analytical transmission electron microscopy (TEM). Our study aims at exploring the potential of sulfide assemblages and microstructures to decipher processes and conditions of chondrite petrogenesis. Complex NC-pyrrhotite-troilite-pentlandite exsolution textures occur in grains of Y-791198 and Y-793321 and, polycrystalline 4C-pyrrhotite-pentlandite-magnetite aggregates occur in Y-791198, pointing to diverse conditions of gas-solid interactions in the solar nebula. Coarser exsolution textures of Y-793321 grains indicate higher long term average temperatures in the < 100 °C range compared to Y-791198 and other CM chondrites. Sulfide mineralogy of Y-86720 and B-7904 is dominated by aggregates of pure troilite and metal, indicating metamorphic equilibration at fS_2 of the iron-troilite buffer. Absence of magnetite in equilibrium with sulfide and metal in Y-86720 indicates higher peak temperatures compared to B-7904, in which coexistence of troilite, metal, and magnetite constrains metamorphic temperature to less than 570 °C. NC-pyrrhotite occurs in both meteorites as nm-wide rims on troilite grains and, together with frequent anhydrite, indicates a retrograde metamorphic stage at higher fS_2 slightly above the FMQ-Po buffer. Fine-grained troilite-olivine intergrowths in both meteorites suggest the pre-metamorphic presence of tochilinite-serpentine interlayer phases, pointing to mineralogical CM affinity. Pseudomorphs after euhedral pyrrhotite crystals in Y-86720 in turn suggest CI affinity as do previously published O isotopic data of both meteorites.

3.2. Introduction

3.2.1. CM and CM/CI-like Chondrites

CM chondrites are one of the cosmochemically most primitive meteorite groups, but at the same time, they are probably one of the mineralogically most complex rock types. Most characteristically, they are rich in fine-grained matrix material and experienced extensive aqueous alteration (McSween 1979; Zolensky et al. 1997), documented by the presences of phyllosilicates (typically Fe-rich serpentines; Bunch and Chang 1980; Browning et al. 1996), tochilinite (a complex Fe-rich hydroxide/sulfide interlayer mineral; Zolensky 1987), and Ca and Ca-Mg carbonates (Johnson and Prinz 1993; Benedix et al. 2003). The low temperature mineral assemblage (typically formed at temperatures significantly less than 100 °C; Guo and Eiler 2007; Zolensky et al. 1993) indicates an episode of exposure of primary, anhydrous minerals to a water-rich environment. While most alteration probably occurred on the CM parent body, there is ample evidence that some components might have been hydrated in the solar nebula (Metzler et al. 1992; Bischoff 1998; Ciesla et al. 2003). A similar issue is the origin of pyrrhotite and pentlandite present in CM chondrites (Bunch and Chang 1980). Pentlandite and pyrrhotite have frequently, and often implicitly, been assumed to be products of parent-body alteration of troilite or metal (e.g., Hanowski and Brearley 2001), while pyrrhotite itself (Fe deficient $Fe_{1-x}S$) has often been overlooked due to its similarity to troilite (stoichiometric FeS). Pyrrhotite is an extremely variable mineral and, depending on formation conditions, can occur in several compositionally and crystallographically distinct forms (e.g., Wang and Salveson 2005; Harries et al. 2011). Zolensky and Thomas (1995) showed that pyrrhotite is abundant in interplanetary dust particles (IDPs) and suggested its formation via extended sulfidation of troilite in the solar nebula. Similarly, Boctor et al. (2002) and Brearley and Martinez (2010) suggested that pyrrhotite- and pentlandite-bearing grains in CM chondrites are primary products of the nebula − yet, there has been little exploration of these minerals in chondrites.

Some CM and CM/CI-like chondrites experienced thermal metamorphism that partially led to the dehydration of phyllosilicates. Particularly among the meteorites collected in Antarctica by Japanese NIPR field parties (Yamato and Belgica recovery sites) a large fraction of CM- and CI-like chondrites displays thermo-metamorphic overprints, which have sparked extensive studies of these rocks (e.g., Akai 1988; Ikeda 1992 and ref. therein). The number of CM and CM/CI-like chondrites known to have been thermally

affected is steadily growing (e.g., Nakato et al. 2011), indicating that metamorphism and dehydration might be a relatively common process in the evolution of hydrous asteroids. Due to the complex phase relationships and thermochemistries of Fe and Fe,Ni sulfides, their petrogenetic record within these meteorites is interesting and in the process of being tapped (e.g., Kimura et al. 2011).However, the study of sulfides remains challenging for at least two reasons: First, the small sizes and small-scale intergrowths of different sulfide phases. Second, the relatively unconstrained nature and history of sulfides in the pre-metamorphic chondrites.

In this contribution we focus on the sulfide mineralogies of Antarctic CM and CM/CI-like chondrites that experienced very different degrees of thermal metamorphism, from none to severe. We overcome the challenge of small size by using focused ion beam (FIB) preparation and analytical transmission electron microscopy (TEM). The aim is to decipher the phase assemblages and microstructures of Fe sulfides, in particular those of pyrrhotites, in order to obtain constraints on key parameters of primary formation and secondary alteration and metamorphisms, including sulfur and oxygen fugacities, metamorphic temperatures, and cooling rates.

3.2.2. Previous Work and Constraints on Metamorphic Histories

Prominent members of the anomalous group of metamorphosed CM/CI-like meteorites are Y-82162, Y-86720, and B-7904 (often referred to as Belgica grouplet). Besides mineralogical evidence for anomalous thermal histories, these rocks also display petrographic, mineralogical, geochemical, and isotopic characteristics that place them in uncertain relationship with both CM and CI chondrite groups (Bischoff and Metzler 1991; Ikeda 1992). Oxygen isotopic compositions of Y-82162, Y-86720, and B-7904 discussed by Clayton and Mayeda (1999) are very similar but distinct from typical CM and CI chondrites, although a genetic link to the CI group may be possible through mass-dependent oxygen isotope fractionation during dehydration. Y-793321 is an atypical CM2 chondrite that has experienced metamorphic heating, leading to the breakdown of tochilinite and partial dehydration of phyllosilicates (Nakamura 2006). On the contrary to the Belgica grouplet, Y-793321 shows O isotopic ratios much closer to the CM trend and could have originated from a rather weakly hydrated CM precursor (Clayton and Mayeda 1999). Trace element geochemistry (Paul and Lipschutz 1990; Yamamoto and Nakamura 1990) places Y-86720 in proximity to the CM group or between CM and CI, and B-7904

also in proximity to the CM group. The trace element composition of Y-793321 is reported to be well consistent with typical CM2 chondrites (Tonui et al. 2002). The Belgica grouplet chondrites have experienced metamorphic heating in the range of about 500 to 800 °C. Y-793321 was heated to a much lesser degree. A compilation of estimated metamorphic temperatures is given in Table 3-1. A large uncertainty factor in these estimates arises from the unknown duration of heating, because many criteria rely on strongly kinetically controlled processes, such as phyllosilicate dehydration and migration of mobile trace elements. Nakato et al. (2008), for example, estimated the heating time of B-7904 in the order of 10 to 1000 days at 700 °C and 1 to 100 hours at 890 °C. Organic geochemistry studies by Shimoyama et al. (1991), Kitajima et al. (2002), and Naraoka et al. (2004) mostly agree with the reported relative degrees of metamorphic heating, but also indicate some inconsistencies.

TABLE 3-1. Compilation of reported metamorphic temperatures for Y-793321 and the Belgica grouplet chondrites.

Meteorite	Stage*	Temperature range (°C)	Source
Y-793321	II, B	300-500	2
Y-793321	II, B	<500	7, 8
Y-793321	II, B	<500	9, 10
Y-82162	III/II	600-800	2, 5
Y-82162	III/II	600-700, <Y-86720	3
Y-82162	III/II	<400	6
Y-82162	III/II	<700, <Y-86720	7, 8
Y-86720	IV, C	700-850	2, 5
Y-86720	IV, C	600-700, >Y-82162	3
Y-86720	IV, C	500-700	6
Y-86720	IV, C	>500	1
Y-86720	IV, C	≤700	7, 8
B-7904	IV, C	750-900	2, 5
B-7904	IV, C	600-700, <Y-82162	3
B-7904	IV, C	<600, 400-500	4
B-7904	IV, C	>500, ≈Y-82162	7, 8
B-7904	IV, C	700-890	11

*Heating stage (numerals I to IV) of Nakamura (2005), metamorphic category (letters A to C) of Kimura et al. (2011). 1: Tomeoka et al. (1989b), 2: Akai (1990), 3: Paul and Lipschutz (1990), 4: Zolensky et al. (1991), 5: Akai (1992), 6: Zolensky et al. (1993), 7: Lipschutz et al. (1999), 8: Tonui et al. (2002), 9: Nakamura (2005), 10: Nakamura (2006), 11: Nakato et al. (2008).

We have included Y-791198 into our study, because this meteorite is regarded as one of the most primitive CM chondrites known. Textural and chemical evidence indicates that

this meteorite is a primary accretionary rock that experienced little to intermediate degrees of parent body aqueous alteration (Metzler et al. 1992; Rubin et al. 2007), no thermal metamorphism (Shimoyama et al. 1991; Kitajima et al. 2002; Naraoka et al. 2004), and no impact-induced brecciation (Metzler et al. 1992).

3.2.3. Pyrrhotites in the Fe(+Ni)-S System

Despite its simple composition, pyrrhotite is a remarkably complex mineral, demanding here a short overview of its mineralogy. Pyrrhotite, being $Fe_{1-x}S$ with x typically between 0 and 0.125, is a non-stoichiometric iron sulfide with Fe-site vacancies. Relevant pyrrhotite compositions occupy the Fe-S system between 46 and 50 at% Fe and form a series between Fe0.875S and stoichiometric FeS (troilite). The (omission) solid solution is mostly complete at temperatures above 320 °C and the Fe vacancies are randomly distributed in the hexagonal, NiAs based lattice (1C-pyrrhotite; Grønvold and Stølen 1992; Wang and Salveson 2005). It has been shown by several studies that the Fe/S ratio and the corresponding x value of solid 1C-pyrrhotite at T > 500 °C is primarily a function of temperature and sulfur fugacity (fS_2 ; e.g., Rau 1976; Toulmin and Barton 1964) as shown in Figure 3-1a. At given T > 320 °C, a specific pyrrhotite composition is in equilibrium with gaseous S_2 of determined fugacity. The pyrrhotite field is bounded by the reactions:

$$FeS_{(s)} \rightarrow Fe_{(s)} + 0.5S_{2(g)} \qquad (3\text{-}1)$$

$$Fe_{1-x}S_{(s)} + (0.5\text{-}x)S_{2(g)} \rightarrow (1\text{-}x)FeS_{2(s)} \qquad (3\text{-}2)$$

Reaction 3-1 describes the iron-troilite buffer (IT; e.g., Froese and Gunter 1976), which fixes fS_2 as function of temperature. Reaction 3-2 is the pyrite-pyrrhotite buffer. The addition of Ni into the hexagonal monosulfide solid solution (MSS, $Fe_{1-x}S$ – $Ni_{1-x}S$) at 600 °C increases the metal/sulfur (M/S) ratio at given fS_2 and decreases the metal deficiency x (Kosyakov et al. 2003; Raghavan 2004). For example, the equilibrium log fS_2 for approx. x = 0.08 increases from −5 for $Fe_{0.92}S$ to −4 for $(Fe_{0.55}Ni_{0.37})S$. In the presence of suitable redox couples, fS_2 is constrained by oxygen fugacity fO_2 and vice versa, e.g., through the reaction with magnetite (Whitney 1984):

$$3Fe_{1-x}S_{(s)} + (2-2x)O_{2(g)} \rightarrow (1-x)Fe_3O_{4(s)} + 1.5S_{2(g)} \qquad (3\text{-}3)$$

These relationships allow formulating fS_2-fO_2 buffers as for example the FMQ-Po buffer of Eggler and Lorand (1993) shown in Figure 3-1b.

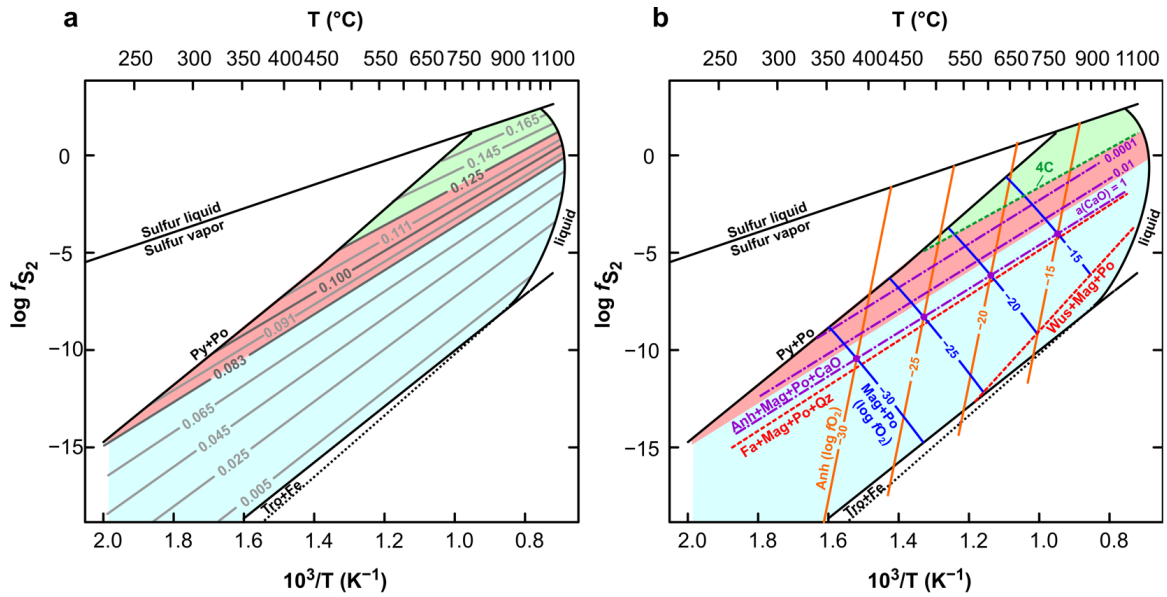

FIGURE 3-1. fS_2-T plots for the Fe-S system and various buffer assemblages at 1 bar total pressure. (**a**) Bounding reactions and Fe-deficiency isopleths for disordered 1C-pyrrhotite expresses as x in $Fe_{1-x}S$. Isopleths are based on Rau (1976), the iron-troilite (Tro+Fe) buffer is also shown based on Toulmin and Barton (1964) (dotted line). The sulfur condensation curve is based on JANAF data (Chase et al. 1985), the pyrite-pyrrhotite (Py+Po) buffer on Lusk and Bray (2002), and the melting curve on Rau (1976). (**b**) Mineral reaction isopleths for the fayalite-magnetite-quartz-pyrrhotite (Fa+Mag+Qz+Po) buffer of Eggler and Lorand (1993) and the wüstite-magnetite-pyrrhotite (Wus+Mag+Po) buffer (based on Frost 1991 and Whitney 1984). Also shown are isopleths for the anhydrite-magnetite-pyrrhotite assemblage at different activities of CaO (Anh-Mag-Po-CaO). The isopleths are defined by the intersection of common fO_2 isobars (labeled in log units) of the anhydrite dissociation (Anh, Eq. 6, data from Barin et al. 1989 and JANAF/Chase et al. 1985) and the magnetite-pyrrhotite reaction (Mag+Po, Eq. 3; Whitney 1984). This is shown for unity activity of CaO.

The formation of pyrrhotite in the solar nebula was attributed by Kerridge (1976) and Zolensky and Thomas (1995) to extended sulfidation of previously formed troilite by H_2S. In a simple system, this can be expressed by the reactions:

$$Fe_{(s)} + H_2S_{(g)} \rightarrow FeS_{(s)} + H_{2(g)} \qquad (3\text{-}4a)$$

$$(1-x)FeS_{(s)} + xH_2S_{(g)} \rightarrow Fe_{1-x}S_{(s)} + xH_{2(g)} \qquad (3\text{-}4b)$$

The reactions are more complex in nature, because the initial metal contains Ni and other components, leading to potentially complex reaction paths (Lauretta et al. 1997). As outlined above and shown in Figure 3-1a, the compositional variable x of non-stoichiometric pyrrhotite depends on T and fS_2, the latter being determined by T, P, and the H_2S/H_2 ratio. Notably, the pressure-dependence of the $Fe_{1-x}S+S_2$ equilibrium is rather small (Toulmin and Barton 1964). This suggests that pyrrhotite formation in exchange with a gas phase can, in principle, be attributed to fS_2 at values higher than the IT-buffer. Hence, pyrrhotite will not form at conditions when troilite, Fe,Ni metal, and ambient gas are in equilibrium.

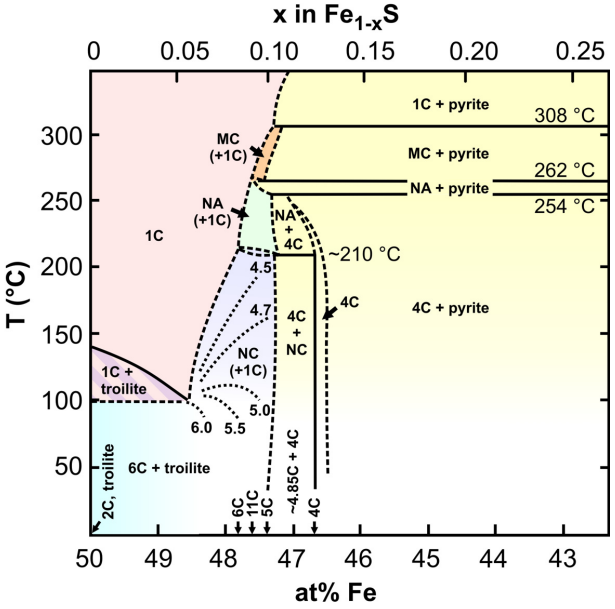

FIGURE 3-2. Simplified, low temperature phase diagram of the Fe-S system based on Nakazawa and Morimoto (1970) and Kissin and Scott (1982). Many of the phase boundaries are tentative and shown dashed. 2C, 4C, 5C, 11C, 6C designate pyrrhotite superstructures with their *c*-dimension multiplicity of the fundamental NiAs-type cell. 2C is troilite, 4C is monoclinic pyrrhotite (Fe_7S_8 or $Fe_{0.875}S$). 5C, 11C, and 6C are 'hexagonal' pyrrhotites (Fe_9S_{10}, $Fe_{10}S_{11}$, and $Fe_{11}S_{12}$, respectively). NC designates pyrrhotites with variable and often non-integral *c* dimension superstructure multiplicity, N values are given as dotted lines (Nakazawa and Morimoto 1970). 4.85C is a NC-pyrrhotite with non-integral multiplicity that commonly coexists with 4C-pyrrhotite at room temperature (Harries et al. 2011). MC- and NA-pyrrhotites are high temperature superstructures. 1C-pyrrhotite has completely disordered vacancies and a NiAs-type unit cell.

At temperatures below 320 °C, the Fe-S system within the pyrrhotite compositional range contains several one- and two-phase fields, which arise from (partial) ordering of Fe vacancies and formation of complex superstructures (Fig. 3-2). At ambient temperatures, NC-pyrrhotites exist, in which the c dimension of the superstructure is N times that of the fundamental NiAs-type cell. N ranges mostly between 4 and 6 and can take integral (4C, 5C, 6C) as well as non-integral values. The most common and best established pyrrhotite structure at ambient conditions is monoclinic 4C-pyrrhotite ($Fe_{0.875}S$ or Fe_7S_8), in which the vacancy ordering quadruples the NiAs based c lattice dimension (Bertaut 1953; Powell et al. 2004). In terrestrial samples, 4C-pyrrhotite is typically associated with NC-pyrrhotites, in which N takes non-integral values between 4 and 5, due to aperiodic

structural modulations, and is positively correlated with the Fe/S ratio (Harries et al. 2011; Morimoto et al. 1975b). At Fe/S close to unity, 1C-pyrrhotite can persist down to temperatures of approximately 100 °C before vacancies order into superstructures. In this compositional range, troilite is a commonly observed exsolution phase coexisting with NC-pyrrhotites, which formed from the disordered 1C phase. Experimental studies by Novikov et al. (1977) showed that during cooling and exsolution of troilite the structural evolution of coexisting pyrrhotite is rather complicated and proceeds in at least two stages.

NC-pyrrhotite coexisting with troilite at room temperature shows either non-integral N values of around 5.5 (~$Fe_{0.91}S$ or $Fe_{10}S_{11}$; Harries et al. 2011; Morimoto et al. 1975b) or an integral value of 6 ($Fe_{0.92}S$ or $Fe_{11}S_{12}$; Becker et al. 2010a; Morimoto et al. 1975a; Nakazawa and Morimoto 1970).The origin of this dichotomy is not well known. Experimental results by Nakazawa and Morimoto (1970) shown in Figure 3-2 suggest that during cooling of NC-pyrrhotite the N value increases continuously, and some of the non-integral NC-pyrrhotites might be metastable due to sluggish ordering kinetics. Hence, some of the observed assemblages might not represent equilibrium states at room temperature but rather frozen-in stages of their cooling history. The influence of Ni contents on the phase relationships of pyrrhotite below 320 °C is not well known, but generally Ni concentrations are low (typically less than 0.3 at%; Vaughan and Craig 1978; Etschmann et al. 2004) due to exsolution of pentlandite, $(Fe,Ni)_9S_8$. The latter is the typical carrier of Ni in exsolved terrestrial MSS. The onset of pentlandite exsolution depends on the M/S ratio and Ni content of the MSS and commences between 610 and 300 °C (Naldrett et al. 1967; Kelly and Vaughan 1983; Etschmann et al. 2004).

3.3. Sample Preparation and Analytical Methods

3.3.1. Sample Preparation

We have selected fresh interior fragments of Yamato-791198 (,97), Yamato-793321 (,101), Belgica-7904 (,114), and Yamato-86720 (,86).in order to avoid weathering effects and thermal overprint from atmospheric passage. Fragments were epoxy mounted and carefully polished. Care was taken not to heat the samples above room temperature in order to avoid any potential deterioration of the original sulfide microstructures.

3.3.2. Analytical Methods

For microprobe analysis, a JEOL JXA-8200 equipped with five wavelength dispersive

spectrometers was used and operated at 20 kV acceleration voltage, 20 nA beam current and focused probe size (counting 30 s on peak, 15 s on background). Reference material for Fe and S calibration was Ni-free Dalnegorsk 4C-pyrrhotite. Ni and Co were calibrated using pure metals. X-ray elemental distribution maps of 2×2 mm2 size were obtained on the same machine operated at 20 kV/30 nA using 45 to 50 ms dwell time and 2 μm defocus.

SEM imaging and FIB sample preparation for TEM study were accomplished using a FEI Quanta3D field-emission FIB-SEM equipped with a Pt GIS and an Omniprobe micromanipulator. For excavation of trenches around the targeted TEM foil sites, beam currents from 50 nA down to 3 nA at 30 keV ion energy were used. Cleaning before lift-out was applied using a 30 keV/1 nA beam. The remaining 0.5 to 1 μm thick lamellae were then cut free, extracted with the micromanipulator, and attached to a post type copper TEM grid. Final thinning was applied using beam currents of typically 300 pA, 100 pA, and 50 (or 30) pA at 30 keV energy. In order to minimize Ga implantation and ion beam induced structural damage, the last polishing step usually involved a beam energy of 5 keV and a current of 80 pA or lower. Under these conditions, the stopping depth of Ga^+ ions lies in the order of a few nm at grazing beam incidence relative to the foil surface (e.g., Rubanov and Munroe 2004). Heating effects are negligible in case of thermally well conducting sulfides as discussed by Wozniakiewicz et al. (2011).

For TEM observations we used a Philips CM20 FEG operated at 200 kV acceleration voltage and equipped with a Thermo Noran Ge EDX detector. Images and SAED patterns were recorded on conventional electron imaging film. EDX measurements and X-ray mappings were acquired in dark-field scanning TEM (DF-STEM) mode.

3.4. Results

3.4.1. SEM and EPMA Observations

3.4.1.1. Yamato-791198

Y-791198 shows an unbrecciated texture with abundant coarse grained ferromagnesian objects mantled by fine-grained rims (FGRs; Fig. 3-3a,e). Calcite is abundant and based on a 2×2 mm EPMA X-ray map comprises about 1.5 % (area) of the rock. Accessory oxide phases are predominantly chromite. The fine-grained material of the rims and interstitial material contains scarce, rounded Fe,Ni metal grains of typically 1-3 μm size, attesting a low degree of aqueous alteration. Tochilinite-serpentine intergrowths (“PCP”)

are frequent in the interstices between densely packed mantled objects.

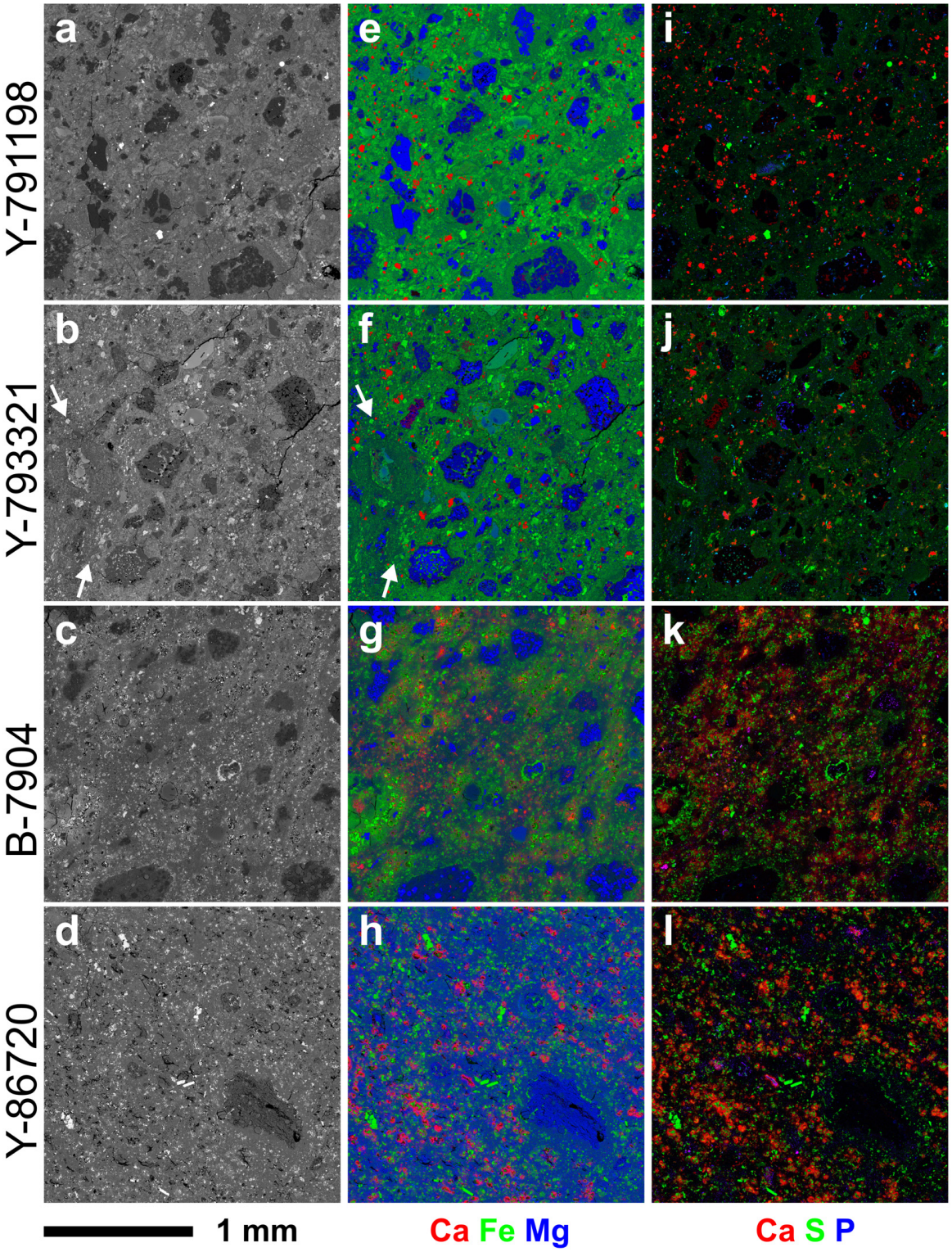

FIGURE 3-3. BSE overviews and WDS X-ray maps of meteorites studied (2×2 mm^2 each). (**a-d**) BSE images. Arrows in (b) mark the border of a distinct clast. (**e-h**) Composite X-ray maps, red = Ca, green = Fe, blue = Mg. (**i-l**) Composite X-ray maps, red = Ca, green = S, B = P. For composite maps, each RGB channel has been linearly scaled to 0.5 % saturation. In Y-791198 and Y-793321 red, distinct grains in (e,f,i,j) are calcite, in B-7904 and Y-86720 no distinct calcite grains are seen, but diffuse red Ca haloes occur.

Coarse grained sulfides (> 8 µm, excluding tochilinite) comprise about 0.5 % of the meteorite by area and are sometimes also mantled by FGRs. The vast majority of sulfide grains are Fe,Ni sulfides with a small contribution of P- and Cr-bearing sulfides occurring together with minor schreibersite or barringerite (Nazarov et al. 2009). BSE images (Fig. 3-4a,b,c) and EPMA (Tab. 3-2) show that most of the Fe,Ni sulfides are intergrowths of a low-Ni Fe sulfide with fine-grained, exsolved pentlandite. The fine-grained nature of the intergrowth did not allow to analyze these phases separately; Table 3-2 lists approximate bulk values. The average M/S ratio of the mixtures is 0.991±0.019 and, hence, practically at unity. Many grains have distinct pentlandite rims (Fig. 3-4c), and some grains contain larger domains or rims of coarse pentlandite, which could be analyzed separately by EPMA. This pentlandite shows variable molar Fe/(Ni+Co) ratios between 1.21 and 1.81 (average 1.59±0.22; Tab. 3-2) and may have a slight metal deficiency (average M/S = 1.108±0.021) compared to the ideal (Fe,Ni)9S8 composition (M/S = 1.125).

Based on our observations, we distinguish two types of sulfide grains in Y-791198. Grains of the first type are the compact sulfide grains described above. In the following, we term these “M-type”, because they mostly contain only one, large monocrystalline domain. Despite sulfides exsolved within these grains, there is usually a crystallographically coherent orientation relationship among the exsolved phases.

The second type are granular aggregates of µm to sub-µm sized crystallites of pyrrhotite/troilite and pentlandite (Fig. 3-4d). In the following, we call these “P-type”, because they are polycrystalline and constituting crystallites do not share common crystallographic orientations. P-type sulfide aggregates often show concentric structures and contain abundant interstitial material. Because of this texture, reliable chemical analysis by EPMA was generally not possible.

3.4.1.2. Yamato-793321

Y-793321 is texturally very similar to Y-791198, but FGRs are much less developed and the meteorite is brecciated (Fig. 3-3b,f). Compared to Y-791198, serpentine and tochilinite form larger and more pure aggregates, and serpentine is distinctly zoned in Fe-Mg content. CAIs, albeit highly altered to phyllosilicates and Ca-phosphate, are distinctly more frequent than in Y-791198. Calcite occurs at approx. 0.8 % by area and is less abundant than in Y-791198 (Fig. 3-3i,j). Magnetite is present and occurs as single grains and rare framboids.

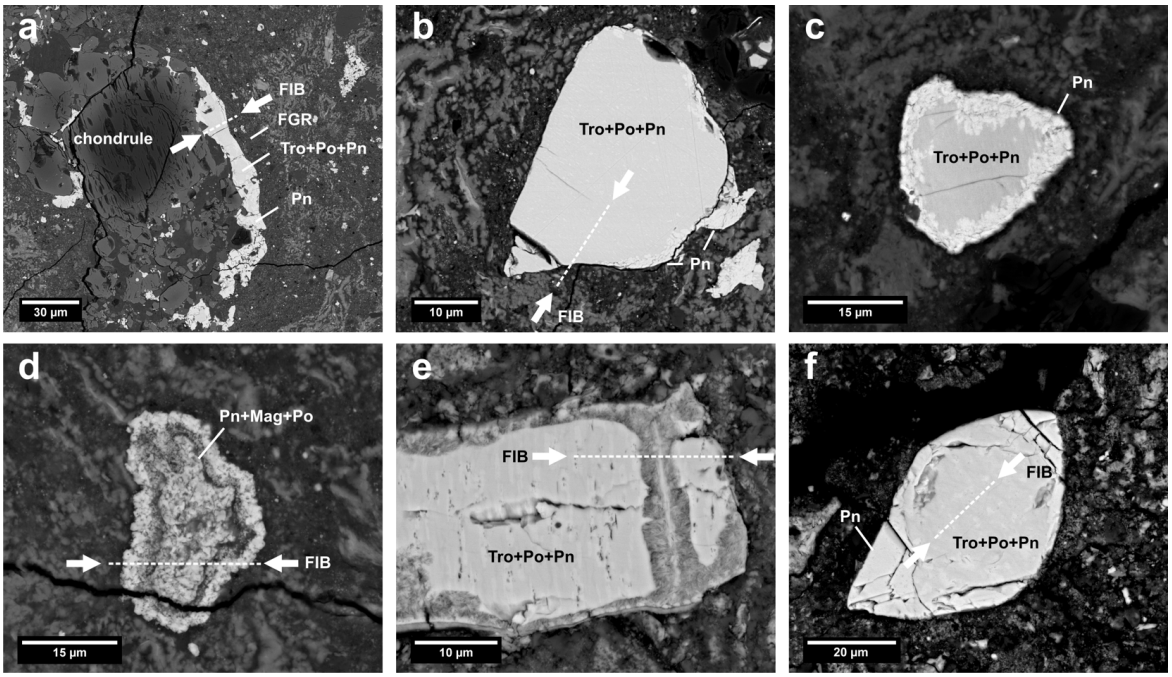

FIGURE 3-4. BSE detail images of sulfides in Y-791198 and Y-793321. Tro = troilite, Po = pyrrhotite, Pn = pentlandite, Mag = magnetite. (**a**) Chondrule in Y-791198, partially surrounded by M-type sulfide and mantled with a fine-grained rim (FGR). FIB foil extraction site is marked (sample 98F01). (**b**) M-type grain in Y-791198 consisting of sub-µm-scale intergrowths of troilite, pyrrhotite, and pentlandite (FIB sample 98F02). (**c**) M-type sulfide grain in Y-791198 with distinct pentlandite rim. (**d**) Microcrystalline, concentric P-type sulfide grain in Y-791198 (FIB sample 98F06). (**e**) M-type grain in Y-793321 with clear signs of alteration and replacement (FIB sample 21F01).(**f**) Pristine M-type grain in Y-793321 with pentlandite rim (FIB sample 21F05).

The sulfide content is approx. 0.5 % by area and similar to that of Y-791198, but sulfide grains are smaller on average. As in Y-791198, a small fraction of sulfides is comprised of P,Cr-bearing Fe,Ni sulfides (plus schreibersite/barringerite), but the majority of grains are common Fe,Ni sulfides of the M-type. Well developed P-type aggregates appear to be absent. Also in Y-793321 small-scale pentlandite exsolution in the low-Ni, M-type sulfide is common and larger, segregated pentlandite areas exist as well. The approximate bulk composition of the fine-scale intergrowths of low-Ni Fe sulfide and pentlandite (Tab. 3-2) is mostly similar to Y-791198 and has an average M/S of 0.979±0.021, being close to unity. BSE images indicate that the textures of intergrown Fe sulfide and pentlandite are similar to those observed in Y-791198 (Fig. 3-4e,f), but distinctly coarser. One of the grains subsequently studied by FIB-TEM showed clear signs of replacement by a Fe-rich fibrous mineral (Fig. 3-4e; see below). Unfortunately, only one pentlandite grain was found large and clean enough for analysis. This grain's composition shows a Fe/(Ni+Co) ratio of 1.35±0.01 and agrees well with the compositions observed in Y-791198. Its M/S ratio corresponds to ideal pentlandite stoichiometry (Tab. 3-2).

3.4.1.3. Belgica-7904

In BSE images B-7904 displays a visual appearance similar to typical CM chondrites, but shows a more uniformly developed fine-grained texture between coarse components (Fig. 3-3c,g). Typical phyllosilicate aggregates as seen in CM chondrites appear to be rare and carbonates in well developed grains and tochilinite are absent (however, patchy aragonite was found by TEM, see below). Irregular aggregates of Ca sulfate are relatively frequent and also Ca phosphates (Cl-rich apatite and merrilite) occur, forming Ca-rich patches (Fig. 3-3g,k). Rare aggregates of Mg,Al spinel grains indicate the presence of relict CAIs.

The sulfide fraction > 8 µm is approx. 1.1 to 1.3 % by area and strongly dispersed (Fig. 3-3k), showing grain diameters mostly below 20 µm. Sulfides are clearly more abundant than in Y-791198 and Y-793321. Sulfide grains have highly irregular shapes, are mostly polycrystalline, often porous, and are frequently accompanied by Fe,Ni metal grains (Fig. 3-5a). Intimate intergrowths between sulfide and minute Mg silicate grains (identified as olivine by TEM, see below) are abundant (Fig. 3-5b). A peculiar component observed are large (several tens of µm), porous, and sometimes spherical aggregates of Fe oxide, Fe,Ni metal, and Fe sulfide (Fig. 3-5c). P,Cr-bearing Fe,Ni sulfide grains are absent. The majority of sulfide grains are Ni-poor and show no evidence for exsolved pentlandite. Their M/S ratio is at unity (0.990±0.013; Tab. 3-2) and consistent with stoichiometric troilite. Only few separate grains of pentlandite have been found, which appear to be Fe-rich. Measured Fe/(Ni+Co) ratios of a large grain and a small matrix grain are approximately 2.4 and 3.5, respectively (Tab. 3-2). These values are consistent with a Fe/Ni ratio of approximately 3.0 based on the analysis by Kimura et al. (2011), but their positions in the Fe-Ni-S ternary indicate mixtures between troilite and pentlandite (see below).

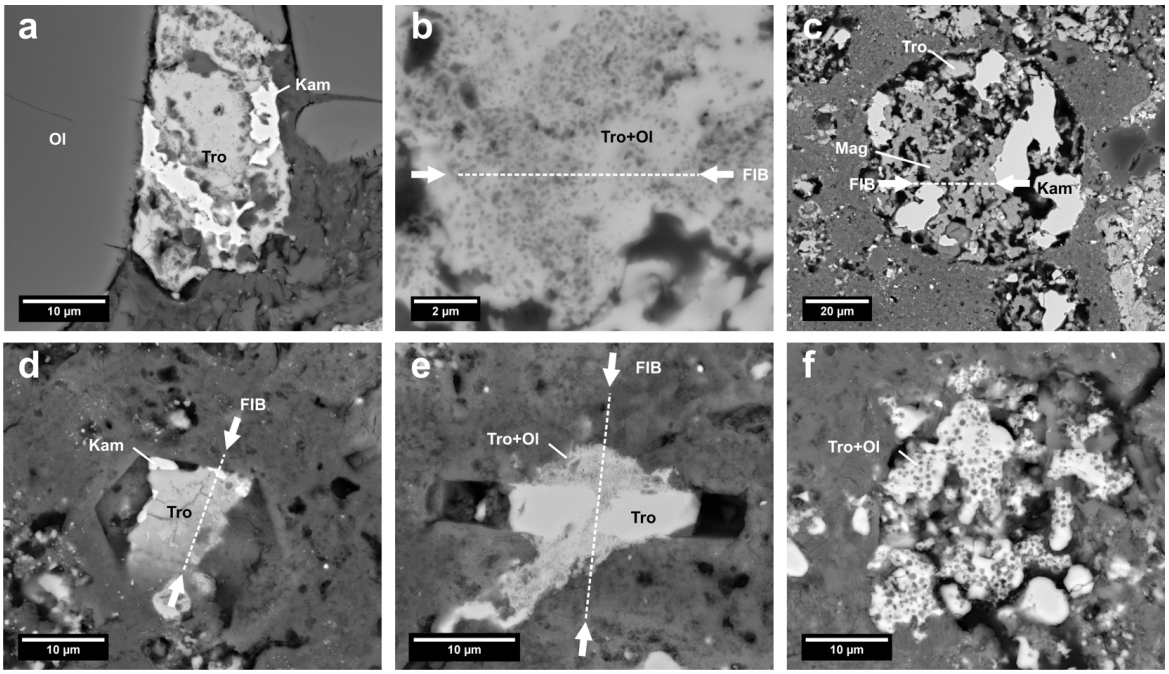

FIGURE 3-5. BSE detail images of sulfides in B-7904 and Y-86720. Ol = olivine, Kam = kamacite, others see Fig. 3-4. (**a**) Troilite-metal grain in-between olivine in B-7904. (**b**) Detail of fine-grained troilite-olivine intergrowths in B-7904 (FIB sample 04F03). (**c**) Porous magnetite-troilite-metal spherule in B-7904 (FIB sample 04F01). (**d**) Troilite, containing kamacite blebs, replacing a euhedral pyrrhotite platelet in Y-86720 (FIB sample 20F02). (**e**) Cross section trough a troilite-replaced platelet in Y-86720 showing fluffy overgrowths of a mixture of troilite and extremely fine-grained olivine (FIB sample 20F03). (**f**) Troilite-olivine intergrowths in Y-86720 with larger grain size than in (e) and (c).

3.4.1.4. Yamato-86720

Y-86720 is, compared to B-7904, more uniform in texture and shows less abundance of large ferromagnesian objects/chondrule (Fig. 3-3d,h). As pointed out by Tomeoka et al. (1989b), its matrix is strongly depleted in Fe compared to B-7904 and the other CM chondrites (Fig. 3-3h). SEM images show hardly any large phyllosilicate and no tochilinite aggregates. Large carbonate grains are absent, but the Ca X-ray distribution map shows Ca-rich 'haloes' surrounding cavities that are partially filled by sulfides (Fig. 3-3h,l). These haloes might represent mobilized Ca of former carbonate grains. Accessory phases are Ca sulfate, Ca phosphate (mostly merrilite), chromite, ilmenite, and abundant metal grains. Despite intensive search, we did not find magnetite in our sample of Y-86720, which confirms the observations of Tomeoka et al. (1989b).

In Y-86720, sulfides > 8 µm comprise approx. 2.0 to 2.4 % by area and occur in two modes: Small, irregular grains of typically less than 20 µm in diameter and relatively large, partially or almost fully euhedral, platelet-shaped grains of up to 100 µm size (Fig.

3-5d,e). The euhedral sulfide grains are generally not associated with the Ca haloes described above. We did not observe pentlandite, neither as exsolved phase nor as separate grains. The morphologically distinct sulfide grains show no significant difference in composition and have M/S ratios indiscernible from unity (0.998±0.007 for large grains, 0.995±0.006 for small, irregular grains) and very low Ni contents (<0.2 % m/m; Tab. 3-2), consistent with troilite. Similarly to B-7904, the fine-grained sulfides are often intimately intergrown with minute Mg silicate grains (Fig. 3-5e,f). Many of the sulfide grains, including the euhedral ones, are associated with Fe,Ni metal grains (Fig. 3-5d), which show large variations in Ni concentrations (Tab. 3-2), ranging from very Ni-poor kamacite to Ni-rich taenite.

3.4.2. Compositions in the Fe-Ni-S Ternary

In a ternary Fe-Ni-S diagram (Fig. 3-6a), including the phase fields and tie lines at 200 °C after Craig (1973), the compositions of coarse pentlandite in Y-791198 fall at the end of tie lines connecting to Ni-rich MSS. These MSS compositions are not observed among the low-Ni sulfides and almost all analyses cluster closely near the edge between the FeS and Fe_7S_8 compositions. The same applies for the low-Ni sulfide compositions observed in Y-793321, which show a slight trend toward pentlandite compositions owing to mixed analyses and slightly coarser pentlandite blebs in Y-793321. Because the MMS field is expected to shrink with decreasing temperatures below 200 °C (Craig 1973), the MMS will become poorer in Ni, and coexisting pentlandite will become richer in Ni. This indicates that the coexisting Fe,Ni sulfides observed in Y-791198 have equilibrated at temperatures well below 200 °C as it is often observed in terrestrial samples, where very Ni-poor pyrrhotite occurs abundantly next to pentlandite (e.g., Etschmann et al. 2004). Unfortunately, it is virtually impossible to obtain the bulk composition of individual sulfide aggregates from the compositions of the constituting phases, because the coarse grained nature of segregated pentlandite renders estimates of its volume fraction highly uncertain.

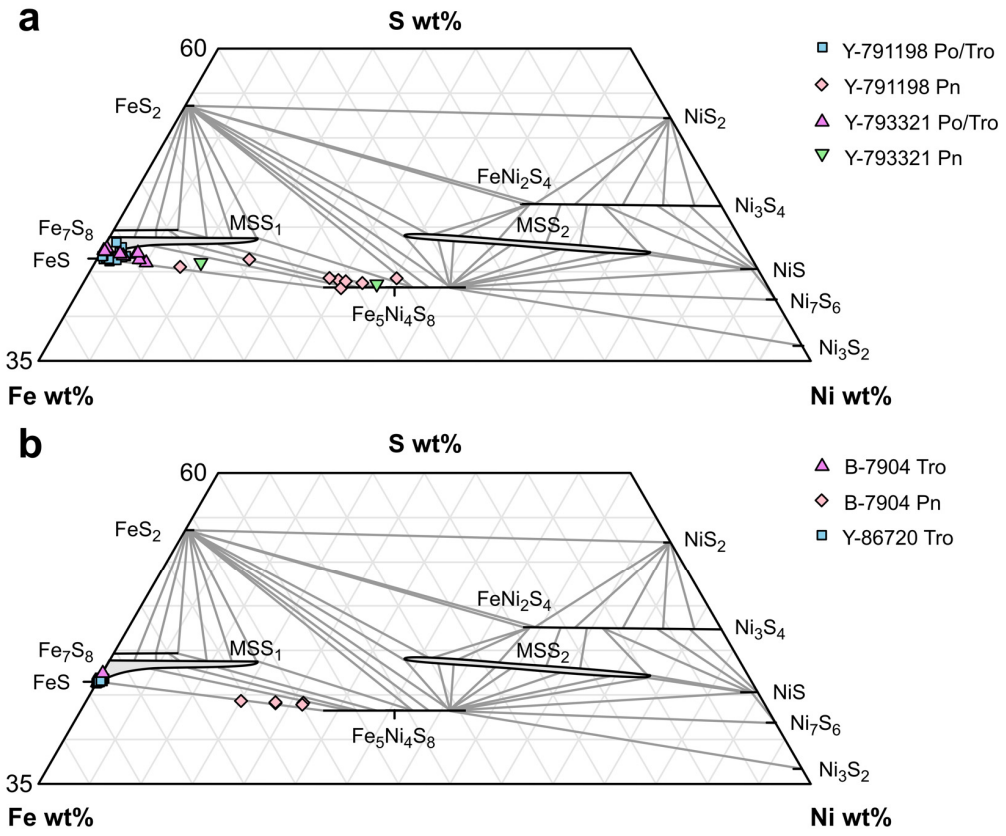

FIGURE 3-6. Fe-Ni-S ternary diagrams of sulfide compositions in the meteorites studied. Phase field and tie lines are drawn for 200 °C based on Craig (1973). At this temperature two extended MSS fields (labeled MSS_1 and MSS_2) still exist. (**a**) Data for Y-791198 and Y-793321. (**b**) Data for B-7904 and Y-86720. Data points outside the MSS_1 field and above the pentlandite line centered at $Fe_5Ni_4S_8$ indicate mixed measurements. The absence of data points of Y-791198 and Y-793321 in the Ni-rich part of the MSS_1 field indicates equilibration below 200 °C.

The alleged pentlandite grains measured in B-7904 (Fig. 3-6b) plot in the Fe-Ni-S ternary between Fe-rich pentlandite and the troilite composition, where all the Ni-poor Fe sulfides of B-7904 and Y-86720 cluster. Likely, these intermediate pentlandite-like compositions represent small scale mixtures of troilite and Fe-rich pentlandite. The pentlandite mixing line in B-7904 nonetheless appears to point to a Fe-rich pentlandite composition, with Fe/Ni of approximately 1.9 to 2.0. According to Kaneda et al. (1986) such Fe-rich pentlandite compositions might point to low fS_2 during equilibration with coexisting MSS.

3.4.3. TEM observations

3.4.3.1. Yamato-791198

We have prepared FIB foils of two pentlandite-bearing M-type grains (98F01, 98F02;

Fig. 3-4b) and one P-type aggregates of microcrystals (98F06; Fig. 3-4d). The internal structure of compact M-type grains consists of nanoscale, flame-like, and crystallographically coherent intergrowths of troilite and twinned NC-type pyrrhotite, associated with sub-µm sized, rod-shaped pentlandite grains (Fig. 3-7a,b,c; Fig. 3-8a). Sample 98F02 shows a thick rim of pure pentlandite enclosing the NC-pyrrhotite-troilite-pentlandite intergrowths (Fig. 3-7a).

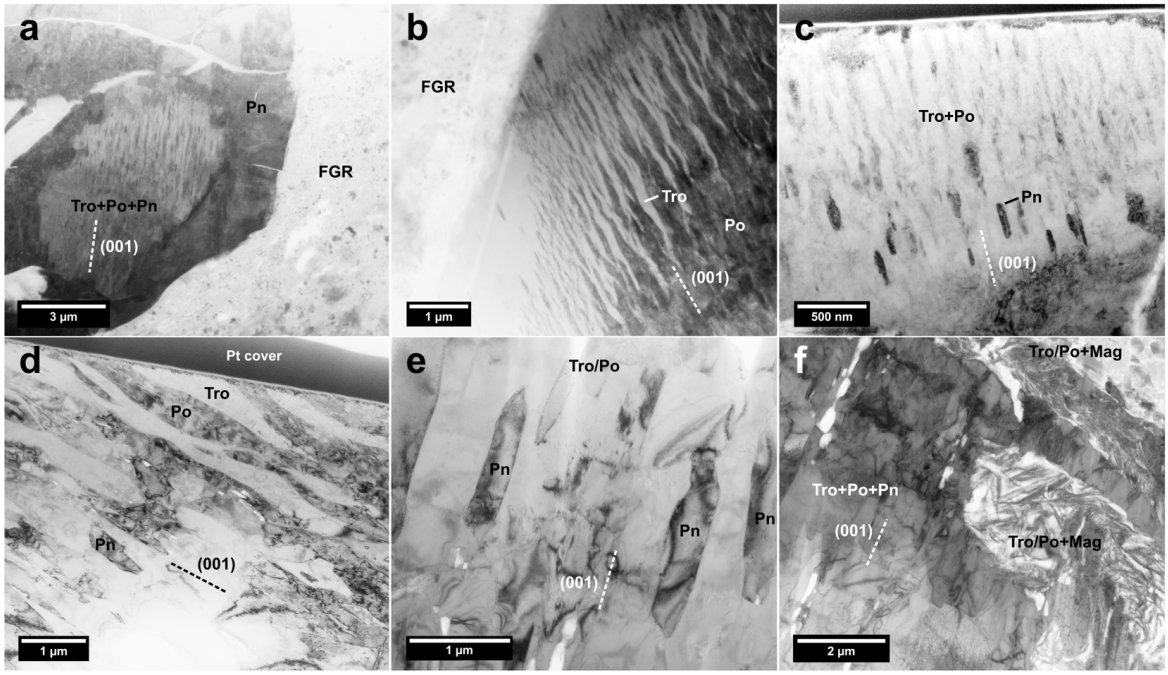

FIGURE 3-7. BF-TEM images of sulfides in Y-791198 and Y-793321. FGR = fine-grained rim. The dashed lines indicate the traces of the (001) lattice planes of troilite and pyrrhotite. (**a**) Y-791198 (98F01) showing a continuous rim of pentlandite around an inner part consisting of troilite + NC-pyrrhotite intergrowths and pentlandite blebs. (**b**) Detail of flame-like troilite + NC-pyrrhotite intergrowths in Y-791198 (98F02), no pentlandite rim is present at the grain margin, adjacent to the matrix. (**c**) Detail of internally exsolved pentlandite blebs in Y-791198 (98F01). (**d**) Troilite + 6C-pyrrhotite intergowths in Y-793321 (21F05). (**e**) Troilite + 6C-pyrrhotite intergrowths and pentlandite in Y-793321 (21F01). The sulfide textures in Y-793321 (d+e) are substantially coarser than in Y-791198 (a-c). (**f**) Scaly, highly porous material replacing the sulfide in Y-793321 (21F01). SAED (Fig. 3-10) shows the replacement to be a mixture of nanocrystalline Fe sulfide and magnetite, likely being thermal breakdown products of tochilinite.

Flame-like troilite-pyrrhotite lamellae in both M-type grains are sub-parallel to (001) and have typical widths in the range of 80 to 200 nm. Troilite and pyrrhotite share a common orientation of their sulfur sublattice and are well distinguishable in $[210]_{NiAs}$ SAED patterns due to their different superstructures (Fig. 3-8e). Table 3-3 lists N values determined from SAED patterns using the length ratios of inverse lattice vectors c* and q (Harries et al. 2011; Fig. 3-8a,e).

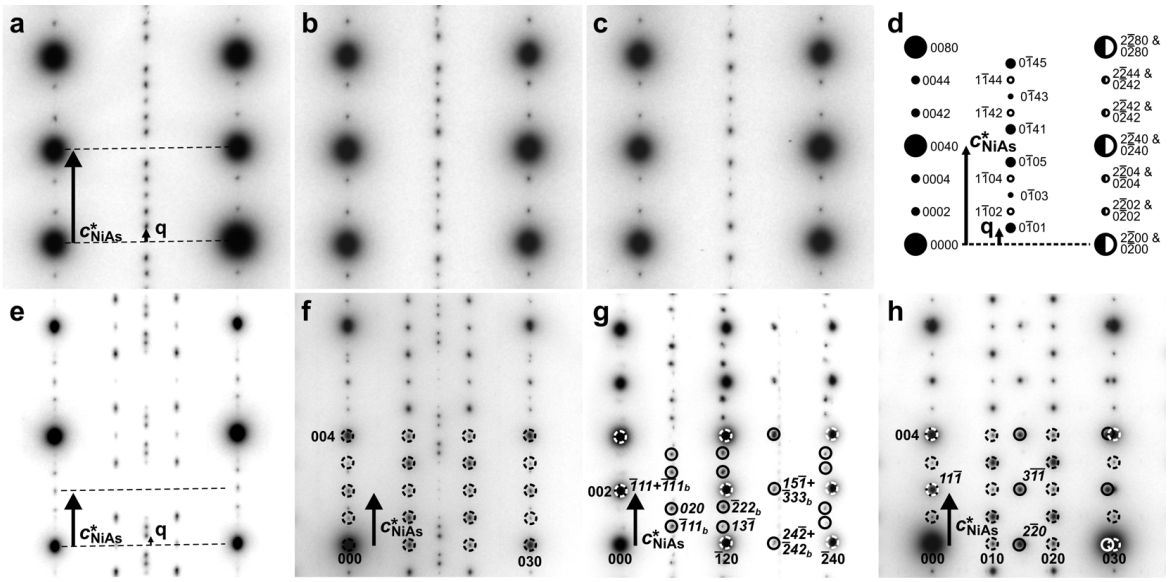

FIGURE 3-8. TEM-SAED patterns of sulfides in Y-791198 and Y-793321. (**a**) Twinned NC-pyrrhotite in Y-791198 (98F02) in combined zone axes (ZA) [100] and [110] (based on NiAs-type subcell). The strong basic reflections are spaced by the inverse lattice vector c^* (~1.72 nm^{-1}) of the primitive NiAs-type cell. The central row of reflection is due to the NC superstructure resulting from vacancy ordering. Their arrangement is determined by the inverse vector q. The ratio c^*/q is the superstructure multiplicity N, here N = 6.01±0.09. Troilite superstructure reflections are not visible in this ZA. (**b+c**) NC-pyrrhotite in Y-793321 (21F01) in the same orientation as in (a). Variations in intensity indicate different contributions of twin domains after minimal shifting of the sample (<3 µm). N = 5.99±0.07 and 5.97±0.07. (**d**) Schematic representation of the SAED patterns in (a-c). Large circle are basic NiAs-type reflections, small circles are superstructure reflections. Filling of circles represents the two twin domains. Indexing is based on the *hklm* scheme discussed by Harries et al. (2011); here only $m > 1$ is used for clarity. (**e**) SAED pattern of Y-791198 (98F02) showing superstructure reflections of twinned NC-pyrrhotite (central row, ZA [210] and [1-10]) and troilite (adjacent rows, ZA [100]). The respective distances c^* and q are marked. N = 5.74±0.12. (**f**) Twinned 6C-pyrrhotite and troilite from Y-793321 (21F01) in same orientation as (e). Troilite reflections are marked (in the lower part only). N = 5.94±0.04. (**g**) Coherent intergrowth of pyrrhotite+troilite and pentlandite in Y-791198 (98F01). Po/Tro reflections are marked with dashed circles, normal typeface, pentlandite reflections with solid circles, italic typeface. Troilite ZA is [210] and only NiAs-type reflections are visible, pentlandite ZA is [101] and at least two orientation variants (Francis et al. 1976) occur, the second is labeled 'b'. (**h**) Same intergrowth in Y-793321 (21F01), marking of reflections is the same as in g. ZAs are [100] for troilite and [112] for pentlandite.

In case of grain 98F01, N values are consistent with 6C-pyrrhotite (ideally N = 6), but the values of grain 98F02 (5.63±0.13 and 5.74±0.12), obtained from two different zone axes of the same crystal, are hardly consistent with an integral NC superstructure and indicate a superstructure intermediate between 5.5C and 6C. However, no splitting of reflections expected for a non-integral superstructure (Harries et al. 2011) could be observed in 98F02 due to the rather broad spots. This is most likely due to the small domain size and intense twinning (see below), leading to somewhat disordered vacancy arrangements and possible disappearance of higher order superstructure reflections (being

responsible for apparent splitting).

SAED patterns show that the NC-pyrrhotite is intimately twinned by 60° or 120° rotation about its c axis, resulting in superposition of two different zone axis patterns (Fig. 3-8b,c,d; due to the reduced symmetry of NC-pyrrhotite by vacancy ordering, the diffraction patterns of equivalent zone axes of the fundamental hexagonal NiAs-type structure are not equivalent any more in terms of the superstructure reflections). The orientation relationship between low-Ni Fe sulfides and pentlandite is equivalent to the one described by Francis et al. (1976) with respect to the NiAs-type fundamental structure of troilite and pyrrhotite (Fig. 3-8g): $(111)_{Pn} \parallel (001)_{NiAs}$, $(0\bar{1}1)_{Pn} \parallel (110)_{NiAs}$, $(\bar{1}\,\bar{1}2)_{Pn} \parallel (100)_{NiAs}$. The NC-pyrrhotite-troilite-pentlandite association occurs regardless of whether sulfide grains are rimmed by pentlandite (98F02) or not (98F01) and occurs also in direct contact with the hydrous, fine-grained rim material (Fig. 3-7b). The observed sulfide assemblage appears identical to the associations in CM2 chondrites described by Brearley and Martinez (2010) and Maldonado and Brearley (2011). Attached to the outer margin of the pentlandite-rimmed grain 98F02, we have found an 800 nm sized subgrain of Fe-rich Zn sulfide, which appears to be in epitactic relationship with the host grain.

The microcrystalline aggregate 98F06 consists of individual grains of abundant pentlandite, magnetite, and minor low-Ni Fe sulfide (Fig. 3-9a,b,d). The quality of the only Fe sulfide grain in suitable orientation (with an accessible zone axis perpendicular to the c direction) was not sufficient to record a very clean SAED pattern, but the presence of superstructure reflections in a $[100]_{NiAs}$-equivalent zone axis clearly excludes troilite and indicates pyrrhotite (Fig. 3-9c). The triplets of superstructure reflections seen along the 00l lattice row between fundamental NiAs reflections are very similar to twinned 4C-pyrrhotite (Fe_7S_8) (Pósfai et al. 2000; Berger et al. 2011) and could indicate a very Fe deficient pyrrhotite. The N value determined as 3.66±0.33 (1σ; large uncertainty due to broadness of spots) is consistent with 4C-pyrrhotite. The majority of interstitial material between sulfide and magnetite grains is rich in Ca phosphate, likely merrilite based on elevated Na concentrations shown by EDX. An isolated 600 nm sulfide grain in the adjacent matrix (Fig. 3-9e) was found to have a suitable crystallographic orientation and the obtained SAED pattern (Fig. 3-9f) indicates a barely twinned NC-pyrrhotite with an N value of 5.48±0.13, being well consistent with 5.5C-pyrrhotite. STEM-EDX elemental mapping indicates that other small sulfide grains in the matrix are in approximately equal

amounts Ni-rich (likely pentlandite) and Ni-poor (likely pyrrhotite).

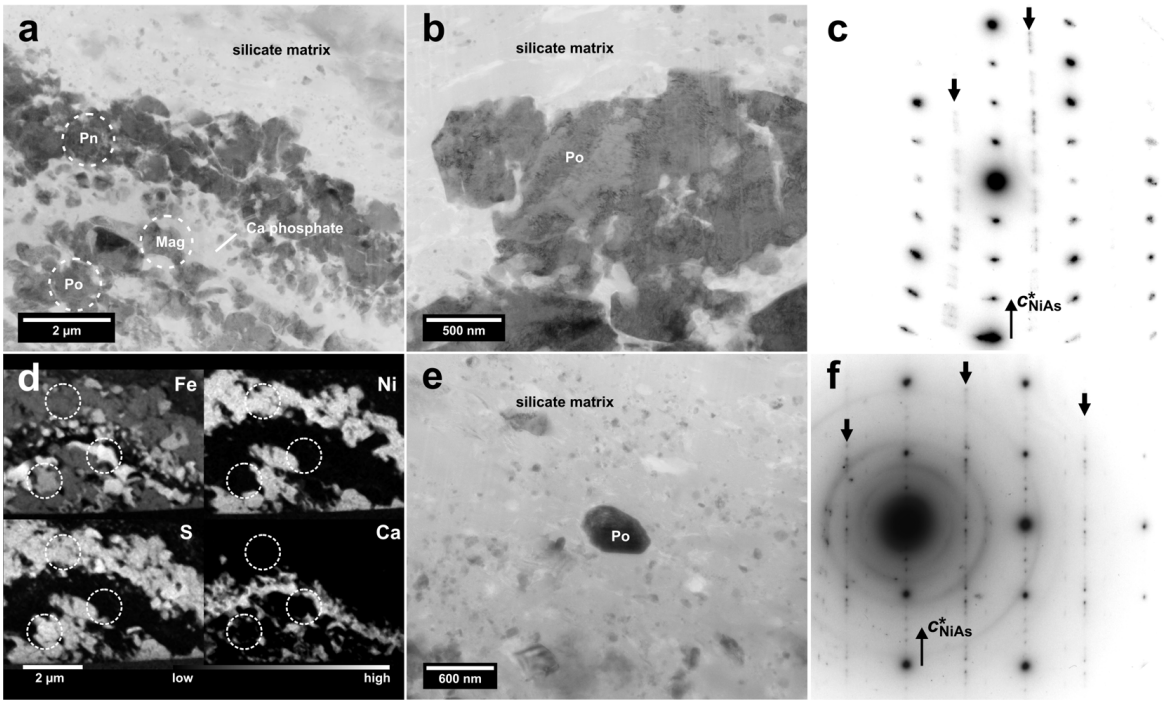

FIGURE 3-9. P-type sulfide aggregate in Y-791198 (98F06). (**a**) BF-TEM image of the fluffy grain aggregate. Center of the concentric aggregate is beneath the lower left corner. Individual grains are pyrrhotite, pentlandite, and magnetite, the latter preferentially in the central part, which is separated from the outer part by a phosphate-rich zone. (**b**) BF-TEM detail of the outer layer. (**c**) SAED pattern of the central grain in (b) showing pyrrhotite superstructure reflections (arrows) consistent with twinned 4C-pyrrhotite (N = 3.66±0.33). (**d**) TEM-EDX X-ray maps of (a), illustrating the distribution of pentlandite, pyrrhotite, magnetite, and Ca phosphate (with minor Ca sulfate). Circles for guidance. (**e**) Isolated pyrrhotite grain in the matrix adjacent to the P-grain. (**f**) SAED pattern of the pyrrhotite isolated matrix grain in (e) in ZA [210]. Only weak troilite reflections are visible. The N value of pyrrhotite is 5.48±0.13 and consistent with 5.5C-pyrrhotite (identical to '11C-pyrrhotite').

3.4.3.2. Yamato-793321

FIB lamellae taken from two M-type grains (21F01, 21F05; Fig. 3-4e,f) show coherent intergrowths of troilite, NC-pyrrhotite, and pentlandite similar to Y-791198. However, compared to Y-791198, the intergrowths in both grains of Y-793321 are much coarser, and lamellae and pentlandite blebs are much better defined (Fig. 3-7d,e), positively affecting the quality of SAED patterns (Fig. 3-8b,c,f,h). N values determined are in all cases well consistent with 6C-pyrrhotite (Tab. 3-3). The orientation relationship between pyrrhotite/troilite and pentlandite is the same as in Y-791198 (Fig. 3-8h). Typical widths of lamellae and pentlandite precipitates are in the order of 300 to 500 nm. Also here, pyrrhotite is intensely twinned, but, contrary to Y791198, shows intensity variations of the twin components in SAED patterns when the sample is moved (Fig. 3-8b,c), indicating a

coarser domain structure (which unfortunately is extremely difficult to image, because of the small distances between superstructure reflections). EDX analysis of pentlandite lamellae indicates no obvious internal zoning.

Grain 21F01 clearly shows signs of replacement by a fibrous mineral (Fig. 3-4e, 3-7f). STEM dark field imaging reveals that the fibrous material consists of numerous nanocrystalline domains and, hence, is itself a replacement by newly formed phases (Fig. 3-10a). SAED shows spotty ring patterns with d-values corresponding to a spinel structured mineral, most closely matching magnetite (Fig. 3-10c). Additional reflections in the SAED pattern point to the presence of a Fe sulfide (either troilite or pyrrhotite, which are hardly discernible in this case). EDX indicates that the crystallites are composed of Fe, O, and S, plus subordinate amounts of Mg and Si. The S content varies strongly regardless of the distance to the interface with the original sulfide, supporting the presence of a two phase mixture of magnetite and Fe sulfide. EDX X-ray mapping shows a significant enrichment of chromium up to 5-10 wt% in the nanocrystalline material close to the sulfide interface (Fig. 3-10b). It is not clear where Cr resides, but likely it is incorporated into the magnetite. The composition and morphology of this magnetite-sulfide assemblage strongly suggests it to be a breakdown product of a relatively pure tochilinite that did not contain substantial interlayered serpentine, since Si and Mg concentrations are low. The

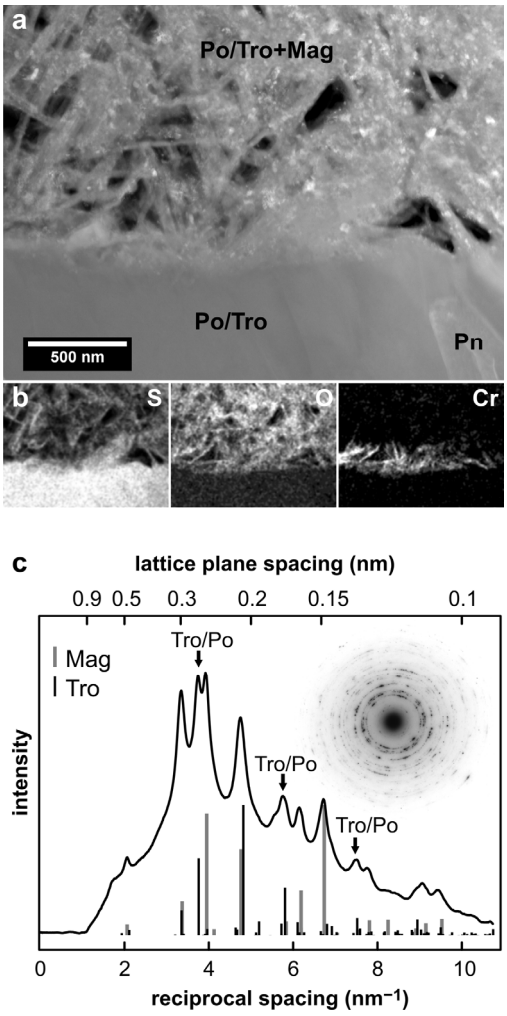

FIGURE 3-10. Detail of replacement around the M-type grain of Y-793321 depicted in Fig. 3-4e and 3-7f. (**a**) DF-STEM image showing the porous, scaly replacement product and nanocrystalline domains within. (**b**) TEM-EDX X-ray maps of (a) showing the distribution of S, O, and Cr. The latter is strongly enriched close to the reaction interface. (**c**) SAED ring pattern and extracted diffractogram of the replacement material. The pattern can be indexed by magnetite and troilite (or pyrrhotite – troilite is shown, but distinction is not possible in this pattern due to low intensity of superstructure reflections).

occurrence indicates that tochilinite replaced the original sulfide grain during aqueous alteration. The Cr enrichment close to the reactive interface suggests local transport by a fluid during aqueous alteration or metamorphism, because Cr is not significantly contained in the Fe,Ni sulfides and must have been derived from the surroundings of the grain.

The fine-grained portion of Y-793321 (21F06) contains monophase pentlandite grains of variable size (several μm to less than 1 μm) without associated Fe sulfides. They are accompanied by magnetite, clinoenstatite, Ca-rich clinopyroxene, Fe-rich serpentine, and a calcium sulfate. The latter shows a fibrous texture and is difficult to be assigned in diffraction patterns. Most probably, the original phase was gypsum which partially dehydrated during sample preparation. The sulfate could be an oxidation product of sulfides during aqueous alteration or terrestrial weathering. However, no obvious Fe-bearing oxidation products such as FeOOH polymorphs or ferrihydrite have been found in the FIB samples.

3.4.3.3. Belgica-7904

In B-7904 we have sampled four sites by FIB: One sulfide-oxide-metal assemblage (04F01, Fig. 3-5c), and three sulfide aggregates (04F02; 04F03, Fig. 3-5b; 04F04). The sulfide-oxide-metal assemblage consists of 1 to 3 μm sized grains of magnetite, troilite, and kamacite (Fig. 3-11a; all identified by SAED). In close association with kamacite, small grains of a Ni-rich alloy occasionally occur (its structure could not be established, but likely it is taenite or awaruite). No pyrrhotite was found. Large fractions of interstitial space are empty pore space, but some pores are filled by anhydrite, which is well crystallized and yields clear zone axis diffraction patterns (Fig. 3-11b). Although evaporitic contamination in Antarctic meteorites is a concern (Losiak and Velbel 2011), the formed phases are generally hydrous (Velbel 1988), and the good quality of the diffraction pattern rules out vacuum dehydration of preexisting gypsum during sample preparation or observation (see remarks on Ca sulfate in Y-793321).

The sampled sulfide aggregates consist of pure, polycrystalline troilite without evidence for exsolution of pyrrhotite. Only at the margins of grain aggregates in 04F02 weak, additional superstructure reflections of pyrrhotite could be detected in SAED patterns (Fig. 3-12a). The reflections are broad, but roughly consistent with 6C-pyrrhotite ($N = 6.14 \pm 0.14$).

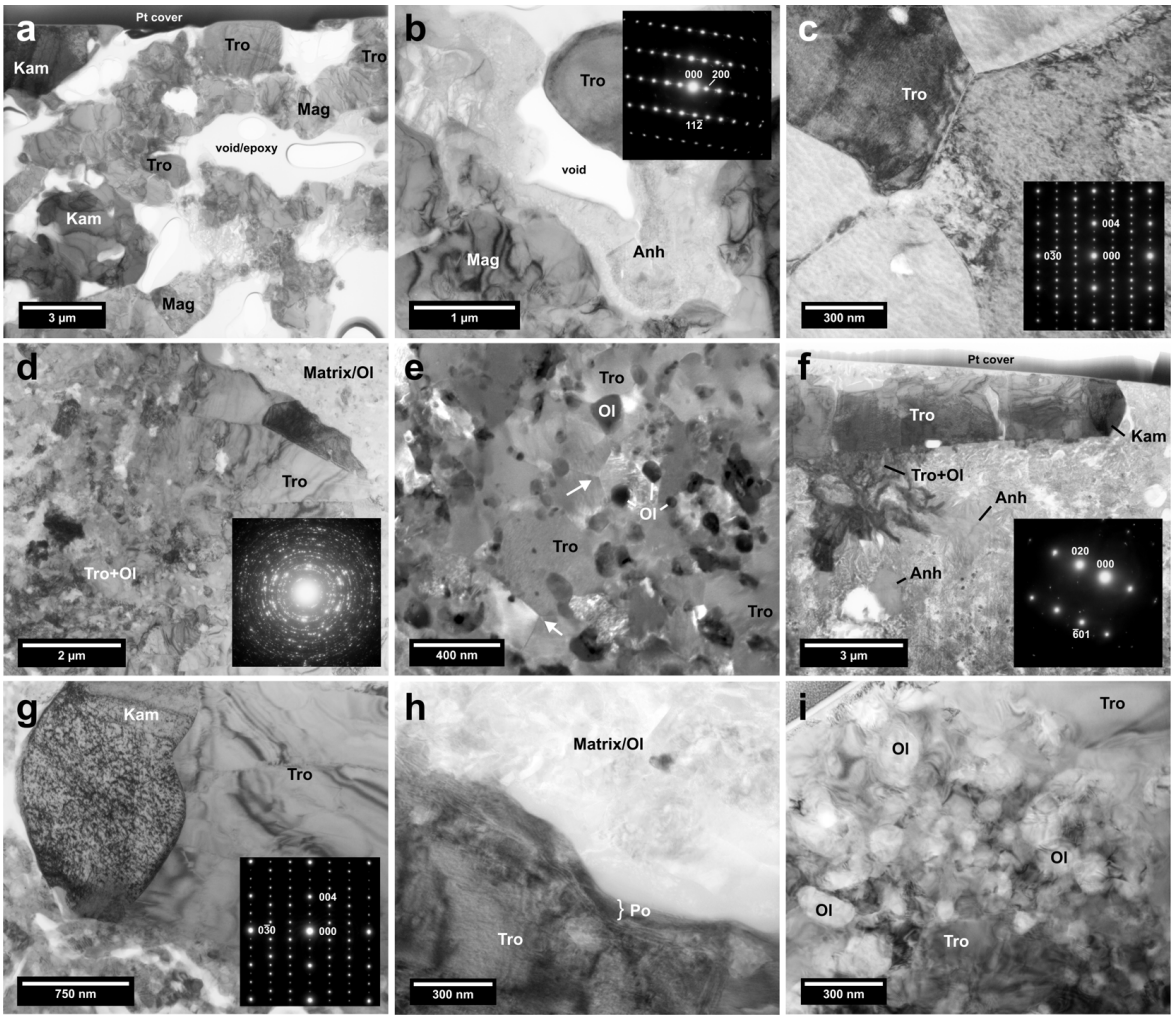

FIGURE 3-11. BF-TEM images of sulfides in B-7904 and Y86720. (**a**) Magnetite-troilite-metal spherule in B-7904 (04F01). Abundant pore space is present between individual grains. (**b**) Detail of spherule shown in (a) with well crystalline anhydrite (Anh) in pore space (Anh SAED pattern as inset). (**c**) Polycrystalline troilite in B-7904 (04F04) showing 120° triple junctions (Tro SAED pattern as inset). (**d**) Polycrystalline troilite aggregate in B-7904 (04F03, see Fig. 3-5b) grading into a fine-grained troilite-olivine mixture (lower left, SAED pattern as inset). (**e**) DF-STEM detail image of the fine-grained troilite-olivine mixture in (d). 120° triple junctions are abundant (arrows). (**f**) Section trough the euhedral troilite grain of Y-86720 (20F02) shown in Fig. 3-5d. A kamacite grain and a fluffy troilite-olivine aggregate occur adjacent to the troilite. The matrix contains patches of well crystalline anhydrite (Anh SAED pattern as inset). (**g**) Detail of (f) showing the large kamacite grain adjacent to troilite (Tro SAED pattern as inset). A high dislocation density in the metal grain contributes to its mottled contrast. (**h**) Pyrrhotite rim on a large troilite grain in Y-86720 (20F01), see Fig. 3-12b for a SAED pattern. (**i**) Fine-grained troilite-olivine mixture in the fluffy overgrowths shown in Fig. 3-5e of Y-86720 (20F03).

A rather compact sulfide grain sampled in 04F04 (Fig. 3-11c) is composed of polycrystalline troilite without any detectable pyrrhotite or pentlandite. TEM-EDX indicates the presence of few and small Ni-poor Fe metal grains. The internal texture shows abundant triple junctions and subgrain boundaries. In sample 04F03 (Fig. 3-11d,e),

compact, polycrystalline troilite grades into fine-grained troilite, which is intimately intergrown with abundant, sub-µm-sized grains of Fe-rich olivine (approx. Fa24 based on TEM-EDX). In this intergrowth, polycrystalline troilite shows frequent 120° (triple junction) grain boundaries. Rarely, approx. 1 µm-sized Ni-poor, but fairly Co-rich Fe metal grains occur (~3 at% Ni, ~8 at% Co). The matrix portion sampled in 04F02 and 04F03 shows SAED ring patterns consistent with a composition dominated by sub-µm sized-olivine. Ca sulfate, most likely anhydrite, occurs as µm-sized, polycrystalline patches within the matrix material. Embedded in silicates and anhydrite, sub-µm-sized grains of a very Ni-rich alloy occur (about equal amounts of Fe and Ni, ~2 at% Co). In close proximity to the sulfide aggregates, a µm-sized patch of Ca carbonate was found and identified as aragonite by SAED. Alongside the margin of the sulfide aggregate sampled in 04F03 small pentlandite grains occur, but most Ni appears to be present as Ni-rich alloy grains within the matrix.

3.4.3.4. Yamato-86720

From Y-86720 we have obtained two FIB samples (20F01; 20F02, Fig. 3-5d) of euhedral, platelet-shaped sulfide crystals with adjacent matrix and one from a partial crystal with adjacent, fine-grained sulfide-silicate intergrowths (20F03, Fig. 3-5e). Imaging and SAED patterns indicate that the euhedral crystals are internally pure troilite. The troilite crystals contain frequent subgrain boundaries and inclusions of Fe,Ni metal (Fig. 3-11f,g), indicating that they are rather pseudomorphs than euhedral single crystals. In case of 20F01 and 20F02, narrow, less than100 nm wide rims of NC-pyrrhotite occur at the external margins of the troilite (Fig. 3-11h, 3-12b). The N values determined for the rims vary consistently around 5.7 (Tab. 3-3). Although uncertainties of individual N values are relatively large, the observations point to rims that have slightly lower Fe contents than those in B-7904. The fine-grained sulfide-silicate intergrowths in 20F03 were identified to be a mixture of troilite and olivine, similar to what is observed in B-7904. Grain sizes in these aggregates are typically in the order of a few 100 nm (Fig. 3-11i). TEM-EDX shows that the olivine is Fe-rich (Fa_{36-40}) and has a molar Fe/Mn ratio of about 44. Many of these intergrowths show amoeboid textures with poorly defined boundaries, suggesting a solid state formation from a local precursor. The grain size of olivine in these aggregates is larger than that of the matrix and the composition is more Fe-rich (see below). We did not find the ferrihydrite-like material associated with or replacing troilite as described by

Tomeoka et al. (1989b). None of the troilite grains measured by TEM-EDX has a detectable Ni content (i.e., < 0.5 wt%). The metal grain attached to the euhedral crystal sampled in 20F02 is kamacite (~6 at% Ni, hardly any Co) and was found to contain a high density of dislocations (Fig. 3-11g).

The sampled matrix portions show fibrous or scaly textures at the sub-µm scale (Fig. 3-11f), typical of phyllosilicates. However, SAED patterns obtained from such areas display spotty rings that can be indexed almost completely as olivine. TEM-EDX yields a (Mg+Fe)/Si ratio of approx. 2.1 and a Fe/(Fe+Mg) of 0.24, consistent with ferroan olivine. In addition, the matrix contains larger, 1-3 µm sized grains and grain aggregates of anhydrite, merrillite, and Ca,Mg carbonate. Similar to B-7904, the crystallinity of the anhydrite is very good (Fig. 3-11f).Based on SAED patterns, the carbonate appears to be a mixture of calcite and dolomite (or Mg-rich calcite with smaller d values compared to pure calcite). Metal, also found in direct association with anhydrite, ranges from Ni-poor (3-4 at %) to Ni-rich (up to 25 at%) compositions.

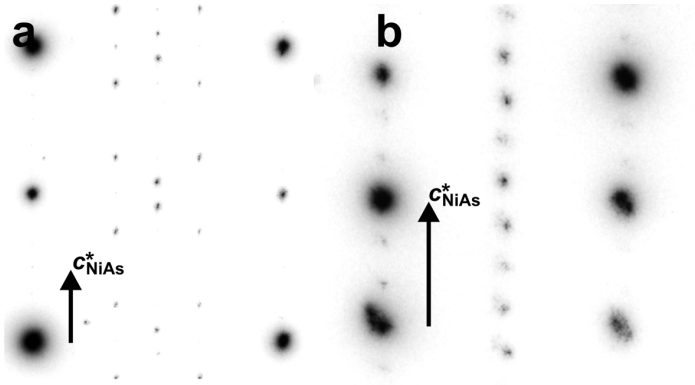

FIGURE 3-12. TEM-SAED patterns of sulfides in B-7904 and Y-86720. (**a**) Rim of untwinned NC-pyrrhotite on troilite in B-7904 (04F02). Central row is NC-pyrrhotite (N = 6.14±0.14) in ZA [210], adjacent reflections are troilite. (**b**) Rim of untwinned NC-pyrrhotite on troilite in Y-86720 (20F02). The N value determined from this is 5.67±0.15 and, hence, pyrrhotite is intermediate between 5.5C and 6C.

3.5. Discussion

3.5.1. Sulfide Formation by Nebula Condensation Processes

The exsolution of pentlandite in pyrrhotite/troilite observed in Y-791198 and Y-793321 strongly indicates a formation of the precursor MSS at temperatures in excess of the MSS-pentlandite solvus, hence, above a minimum of 300 °C. The two modes of occurrence of pentlandite in the compact M-type sulfide grains, as sub-µm-sized blebs within pyrrhotite/troilite and as monomineralic rims, suggest two generations of pentlandite: A first generation forming the rims exsolved when the temperature dropped below the MSS-pentlandite solvus between ~300 to 610 °C (depending on bulk MSS composition). The

grain then consisted of a Ni-poor 1C-pyrrhotite core with M/S ≤ 1 and a pentlandite rim with M/S > 1. In experiments and terrestrial pyrrhotite-pentlandite assemblages the preferred nucleation of pentlandite along grain boundaries or cracks is well documented (e.g., Hawley and Haw 1957, Naldrett et al. 1967, Kelly and Vaughan 1983). Upon further cooling, the 1C-pyrrhotite exsolved troilite when it crossed the troilite-pyrrhotite solvus between 140 and 100 °C (Fig. 3-2). At this point, the second generation of pentlandite likely exsolved in the form of small blebs due to decreased solubility of Ni in the evolving pyrrhotite-troilite assemblage. During cooling below 100 °C the 1C-pyrrhotite lamellae finally formed NC-type pyrrhotite through the ordering of Fe-site vacancies and additional formation of troilite. This scenario suggests a slow or strongly decelerating cooling from above 300 °C to below 100 °C, which allowed the exsolution assemblage to form.

The temperature path recorded by the sulfide assemblage in Y-791198 is clearly inconsistent with the temperatures reached during hydrothermal alteration, which ranged well below 100 °C (Guo and Eiler 2007). Clear contacts between the sub-µm NC-pyrrhotite-troilite-pentlandite intergrowths and the surrounding hydrous matrix without pentlandite rims even at the nm-scale render an aqueous formation of pentlandite highly unlikely. Even in case the pentlandite rims were formed by aqueous processes, the formation temperature of the internal troilite-pyrrhotite intergrowths would still exceed the established CM2 alteration temperatures. Because Y-791198 is one of the least aqueously altered CM2 chondrites (Metzler et al. 1992; Rubin et al. 2007), indicating a combination of lower alteration temperatures, lower water/rock ratios, and shorter duration of aqueous activity than typical for CM2 chondrites, a aqueous formation of pentlandite rims during processing under intense hydrothermal conditions can be effectively ruled out. Furthermore, there is no evidence that Y-791198 experienced any significant metamorphic overprint at temperatures above the pentlandite solvus.

In general, the formation of the observed sulfide assemblages by metamorphism is very unlikely, because such a process would require unrealistic conditions with respect to the precursor phases and diffusion distances: Starting from dispersed troilite and Fe,Ni metal grains, as observed in ordinary chondrites, the high temperature formation of a Ni-rich MSS with M/S of about unity would require a long distance transport of metals (several 10s or 100s of µm) and a high availability of sulfur. However, none of the typical CM2 chondrites, particularly not Y-791198, shows petrographic evidence for thorough metamorphic equilibration and mass transport. An alternative scenario would require

separate but clustered Fe sulfides and pentlandite grains before metamorphism, which then would turn into a MSS. In Y-791198 we have found such clusters of microcrystals as P-type sulfides (sample 98F06), but they exist in close proximity to M-type NC-pyrrhotite-troilite-pentlandite grains. It is highly unlikely that the fine-grained assemblages would have persisted in sub-mm-distance to other grain aggregates that homogenized during the same hypothetic metamorphic overprint. Hence, since aqueous or metamorphic formation of the M-type NC-pyrrhotite-troilite-pentlandite grains can be excluded, the origin of their precursor MSS must predate the accretion into the CM parent body. This supports the suggestions made by Boctor et al. (2002), Brearley and Martinez (2010), and Brearley (2010) that these sulfides are primary products of the solar nebula. Dai and Bradley (2001) described 6C-pyrrhotite from anhydrous IDPs, but suggested pyrrhotite might have formed from an unknown, spinel-type sulfide during atmospheric entry and heating. There has been no subsequent verification of the existence of the supposed precursor and our results indicate that pyrrhotite in anhydrous IDPs might indeed be a primary phase. This parallels the interpretation of the origin of pyrrhotite in IDPs by Zolensky and Thomas (1995), who suggested extended H_2S sulfidation of primary troilite, exfoliated from metal grains, to form Fe-deficient pyrrhotite.

Lauretta et al. (1996, 1997, 1998) showed that troilite is the first sulfide to form on metal of chondritic composition. However, sustained formation of troilite and eventual formation of Fe-deficient pyrrhotite will only occur if the sulfur fugacity remains above the IT-buffer. There are several possible scenarios: (i) The gas-solid mixture equilibrates before Fe metal is consumed. In this case the sulfide should be stoichiometric troilite; (ii) H_2S/H_2 and corresponding fS_2 remain above the IT-buffer values while metal is completely converted. Troilite will then react to pyrrhotite. These two options obviously require a complete, 'global' equilibrium (and sufficient temperature); (iii) Pyrrhotite might form through local equilibrium at high H_2S/H_2 and fS_2, either on the outside of thickly sulfide coated metal grains (Lauretta et al. 1997) or from exfoliated troilite flakes (Zolensky and Thomas 1995); (iv) Other components and phases such as gaseous H_2O and iron oxides might have participated in sulfidation reactions, possibly documented by the 4C-pyrrhotite plus magnetite found in the P-type aggregate of Y-791198.

4C-pyrrhotite in the P-type sulfide in Y-791198 probably points to a distinct formation environment in the solar nebula, likely connected to more oxidizing conditions based on the presence of abundant magnetite. Its formation via aqueous processes on the CM parent

body appears unlikely, as Fe sulfides were probably not stable phases under theses conditions as will be discussed in the next section. Ciesla et al. (2003) pointed out that in the wake of shock waves in ice-rich nebula environments the high vapor pressure of water would rapidly oxidize metallic iron and hydrate forsterite. If at the same time the fugacities of H_2S and S_2 were high, the formation of highly Fe-deficient 4C-pyrrhotite (x = 0.125) plus magnetite might have occurred in such a setting at temperatures above 450 °C and fO_2 above −22 log units (corresponding to log $fS_2 > -5$) as shown in Figure 3-1b.

TABLE 3-2. EPMA results of sulfides and metals.

	Y-791198		Y-793321		B-7904			
Mineral	Sul(+Pn)	Pn	Sul(+Pn)	Pn	Sul	Pn	Pn	Metal
Grain type	M-type	M-type	M-type	M-type	large	large	matrix	matrix
n (*n* grains)	27 (8)	6 (4)	10 (4)	1 (1)	9 (7)	4 (1)	1 (1)	1 (1)
Fe wt%	62.3(9)	39.6(2.7)	60.5(1.5)	37.7(2)	62.9(4)	45.7(1.3)	50.3(2)	96.5(2)
Ni wt%	1.31(59)	25.7(2.0)	2.2(1.8)	28.5(1)	0.09(3)	19.7(1.7)	15.0(1)	3.36(4)
Co wt%	0.04(5)	0.65(13)	0.10(9)	0.89(1)	<0.02	0.63(6)	0.12(1)	0.24(1)
S wt%	36.9(5)	33.49(55)	36.8(5)	33.5(1)	36.6(3)	33.7(3)	34.0(1)	0.05(1)
Total	100.5(7)	99.4(1.0)	99.6(3)	100.7(2)	99.5(4)	99.7(1.0)	99.5(2)	100.2(2)
Fe at%	48.8(6)	32.2(1.9)	47.7(1.0)	30.4(2)	49.7(3)	36.9(1.2)	40.6(2)	96.5(2)
Ni at%	0.98(43)	19.9(1.8)	1.7(1.4)	21.9(1)	0.07(2)	15.2(1.2)	11.5(1)	3.19(4)
Co at%	0.03(4)	0.50(10)	0.08(7)	0.68(1)	<0.01	0.48(5)	0.09(1)	0.22(1)
S at%	50.2(5)	47.4(5)	50.6(5)	47.1(1)	50.3(3)	47.4(1)	47.8(1)	0.08(1)
M/S	0.991(19)	1.108(21)	0.979(21)	1.125(2)	0.990(13)	1.108(5)	1.091(2)	n.a.
Fe/(Ni+Co)		1.59(22)		1.35(1)		2.38(27)	3.51(4)	

	Y-86720			
Mineral	Sul	Sul	Metal	Metal
Grain type	large	matrix	Ni-rich	Ni-poor
n (*n* grains)	37 (8)	8 (8)	3 (3)	1 (1)
Fe wt%	63.4(3)	62.8(7)	52.7(2.3)	99.8(3)
Ni wt%	0.03(3)	0.18(14)	45.6(3.2)	0.37(2)
Co wt%	<0.02	<0.02	1.5(1.1)	<0.02
S wt%	36.5(3)	36.4(4)	0.05(2)	<0.02
Total	100.0(4)	99.3(9)	99.9(4)	100.1(3)
Fe at%	49.9(2)	49.7(2)	54.0(2.3)	99.7(3)
Ni at%	0.02(2)	0.13(11)	44.5(3.1)	0.35(2)
Co at%	<0.01	<0.01	1.4(1.0)	<0.01
S at%	50.1(2)	50.1(2)	0.10(4)	<0.01
M/S	0.998(7)	0.995(6)	n.a.	n.a.
Fe/(Ni+Co)			1.18(11)	

Note: Sul = low-Ni Fe sulfide (pyrrhotite, troilite, or both), Pn = pentlandite, Sul(+Pn) = mixed measurements, M/S = metal/sulfur ratio, *n* = No. of measurements, *n* grains = No. of grains measured. Standard deviations (1σ) of least significant digits in parentheses.

In case of M-type grains, the actual bulk M/S and Fe/Ni ratios of the homogeneous MSS precursors before pentlandite exsolution are interesting parameters to assess nebula conditions such as fS_2 and fH_2S, estimate the onset temperature of pentlandite exsolution, or discuss the role of kinetic effects as described by Lauretta et al. (1997). Unfortunately, the highly heterogeneous distribution of pentlandite in the grains after exsolution renders the determination of the bulk composition exceedingly difficult. On the contrary, the crystallographic parameters of pyrrhotites can be determined very precisely. The N values determined for pyrrhotites in Y-791198 appear to be consistently smaller than 6.0, while values determined for Y-793321 pyrrhotite are close to 6.0. The lower values of Y-791198 between N = 5.5 to 6.0 might indicate an incomplete equilibration between exsolved troilite and the coexisting NC-pyrrhotite, similar to many terrestrial samples. Conversely, the values close to 6.0 in Y-793321 possibly point to a much slower cooling rate in the < 100 °C range. However, rather than reflection nebula processes, these differences are more likely connected to different parent body thermal histories of Y-791198 and Y-793321 (see below).

3.5.2. Parent Body Aqueous Alteration vs. Nebula Processes

As outlined above, the texture of M-type grains are clearly incompatible with low temperature aqueous formation. The case for the P-type microcrystalline cluster of pentlandite and 4C-pyrrhotite (Y-791198, FIB section 98F06) is less clear. The presence of 4C-pyrrhotite in association with magnetite in this aggregate indicates an oxidized assemblage which could be expected to form in a low temperature alteration process. 4C-pyrrhotite is typically found in many terrestrial hydrothermal metal deposits and its presence in highly altered CI chondrites and cometary dust has been described by Berger et al. (2011) based on TEM observations. In addition, its occurrence in CI chondrites can be inferred from EPMA analyses by Kerridge et al. (1979) and Bullock et al. (2005), which show sulfur enrichments consistent with Fe_7S_8. The corrosion and replacement seen in the grain sampled in 21F01 of Y-793321 indicates that high M/S sulfides (with M/S higher than Fe7S8) have been unstable during aqueous alteration and likely transformed into a tochilinite-like phase. The instability of Ni-poor pyrrhotite during progressive alteration of CM chondrites has been described previously (e.g., Rubin et al. 2007) and similar corrosion has been observed by Brearley (2011) in the Mighei CM2 chondrite, who described replacement by a fibrous oxysulfide. A contrasting behavior of 4C-

pyrrhotite, being formed, and 6C-pyrrhotite/troilite, being dissolved and replaced, would be highly enigmatic.

In CI chondrites the alteration conditions reached higher temperatures and were likely more oxidizing than in CM2 chondrites (for these Eh ≤ −0.67 V; Guo and Eiler 2007), allowing magnetite to form instead of tochilinite. Hence, the local formation of 4C-pyrrhotite in section 98F06 might reflect spatially confined oxidizing conditions. Unfortunately very little is known about the low temperature stability relationships among various pyrrhotite variants and even lesser about the, likely strongly kinetically controlled, precipitation behavior in low temperature aqueous systems (including potentially forming phases like smythite and mackinawite). Despite very similar compositions and structures, laboratory studies show differences in reactive behavior of different pyrrhotites (e.g. Belzile et al. 2004; Becker et al. 2010b; Harries in prep.). However, these differences, observed in oxidizing environments (Eh > 0), are rather due to distinct kinetics than reflecting different thermodynamic stabilities. Whether 4C-pyrrhotite could be stable relative to 6C-pyrrhotite or troilite in basic and reducing aqueous solutions of the CM parent body cannot be answered unambiguously, but it appears unlikely. Moreover, we did not find overgrowths of 4C-pyrrhotite on M-type grains in contact with the matrix, even on the nm-scale, suggesting that 4C formation on the CM parent body unlikely occurred. Hence, we favor a nebula formation of the 4C-pyrrhotite-pentlandite-magnetite assemblage in the P-type aggregate as outlined above.

3.5.3. Low Grade Parent Body Metamorphism

With regards to the sulfide assemblages, the least thermally altered sample Y-793321 shows only very subtle signs of metamorphism. The corrosion product of the large sulfide grain in section 21F01 of Y-793321 was likely tochilinite and transformed into a mixture of Fe sulfide and magnetite. The onset of this reaction on laboratory time scales occurs at around 245 °C (Fuchs et al. 1973). The upper temperature limit may be constrained by the compact sulfide assemblages. It appears that the exsolved pentlandite has never been completely resorbed into a MSS, and, hence, it was not heated above the solvus between 300 to 610 °C. After a complete homogenization of the sulfide it could be expected that the exsolving pentlandite would, at least partially, nucleate at the crystal margins as observed in Y-791198 and terrestrial samples (Kelly and Vaughan 1983). However, the grain in section 21F03 of Y-793321 does not show a pentlandite rim, indicating that it

probably did not re-homogenize after aqueous corrosion had taken place.

TABLE 3-3. TEM-SAED results of sulfides.

Meteorite	Sample	Zone axis/axes[§]	**q** (nm^{-1})[#]	**c*** (nm^{-1})[#]	**N = *c**/*q***
Y-791198	98F01 M-type grain	[100]+[110]	0.286(4)	1.719(6)	6.01(9)
Y-791198	98F01 M-type grain	[100]+[110]	0.287(4)	1.716(8)	5.98(9)
Y-791198	98F01 M-type grain	[210]+[1-10]	0.296(12)	1.734(15)	5.86(24)
Y-791198	98F02 M-type grain	[210]+[1-10]	0.302(6)	1.732(4)	5.74(12)
Y-791198	98F02 M-type grain	[100]+[110]	0.308(7)	1.733(10)	5.63(13)
Y-791198	98F06 matrix grain	[210]	0.313(7)	1.715(6)	5.48(13)
Y-791198	98F06 P-type grain	[100]+[110]	0.475(42)	1.737(22)	3.66(33)
Y-793321	21F01	[210]+[1-10]	0.292(2)	1.735(5)	5.94(4)
Y-793321	21F01	[100]+[110]	0.290(3)	1.738(8)	5.99(7)
Y-793321	21F01	[100]+[110]	0.291(3)	1.738(7)	5.97(7)
Y-793321	21F05	[100]+[110]	0.286(2)	1.713(8)	5.99(5)
Y-793321	21F05	[100]+[110]	0.286(4)	1.710(8)	5.98(9)
B-7904	04F02 troilite rim	[210]	0.278(6)	1.708(10)	6.14(14)
Y-86720	20F01 troilite rim	[110]	0.298(4)	1.715(21)	5.76(11)
Y-86720	20F01 troilite rim	[100]	0.300(8)	1.712(16)	5.71(16)
Y-86720	20F02 troilite rim	[100]	0.301(8)	1.706(4)	5.67(15)
Y-86720	20F02 troilite rim	[100]	0.303(6)	1.719(14)	5.67(12)

Note: Standard deviations of least significant digits in parentheses. [§]Two axes given in case of twinning. [#]Each pair of c^* and q values was obtained from the same SAED pattern. The given uncertainty relates to the measurement precision determined by measuring 10 to 15 spot distances, but accuracy of absolute values is not known due to lack of an internal standard and errors in sample height, camera length, etc. The ratio of c^* and q is accurate within given uncertainty, as both c^* and q are affected by the same systematic errors.

Given these observations and data reported by Nakamura (2005, 2006), the peak metamorphic temperatures of Y-793321 surely crossed the troilite solvus occurring at a maximum temperature of 140 °C. As pointed out in the introduction, 6C-pyrrhotite does not form immediately at the start of troilite exsolution but forms from 1C-pyrrhotite through ordering of Fe-site vacancies at temperatures below 100 °C. Given that many terrestrial troilite-bearing pyrrhotites, and maybe pyrrhotites in Y-791198 as well, appear to have been kinetically frozen in the process of low temperature equilibration (showing non-integral NC structures), sulfides in Y-793321 obviously equilibrated well in the stability field of 6C-pyrrhotite + troilite. The considerably coarser internal textures of compact M-type sulfide grains in Y-793321 compared to Y-791198 indicate different thermal histories and point toward prolonged low-temperature thermal annealing of Y-793321 below 100 °C. Condit et al. (1974) showed that self-diffusion of Fe in pyrrhotite is

rather fast. At temperatures below 100 °C, the driving force that leads to vacancy ordering is expected to slow down diffusion (unfortunately no data exist in this temperature range), but still diffusive transport can reasonably be assumed fast relative to other geological materials such as silicates. Hence, based on the data of Condit et al. (1974) we assume that diffusion on the sub-µm scale should be possible even at low temperatures around 0 °C during many hundreds of millions of years. There are two relevant scenarios that could account for the observed differences in sulfide textures of Y-791198 and Y-793321:

First, Nakamura (2006) identified Y-793321 as a regolith breccia and suggested short duration-heating by impacts during near-surface residence. For dark, chrondritic material, the equilibrium temperature of a small sized asteroid or asteroidal surface should be in the range of −50 to −100 °C in the main asteroid belt at 2.8 AU (Butler 1966) and colder at larger distance or during lower radiation output of the young sun. In order to achieve prolonged low-temperature annealing and coarsening of the pyrrhotite-troilite mixture, it would have been necessary to sustain regolith temperatures above the expected equilibrium temperature in the main belt by a suitably high rate of impacts. At the same time, peak heating during episodic impact events must not have exceeded temperatures above the respective solvi, in order to avoid partial re-homogenization or erasing of existing exsolution texture.

In a second scenario, Y-793321 could have experienced higher long-term average temperatures than Y-791198 by receiving stronger radiation heating through relatively stable orbital parameters that brought the parent asteroid closer to the sun during much of its lifetime. At average solar distances in the vicinity of the orbits of Earth and Mars the equilibrium temperature of a dark chondrite is expected to be around 0 °C and, hence, long-term residence in this region could be responsible for the different textural evolution of Y-793321 sulfides.

As pointed out by Nakamura (2006) based on missing Fe-Mg zoning in chondrule silicates, the peak heating of Y-793321, up to supposed 500 °C, was likely transitional and not due to prolonged radiogenic heat production. Hence, heating must have occurred while the material resided close to the asteroid's surface. Heating by impacts is transient with relatively rapid cooling rates (Wittmann et al. 2010) and is mostly regarded as insufficient to cause long-term, large-scale heating of asteroidal bodies (Keil et al. 1997). On the other hand, solar heating up to the breakdown temperatures of phyllosilicates would require close perihelion distances of less than 0.1 AU (Nakamura 2005), which appears

incompatible with a long-term survivable orbit. This suggests that impact-generated heat is most likely the explanation for the high temperature metamorphic overprint, which is supported by shock metamorphic features (planar fractures, Nakamura 2006) observed in Y-793321. However, despite the low thermal diffusivity of regolith material might increase the retention of impact-generated heat, it appears questionable whether the rate of repeated impacts could have been high enough to keep the long-term average regolith temperature in a reasonable range to allow coarsening of sulfides in Y-793321 relative to Y-791198. A long-term residence of the Y-793321 parent body in the vicinity of the orbits of Earth and Mars and corresponding higher surface equilibrium temperatures appear to be better explanations for this phenomenon.

3.5.4. High Grade Parent Body Metamorphism

The troilite-metal assemblages of B-7904 and Y-86720 are unlike the sulfides and metals observed in CM chondrites studied here and reported elsewhere. In terms of sulfide mineralogy, the euhedral, metal-bearing troilite pseudomorphs seen in Y-86720 are the most telling evidence for strong metamorphic overprint of these rocks. We interpret them to represent the replacement of former euhedral pyrrhotite crystals, similar to those known from CI chondrites. Assuming the original pyrrhotite to have been Fe_7S_8 (x = 0.125) as observed in CI chondrites (Berger et al. 2011), the following reactions describe the process:

$$Fe_{1-x}S_{(s)} \rightarrow (1-x)FeS_{(s)} + (0.5x)S_{2(g)} \rightarrow (1-x)Fe_{(s)} + 0.5S_{2(g)} \quad (3\text{-}5)$$

The reactions are driven to the product sides by low fS_2 and the troilite-metal assemblages in B-7904 and Y-86720 essentially constrain the sulfur fugacity at peak metamorphic temperatures to that of the IT buffer. As outlined in the introduction, the stable coexistence of Fe oxides and pyrrhotite couples fS_2 and fO_2. Figure 3-1b shows fO_2 isobars for coexisting magnetite (Whitney 1984). Isobars for other coexisting oxidic Fe minerals (including wüstite) can be calculated accordingly. In fS_2-T space, the intersections of isobars of equal fO_2 for two pairs of pyrrhotite-oxide assemblages define the curves of joint fS_2-fO_2 buffers, along which both fugacities are fixed at given temperature. The iron-magnetite-pyrrhotite (IM-Po) and iron-wüstite-pyrrhotite (IW-Po)

buffers coincide with the IT buffer, because the sulfide in equilibrium with metal is always stoichiometric troilite. The magnetite-wüstite-pyrrhotite (MW-Po) buffer becomes relevant at temperatures above 570 °C.

Despite wüstite is not expected to be a stable phase in association with magnesian silicates and will likely dissolve in them (depending on SiO_2 activity), the buffer reaction can approximately constrain the metamorphic temperature, at which magnetite becomes instable along the IT buffer line. For unity activity of FeO, the MW-Po line intersects the IT line in an invariant point at approx. 572 °C, corresponding to an fS_2 of −12.7 to −13.1 log units (depending on the source of fS_2 data; Toulmin and Barton 1964, Rau 1976) and an fO_2 of −25.8 log units. FeO activities of less than one strongly shift the intersection toward lower temperatures (e.g., ~400 °C for aFeO = 0.6). Texturally, especially with regards to sulfide morphology, Y-86720 bears much resemblance to CI chondrites, which carry abundant magnetite. Even if the precursor mineralogy was more CM-like, magnetite would have been a ubiquitous accessory phase. If we interpret the complete lack of magnetite in Y-86720 to be the result of reduction to FeO and assume that both Y-86720 and B-7904 initially had similar FeO and SiO_2 activities in their silicate portions, then the following scenario arises: Y-86720 has experienced peak metamorphic temperatures above the stability limit of magnetite, while B-7904 was subjected to lower temperature at conditions in favor of magnetite conservation. This constrains the peak metamorphic temperature of B-7904 to less than 570 °C and suggests fS_2 and fO_2 to have been below those values given above for the invariant point at which troilite, iron, magnetite, and wüstite coexist. The temperature estimate compares well to the range derived by Zolensky et al. (1991), but is lower than the temperatures suggested by Akai (1990, 1992).

The 6C-like pyrrhotite occurring as rims on troilite in B-7904 and Y-86720 is apparently not in equilibrium with the coexisting metal, since Fe-deficiency in NiAs-structured sulfide would not be allowed by the low fS_2 that led to the formation of Fe,Ni metal. Figure 3-1a shows that a composition of $Fe_{0.917}S$ (x = 0.083), corresponding to 6C-pyrrhotite, forms at fS_2 of about 5 to 8 log units above the IT buffer. However, since any composition formed between the x = 0 (troilite) and x = 0.083 isopleths would decompose into troilite and 6C-pyrrhotite below 100 °C, it cannot be ruled out that the Fe-deficient troilite rims formed in this intermediate region. Clearly, the rims formed at elevated fS_2 relative to the IT buffer, at which the bulk of the sulfides equilibrated. We interpret the

formation of rims to represent a late-stage, low-temperature reaction during cooling when fS_2 was no longer in equilibrium with the troilite-metal assemblage. At this stage low amounts of post-metamorphic, hydrous fluids might have been involved in the alteration as documented by heat sensitive minerals such as calcite and aragonite. Thermodynamic calculations show that anhydrite is not a stable phase under conditions of troilite formation. Figure 3-1b shows fS_2 isopleths for an assemblage involving pyrrhotite, magnetite, anhydrite, and CaO (dissolved in silicates). The location of isopleths is given by the intersections of fO_2 isobars of reaction 3-3 and corresponding isobars of the reaction:

$$CaSO_{4(s)} \rightarrow CaO_{(ss)} + 0.5S_{2(g)} + 1.5O_{2(g)} \qquad (3\text{-}6)$$

At aCaO = 1 the isopleth is located closely to the FMQ-Po buffer of Eggler and Lorand (1993), lying just below the x = 0.083 isopleth of 6C-pyrrhotite. Lower CaO activities shift the anhydrite isopleth toward higher fS_2 into the field, where 4C-pyrrhotite (x = 0.125) would be expected to form. Hence, at relatively high CaO activity (possibly documented by calcite/aragonite formation) and fS_2 just above the FMQ-Po buffer, conditions would have been favorable of forming both anhydrite and the Fe-deficient rims on troilite. This clearly indicates a two-stage evolution of the observed assemblage – a peak metamorphic stage and a retrograde, maybe hydrous, stage.

3.5.5. Relations among Metamorphosed and Pristine CM/CI Chondrites

The oxygen isotopic compositions of B-7904 and Y-86720 are distinct from CI and CM chondrites, but could be related to CI chondrites through mass-dependent fractionation (Mayeda and Clayton 1998). Clayton and Mayeda (1999) suggested an isotopic model involving mixing between anhydrous rock and a water reservoir and point out possible genetic relationships between CI and CM chondrites. These could have been formed by mixing along a common or very similar mixing line, but were subsequently processed at different temperatures and water/rock ratios. The relationships are exemplified by the existence of anomalous, transitional CM/CI-like members, such as the meteorites Bells and Essebi, which not only have transitional oxygen isotopic compositions, but also contain abundant CI-like magnetite.

From the perspective of sulfide mineralogy, the pre-metamorphic precursors of B-7904 and Y-86720 might have been similar transitional cases. Assuming that the ^{17}O- and ^{18}O-rich compositions are due to dehydration and evolution along an expected slope 0.5 line, the precursor probably had CI-like oxygen isotopic ratios. On the other hand, the fine-grained troilite-olivine intergrowths observed in Y-86720 and B-7904 suggest the former presence of interlayered tochilinite-serpentine aggregates, which thermally broke down into troilite, as suggested by Tomeoka et al. (1989b), plus olivine. Because the sub-µm-sized, highly dispersed olivine grains unlikely formed as a result of exsolution, and amoeboid aggregate shapes exclude crystallization from a sulfide-silicate melt, there are hardly alternatives to assuming an initially uniform, sulfide- and silicate-rich mixture. The possibility that sulfide infiltrated the olivine-rich matrix during the retrograde stage appears possible but remote, because this sulfide should have been pyrrhotite with little textural equilibration. Instead, we find texturally fairly equilibrated troilite with abundant triple junctions and relatively large olivine grains unlike those in the matrix (e.g., Fig. 3-5f). The inferred presence of tochilinite indicates that the precursor mineralogies of both meteorites might have been indeed CM-like, since sulfide-bearing interlayer minerals are generally absent in CI chondrites. The preservation of primary silicates in B-7904 and Y-86720 also texturally supports a rather weakly altered, CM-like pre-metamorphic mineralogy, while preserved euhedral sulfide morphologies in Y-86720 indicate CI similarities.

3.6. Conclusions

The sulfide mineralogies of CM and CI chondrites and their anomalous relatives proof to be very diverse and record complex evolutionary histories. In CM2 chondrites Y-791198 and Y-793321, the NC-pyrrhotite-troilite-pentlandite association found in M-type grains indicates high temperature formation from a once homogeneous MSS. This is inconsistent with parent body aqueous alteration and strongly points to processing in the solar nebula. An assessment of nebula conditions that led to the formation of the MSS precursors, instead of the usual Ni-poor troilite, is difficult due to the lack of knowledge about the bulk composition of now exsolved and highly heterogeneous sulfide grains. 4C-pyrrhotite in association with magnetite and pentlandite in P-type sulfide aggregates possibly points to a relatively oxidizing nebula environment during sulfidation and formations of these peculiar aggregates.

The microstructure of complex sulfide grains can further add information on low temperature cooling rates and thermal evolution, suggesting that Y-793321 experienced higher long term average temperatures than Y-791198 in the < 100 °C temperature regime. TEM studies in combination with kinetic modelling of the exsolution process could provide better constraints on actual cooling rates. However, while data on diffusivity in disordered, high-temperature pyrrhotites is available, data on low temperature diffusion rates in ordered pyrrhotites is still needed for such calculations. Also detailed knowledge about low temperature phase relations in the Fe-Ni-S system is desirable, specifically addressing the relationships between different pyrrhotite variants below 100 °C and the solubility of Ni in them. Our observations of two-stage pentlandite exsolution in Y-791198 sulfides suggest a decrease in Ni solubility during the troilite exsolution and/or the subsequent 1C- to NC-pyrrhotite ordering. Sub-µm pentlandite exsolution in Fe-rich pyrrhotite ($x < 0.083$) might therefore not necessarily constrain high temperature processing near the classical pentlandite solvus, but rather point to processes in the 100 to 140 °C range.

Corrosion of NC-pyrrhotite, troilite, and pentlandite in M-type grains of Y-793321 is scarce, but indicative of instability of these phases during aqueous alteration. The corrosion product likely was tochilinite, which converted to magnetite plus troilite during the thermal overprint on Y-793321.

The highly metamorphic Belgica grouplet meteorites Y-86720 and B-7904 show troilite as dominant sulfide phase without any resemblance to sulfides in pristine or lowly metamorphosed CM2 chondrites. In both meteorites, troilite coexists with Fe,Ni metal indicating peak metamorphism at fS_2 of the IT-buffer under strongly reducing conditions. The absence of magnetite in Y-86720 suggests crossing into the wüstite field and indicates a higher metamorphic grade than B-7904, in which magnetite is preserved. The metamorphic conditions of B-7904 can be constrained to T < 570 °C, $fS_2 < -13.1$ and $fO_2 < -25.8$ log units. Troilite in Y-86720 and B-7904 shows rims of 6C-like pyrrhotite and the matrix of both meteorites contains anhydrite. Both phases are not stable under the conditions of the IT-buffer and must have formed during cooling after the metamorphic event.

Texturally, the Belgica gouplet meteorites are very diverse, but observations on sulfide mineralogies link them among each other and to CM and CI chondrites. In Y-86720 euhedral, platelet shaped troilite pseudomorphs occur akin to pyrrhotite crystals seen in CI

chondrites. In Y-86720 and B-7904 extremely fine-grained and closely intergrown troilite-olivine mixtures occur, which most probably originated from the breakdown of tochilinite-serpentine intergrowths typically present in CM chondrite. Especially in case of Y-86720, these observations imply an intermediate mineralogical composition of the precursor rock between CM and CI chondrites.

3.7. Acknowledgements

We gratefully acknowledge sample loan by the National Institute of Polar Research (NIPR) of Japan and financial support by the Leibniz program of the German Research Foundation (DFG; LA 830/14-1 to F.L.) and the ENB program of the Bavarian State Ministry of Sciences, Research and the Arts (to D.H.).

CHAPTER 4 Oxidative Dissolution of 4C- and NC-Pyrrhotite: Intrinsic Reactivity Differences, pH Dependence, and the Effect of Anisotropy

by Dennis Harries[1,2]*, Kilian Pollok[2], and Falko Langenhorst[2]

[1]Bayerisches Geoinstitut, University of Bayreuth, D-95440 Bayreuth, Germany. [2]Institut für Geowissenschaften, Friedrich-Schiller-Universität Jena, Carl-Zeiss-Promendae 10, D-07745 Jena, Germany.
*Corresponding author. Email: dennis.harries@uni-bayreuth.de

4.1. Abstract

We have conducted oxidative dissolution experiments on monoclinic 4C-pyrrhotite and 'hexagonal' NC-pyrrhotite in aqueous H_2O_2/H_2SO_4 and $FeCl_3$/HCl media at pH between 1.8 and 2.9 using polished surfaces of single crystals. Quantification and detailed characterization of the reaction interfaces has been accomplished by confocal 3D topometry and transmission electron microscopy (TEM) in conjunction with focused ion beam (FIB) preparation. Crystallographically coherent intergrowths of 4C- and NC-pyrrhotite in a single sample allowed unambiguous identification of strong intrinsic reactivity differences between the two closely related phases. On {110} faces in the H_2O_2 medium at 35 °C and pH below 2.70, NC-pyrrhotite (N ~4.85) reacts about 50 to 80 % faster than 4C-pyrrhotite. Above pH 2.70 the behavior inverts and 4C-pyrrhotite dissolves faster, while overall reaction rates drop drastically by up to two orders of magnitude. Because the two pyrrhotite phases show only marginally different Fe/S ratios but substantial differences in structural complexity with regards to vacancy ordering, we attribute the reactivity differences to structurally controlled processes at the mineral-water interface. The transition at pH 2.70 is close to the reported isoelectric point of pyrrhotite. We attribute the pH dependent changes in reaction rates and behaviors to protonation/deprotonation of surface sulfhydryl groups and related changes in speciation and bonding mode of reactive oxygen species at the mineral interface. At pH < 2.70 we find elemental sulfur as a frequent reaction product in H_2O_2 and $FeCl_3$ media, indicating incomplete sulfur oxidation. Above pH 2.70, elemental sulfur was not found in H_2O_2 experiments (no data for $FeCl_3$). Our results show that the effects of crystal anisotropy are strong and directional preference of dissolution changes at the pH 2.70 transition point as well, leading to complex sub-µm-scale textural development at the reaction interfaces throughout the pH range studied. High resolution TEM imaging of FIB cross sections through reacted mineral surfaces show crystalline pyrrhotite up to the reaction interface

and the absence of significant non-equilibrium layers or S-enriched (poly)sulfides.

4.2. Introduction

4.2.1. General Introduction

Pyrrhotite comprises a group of non-stoichiometric iron monosulfides ($Fe_{1-x}S$), which occur as frequent accessory phases in crustal rocks of Earth (Rochette et al. 1990) and are present in large amounts in many base and noble metal ore deposits (e.g., Bowles et al., 2011). Despite their simple and very similar compositions, pyrrhotites show a large variability in structures and magnetic properties (e.g., Schwarz and Vaughan 1972; Bennett and Graham 1980). The weathering of pyrrhotite under influence of atmospheric oxygen proceeds approximately 20 to 100 times faster than that of pyrite (Nicholson and Scharer 1994) and can generate acidic mine drainage (AMD) and concurrent release of heavy metals into the environment (Belzile et al. 2004). Reactivity differences exist among different varieties of pyrrhotite, but a comprehensive picture of the systematics of its weathering behavior is still lacking (Belzile et al. 2004). Therefore, the understanding of the intrinsic differences in chemical behavior of pyrrhotites is a crucial part in evaluating and modeling the environmental impact of mining pyrrhotite-bearing ores. Because biological activity of chemolithotrophic microbes is known to enhance reaction rates and plays a significant role in the chemical evolution of mining environments (e.g., Schippers and Kock 2009; Gunsinger et al. 2006), such understanding is needed to resolve the contribution of microbiological communities to pyrrhotite weathering. On the technological side, efficient mineral processing depends on well constrained mineral properties. Becker et al. (2010) recently showed that different varieties of pyrrhotite perform significantly different in flotation experiments. The differences are attributed to different intrinsic susceptibilities to surface oxidation.

4.2.2. Mineralogy of Pyrrhotite

At ambient conditions pyrrhotite occurs in three major forms: troilite (stoichiometric FeS), 4C-pyrrhotite ($Fe_{0.875}S$ or Fe_7S_8), and NC-pyrrhotite (approx. $Fe_{0.88-0.92}S$). All forms are based on a layered NiAs-type substructure, on which superstructures are imposed by ordering of Fe-site vacancies in the non-stoichiometric pyrrhotites. In 4C-pyrrhotite Fe site vacancies arrange highly regular and superpose a monoclinic superstructure by strict alternation of filled and partially vacant Fe layers (Bertaut 1953; Powell et al. 2004). The

greatly variable NC-pyrrhotites form a series of superstructures, which are characterized by integral or non-integral N values describing the multiplicity of the superstructure period along the hexagonal c axis relative to the NiAs substructure (Morimoto et al. 1975a). This N value is 4 for 4C-pyrrhotite and ranges from approx. 4.2 to 6.6 in NC-pyrrhotites (e.g., Morimoto et al. 1975b; Pósfai et al. 2000). Recently, Harries et al. (2011) showed by transmission electron microscopy (TEM) that the NC-pyrrhotites can be understood as derivatives of the 4C structure, which is being modulated by non-conservative ('chemistry changing') anti-phase domain boundaries (APBs). While in 4C-pyrrhotite a strict alternation of filled and vacancy bearing Fe-layers occurs, the slightly higher Fe content in NC-pyrrhotites results in the occurrence of APBs that can be described as pairs of subsequently filled ('double filled') Fe layers.

Coexistence of different pyrrhotite types is a commonly observed feature in natural samples and related to exsolution at low (<140 °C) temperature. Two principal associations appear to occur frequently (Morimoto et al. 1975ab; Harries et al. 2011): 4C-pyrrhotite with NC-pyrrhotite (N = 4.7 to 5) and troilite with NC-pyrrhotite (N = 5.5 to 6). At present, the stable phase relations at ambient temperatures are not well known and some observed associations might represent metastable states, which are kinetically hindered in further equilibration. However, the structurally well defined interfaces between coherently intergrown 4C- and NC-pyrrhotite (N ≈ 4.85) observed by Harries et al. (2011) point to a well equilibrated state of this association, lacking any stranded diffusion profiles.

4.2.3. Reactions at Pyrrhotite Surfaces

The dissolution of pyrrhotite in natural or mining environments proceeds via acidic dissolution under anoxic conditions or via oxidative dissolution when oxygen can access the reaction site. Both processes appear to compete at low pH under oxic conditions (Belzile et al. 2004). In nature, dissolved oxygen is the ultimate oxidizing agent leading to sulfide dissolution, but often dissolved Fe^{3+} acts as an intermediate agent in a reaction cycle, in which the resulting Fe^{2+} ions are back-converted to Fe^{3+} via oxidation by O_2 (Nicholson and Scharer 1994; Belzile et al. 2004):

$$Fe_{1-x}S_{(s)} + (8-2x)Fe^{3+}_{(aq)} + 4H_2O_{(l)} \rightarrow (9-3x)Fe^{2+}_{(aq)} + SO_4^{2-}{}_{(aq)} + 8H^+_{(aq)} \quad (4\text{-}1)$$

$$Fe^{2+}_{(aq)} + 0.25O_{2(aq)} + H^+_{(aq)} \rightarrow Fe^{3+}_{(aq)} + 0.5H_2O_{(l)} \quad (4\text{-}2)$$

However, if pH is not sufficiently low, reaction (1) will compete with the precipitation of ferric hydroxides or oxyhydroxides:

$$Fe^{3+}_{(aq)} + 2H_2O_{(l)} \rightarrow FeO(OH)_{(s)} + 3H^+_{(aq)} \quad (4\text{-}3)$$

Observations indicate that the initial oxidation of sulfide to sulfate is often not complete but generates elemental sulfur instead (e.g., Steger 1982; Nicholson and Scharer 1994; Kalinkin et al. 2000):

$$Fe_{1-x}S_{(s)} + (2-2x)Fe^{3+}_{(aq)} \rightarrow (3-3x)Fe^{2+}_{(aq)} + 0.125S_{8(s)} \quad (4\text{-}4)$$

The extend to which these (and likely other) individual reactions are involved in the net reaction determines whether acidity is produced or not, owing to the fact that some reactions produce H^+ (1, 3) and others consume it (2) or do not involve it at all (4). In contrast to oxidative dissolution of pyrrhotite, non-oxidative acidic dissolution results in release of sulfur either as H_2S or HS^- (e.g., Thomas et al. 1998) and preserves iron in its original oxidation state (mostly Fe^{2+}). Nicol and Scott (1979) suggested that non-oxidative dissolution of pyrrhotite would be limited to stoichiometric FeS and Fe-rich members.

Based on X-ray photoelectron spectroscopy (XPS) and other surface sensitive spectroscopic techniques, several studies on pyrrhotite oxidation and dissolution suggested the development of nm-wide, S-enriched surface layers (e.g., Wang, 2007 and references therein). Such non-equilibrium layers are Fe-depleted regions measuring several nm to tens of nm or more in thickness and may consist of amorphous sulfide with gradually changing composition or sequences of di- and polysulfides such as FeS_2 and Fe_2S_3 (Buckley and Woods 1985ab; Jones et al. 1992; Pratt et al. 1994; Mycroft et al. 1995; Mikhlin et al. 1998).

Experimental studies of sulfide oxidative dissolution showed that hydrogen peroxide (H_2O_2) is a convenient oxidizing agent, because it is very reactive and can be used over a wide pH range without inducing strong precipitation of Fe oxyhydroxides. The accuracy of H_2O_2 in studying the acid generation potential of pyrite has been demonstrated by O'Shay et al. (1990), and was applied by Jennings et al. (2000) to pyrrhotite. Analogous to the reactions given above, the reaction with pyrrhotite may be represented as:

$$Fe_{1-x}S_{(s)} + (4\text{-}x)H_2O_{2(aq)} \rightarrow (1-x)Fe^{2+}{}_{(aq)} + SO_4{}^{2-}{}_{(aq)} + (2x)H^+ + (4\text{-}2x)H_2O_{(l)} \quad (4\text{-}5)$$

$$Fe^{2+}{}_{(aq)} + 0.5H_2O_{2(aq)} + H^+{}_{(aq)} \rightarrow Fe^{3+}{}_{(aq)} + H_2O_{(l)} \quad (4\text{-}6)$$

Experimental results by Buckley and Woods (1985a) suggest that also here the sulfide oxidation is incomplete and reaction (5) may be replaced or accompanied by:

$$Fe_{1-x}S_{(s)} + (1\text{-}x)H_2O_{2(aq)} + (2\text{-}2x)H^+{}_{(aq)} \rightarrow (1-x)Fe^{2+}{}_{(aq)} + 0.125S_{8(s)} + (2\text{-}2x)H_2O_{(l)} \quad (4\text{-}7)$$

Jennings et al. (2000) showed that the net reaction of pyrrhotite with H_2O_2 produces acidity and is accompanied by the precipitation of ferric hydroxide or oxyhydroxide (e.g., through reaction 3). The oxidation mechanism of H_2O_2 is not well known, but its action may be linked to other reactive oxygen species such as singlet oxygen and radical ions, which have been suggested to play roles in the oxidation of ferrous to ferric iron during Fe sulfide weathering (Lowson 1982) and detrimentally form in the oxic metabolism of cells (e.g., Imlay 2003).

Despite hydrogen peroxide plays no known role in natural sulfide oxidation processes, it has been suggested as reagent in the technical processing of pyrrhotite mine tailings, aiming at passivation through creating resistant iron phosphate coatings (Georgopoulou et al. 1996):

$$Fe_{1-x}S + (4.5-1.5x)H_2O_2 + (1-x)H_2PO_4{}^- \rightarrow (1-x)FePO_4 + SO_4{}^{2-} + (1+x)H^+ + (5-3x)H_2O \quad (4\text{-}8)$$

This reaction couples the oxidation of pyrrhotite with the concomitant precipitation of ferric phosphate. The so treated grains showed significantly lower Fe release rates during leaching experiments.

4.2.4. Outline of Approach

Despite it has been suggested that differences in crystal structure can affect the oxidation behavior of pyrrhotite (Belzile et al. 2004 and references therein), no clear correlation between reactivity and structure has been shown yet. Oxidation experiments by

Janzen et al. (2000) at pH 2.50-2.75 indicated no apparent effect of crystal structures. Belzile et al. (2004) reported unpublished results suggesting that monoclinic 4C-pyrrhotite reacts less rapidly than the NC form. Flotation experiments at pH 7-10 (Becker et al. 2010) show however that magnetic, 4C-rich pyrrhotite is more reactive in terms of oxygen uptake than the NC form. Experimental studies conducted on pyrrhotite reactivity, mainly focusing on oxidative dissolution (Belzile et al. 2004), commonly used powders and rarely obtained direct observations at the reaction interface. Under such circumstances it appears to be difficult to resolve intrinsic reactivity differences between pyrrhotite types, because the phase proportions are difficult to constrain in powders and effects of crystallographic orientation can not be addressed.

Coherent intergrowths of 4C- and NC-pyrrhotite, as described by Harries et al. (2011), share the same crystallographic orientations and are ideal subjects for comparative study of reactivity differences at the micrometer to sub-micrometer scale using 3D topometry and electron microscopy. Polished surfaces of intergrown pyrrhotites allow to separate effects of anisotropy of the reacting surfaces from intrinsic reactivity differences among different pyrrhotite types. In conjunction with the orthogonal view on the reacted surface, the now widely available focused ion beam (FIB) method for preparing TEM samples offers unprecedented ways in studying mineral-fluid interactions directly at the reactive interface in cross-section with sub-micrometer precision. Here we present a combined experimental study that integrates phase-specific rate determinations from surface topometry and detailed study of alteration mineralogy by analytical electron microscopy. Instead of focusing on detailed kinetic characterizations, we aim at clarifying to what extend pyrrhotite structures affect the dissolution behavior.

4.3. Samples and Experimental Procedure

4.3.1. Sample Description

We have examined two natural, cm-sized single crystal pyrrhotite samples, designated DAL and EUL. DAL is 4C dominant pyrrhotite from Dalnegorsk (Russia). Electron microprobe (EMP) analysis using a JEOL JXA-8200 (20 kV/ 20 nA, 20 µm defocus, ZnS and pure metal standards) revealed a composition of $Fe_{0.877}S$ (Tab. 4-1); it is thus almost ideal Fe_7S_8 (1σ precision of Fe/S ratio: ±0.001 for n = 30). Ni and Co could not be detected above detection limits (approx. 0.02 % m/m). The composition was checked against stoichiometric troilite and systematic deviations from the ideal 4C Fe/S ratio of

0.875 were found to be less than 0.005. The pure DAL material was subsequently used as calibrant for further EMP analysis (15 kV, 20 nA, focused probe) in order to minimize matrix corrections (JEOL CITZAF PRZ). The part of the DAL crystal used for reactivity experiments contains very small NC exsolution lamellae with lengths up to 100 µm and widths up to 10 µm (Fig. 4-1b). BSE image analysis indicates that their area fraction on polished surfaces locally reaches maximum values of 5 to 7 %. These NC lamellae have compositions of $Fe_{0.898}S$ (Tab. 4-1).

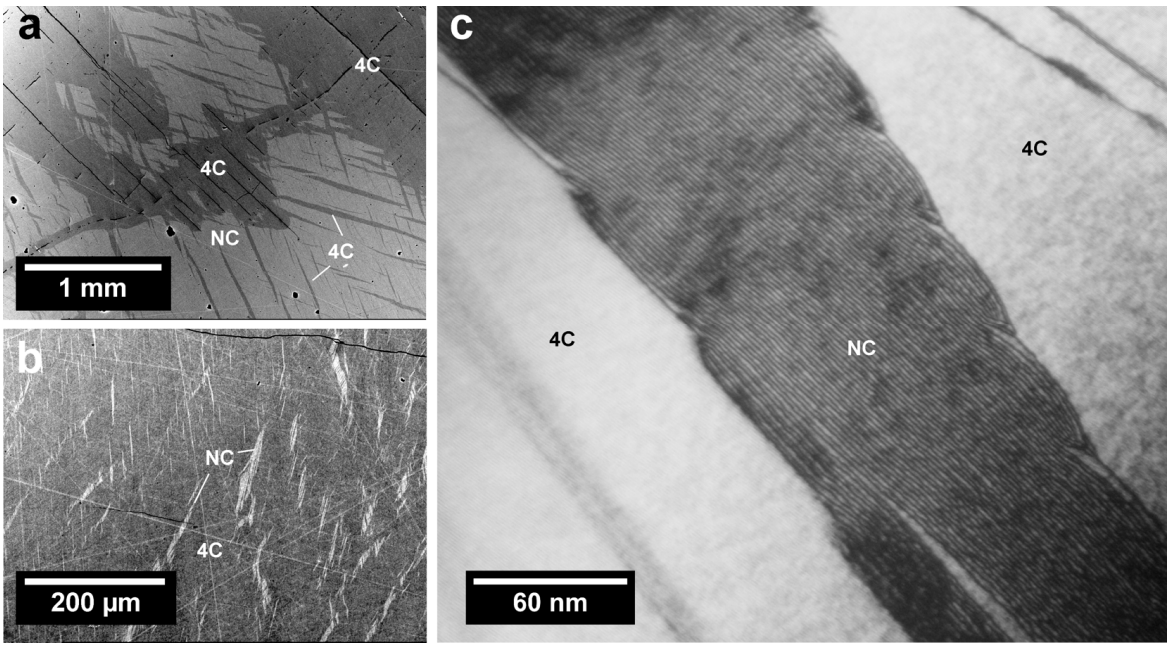

FIGURE 4-1. (**a**) SEM-BSE image of EUL pyrrhotite. 4C-pyrrhotite forms exsolution lamellae in NC-pyrrhotite (N = 4.81−4.87) and occurs along fractures parallel to (001), likely due to preferred nucleation. (**b**) SEM-BSE image of DAL pyrrhotite. Here the exsolution relationship is reverse and NC-pyrrhotite (N = 4.90−4.92) occurs as small lamellae in 4C-pyrrhotite. (**c**) SDF-TEM image of a NC lamella in DAL pyrrhotite obtained using the preparation and imaging procedures described in Harries et al. (2011). Dark stripes in the NC portion are double filled iron layers, being equivalent to anti-phase domain boundaries (APBs), which terminate in complex node structures at the phase interface (cf. Harries et al. 2011).

EUL is an intergrowth of 4C- and NC-pyrrhotite from the Sta. Eulalia mining district in Chihuahua, Mexico (Fig. 4-1a). It contains 4C exsolution lamellae in a matrix of NC-pyrrhotite, but also larger areas of 4C-pyrrhotite exist, mostly along (001) cleavage fractures probably acting as preferred nucleation sites. The composition of the NC portion was determined by EMP analysis to be $Fe_{0.894(1)}S$ (Tab. 4-1). Hence, the Fe/S ratio of the NC phase is approx. 2.4 % higher relative to 4C. Ni and Co were not present above detection limits. EUL has been intensively studied by TEM by Harries at al. (2011). Crystallographic information obtained by selected area electron diffraction (SAED) is

consistent with the 4C- and NC-type compositions. The N value of the NC portion ranges between 4.81 and 4.87, and the crystallographic orientations of the intergrown 4C and NC phases are mutually identical with respect to the NiAs base cell and coherent along their interfaces. The 4C lamellae are strongly twinned by rotation about the NiAs *c* axis (as typically observed 4C-pyrrhotite; e.g., Putnis 1975; Pósfai et al. 2000) and we estimate the density of twin boundaries to be approx. 0.5 to 2 μm^{-1} (rarely up to 6 μm^{-1}). The NC portion also shows twinning according to the same law but twin boundaries are very rare.

We have applied the same TEM preparation and analysis methods to the DAL sample and confirmed the bulk of the material to be 4C-pyrrhotite. Here the densities of twin boundaries are considerably lower than in 4C lamellae of EUL. NC exsolution lamellae occur in the same coherent intergrowth relationship as previously reported for EUL and show the same modulated APB superstructures (Fig. 4-1c), except that here the NC phase exhibits an inverse exsolution relationship (small NC lamellae within hosting 4C-pyrrhotite) and constitutes only a small portion (~5-6 % v/v) of the whole sulfide. For the NC lamellae we have determined N values of 4.90 and 4.92 (the number of single phase SAED patterns was limited due to the small size and number of accessible NC lamellae in the TEM sample).

TABLE 4-1. EPMA composition data of pyrrhotites studied (% m/m).

Sample	**EUL**		**DAL**	
Phase	**NC (host)**	**4C (lamellae)**	**NC (lamellae)**	**4C (host)**
n	30	25	17	30
Fe	60.84(2)	60.26(3)	60.97(5)	60.17(4)
S	39.07(3)	39.64(2)	38.99(2)	39.41(3)
Total	99.91(3)	99.90(4)	99.59(5)	99.97(5)
		Formula per 1 S		
Fe	0.894(1)	0.873(1)	0.898(1)	0.877(1)
***x* in $Fe_{1-x}S$**	0.106(1)	0.127(1)	0.102(1)	0.123(1)

Note: Ni and Co are below detection limit (0.02 % m/m) in both samples. *n*: No. of analysis points. Standard deviations (1σ) of least significant digits in parentheses.

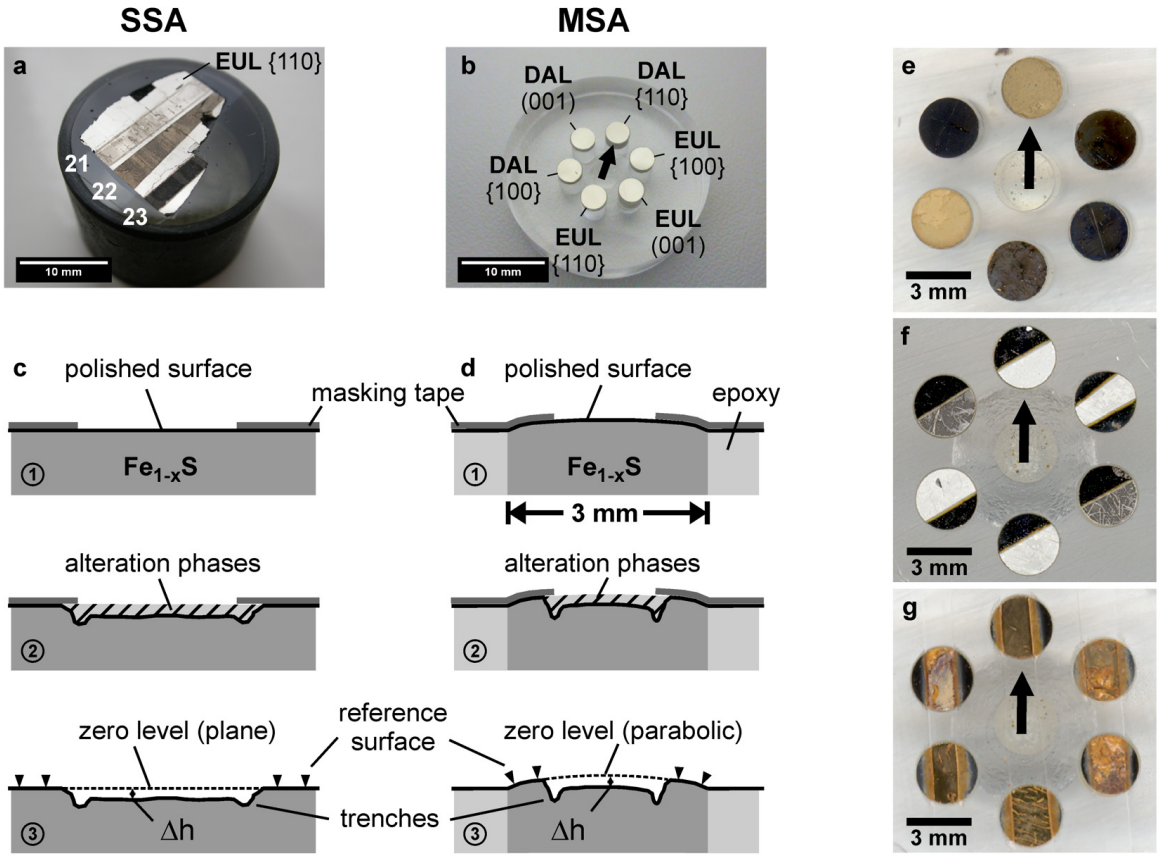

FIGURE 4-2. (**a-d**) Experiment types and experimental procedure applied to single sample assemblies (SSA) and multi-sample assemblies (MSA). (**a**) SSA is a polished single crystal (EUL1inL) shown after three experiments (stripes with experiment numbers, see Tab. 4-2). (**b**) MSA consist of 3 mm cylinders of pyrrhotite in different orientations set in a 25.4 mm PMMA holder. (**c+d**) Experimental procedure. (1) After polishing. Due to the hardness difference between pyrrhotite and PMMA the sulfide surface is curved (exaggerated here). (2) After experimental alteration. Pyrrhotite has dissolved and alteration phases have precipitated. Typically, trenches develop along the edges of the masked areas (see text). (3) After removal of alteration layers and masks. Formerly masked pyrrhotite serves as reference level for the determination of etching depths (Δh). For MSA samples parabolic reference levels were used to account for surface curvature. (**e-g**) Visual appearance of MSA samples after experiments (arrow for reference). (**e**) After 651 hours in $FeCl_3$+HCl solution (0.01 mol/L Fe^{3+}, pH 1.80−1.92) at 30 °C. Yellowish surfaces contain abundant elemental sulfur and Fe oxyhydroxides, dark surfaces reacted little, except EUL {110}, which showed enhanced roughness and surface pitting (cf. Fig. 4-4e). (**f**) After 13 hours in H_2O_2+H_2SO_4 solution (0.1 mol/L H_2O_2, pH 2.05) at 35 °C. White and grayish crusts are elemental sulfur with little Fe oxyhydroxide, dark areas had been masked. {hk0} surfaces reacted stronger than (001) surfaces, the latter showing thinner sulfur crusts. (**g**) After 44 hours in H_2O_2+H_2SO_4 solution (0.1 mol/L H_2O_2, pH 2.88) at 35 °C. Strong precipitation of Fe oxyhydroxides occurred and masking deteriorated due to solution creeping underneath. (001) surfaces reacted strongest under these conditions.

4.3.2. Sample Preparation

The idiomorphically developed, 2-3 cm sized crystals of EUL and DAL were cut according to external morphology using a slow speed diamond wavering saw. Both

crystals were six-sided prisms with simple basal faces. Three mutually perpendicular sections were obtained parallel to planes of the hexagonal forms (001), {110}, and {100}. Precise identification of orientations was accomplished by use of electron back-scatter diffraction (EBSD). For this purpose we used a HKL Nordlys camera attached to a LEO 1530 FEG SEM (25 kV/ ~4 nA).

From the obtained slabs cylinders of 3 mm diameter and 2 to 5 mm length were obtained using a Gatan 601 ultrasonic disc cutter. The cylinders were then mounted into 3 mm holes of 25 mm diameter PMMA discs with each disc receiving a total of 6 pyrrhotite samples, comprising each of the three orientations for EUL and DAL (Fig. 4-2b). This multi sample assembly (MSA) assured identical surface finish of all individual samples after polishing. Alternatively, larger crystal slabs were mounted in 25 mm Buehler phenolic ring forms (single sample assembly, SSA). All mounting involved use of chemically resistant Struers EpoFix epoxy resin cured at room temperature.

Preparation for EBSD analysis and later exposure to reactive solutions was done using stepwise lapping and polishing: Rough wet sanding, 1200 SiC lapping, 4000 SiC or 3 μm diamond polishing, and final chemomechanical polishing using Struers OP-U colloidal silica suspension (2 to 5 hours). The chemomechanical polishing step serves to reduce surface damage obtained during previous polishing steps. Surface damage originates from mechanical stresses induced by polishing grit and is characterized by high dislocation densities extending down to several μm into the material (e.g., Nouruzi-Khorasani et al. 1990). This damage strongly deteriorates EBSD patterns, because the escape depth of coherently scattered electrons is limited to the uppermost 10 to 50 nm of the sample, which are practically amorphous. Such highly disordered layers likely change the physicochemical surface properties and therefore, we generally used OP-U polished samples in our reactivity experiments. Because colloidal silica tends to adhere to the sulfide surfaces and carbon coating had to be removed, final cleaning using 250 nm diamond suspension was occasionally needed and applied manually on soft polishing cloth for a few seconds. TEM cross section through such samples confirmed low dislocation densities not extending below the uppermost 200 nm, which is small compared to typical etching depths of several μm achieved in this study.

In order to derive absolute etching depths from 3D surface topometry we applied masking to some parts of the sulfide surfaces during most runs (Fig. 4-2). Clear, self-adhesive tape and Kapton tape cut sharply by a razor blade were found to be most suitable.

Diverse lacquers tested turned out to be insufficient due to dissolving in the medium or allowing fluid to leak under them due to capillary force. The exposed areas were approximately half the areas of core samples in MSAs and stripes of 1 to 2 mm width and 1 to 1.5 cm length in SSAs.

4.3.3. Experimental Setup and Conditions

Dissolution experiments on polished surfaces were conducted under a variety of chemical conditions (Tab. 4-2). Two runs involving ferric iron as oxidant commenced in a 0.01 mol/L ferric chloride ($FeCl_3$) solution with initial pH adjusted to 1.8-2.0 using hydrochloric acid. The duration of each run was approx. 650 hours (~27 days) during which the temperature was held constant at 30 or 35 °C. The reaction vessel for these experiments was a water jacketed borosilicate glass reactor with a volume of 150 mL. The sample mount was held in place by a Teflon spacer and the solution was stirred magnetically. Temperature was kept constant (±1 °C) by a Haake Fisons DC1 thermostatic circulator and monitored by a fluoropolymer coated NTC temperature probe attached to a WTW pMX 3000 pH/ion meter. The oxidation reduction potential (ORP) was recorded on the same unit using a Mettler-Toledo InLab Redox-L Ag/AgCl electrode. The pH in the reactor was measured intermittently with a Mettler-Toledo InLab Routine Pro-L electrode which was calibrated against pH 2 and pH 4 reference buffers. Generally, the pale yellow Fe^{3+} solution turned orange during the first 20 to 40 hours of heating and precipitated colloidal akaganeite, β-FeO(OH,Cl), was confirmed by TEM. The precipitation was accompanied by a decrease in measured ORP which dropped from initially 910 mV (standard hydrogen electrode, SHE) to around 890 mV (SHE). Therefore, the sulfide sample was not added to the solution until it had stabilized. The precipitation of Fe oxihydroxide limited the accessible pH range to values below 2, as at larger pH strong precipitation would occur. Due to the long duration of almost one month no masking was applied, because prior test experiments showed that solution inevitably crept under the masks if exposed for longer periods of time.

As an alternative oxidant we used a solution of 0.1 mol/L hydrogen peroxide (H_2O_2) acidified by sulfuric acid (H_2SO_4). This offered the possibility to vary pH in a wider range (1.8 to 2.9) as permitted by Fe^{3+}, and allowed rapid reaction rates and therefore many runs (including repetitions) and stable masking. Also, this approach kept the chemical system relatively simple with a minimum of precipitating phases. Because reactions were rapid,

resulting in etching depths of several µm within 3 to 14 hours at 35 °C, the experiments were conducted without in situ monitoring in 250 mL Erlenmeyer flasks filled with 200 mL solution and shaken at 180 rpm in temperature controlled microbiological incubators (New Brunswick Scientific Innova 42 and Excella E24). pH was checked before and after each run and generally did not change significantly (< 0.05 units). In addition to experiments using 0.1 mol/L H_2O_2 and sulfuric acid only, some runs were conducted with the addition of 0.01 to 0.1 mol/L $FeSO_4$ or 0.7 mol/L 2-propanol in order to test for possible deviations in the reaction behavior (see section 4.4.2.2.). For the same purpose one SSA experiment was conducted using a pure 0.05 mol/L solution of $Fe_2(SO_4)_3$ (i.e., 0.1 mol/L Fe^{3+}) at pH 1.80-1.85 with no addition of H_2O_2 or H_2SO_4 (higher pH not attainable).

4.3.4. Analytical Methods

After experimental runs samples were washed with demineralized water and dried. Reaction products on the pyrrhotite surfaces were checked by Raman spectroscopy using a Jobin Yvon Labram micro-spectrometer equipped with a 632.8 nm He-Ne laser. Laser power was adjusted to a level which avoided visible burn marks on the surfaces.

Selected samples were imaged without conductive coating in a FEI Quanta 3D FEG SEM operated in low vacuum mode (0.6 to 1.2 mbar) at 5 keV electron energy. Samples were then leached with cyclohexane in order to remove possibly present elemental sulfur and subsequently carbon coated for further imaging using the FEI Quanta 3D and a LEO 1530 FEG SEM. The removal of sulfur was necessary due to its volatility in high vacuum and its obstruction of the reacted sulfide surface.

For TEM sample preparation we applied the FIB method provided by the FEI Quanta 3D FEG dual beam system (Ga^+ ions). Because the preservation of the uppermost sample surface is crucial for a meaningful TEM study, the sample was either coated with a very thick carbon coating (~50 nm) or locally protected by electron beam assisted platinum deposition (5 keV electron energy) before the ion beam was utilized to apply the usual protective platinum strap. For excavation of trenches around the targeted TEM foil sites ion beam currents from 50 nA down to 3 nA at 30 keV ion energy have been used, decreasing as the prospective sample site was approached. Cleaning before lift-out was applied using a 30 keV/1 nA beam. The remaining 0.5 to 1 µm thick lamellae were then cut free, extracted with an Omniprobe tungsten needle micromanipulator, and attached to a

post-type copper TEM grid. Final thinning then proceeded using beam currents of typically 300 pA, 100 pA, and 50 (or 30) pA at 30 keV energy. In order to minimize Ga implantation and ion beam induced structural damage the last polishing step usually involved a beam energy of 5 keV and a current of 80 pA or lower. At these conditions the stopping depth of Ga^+ ions lies in the order of a few nm at grazing beam incidence relative to the foil surface (e.g., Rubanov and Munroe 2004; Miller and Russell 2007). Heating effects during FIB preparation of Fe sulfides are mostly negligible (Wozniakiewicz et al. 2011).

For imaging and selected area electron diffraction (SAED) we used a Philips CM20 FEG TEM operated at 200 kV and equipped with a Thermo Noran Ge EDS detector. EDS measurements and X-ray mappings were acquired in scanning TEM (STEM) mode.

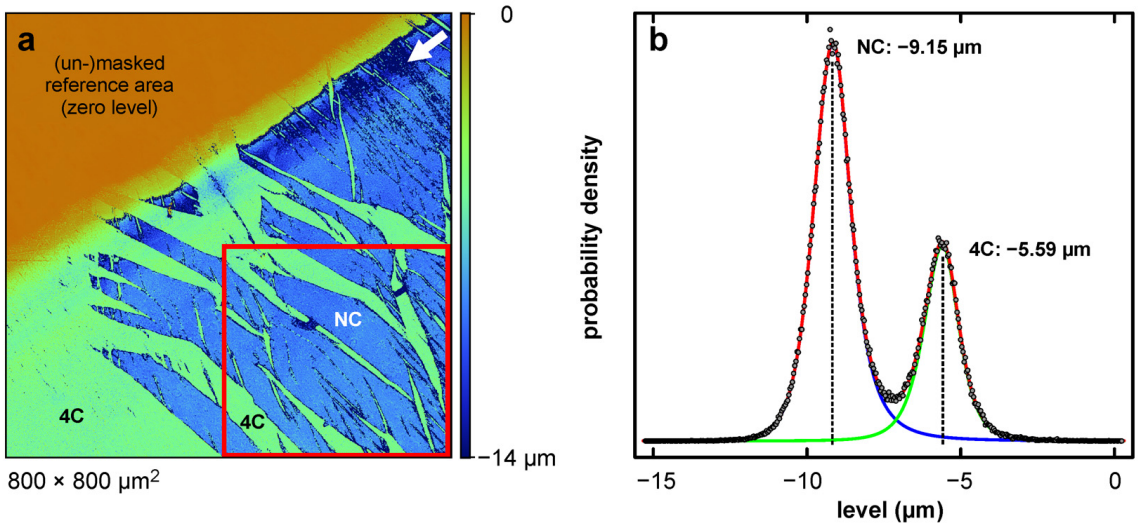

FIGURE 4-3. Quantitative 3D surface topometry. (**a**) After13 hours at pH 2.05 in H_2O_2+H_2SO_4 and subsequent cleaning (see text). Lamellae and regions of 4C-pyrrhotite clearly stand out against the NC matrix. The arrow marks a modestly developed trench along the former mask edge. (**b**) Exemplary height distribution obtained from the square region marked in (a). The level is given relative to the masked/unaltered reference plane.

3D topometry of masked samples was obtained with a Nanofocus µsurf custom confocal microscope. The sample surface is thereby illuminated by a green light emitting diode while a piezo-driven microscope objective scans through a series of focal distances. The insertion of a multi-pinhole (Nipkow) disc in the optical path effectively limits the intensity received at the CCD detector to a very narrow focal depth range, allowing the 3D reconstruction of the sample's surface topography from the obtained image stack (Fig. 4-3a). The achievable height resolution can be as good as a few tens of nm on low roughness surfaces. For our work we used 20× (NA 0.45, WD 3.1 mm) and 100× (NA 0.90, WD 1.0

mm) objectives, yielding fields of view of 800×800 μm^2 and 160×160 μm^2, respectively. In some cases, several adjacent height images were stitched in order to enlarge the covered area. The mean height difference Δh between the original surface preserved under the mask and the altered sulfide surfaces yields the amount of reacted material and the linear reaction rate r in terms of reacted moles of Fe:

$$r = \frac{\Delta h}{t} \frac{\rho_{\mathrm{Po}}}{M_{\mathrm{Po}}} (1 - \mathrm{x})$$

t is the reaction time, ρ_{Po} is the density of pyrrhotite, and M_{Po} is the molar mass (in terms of the $Fe_{1-x}S$ formula). In this relation the rate is fully represented by the mean height difference and independent of the exposed (geometric) area (cf. Asta et al. 2008). Meaningful measurements of Δh require that any coatings on the reacted surfaces must be removed. This was done using cyclohexane for removal of sulfur and Waller's solution (0.25 mol/L trisodium citrate, 0.1 mol/L sodium hydrogen carbonate, 0.1 mol/L sodium dithionite in water) for removal of Fe oxyhydroxides when present. Waller's solution has close to neutral pH (approx. 7.45) and is strongly reducing (approx. −460 mV SHE), converting Fe^{3+} into Fe^{2+} which is complexed by citrate ligands. The sample was immersed into the solution for a few minutes under ultrasonic agitation at room temperature. Inspection of the original, polished pyrrhotite surface indicated no detectable etching effect on the sulfide during the short exposure.

The obtained height images were processed using the Gwyddion analysis software (Nečas and Klapetek 2012). Processing involved height calibration by leveling the original surface beneath the removed mask to zero height and producing depth histograms of the reacted areas. In mixed 4C/NC samples the obtained depth distributions were typically bimodal due to height differences between the 4C and NC portions (Fig. 4-3b). The distributions were then processed using the Fityk peak fitting program (Wojdyr 2010) in order to determine averaged depths and approximate spreads of the individual depth components contribution to the surface topography. For fitting we used Pearson type VII and lognormal functions (usually not more than two per fit) which generally provided the best approximation of the depth distributions. Fits were optimized in order to obtain good fitting in the areas of peak maxima, while the low frequency bases of the distributions were considered to be of secondary importance due to the possible contribution of surface

irregularities like cracks, inclusions, scratches or dust particles, leading to locally anomalous etching behavior.

During the quantitative topometric evaluation of experiments two difficulties became apparent. (i) In almost all experimental runs relatively deeply etched trenches developed along the boundary between the masked and exposed sulfide surfaces. These trenches developed beneath the outermost portion of the masking tape, where solution was able to creep under the protective cover. In consequence, the direct measurement of the step height along the masking boundary was usually difficult. However, in case of the SSA the masked surface was plane enough for easy and reliable extrapolation of the zero level onto the reacted area, such that no topographic gradient was superimposed. (ii) In case of the MSA, the situation was typically more difficult, because the polished 3 mm samples did not have perfectly plane surfaces but were rather rounded due to their higher polishing resistance of pyrrhotite compared to the surrounding PMMA. The resulting errors in definition of the zero level were minimized by applying a parabolic flattening to the height images, based on the masked regions (Fig. 4-2d). The resulting systematic errors are estimated to be less than 1 μm based on the typically observed polishing relief before treatment. The uncertainty of the dissolution rates is typically in the range of 5×10^{-7} mol Fe/m^{2}s or less for etching depths > 1 μm and stems mainly from variations of measured high differences across the reacted surfaces. In case of etching depths < 1 μm relative uncertainties become larger, due to larger contribution of errors related to the polishing relief before reaction.

4.4. Results

4.4.1. General Observations and Identification of Alteration Phases

4.4.1.1. Experiments with $FeCl_3$ Solution−Surface Mineralogy

After experimental treatment, exposed pyrrhotite surfaces showed coatings of variable thickness and composition. $FeCl_3$ experiments at pH 1.8-2.0 resulted in either thick (4-5 μm), yellowish crusts or very thin (< 200 nm), iridescent coatings, depending on the sample and crystallographic orientation of the surface (Fig. 4-2e). Raman spectroscopy attests the presence of elemental sulfur in the thick crusts and powder XRD of scraped material indicates it to be orthorhombic α-sulfur, indicating an incomplete sulfide oxidation according to reaction 4-4. Low vacuum SEM images show few euhedral sulfur crystal (1-10 μm) and dominantly colloform or slightly fan-shaped aggregates (Fig. 4-

4a,b). Underlying pyrrhotite showed a fibrous or mesh-like texture (Fig. 4-4c). SEM in situ imaging and TEM imaging of scraped and FIB sectioned crusts (Fig. 4-4d) shows that this material forms a sponge-like network containing dispersed or clumped rod-like Fe oxyhydroxide crystals and abundant voids, which likely originated from evaporated sulfur, which is not stable in high vacuum (Fig. 4-5a,b). The small (< 80 nm) rod shaped crystals have been identified as akaganeite by TEM-SAED (Fig. 4-5d). In addition, FIB-sections of the crusts show broad diffraction rings that are consistent with poorly crystalline 2-line (2L-) ferrihydrite (Fig. 4-5d,e).

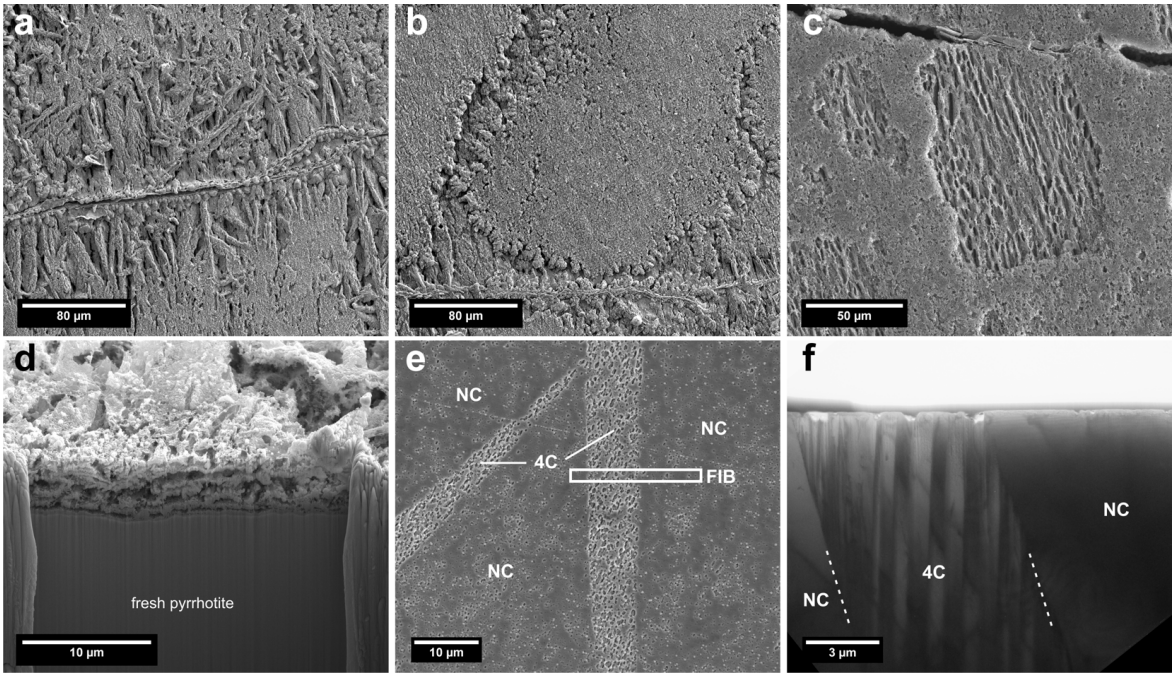

FIGURE 4-4. SEM-SE images of pyrrhotite altered in $FeCl_3$+HCl solution for ~650 hours. (**a**) Elemental sulfur crystals and fan-shaped aggregates (low vacuum SEM). (**b**) Colloform aggregates of elemental sulfur (low vacuum SEM). (**c**) Fibrous, mesh-like texture of pyrrhotite beneath the alteration layer. (**d**) FIB cross section through the alteration layer showing a thickness of 4.5 to 5 µm. (**e**) EUL {110} surface, on which no elemental sulfur formed. 4C-pyrrhotite lamellae were attacked stronger and show more intense pitting. The box marks the location of an extracted FIB foil for TEM study. (**f**) BF-TEM image of FIB section marked in (e). 4C-pyrrhotite is strongly twinned and shows larger and deeper etch pits than adjacent NC-pyrrhotite.

TEM-EDX mappings of the sulfide interface region (Fig. 4-5f) reveal strong enrichment of oxygen directly (< 100 nm) at the interface. This oxygen is bound to a dense layer of Fe oxide or oxyhydroxide attached to the sulfide and sulfur shows an abrupt decrease at the sulfide-oxide interface. We found no evidence for sulfur enrichment at the interface on scales of several tens of nm. Filter residues from the reaction solution contain akaganeite crystals identical to those found in the crusts, suggesting that akaganeite precipitated from the solution and was trapped in the forming alteration crusts. 2L-

ferrihydrite and α-sulfur likely formed in situ during oxidative dissolution of the pyrrhotite.

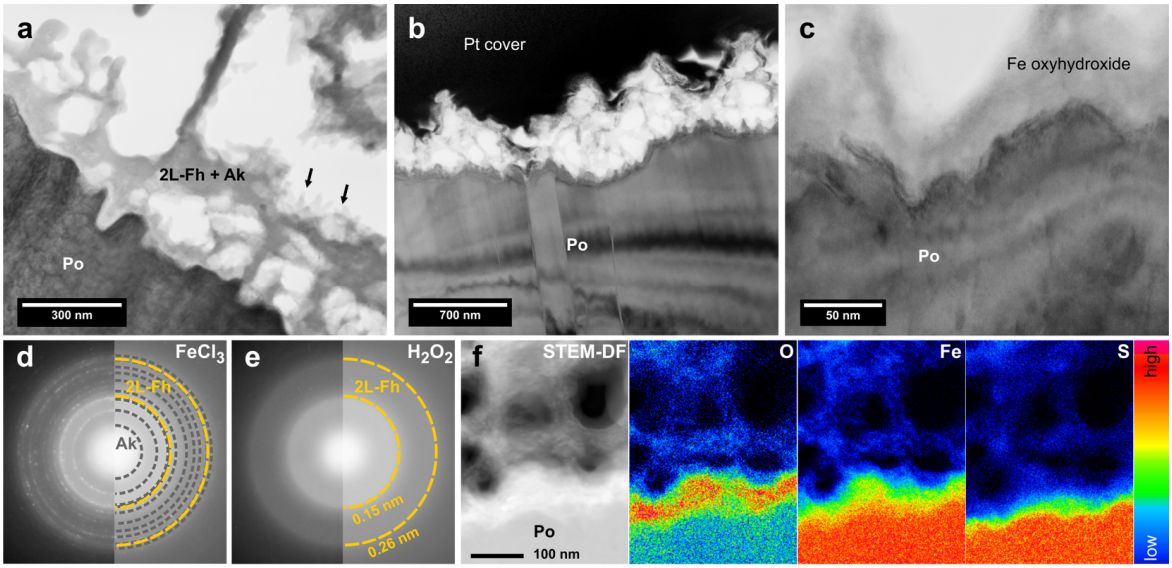

FIGURE 4-5. Analytical TEM results of alteration phases on pyrrhotite reacted in $FeCl_3$+HCl solution for ~650 hours at 30 or 35 °C. For the context see Fig. 4-4c and d, which shows the crusts before and during FIB preparation. (**a**) BF-TEM. Sponge-like alteration layer composed of 2-line ferrihydrite (2L-Fh) and akaganeite (Ak, rod-like crystals, arrows) on corroded pyrrhotite. Voids were likely filled by elemental sulfur, which evaporated in vacuum. (**b**) BF-TEM. Alteration layer on corroded 4C-pyrrhotite (twinned). A Pt layer has been deposited by FIB to protect the oxyhydroxide crust from the ion beam. (**c**) BF-TEM. Detail of (b) showing the rough pyrrhotite-oxyhydroxide interface. (**d**) TEM-SAED pattern obtained from the oxyhydroxide crust in (a). Spotty diffraction rings of akaganeite and diffuse diffraction from 2-line ferrihydrite are present. (**e**) TEM-SAED pattern from the alteration layer of a H_2O_2-H_2SO_4 experiment at pH 2.90 for comparison. Akaganeite is absent here and the two broad diffraction rings of 2-line ferrihydrite dominate. (**f**) Scanning TEM dark-field image (STEM-DF) and corresponding EDX X-ray elemental distribution maps of the sulfide-oxyhydroxide interface depicted in (b) and (c). Oxygen is clearly enriched at the reaction interface and sulfur shows a sharp drop without any evidence for enrichment.

4.4.1.2. Experiments with $FeCl_3$ Solution−Pyrrhotite Reactivity and Experimental Reproducibility

In two replicate experiments (using two different MSA: H03 and H05) we found evidence that the 4C-dominant DAL sample reacted stronger than EUL. The {hk0} faces of DAL reacted strongest and produced thick alteration crusts and elemental sulfur in both experiments. The (001) faces reacted least, showing only very thin Fe oxyhydroxide coatings and no sulfur. In case of EUL, more variation was observed. Exposed {110} faces showed strongest reactivity, but produced elemental sulfur only in one replicate run (H03_02), while in the other run (H05_01) strong and preferred pitting of the 4C lamellae was observed (Fig. 4-4e,f). {100} faces reacted weakly in both runs and produced no

sulfur. (001) faces reacted weakly as well and produced no sulfur, analogous to the DAL sample.

The failure to reproduce the EUL {110} results most likely originated from heterogeneities in the ratio 4C-/NC-pyrrhotite, which can be locally dominated by 4C-pyrrhotite, causing reactivity similar to the 4C-dominant DAL sample. The EUL samples of the H05 MSA were confirmed to contain fully mixed 4C-/NC-pyrrhotite and subsequent experiments involving H_2O_2 were conducted using this sample assembly. Determination of absolute rates and reactivity differences between 4C- and NC-pyrrhotite in the $FeCl_3$-runs faced several difficulties: (i) Masking of the sulfide surfaces was generally not stable enough for the long run duration of one month and solution crept under the supposedly protective tape, causing locally enhanced dissolution along the mask edges. The cause of this behavior is probably the local formation or accumulation of acid or oxidant species due to poor exchange with the bulk solution. This apparently leads to increased dissolution speeds in the affected regions. (ii) After one month of reaction, intentionally exposed pyrrhotite surfaces had either reacted very strongly and were too rough to resolve 4C and NC areas or reacted very slowly with differences between 4C and NC being too small for reliable evaluation (i.e., < 100 nm). Only in one instance, the non-sulfur-producing EUL {110} surface of H05, showed much stronger pitting of the 4C lamellae compared to the NC matrix, as noted above.

4.4.1.3. Experiments with H_2O_2 Solution−Surface Mineralogy

Experiments involving H_2O_2 as oxidant were quicker and produced soundly evaluable results (Fig. 4-2f,g). Similarly to the $FeCl_3$ experiments, they showed µm-thick alteration crusts composed of elemental sulfur, but produced little Fe oxyhydroxides at comparable pH. Also here, the formation of elemental sulfur indicates incomplete oxidation of the sulfide (reaction 4-7). A change in phase composition was observed to take place at pH 2.65-2.70, above which elemental sulfur did not form anymore and precipitation of Fe oxyhydroxide strongly increased (Fig. 4-2g). This change corresponds to an overall change in reaction behavior of pyrrhotite as detailed below. SAED pattern and TEM-EDX spectra show that the Fe oxyhydroxide forming at higher pH is similar to 2L-ferrihydrite, but contains appreciable amounts of sulfate with a molar SO_4^{2-}/Fe^{3+} ratio of approx. 0.22. This composition is rather close to a sulfate-rich schwertmannite (Bigham et al. 1994). Elemental sulfur is absent in these crusts and a tendency to stronger reactivity on (001)

faces was observed qualitatively based on precipitation extent. At lower pH elemental sulfur formed abundantly and was easily detected by Raman spectroscopy. Strong precipitation generally occurred on {hk0} surfaces, while (001) surfaces formed less sulfur. Generally, dissolution in the H_2O_2 medium proceeded rather uniformly across the various exposed pyrrhotite surfaces, leaving little pitting and surface irregularities. However, irregularities of the etched surfaces became more pronounced at higher pH, likely owing to lower reaction rates and stronger susceptibility to enhancing local surface anomalies. One particular example are etch pits on (001) faces of DAL produced by etching at pH 2.90. These pits predominantly formed around extremely thin (< 1 μm) fibers, being most likely primary inclusions of an asbestiform amphibole with tremolite-like composition (based on qualitative EDX analysis). Particularly under high pH conditions, trenches developed along the mask edge as described above.

4.4.2. Phase-specific Quantification of Dissolution Rates from H_2O_2 Experiments

4.4.2.1. Reactivity of NC-Pyrrhotite vs. 4C-Pyrrhotite

Quantification of oxidative dissolution rates was only applied to H_2O_2 experiments due to the above mentioned limited reproducibility of results in FeCl3 experiments. Based on 3D topometry and height distributions derived from surface topographies (Fig. 4-3a,b), we demonstrate the effect of pH on the reaction rates and differential behaviors of 4C- and NC-pyrrhotite observed on a EUL {110} slab set in a SSA. Reactivity differences Δr are reported as % relative to 4C, i.e., Δr (%) = $100(r_{NC}\text{-}r_{4C})/r_{4C}$, where r are the absolute reaction rates (Tab. 4-2). The reported pH values are at 35 °C, where they are about 0.05 units higher as measured at 20 °C (where measurements were easier to conduct).

The pH dependence of reaction rates follows similar paths for both 4C- and NC-pyrrhotites (Fig. 4-7a): Below pH 2.3 reaction rates expressed as Fe equivalents of oxidized pyrrhotite are about 4×10^{-6} to 1×10^{-5} mol $m^{-2}s^{-1}$ (3 to 19 h reaction time, assuming compositions $Fe_{0.875}S$ for 4C and $Fe_{0.900}S$ for NC). Between pH ~2.3 and 2.70 reaction rates rise up to around 3×10^{-5} mol $m^{-2}s^{-1}$ at pH 2.5 and then decline toward a sharp drop at pH 2.70. Above pH 2.70 reaction rates are about 1×10^{-7} to 6×10^{-7} mol $m^{-2}s^{-1}$ (~44 h reaction time). Dissolution rates determined in MSA experiments on EUL {hk0} faces agree very well with the results obtained from the SSA runs (Tab. 4-2).

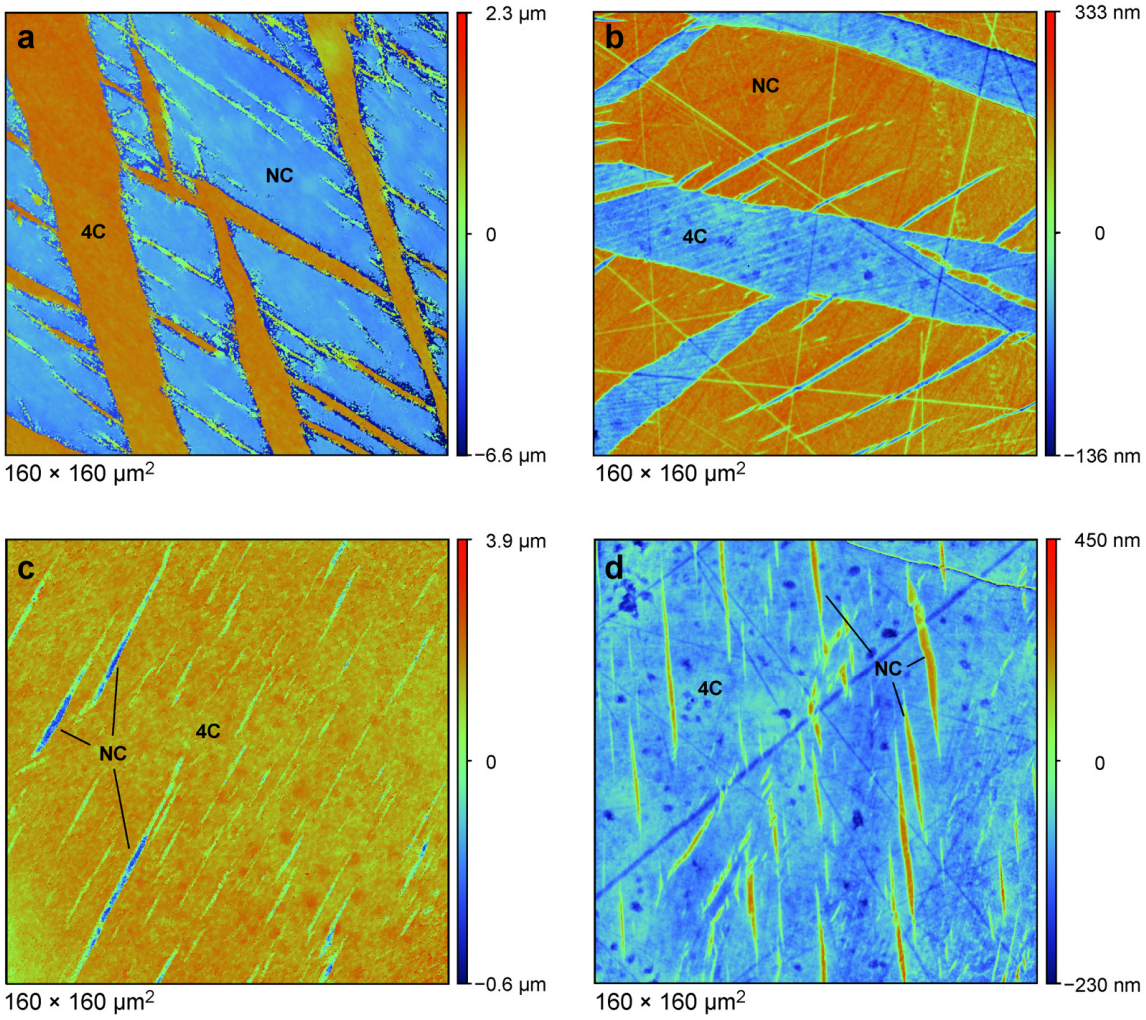

FIGURE 4-6. 3D topometry of pyrrhotite surfaces reacted in H_2O_2+H_2SO_4 solution at 35 °C. (**a**) Detail of EUL {110} surface reacted for 13 hours at pH 2.05. The NC matrix dissolved faster than the 4C lamellae. (**b**) EUL {110} surface reacted for 44.3 hours at pH 2.90. 4C lamellae dissolved faster than the NC matrix and the total relief height is about one order of magnitude smaller compared to (a). Faint, parallel striations on the 4C surfaces are twin domains that reacted at slightly different rates. Non-parallel striations crossing the entire field of view are scratches from polishing. (**c**) DAL {110} surface reacted for 13 hours at pH 2.05. NC lamellae dissolved faster than the 4C matrix. (**d**) DAL {110} surface reacted for 44.3 h at pH 2.92. The 4C matrix dissolved faster than the NC lamellae.

Under all conditions studied, differences between 4C- and NC-pyrrhotite surfaces of the sample could be resolved (Fig. 4-7b). Below pH ~2.3 NC-pyrrhotite reacts about 50 to 80 % faster than neighboring 4C-pyrrhotite (Fig. 4-6a). Increasing pH, in the area of the reactivity maximum, leads to a decrease in the reactivity difference up to the switch point at pH 2.70, where rates are about equal. Beyond this point 4C-pyrrhotite shows approximately 50 % higher dissolution rates compared to NC-pyrrhotite. The reproducibility of dissolution rates particularly below pH 2.70 is very good and also

experiments done after complete re-polishing of the sample consistently fit into the observed, systematic variations of reactivity.

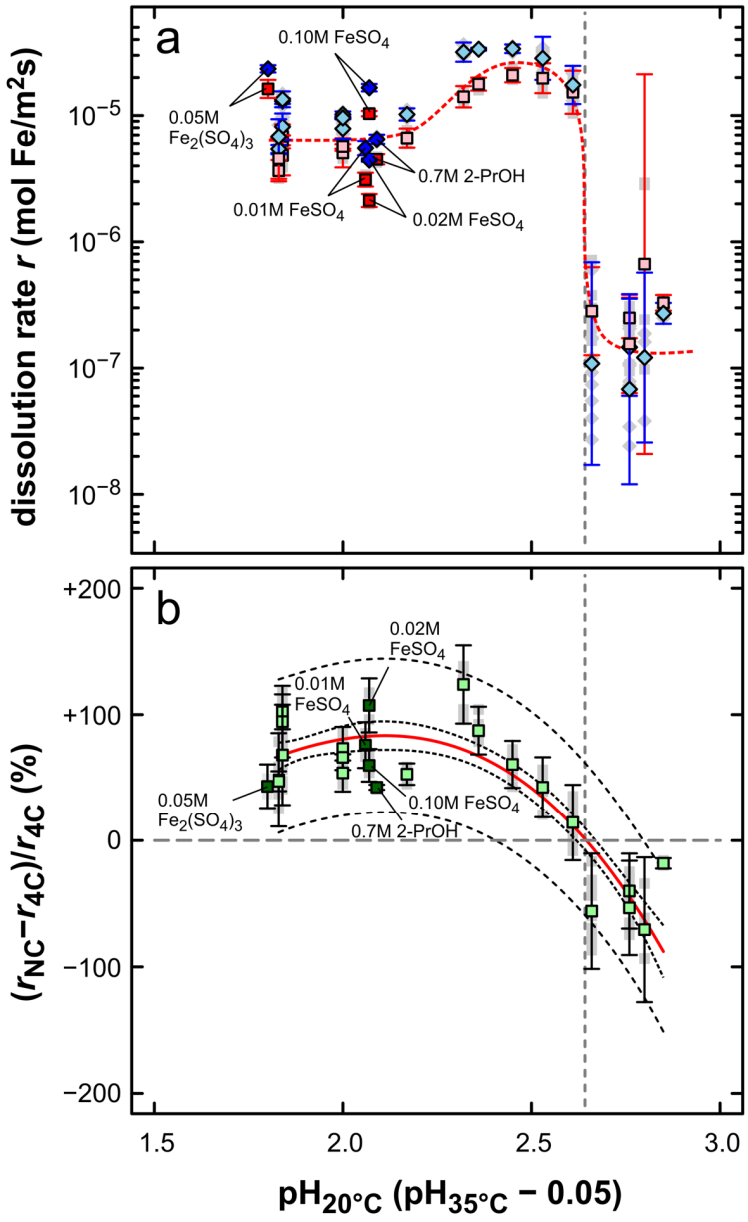

FIGURE 4-7. Quantitative 3D topometry of EUL {110} SSA surfaces reacted in H_2O_2+H_2SO_4 (0.1 mol/L H_2O_2) solution at 35 °C and various pH. (**a**) Individual reaction rates of 4C- (squares) and NC-pyrrhotite (diamonds). Reaction rates increase upon approaching pH 2.70 but then suddenly drop by a factor of 100. Error bars are 2σ based on multiple height distribution obtained on the reacted surfaces (individual measurements indicated by light gray symbols). The dashed curve is guidance for the eye. Variation of solution chemistry (dark symbols) at did not result in significant variations in reaction rates (see text). (**b**) Relative reaction rates of NC-pyrrhotite expressed relative to 4C-pyrrhotite. Below pH 2.70 NC-pyrrhotite reacts about 50 to 80 % faster than 4C-pyrrhotite, above pH 2.70 NC-pyrrhotite reacts approximately 50 % slower. The central solid curve is a polynomial fit to the data points (not based on a physical model), the inner dashed curves are the 95 % (~2σ) confidence interval of the fit and the outer dashed curves are the 95 % prediction interval. Error bars are 2σ. Also here, variations in chemistry did not influence the results.

TABLE 4-2. Topometry results of oxidative dissolution experiments at 35° C in H_2O_2 +H_2SO_4.

Run	Surface	Type	*t* (h)	pH	Δ*h* NC (µm)	Δ*h* 4C (µm)	$\log_{10} r_{NC}$ (mol Fe/m^{2}s)	$\log_{10} r_{4C}$ (mol Fe/m^{2}s)	$(r_{NC}-r_{4C})/r_{4C}$ (%)
EUL1inL_2	EUL {110}	SSA	13.5	1.89	-12.58(30)	-6.22(27)	-4.89(1)	-5.20(2)	104(8)
EUL1inL_6	EUL {110}	SSA	3.0	1.89	-2.89(21)	-1.49(16)	-4.87(3)	-5.16(5)	97(14)
EUL1inL_8	EUL {110}	SSA	6.9	1.89	-4.05(50)	-2.45(47)	-5.09(5)	-5.31(8)	69(20)
EUL1inL_9	EUL {110}	SSA	7.0	1.88	-2.72(10)	-1.86(18)	-5.26(2)	-5.44(4)	49(19)
EUL1inL_10	EUL {110}	SSA	7.0	1.88	-3.44(56)	-2.34(44)	-5.17(7)	-5.34(8)	49(4)
EUL1inL_12	EUL {110}	SSA	19.0	2.81	-0.22(8)	-0.35(6)	-6.83(19)	-6.60(8)	-39(15)
EUL1inL_13	EUL {110}	SSA	15.5	2.37	-35.2(3.2)	-15.8(1.5)	-4.50(4)	-4.85(4)	126(16)
EUL1inL_14	EUL {110}	SSA	13.0	2.58	-26.7(4.9)	-18.6(2.3)	-4.55(8)	-4.70(6)	44(12)
EUL1inL_15	EUL {110}	SSA	13.0	2.66	-16.5(2.9)	-14.6(2.6)	-4.76(8)	-4.82(9)	15(15)
EUL1inL_16	EUL {110}	SSA	13.1	2.81	-0.08(7)	-0.16(7)	-7.16(38)	-6.81(19)	-53(19)
EUL1inL_17	EUL {110}	SSA	13.1	2.71	-0.15(16)	-0.29(15)	-6.96(40)	-6.55(17)	-56(23)
EUL1inL_18	EUL {110}	SSA	13.0	2.50	-31.3(1.2)	-19.6(1.3)	-4.47(2)	-4.68(3)	62(9)
EUL1inL_21	EUL {110}	SSA	16.7	2.85	-0.17(9)	-1.8(1.9)	-6.91(34)	-6.17(75)	-70(29)
EUL1inL_22	EUL {110}	SSA	13.0	2.05	-9.49(27)	-5.49(29)	-4.99(1)	-5.23(2)	75(8)
EUL1inL_23	EUL {110}	SSA	13.0	2.41	-31.03(44)	-16.6(1.0)	-4.47(1)	-4.75(3)	89(10)
EUL1inL_24	EUL {110}	SSA	13.0	2.22	-9.49(55)	-6.22(55)	-4.99(2)	-5.18(4)	54(5)
EUL1inL_26*	EUL {110}	SSA	14.7	2.14	-6.80(28)	-4.77(22)	-5.19(2)	-5.35(2)	44(1)
EUL1inL_27[#]	EUL {110}	SSA	15.6	2.12	-4.94(8)	-2.39(14)	-5.35(1)	-5.67(3)	109(10)
EUL1inL_28[#]	EUL {110}	SSA	13.6	2.11	-5.37(33)	-3.05(19)	-5.26(3)	-5.51(3)	78(10)
EUL1inL_29[#]	EUL {110}	SSA	14.7	2.12	-17.46(55)	-10.99(29)	-4.78(1)	-4.98(1)	60(7)
EUL1inL_30[§]	EUL {110}	SSA	14.5	1.85	-24.44(76)	-17.1(1.5)	-4.63(1)	-4.79(4)	44(8)
H05_04	EUL {110}	MSA	44.3	2.90	-0.86(8)	-1.06(8)	-6.56(4)	-6.48(3)	-18(2)
H05_05	EUL {100}	MSA	13.0	2.05	-7.35(70)	-4.80(65)	-5.10(4)	-5.29(6)	55(8)
H05_05	EUL {110}	MSA	13.0	2.05	-8.91(11)	-5.35(11)	-5.02(1)	-5.24(1)	68(2)

Run	Surface	Type	*t* (h)	pH	Δ*h* bulk (µm)	$\log_{10} r_{bulk}$ (mol Fe/m^{2}s)
H05_04	DAL (001)	MSA	44.3	2.90	-9.70(35)	-5.52(2)
H05_04	DAL {100}	MSA	44.3	2.90	-1.25(12)	-6.41(4)
H05_04	DAL {110}	MSA	44.3	2.90	-23.90(57)	-5.12(1)
H05_04	EUL (001)	MSA	44.3	2.90	-11.58(49)	-5.44(2)
H05_04	EUL {100}	MSA	44.3	2.90	-1.57(26)	-6.31(8)
H05_04	EUL {110}	MSA	44.3	2.90	-0.99(5)	-6.51(2)
H05_05	DAL (001)	MSA	13.0	2.05	-1.88(12)	-5.70(3)
H05_05	DAL {100}	MSA	13.0	2.05	-4.63(10)	-5.30(1)
H05_05	DAL {110}	MSA	13.0	2.05	-4.14(11)	-5.35(1)
H05_05	EUL (001)	MSA	13.0	2.05	-1.44(13)	-5.82(4)
H05_05	EUL {100}	MSA	13.0	2.05	-6.07(30)	-5.19(2)
H05_05	EUL {110}	MSA	13.0	2.05	-7.13(5)	-5.12(1)
H05_06	DAL (001)	MSA	44.0	2.88	-12.7(1.2)	-5.40(4)
H05_06	DAL {100}	MSA	44.0	2.88	-0.56(14)	-6.83(13)
H05_06	DAL {110}	MSA	44.0	2.88	-0.63(5)	-6.70(4)
H05_06	EUL (001)	MSA	44.0	2.88	-9.32(57)	-5.53(3)
H05_06	EUL {100}	MSA	44.0	2.88	-0.39(12)	-7.02(16)
H05_06	EUL {110}	MSA	44.0	2.88	-1.68(27)	-6.28(7)
H05_07	DAL (001)	MSA	44.2	2.92	-11.5(1.3)	-5.45(5)
H05_07	DAL {100}	MSA	44.2	2.92	-27.2(1.6)	-5.07(3)
H05_07	DAL {110}	MSA	44.2	2.92	-0.82(7)	-6.59(4)
H05_07	EUL {110}	MSA	44.2	2.92	-0.32(11)	-7.05(14)

see notes on next page

Note (to Tab. 4-2): All experiments, except EUL1inL_30, were done with 0.1 mol/L H_2O_2. *Addition of 0.7 mol/L 2-propanol. #Addition of $FeSO_4$: 0.02 mol/L (No. 27), 0.01 mol/L (No. 28), 0.1 mol/L (No. 29). §0.05 mol/L $Fe_2(SO_4)_3$ instead of H_2O_2+H_2SO_4. EUL1inL experiments 3, 4, 5, and 7 were done at 50 °C and are not considered here due to problems in pH determination. Experiment 11 was done at pH 3.81 for a short time and did no yield measurable results. Experiments 1, 19, 20, and 25 were tests and did not yield usable quantitative results.

At higher pH > 2.70, slow reaction, less permeable Fe oxyhydroxide crusts, and increased spatial heterogeneity of dissolution impact the precision, but the higher reactivity of 4C-pyrrhotite on the EUL {110} surface is clearly resolvable in almost all cases (Fig. 4-6b). The NC lamellae in DAL samples were usually too small to allow reliable (absolute) quantification of reactivity differences. However, topometry showed that also in case of DAL the NC phases reacted analogously as observed in the EUL sample (Fig. 4-6c,d).

4.4.2.2. Effect of Additional Solutes

Compared to pure H_2O_2+H_2SO_4 experiments, the addition of 0.7 mol/L 2-propanol as potential scavenger of oxygen radical species (Hug and Leupin 2003) did not result in any significant change in reaction behavior, the addition of Fe^{2+} as promoter of radical formation (see discussion) did strongly reduce the precipitation of elemental sulfur, which was only detectable as weak signal by Raman spectroscopy, but did not significantly impact the dissolution rates (reaction surfaces were black as opposed to whitish in $FeSO_4$-free experiments where sulfur precipitation was strong). The use of a pure 0.05 mol/L iron(III) sulfate solution resulted in dissolution rates similar to the H_2O_2/H_2SO_4 mixtures at similar pH, with the exception that little elemental sulfur was formed and a barely removable black crust precipitated on the etched surface. Due to limited material an identification of the crust material was not possible.

4.4.3. Orientation Dependence of Pyrrhotite Dissolution

4.4.3.1. Reaction at pH 2.05

Using the MSA of EUL and DAL we evaluated reactivity variations as function of surface orientation (Fig. 4-8a, Tab. 4-2). In order to obtain bulk reaction rates for the heterogeneous EUL sample, we assumed a 50 % contribution of both the 4C- and NC-phase, which approximately corresponds to the modal abundances. At pH 2.05 the prismatic {hk0} surfaces {100} and {110} of DAL and EUL show approximately 150 to

300 % higher reaction rates compared to the basal (001) surfaces, which dissolve at rates of about 1.5 to 2.0×10^{-6} mol $m^{-2}s^{-1}$ with no resolvable difference between DAL and EUL samples. EUL {hk0} surfaces show an averaged bulk dissolution rate of approximately $(7.0\pm0.4)\times10^{-6}$ mol $m^{-2}s^{-1}$, consistent with results obtained from the EUL {110} SSA experiments. The mixed 4C+NC EUL {hk0}surfaces react about 50 % faster (Fig. 4-8a) compared to the 4C-dominant DAL {hk0} surfaces, which show an average of $(4.7\pm0.2)\times10^{-6}$ mol $m^{-2}s^{-1}$. This is also consistent with the SSA results of higher reactivity of NC-pyrrhotite under these conditions.

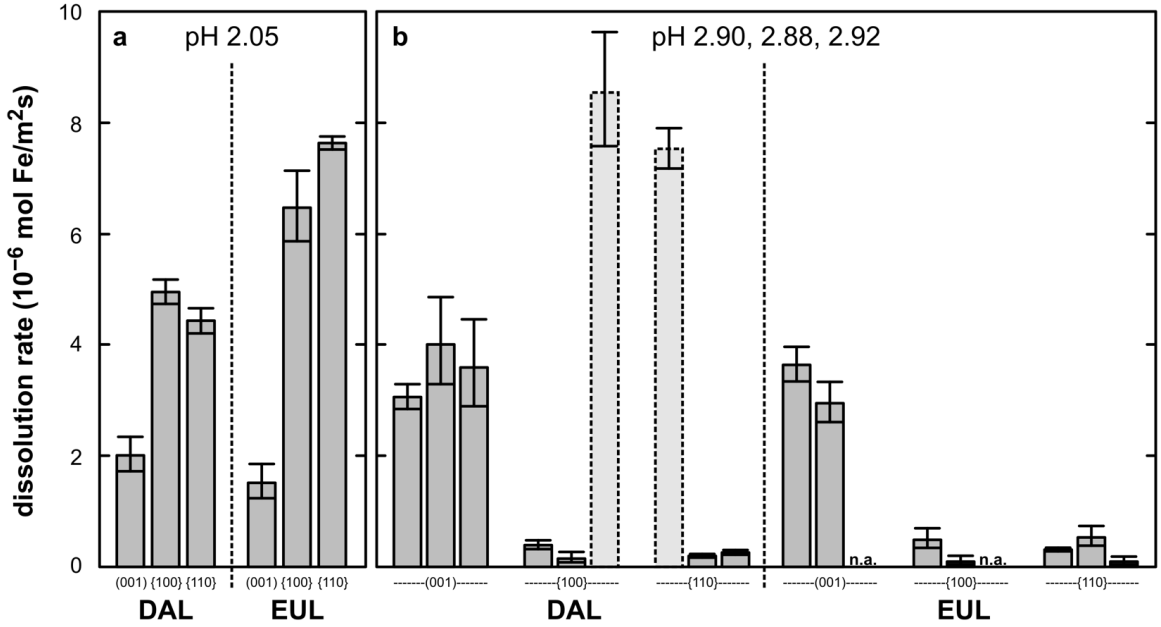

FIGURE 4-8. Quantitative evaluation of the effect of crystal aniostropy (MSA experiments) on dissolution rates in H_2O_2+H_2SO_4 (0.1 mol/L H_2O_2) solution at 35 °C. Error bars are 2σ. (**a**) Reaction at pH < 2.70. {hk0} surfaces reacted significantly faster than (001) faces. Despite only one experiment, we assume good reproducibility based on results obtained in SSA experiments. (**b**) Reaction at pH > 2.70. Shown are three replicate runs, unfortunately two EUL samples (n.a.) have been lost during re-polishing. Here, (001) reacted about ten times faster than {hk0} faces. Two anomalous DAL {hk0} experiments stand out (dashed bars) and are likely the results of strong lateral dissolution starting from deep trenches along the mask edges (see section 4.4.3.4.).

4.4.3.2. Reaction at pH 2.88 to 2.92

At pH 2.88 to 2.92 we observed that (001) surfaces of EUL and DAL react more than 200 % faster compared to {hk0} surfaces of the same samples (Fig. 4-8b, Tab. 4-2). There is practically no resolvable difference in dissolution rates on (001) surfaces of DAL and EUL, which show averages of $(3.5^{+0.6}{}_{-0.5})\times10^{-6}$ and $(3.3\pm0.3)\times10^{-6}$ mol $m^{-2}s^{-1}$. The rates on {hk0} surfaces are generally less than 1×10^{-6} mol $m^{-2}s^{-1}$ and agree well in all runs and samples with two exceptions: In two instances (out of six), {hk0} faces of DAL reacted

surprisingly strong with rates larger than 7×10^{-6} mol $m^{-2}s^{-1}$. Because the majority of {hk0} faces of DAL and EUL reacted very slowly under these conditions, we interpret this behavior as anomalous as outlined in section 4.4.3.4. Nonetheless, the observations at pH 2.88 to 2.92 demonstrate that the change in reaction behavior at pH 2.70 is accompanied by a change in the anisotropy of reaction speeds. This is most prominently characterized by a decrease of reactivity on {hk0} surfaces by a factor of 10 when the pH becomes larger than 2.70. Although at pH < 2.70 the (001) surfaces are the most stable ones, they are the least stable ones at pH > 2.70. This behavior is consistent with microstructural observations obtained on the sulfide interfaces by SEM as detailed in section 4.4.4.

4.4.3.3. Control of Superstructure on Dissolution Anisotropy

The superstructures of pyrrhotite appear to influence the direction dependence of dissolution only very little, because no significant differences between {100} and {110} in 4C-rich DAL pyrrhotite and among DAL and EUL pyrrhotite are observed. With respect to the monoclinic 4C superstructure, the prismatic {hk0} planes (based on the hexagonal substructure) are no longer symmetry equivalent due to vacancy ordering and, hence, {100} and {110} surfaces might react systematically differently if the vacancy arrangement strongly controls the anisotropic behavior. Since no such systematic differences have been observed, the anisotropic behavior appears to depend primarily on the hexagonal NiAs-type substructure. Occasionally the strong twinning in EUL 4C-pyrrhotite becomes apparent on etched surfaces by slight reactivity differences between the individual twin domains (Fig. 4-6b). This can be attributed to weak reaction anisotropy with respect to the 4C superstructure, because the twinning arises solely from the ordering of vacancies and rotation of the ordering scheme by 60 or 120° about the *c* axis, which would be a symmetry operation with respect to the basic hexagonal NiAs-type crystal structure. However, this effect is too small to be quantified.

4.4.3.4. Anomalous Dissolution Behavior in Microenvironments

To test for orientation dependence, the same sample assembly was used in all MSA runs and all individual samples within the assembly had been polished simultaneously to identical surface finishes just prior to the runs. Hence, we exclude grossly differing starting conditions, such as sample misorientation or surface roughness as cause for the observed anomalous behavior of DAL {100} and {110} surfaces (Fig. 4-8b). As outlined

above (section 4.4.1.3.), the experiments above pH 2.70 showed strong development of Fe oxyhydroxide crusts and generally we observed that under these conditions also strong deterioration of the masks occurred from solution creeping and reacting under the protective tape (Fig. 4-2d,g). Owing to the thick oxyhydroxide crusts, this led in many instances to the formation of deep trenches along the mask edges due to localized formation or accumulation of acid or oxidant species. We think that the two cases of anomalous dissolution resulted from such reactive microenvironments, which caused preferred lateral dissolution starting from the trenches. Considering (001) being the most reactive surfaces under these conditions, this lateral dissolution could have easily outpaced the dissolution normal to the {hk0} faces under favorable conditions when the oxyhydroxide crust did not allow exchange with the bulk solution of the experiment. The reactive microenvironment created in this way did not induce a reversal to the reaction mechanism observed at pH < 2.70, because also in case of the anomalous behavior we did not detect the formation of elemental sulfur. Likely the driving mechanism in this case was an increase in concentration of oxidant (dissolved Fe^{3+}, reactive oxygen species, or both). This behavior demonstrates that the reaction interface region, comprising the sulfide interface and the adjacent layer of secondary phases, is a complex, dynamical system that can undergo abrupt changes as consequence of small disturbances.

4.4.4. Interface Morphology

The pH dependent changes in reaction behavior also manifest themselves in the micro-scale morphology of the sulfide reaction interfaces (Fig. 4-9). After removal of the alteration layers, SEM secondary electron imaging of the SSA EUL {110} experimental series shows that at the reactivity maximum between pH 2.3 and 2.7 the interfaces developed very rough and scaly morphologies (Fig. 4-9a,b,c). The pyrrhotite scales are dominated by (001) faces, have thicknesses in the order of tens to hundreds of nm, and protrude vertically out of the {110} plane. This indicates reduced reactivity on the (001) faces and preferred dissolution along the cleavage planes in the directions perpendicular to [001]. The resulting surface textures are very similar to the saw tooth patterns found in artificially and naturally (terrestrial and martian) weathered pyrrhotite (e.g., Cruz et al. 2005; Chevrier et al. 2011). Images of experiments conducted at pH 2.03 and 2.22, i.e., below the reactivity maximum, show that the development of pyrrhotite scales somewhat decreases, but dissolution still proceeds preferably perpendicular to [001].

At higher pH, closer to the transition point at pH 2.70, the surface textures were found to become smooth, indicating increasingly preferred dissolution on (001) faces. Based on images showing rough 4C surfaces next to smooth NC surfaces at pH 2.58 (Fig. 4-9b), the experiments suggest that the change in anisotropic behavior occurs at slightly lower pH for the NC phase compared to the 4C phase. At pH 2.66 (Fig. 4-9d,f) we found mostly smooth surface textures of both 4C- and NC-pyrrhotite, while the NC phase still reacted slightly faster than the 4C phase. Some 4C areas in this experiment showed the rough, scaly texture typical of lower pH, suggesting that acid production might have locally decreased the pH. Beyond the transition point smooth textures developed on all pyrrhotite surfaces, albeit dissolution proceeded at strongly reduced rates (Fig. 4-9e). Locally increased pitting could be observed in some cases.

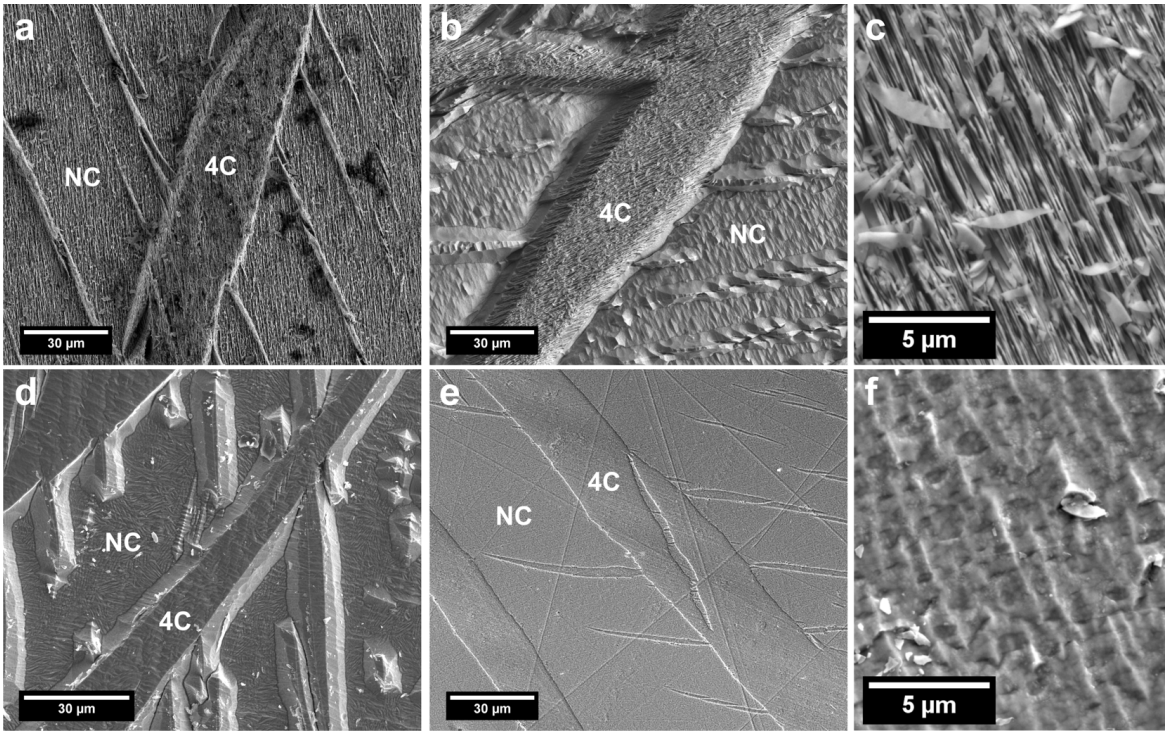

FIGURE 4-9. SEM-SE images of cleaned pyrrhotite reaction interfaces of H_2O_2-H_2SO_4 experiments at 35 °C. A pH dependent trend in interface textures is apparent, mimicking the changes in reaction anisotropy. (**a**) pH 2.41 (13 h). Both 4C- and NC-pyrrhotite are rough with strong development of a scaly texture dominated by (001) surfaces. (**b**) pH 2.58 (13 h). 4C-pyrrhotite still shows a rough and scaly texture, but NC-pyrrhotite has become smooth, indicating a change of the reaction mechanism at slightly lower pH. (**c**) pH 2.58 (13 h). Detail of the scaly 4C-pyrrhotite surface in (b). Individual scales have thicknesses of 10s to 100s of nm. (**d**) pH 2.66 (13 h). Close to pH 2.70 both 4C- and NC-pyrrhotite develop smooth interfaces. NC-pyrrhotite still reacts slightly faster than 4C-pyrrhotite (approx. 15 %). (**e**) pH 2.90 (44 h). The sulfide interfaces are very smooth, 4C-pyrrhotite reacts faster than NC-pyrrhotite at strongly reduced overall rates. (**f**) pH 2.66 (13 h). Detail of the smooth 4C-pyrrhotite surface in (d). Scale and orientation are the same as in (c).

4.4.5. HR-TEM Interface Observations

From two experimental runs we obtained FIB-prepared foils suitable for high-resolution (HR) TEM study of the reaction interface in order to search for evidence of incomplete dissolution and/or the formation of S-enriched sulfides (Fig. 4-10). The DAL {100} surface reacted at pH 1.95-1.99 for 647.8 h in 0.01 mol/L $FeCl_3$ solution showed beneath the sponge-like 2L-ferrihydrite crust a sharp transition toward pristine 4C-pyrrhotite, which superstructure could be detected less than 15 nm from the sulfide/oxide interface by fast Fourier transformation (FFT) of the HR image (Fig. 4-10a). Within the ~15 nm interval between 4C-pyrrhotite and the interface, FFT shows no superstructure periodicity but clearly attests the presence of the NiAs based fundamental structure of pyrrhotite. This indicates that no crystallographically distinct or amorphous phase formed at the interface and the surface layer rather consists of a disordered pyrrhotite. Surveys by TEM-EDX on this foil did not indicate the presence of marcasite (FeS_2), which is analytically resolvable from pyrrhotite by TEM-EDX and could be expected to form, based on known topotactic relationships with pyrrhotite (Fleet 1978). Also the defective tetragonal Fe_2S_3 phases proposed by Jones et al. (1992) should have been resolvable if occurring on nm-scales. In the foil taken from the DAL (001) surface (MSA H05) reacted at pH 2.86-2.93 for 44.3 h in 0.1 mol/L H_2O_2 we found well ordered 4C-pyrrhotite less than 5 nm from the sulfide/oxide interface (Fig. 4-10b). FFT suggests the presence of a pyrrhotite superstructure even closer to the interface, but this may due to delocalization in HR imaging. These observations, as well as surveys of several other FIB sections, which unfortunately were too thick for HR-TEM study, but showed no presence of FeS_2 based on TEM-EDX, suggest that the oxidative dissolution of pyrrhotite under the conditions studied is, with the exception of sulfur precipitation, mostly complete and may proceed with the formation of vacancy-disordered pyrrhotite in some cases.

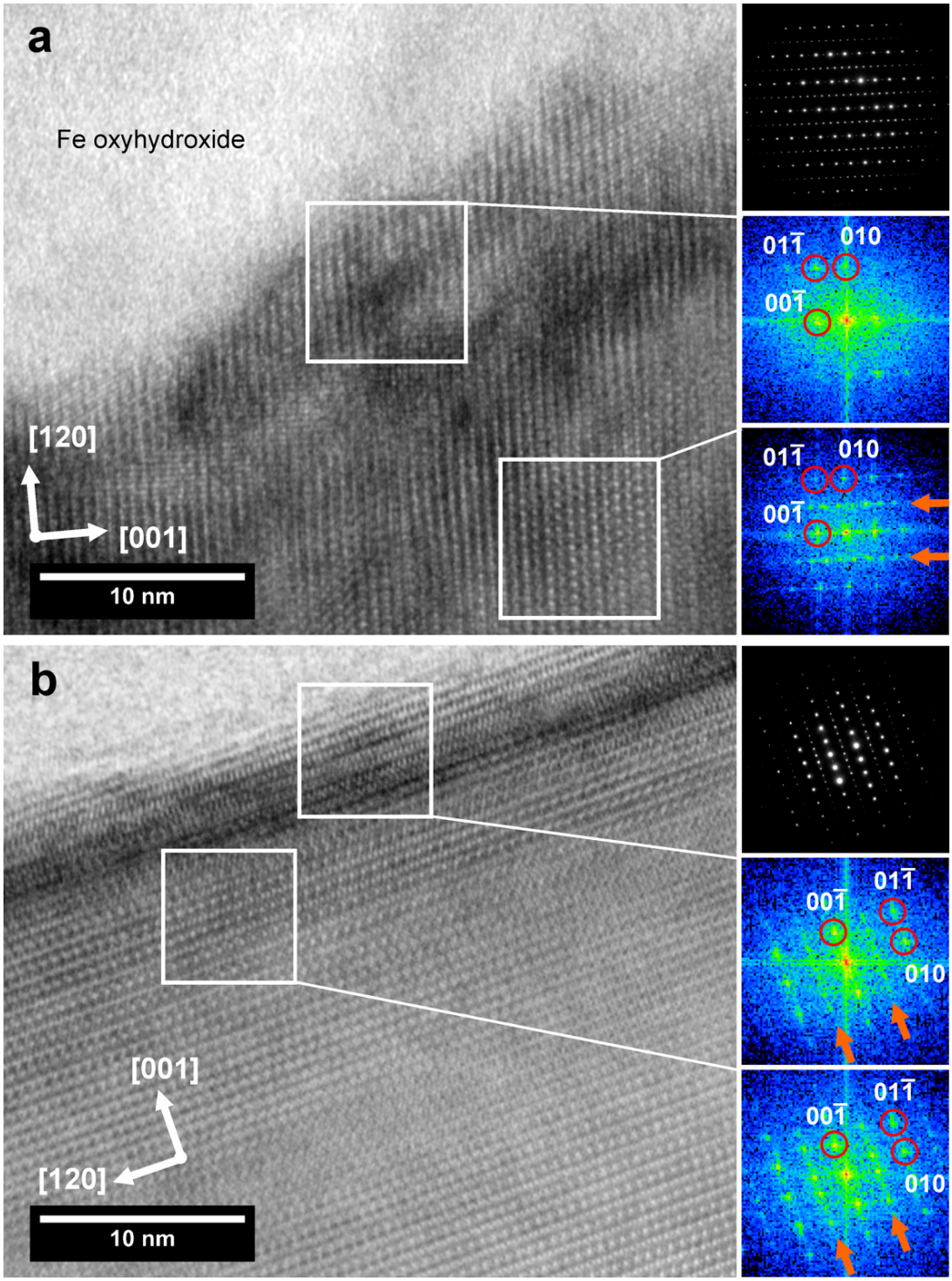

FIGURE 4-10. High resolution TEM images of the sulfide-oxyhydroxide interface. For marked squares Fast-Fourier-Transforms (FFT) are shown, accompanied by the bulk SAED patterns. (**a**) DAL {100} surface reacted in $FeCl_3$+HCl solution at 35 °C for 648 hours at pH 1.95−1.99 (detail of interface shown in Fig. 4-5c). 4C-pyrrhotite with clearly identifiable superstructure periodicity (arrows in FFT pattern) is present less than 15 nm from the sulfide-oxyhydroxide interface. Closer to the interface, the NiAs-type substructure of pyrrhotite can be detected, but superstructures are not detectable. (**b**) DAL (001) surface reacted in H_2O_2+H_2SO_4 solution at 35 °C for 44.3 hours at pH 2.90. Superstructure periodicity of 4C-pyrrhotite (arrows) is detectable directly at and below the sulfide-oxyhydroxide interface.

4.5. Discussion

4.5.1. pH Dependence of Dissolution Rates and Anisotropy

4.5.1.1. Dissolution Rates and the Isoelectric Point

Our experimental results show two effects taking place as the pH of the H2O2 solution changes. The first effect is the change in anisotropy of rates of dissolution, leading to an increase of reaction speed on (001) surfaces and decrease of speed on {hk0} surfaces as pH increases beyond the transition point at pH 2.70. The second effect is the change in relative reaction rates between 4C- and NC-pyrrhotite at this critical pH. The change in relative reaction rates is a second-order effect due to different degrees of absolute reactivity change of 4C and NC imposed at the critical pH: On {hk0} surfaces at pH 2.70 the drop in absolute rates for NC-pyrrhotite is larger than that for 4C-pyrrhotite, leading to reversal of the relative rates.

The sharp drop in absolute reaction rates close to the transition point at pH 2.70 is associated with a change in the reaction mechanism as the production of elemental sulfur ceases. In principle, the observed changes in reaction behavior could be due to a change in the oxidant's speciation. However, H_2O_2 is a weak acid with a pK_a of approx. 11.4 at 35 °C (Perrin 1969) and, hence, there are no deprotonation reactions expected in the low pH range of our experiments. This leads us to infer that the observed behavior is primarily controlled by intrinsic properties of the pyrrhotite-fluid interface and not by the speciation of the bulk solution. The transition point at pH 2.70 approximately coincides with the isoelectric point (IEP) of synthetic pyrrhotite determined by Dekkers and Schoonen (1994) to occur between pH 2.0 and 2.5. Later work on natural pyrrhotite showed that the IEP may lie closer to 3.0-3.3 (Bebie et al. 1998). At pH below the IEP, the zeta potential of the pyrrhotite-fluid interface is positive and turns steeply negative above the IEP. Because the above studies determined bulk IEPs based on electrophoresis of finely dispersed pyrrhotite, differences to actual IEPs of plane, single crystal surfaces could be expected due to anisotropy. According to the interpretation of Dekkers and Schoonen (1994), changing surface charges are primarily linked to the speciation of thiol(*sic*)/sulfhydryl groups ($\equiv S{-}H^0$) on the pyrrhotite surface, which result from the hydrolysis of uncoordinated sulfur atoms. These groups might be neutral, protonated ($\equiv S{-}H_2^+$) or deprotonated ($\equiv S{-}^-$) depending on pH. Metal hydroxide groups ($\equiv Fe{-}OH$) are expected to contribute little to the surface speciation when activities of dissolved ferrous iron and sulfide are low. Increased Fe^{2+} activities relative to sulfide will increase the proportion of

Fe hydroxide surface groups and might lead to additional charge reversals at higher pH, but the first charge reversal/IEP at lowest pH is little affected. Hence, in our experiments the sulfur surface speciation appears to be an important controlling factor on dissolution rates. However, as detailed below, sulfhydryl groups may not necessarily be the prominent reactive centers on the surfaces, at least at low pH < 2.70.

4.5.1.2. Dissolution Anisotropy and Chemical State of Pyrrhotite Surfaces

The different reaction behavior of distinct crystal surfaces observed in our experiments indicates that the availability of surface groups is intrinsically controlled by the crystal's anisotropy. Despite strong nm- to µm-scale roughness develops during the dissolution, the anisotropy still statistically determines the contributions of surface species involved at the reaction interface. Becker et al. (1997) presented STM and other experimental evidence as well as quantum mechanical calculations suggesting that pyrrhotite (001) surfaces are terminated by sulfur atoms in vacuum. Through reaction with gaseous oxygen they observed strongest oxidation near the corners of (001) surface terraces, where Fe atoms are more readily available compared to the S dominated terrace planes. Accordingly, they suggest that the surface oxidation via the initial formation of Fe(III) oxyhydroxides is hindered by the small number of Fe atoms exposed on the (001) surfaces. If this situation applies to pyrrhotite in aqueous media as well, the slow dissolution on (001) surfaces at low pH can be interpreted in terms of decreased availability of iron relative to the {hk0} surfaces, on which Fe layers are exposed, and ≡Fe−OH groups readily form. These groups are likely the prime reactive centers that are involved in the oxidation to Fe(III) oxyhydroxides and dissolved Fe^{3+}. Reasons for quicker Fe oxidation by O_2 relative to sulfur may lie in the easier transfer of spin to the electronic system of iron as discussed by Becker et al. (1997). Compared to Fe, oxidation of S requires relatively high activation energy, because O_2 in this case has to change its spin state from triplet to singlet (high to low spin). The preferred oxidation of Fe in our experiments is clearly indicated by the formation of elemental sulfur at pH < 2.70. The documented formation of polysulfide in XPS investigations on pyrrhotite oxidation (e.g., Buckley and Wood 1985ab; Jones et al. 1992; Pratt et al. 1994) is consistent with such a route as polymerized sulfur chains would eventually merge into S_8 rings of elemental sulfur through further oxidation (Wang 2007). Increased reactivity of the (001) surfaces above pH 2.70 and the concomitant disappearance of elemental sulfur as reaction product strongly points to a change in the

reaction mechanism. Assuming dominant sulfur termination on (001) surfaces, the observations are consistent with a mechanism that attacks preferentially at sulfur sites and involves rapid and complete sulfide to sulfate oxidation.

4.5.1.3. Oxidant Species

The oxidant species in experiments involving H_2O_2 are important to the understanding of the dissolution process. Triplet O_2 and H_2O_2 themselves are likely the least reactive species (the latter due to its relatively stable O-O bond), but dissociation of H_2O_2 might yield a range of other reactive oxygen species (ROS) capable of oxidizing the pyrrhotite surfaces. Besides singlet O_2, radical species such as superoxide ($\cdot O_2^-$) and hydroxyl ($\cdot OH$) radicals are candidates for ROS. Particularly the hydroxyl radical can form in Fenton-type reactions in the presence of Fe^{2+} (e.g., Aust et al. 1985; Koppenol 1993; Hug and Leupin 2003). Neither the H_2O_2/ROS system, nor the speciation of iron (i.e., Fe^{3+} vs. $Fe[OH]^{2+}$) is expected to show a comparably sharp change around pH 2.70 as observed in our experiments. Li et al. (2010) showed that pyrrhotite Fenton reactions probably can occur at the mineral fluid interface due to release of Fe^{2+} from the sulfide. Hug and Leupin (2003) demonstrated through use of 2-propanol as radical scavenger (producing acetone) that the production of radical species in Fenton-type reactions is gradually increasing as pH is lowered to pH 3. The addition of 0.7 mol/L 2-propanol (i.e., the sevenfold concentration of the oxidant H_2O_2) did not change the dissolution behavior in our experiment – it is, however, unclear whether the availability of the radical scavenger 2-propanol at the reaction front was suitable and the reaction kinetics of acetone formation capable of interfering with the production and reaction of radical ROS at the sulfide interface. Addition of up to 0.1 mol/L $FeSO_4$ as promoter of Fenton-type reactions did not produce significant differences, except that the precipitation of elemental sulfur was strongly inhibited. The H_2O_2-free control experiment using $Fe_2(SO_4)_3$ as sole oxidant (except atmospheric O_2) yielded reaction rates and diminished sulfur production similarly to the $FeSO_4$+H_2O_2 experiments. In this regard, it must be reasoned that dissolved Fe^{3+}, formed by the reaction of added Fe^{2+} and H_2O_2, was rather the controlling factor than the radical ROS formed in the solution. Eventually the action of radical ROS can not be excluded conclusively, but their effect seems not to be considerably strong compared to Fe^{3+} as oxidant of pyrrhotite.

Based on results of Dekkers and Schoonen (1994) and Bebie et al. (1998) the pyrrhotite

surfaces at pH < IEP are likely dominated by positively charged Stern layers of protonated sulfhydryl groups. This view implies that the oxidant species relevant to the oxidation of Fe sites might carry negative charge, causing repulsive Coulomb interactions and greatly reduced reaction rates at pH > IEP, when sulfhydryl groups are deprotonated. A candidate for this species may be the superoxide ion ($\cdot O_2^-$) forming through Fenton-type reactions in the Fe-rich interface region. At pH > IEP, the reversed zeta potential might allow other, yet elusive, oxidant species to attack the sulfur dominated (001) faces.

4.5.1.4. Non-oxidative Dissolution and the Role of Fe^{3+}

An alternative explanation for the strong change in dissolution behavior at the IEP might be a fundamental switch between the contribution of oxidative and non-oxidative dissolution. Thomas et al. (1998) showed that non-oxidative dissolution of pyrrhotite is about 1000 times faster than oxidative dissolution and, hence, at pH < IEP increased contribution of non-oxidative dissolution might explain strongly enhanced reaction rates. However, the abundant precipitation of elemental sulfur argues against non-oxidative dissolution, which would rather produce dissolved sulfide species. Moreover, experiments by Janzen et al. (2000) indicate a factor 10 faster pyrrhotite dissolution in aerated hydrochloric acid at pH 2.75 compared to the analogous experiment under oxygen-free conditions, indicating that non-oxidative dissolution is not necessarily faster.

The non-formation of significant amounts of elemental sulfur when pyrrhotite is exposed to $FeSO_4$+H_2O_2 and $Fe_2(SO_4)_3$ media indicates that the oxidation toward sulfate advances to more completeness under conditions when significant Fe^{3+} is present. Also our MSA experiments using $FeCl_3$ showed that, aside from orientation dependence, DAL pyrrhotite precipitate abundant sulfur while EUL precipitated little or none. The reason for this behavior is unclear. Variations in the contribution of oxidative versus non-oxidative dissolution, which may depend on the structure type or other factors such as trace element or oxygen contents within the pyrrhotite, might affect the precipitation of sulfur.

4.5.2. Reactivity Differences between 4C- and NC-Pyrrhotite

Significant differences between 4C- and NC-pyrrhotite are clearly evident in our H2O2 dissolution experiments. As outlined above, the change in reactivity of NC-pyrrhotite relative to 4C-pyrrhotite is due to a different degree of change in individual, absolute dissolution rates at the transition point close to pH 2.70. The 50 to 80 % reactivity

difference of NC-pyrrhotite relative to 4C-pyrrhotite is quite outstanding, considering that both phases are extremely similar in composition with a just 2.4 % higher Fe/S ratio in NC-pyrrhotite. Although there is evidence that Fe availability on the surfaces is a controlling factor of oxidative dissolution rates, there must be other factors to explain the large effect of minor variation in the Fe/S ratios. Given identical basic structures, this factor must be the nature of the vacancy superstructures. The most striking difference between the 4C and NC superstructures is the presence of double filled Fe layers in the idealized NC structure as shown in Figure 4-1c and previous work (Harries et al. 2011). Unlike 4C-pyrrhotite, which has no double filled Fe layers, NC-pyrrhotite with an N value of 4.8 to 4.85 (as applicable to our EUL sample) is expected to have about 35 % of its Fe sublattice constituted by double filled layers (Fig. 4-11a). Because this figure, in contrast to the relative Fe/S ratios, is comparable to the magnitude of observed reactivity differences, we suggest that the surface expression of this difference in bulk structure is a significant factor for the distinct rates of oxidative dissolution of NC- and 4C-pyrrhotites. The $FeCl_3$ MSA experiments showed that 4C-pyrrhotite has a tendency to react faster than NC-pyrrhotite even at pH as low as 1.8 to 1.9 in presence of significant concentrations of dissolved Fe^{3+}. This indicates that the distinct surface reaction mechanisms operate in case of Fe^{3+} or ROS as oxidants.

Unfortunately, there is little possibility of making ad hoc inferences about the actual surface termination of complex pyrrhotite superstructures on {hk0}surfaces. XPS studies by Nesbitt et al. (2001) indicate that fresh pyrrhotite surfaces harbor monomeric S^{2-} surface species and show no clear evidence for dimerization of sulfur. This may point to rather little surface reconstruction. Hence, one prominent bulk-structural feature that might contribute to surface reactivity is the presence of face-sharing Fe-S coordination octahedra, which occur in chains parallel to the [001] stacking direction. The rather unusual face-sharing of Fe polyhedra with short Fe-Fe distances of about 0.289 nm (de Villiers et al. 2009) leads to relatively strong electronic interactions among the chain atoms. Fe-Fe separation of less than 0.3 nm is expected to result in overlapping of Fe 3d t_{2g} orbitals and creation of π-bonded crystal orbitals along the [001] direction in stoichiometric FeS, which strongly enhance electronic transport properties in this direction (Goodenough 1962; Wang and Salveson 2005). Due to vacancies within the Fe layers these chains are truncated in non-stoichiometric pyrrhotite, resulting in a length of 7 Fe atoms in case of 4C-pyrrhotite (Fig. 4-11b). Addition of double filled Fe layers (or more

appropriate: the introduction of non-conservative APBs; Harries et al. 2011) increases the length of face-sharing chains to 9 in 5C-pyrrhotite and creates two types of chains in intermediate, non-integral pyrrhotites, e.g., length 8 and 9 in case of N = 4.85.

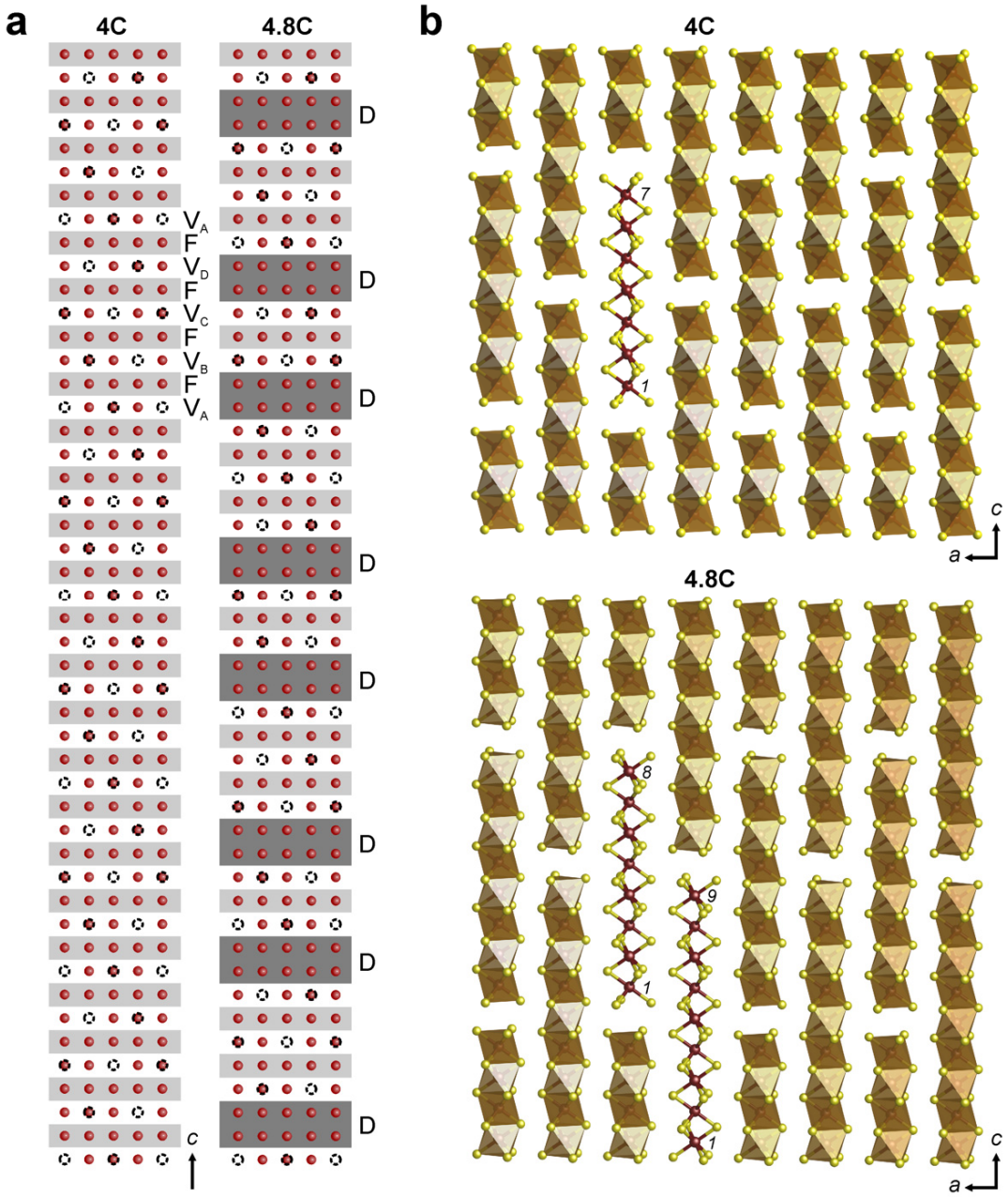

FIGURE 4-11. (**a**) Schematic representation of the superstructures of 4C- and NC-pyrrhotite (N = 4.8) based on the model of Izaola et al. (2007) (cf. Harries et al., 2011). Fe atoms are red and Fe site vacancies are outlined in black (also in projection). Four different vacancy-bearing layer types exist ('V_A' to 'V_D'). Completely filled Fe layers are shaded in light gray ('F'), doublets of filled Fe layers/anti-phase domain boundaries are shaded in dark gray ('D'). (**b**) Sections of the idealized crystal structures of 4C- and 4.8C-pyrrhotite showing chains of face-sharing FeS_6 octahedra. In 4C-pyrrhotite the chain length is 7, in 4.8C-pyrrhotite the chain length is 8 and 9. With increasing N values the fraction of length 8 chains decreases and for N = 5 only length 9 chains exist.

If face-sharing of Fe octahedra still persist on the {hk0} surfaces, the 14 to 28 % increased lengths of chains relative to 4C and therefore the increased extent and enhanced polarizability of the axial π-systems may enhance the efficiency of electron transfer between the NC-pyrrhotite surface and oxidant species. This is a possible explanation for its larger intrinsic reactivity at pH < 2.70, when surficial ≡Fe−OH is probably the surface species most prone to oxidation. If indeed chain lengths play an important role in determining the physicochemical properties of pyrrhotite superstructure, the common, quasi 2-dimensional view of layer stacking in pyrrhotite 'polytypes' (e.g., Wang and Salveson 2005 and references therein) should be carefully re-considered in favor of a more dynamic view of how individual vacancies behave within the framework of the hexagonal close-packed sulfur sublattice.

4.5.3. Existence of Sulfidic Non-equilibrium Layers

Our HR-TEM observations of 4C-pyrrhotite reaction interfaces in cross section do not show the formation of non-equilibrium layers (NLs) composed of amorphous sulfide or any newly formed S-enriched sulfide phase. Based on reported thicknesses in the order of nm to tens or hundreds of nm (Pratt et al. 1994; Mycroft et al. 1995; Thomas et al. 2001; Mikhlin et al. 2000), and sharp boundaries with the original pyrrhotite (Jones et al. 1992), the presence of such features should have been detectable by TEM at least in our month-long $FeCl_3$ experiment, which clearly showed build-up of an elemental sulfur layer, attesting incomplete oxidation of sulfur. This concurs with observation of Mikhlin et al. (2000), who detected formation of extensive NLs by non-oxidative acid leaching of pyrrhotite, but reported only little development of this feature under oxidizing leaching conditions. If present on our experimentally oxidized pyrrhotite, NLs had thicknesses at the atomic level or were strongly discontinuous, preventing detection. Although the concept of continuous NLs in case of oxidation in air or under conditions of small mass loss is well established, it appears hardly applicable to the oxidative dissolution of pyrrhotite when significant mass is lost to the solution at high rates, and intrinsic anisotropy of pyrrhotite leads to the development of roughness down to the nm-scale. Under such circumstances, the control on dissolution speed would rather not be exerted by the diffusion of Fe through the spatially extensive, Fe-depleted NL (e.g., Wang 2007), but through diffusion and reaction processes in the complexly structured interface region, which contains mostly unaltered pyrrhotite (including sub-µm scales), Fe oxyhydroxides

(e.g., 2L-ferrihydrite), and precipitates of elemental sulfur. Future investigations by FIB-TEM may provide details on interface regions and the occurrence and nature of NLs.

4.6. Conclusions

Our experiments show that the crystal structure of pyrrhotite exerts a strong control on its oxidative dissolution. The pronounced directional dependence of dissolution rates is primarily determined by the anisotropy of the hexagonal NiAs-type substructure and appears to depend strongly on the availability of bound ferrous iron on the sulfur-dominated crystal surfaces. The abundant precipitation of elemental α-sulfur at pH < 2.70 indicates incomplete sulfide oxidation and strengthens the interpretation that exposed Fe atoms are the more reactive sites on the crystal surface under these conditions. At pH > 2.70 complete sulfide to sulfate oxidation indicates a change in reaction mechanism toward relatively stronger reactivity of sulfhydryl surface groups. The change is accompanied by an overall drop of absolute reaction rates at pH 2.70 and is obviously associated with a change in surface charge at the isoelectric point of pyrrhotite. The comparison of chemically very similar 4C and NC (N ~4.85) superstructures of pyrrhotite reveals large reactivity differences that originate from different arrangements of Fe site vacancies. Particularly the variable lengths of face-sharing chains of octahedrally coordinated Fe within the pyrrhotite superstructures may strongly influence the surface reactivity due to strong axial electronic interaction of Fe atoms inside the chains.

4.7. Acknowledgements

This publication is part of the R&D program GEOTECHNOLOGIEN funded by the German Ministry of Education and Research (BMBF) and German Research Foundation (DFG; grant 03G0718A to K.P.). We also acknowledge financial support provided by the DFG Leibniz program (LA 830/14-1 to F.L.) and the ENB program of the Bavarian State Ministry of Sciences, Research and the Arts (to D.H.). The authors are grateful to N. Miyajima for assistance with TEM work.

BIBLIOGRAPHY

Akai J. (1988) Incompletely transformed serpentine-type phyllosilicates in the matrix of Antarctic CM chondrites. *Geochimica et Cosmochimica Acta* **52**, 1593−1599.

Akai J. (1990) Mineralogical evidence of heating events in Antarctic carbonaceous chondrites, Y-86720 and Y-82162. *Antarctic Meteorite Research* **3**, 55−68.

Akai J. (1992) TTT diagram of serpentine and saponite, and estimation of metamorphic heating degree of Antarctic carbonaceous chondrites. *Antarctic Meteorite Research* **5**, 120−135.

Alexander C.M.O'D. (2001) The early evolution of the inner Solar System: a meteoritic perspective. *Science* **293**, 64–68.

Amelinckx S. (1972) The geometry and interfaces due to ordering and their observations in transmission electron microscopy and electron diffraction. *Surface Science* **31**, 296–354.

Amelinckx S. and van Dyck D. (1993) Electron diffraction effects due to modulated structures. In *Electron diffraction techniques Vol. 2* (ed. J.M. Cowley) 309-373. IUCr/Oxford Science Publications, Oxford, 423 p.

Amelinckx S., van Tendeloo G., van Dyck D. and van Landuyt J. (1989) The study of modulated structures, mixed layer polytypes and 1-D quasi-crystals by means of electron microscopy and electron diffraction. *Phase Transitions* **16**, 3−40.

Anderson S.P., von Blanckenburg F. and White A.F. (2007) Physical and chemical controls on the critical zone. *Elements* **3**, 315–319.

Andersson S. and Wadsley A.D. (1966) Crystallographic shear and diffusion paths in certain higher oxides of niobium, tungsten, molybdenum and titanium. *Nature* **211**, 581−583.

Arnold R.G. (1966) Mixtures of hexagonal and monoclinic pyrrhotite and the measurement of the metal content of pyrrhotite by X-ray diffraction. *American Mineralogist* **51**, 1221–1227.

Asta M. P., Cama J., Soler J. M., Arvidson R. S. and Lüttge A. (2008) Interferometric study of pyrite surface reactivity in acidic conditions. *American Mineralogist* **93**, 508−519.

Aust S.D., Morehouse L.A. and Thomas C.E. (1985) Role of metals in oxygen radical reactions. *Journal of Free Radicals in Biology and Medicine* **1**, 3−25.

Barin I. (1989) *Thermochemical data of pure substances, part I*. VCH, Weinheim, 1739 p.

Bebie J., Schoonen M.A.A., Fuhrmann M. and Strongin D.R. (1998) Surface charge development on transition metal sulfides: an electrokinetic study. *Geochimica et Cosmochimica Acta* **62**, 633−642.

Becker M., de Villiers J. and Bradshaw D. (2010a) The flotation of magnetic and non-magnetic pyrrhotite from selected nickel ore deposits. *Minerals Engineering* **23**, 1045−1052.

Becker M., de Villiers J. and Bradshaw D. (2010b). The mineralogy and crystallography of pyrrhotite from selected nickel and PGE ore deposits. *Economic Geology* **105**, 1025−1037.

Becker U., Munz A.W., Lennie A.R., Thornton G. and Vaughan D.J. (1997) The atomic and electronic structure of the (001) surface of monoclinic pyrrhotite (Fe_7S_8) as studied using STM, LEED and quantum mechanical calculations. *Surface Science* **389**, 66−87.

Belzile N., Chen Y.W., Cai M.F., and Li Y. (2004) A review on pyrrhotite oxidation. *Journal of Geochemical Exploration* **84**, 65−76.

Benedix G.K., Leshin L.A., Farquhar J., Jackson T. and Thiemens M.H. (2003) Carbonates in CM2 chondrites: constraints on alteration conditions from oxygen isotopic compositions and petrographic observations. *Geochimica et Cosmochimica Acta* **67**, 1577−1588.

Bennett C.E.G. and Graham J. (1980) New observations on natural pyrrhotites. Part III. Thermomagnetic experiments. *American Mineralogist* **65**, 800−807.

Berger E.L., Zega T.J., Keller L.P. and Lauretta D.S. (2011) Evidence for aqueous activity on comet 81P/Wild 2 from sulfide mineral assemblages in Stardust samples and CI chondrites. *Geochimica et Cosmochimica Acta* **75**, 3501−3513.

Bertaut E.F. (1953) Contribution a l'etude des structures lacunaires: la pyrrhotine. *Acta Crystallographica* **6**, 557−561.

Bigham J.M., Carlson L. and Murad E. (1994) Schwertmannite, a new iron oxyhydroxy-sulphate from Pyhasalmi, Finland, and other localities. *Mineralogical Magazine* **58**, 641−641.

Bischoff A. (1998) Aqueous alteration of carbonaceous chondrites: evidence for preaccretionary alteration – a review. *Meteoritics and Planetary Science* **33**, 1113−1122.

Bischoff A. and Metzler K. (1991) Mineralogy and petrography of the anomalous carbonaceous chondrites Yamato-86720, Yamato-82162, and Belgica-7904. *NIPR Symposium on Antarctic Meteorites* **4**, 226−246.

Bischoff A. and Stoeffler D. (1992) Shock metamorphism as a fundamental process in the evolution of planetary bodies; information from meteorites. *European Journal of Mineralogy* **4**, 707–755.

Boctor N., Kurat G., Alexander C. and Prewitt C. (2002) Sulfide mineral assemblages in Boriskino CM chondrite (abstract #1534). *Proceedings, 33rd Lunar and Planetary Science Conference.*

Boss A.P. (2003) The solar nebula. In *Treatise on Geochemistry*, 63–82 (eds. H.D. Holland and K.K. Turekian). Elsevier, Amsterdam, 7800 p.

Bowles J.F.W., Howie R.A., Vaughan D.J. and Zussman J. (2011) *Rock-forming minerals Non-silicates: Oxides, Hydroxides and Sulphides*. The Geological Society, London, 920 p.

Brearley A.J. (2006) The action of water. In *Meteorites and the Early Solar System II*, 587–624 (eds. D.S. Lauretta and H.Y. McSween Jr.). University of Arizona Press, Tucson, 942 p.

Brearley A.J. (2010) Further complexities in sulfides in the TIL 91722 CM2 chondrite: Microstructures of pentlandite coexisting with pyrrhotite (abstract #5159). *Meteoritics and Planetary Science* **45**, A21.

Brearley A.J. (2011) Alteration of coarse-grained Fe and Fe,Ni sulfides in the Mighei CM2 carbonaceous chondrite: Evidence for the instability of primary pyrrhotite-pentlandite grains during aqueous alteration (abstract #2233). *Proceedings, 42nd Lunar and Planetary Science Conference.*

Brearley A.J. and Martinez C. (2010) Ubiquitous exsolution of pentlandite and troilite in pyrrhotite from the TIL 91722 CM2 carbonaceous chondrite: A record of low temperature solid state processes (abstract #1689). *Proceedings, 41st Lunar and Planetary Science Conference.*

Broddin D., Van Tendeloo G. and Amelinckx S. (1990) The long-period superstructures in binary $Au_{3+x}Zn_{1-x}$ alloys: stability and off-stoichiometry effects. *Journal of Physics: Condensed Matter* **2**, 3459–3477.

Browning L.B., McSween H.Y. and Zolensky M.E. (1996) Correlated alteration effects in CM carbonaceous chondrites. *Geochimica et Cosmochimica Acta* 60, 2621–2633.

Buckley A.N. and Riley K.W. (1991) Self-induced floatability of sulphide minerals: examination of recent evidence for elemental sulphur as the hydrophobic entity. *Surface and Interface Analysis* **17**, 655–659.

Buckley A.N. and Woods R. (1985b) X-ray photoelectron spectroscopy of oxidised pyrrhotite surfaces: II. Exposure to aqueous solutions. *Applied Surface Science* **20**, 472−480.

Buckley A.N. and Woods R. (1985a) X-ray photoelectron spectroscopy of oxidized pyrrhotite surfaces. I. Exposure to air. *Applied Surface Science* **22**, 280−287.

Bullock E.S., Gounelle M., Lauretta D.S. Grady M.M. and Russell S.S. (2005) Mineralogy and texture of Fe-Ni sulfides in CI1 chondrites: Clues to the extent of aqueous alteration on the CI1 parent body. *Geochimica et Cosmochimica Acta* **69**, 2687–2700.

Bunch T.E. and Chang S. (1980) Carbonaceous chondrites II. Carbonaceous chondrite phyllosilicates and light element geochemistry as indicators of parent body processes and surface conditions. *Geochimica et Cosmochimica Acta* **44**, 1543–1577.

Burrows B.L. and Sulston K.W. (1991) Measurement of disorder in non-periodic sequences. *Journal of Physics A* **24**, 3979–3987.

Buseck P.R. (ed.) (1992) Minerals and reactions at the atomic scale. Transmission electron microscopy. *Reviews in Mineralogy* **27**. Mineralogical Society of America, Chantilly, 516 p.

Butler C.P. (1966) Temperatures of meteoroids in space. *Meteoritics* **3**, 59–70.

Chapuis G. (2003) Crystallographic excursion in superspace. *Crystal Engineering* **6**, 187–195.

Chase M.W., Davies C.A., Downey J.R., Frurip D.J., McDonald R.A. and Syverup A.N. (1985) *NIST JANAF Thermochemical Tables*. National Institute of Standards and Technology, Gaithersburg.

Cheng H., Hu Y., Luo J., Xu B. and Zhao J. (2009) Geochemical processes controlling fate and transport of arsenic in acid mine drainage (AMD) and natural systems. *Journal of Hazardous Materials* **165**, 13–26.

Chevrier V., Lorand J.-P. and Sautter V. (2011) Sulfide petrology of four nakhlites: Northwest Africa 817, Northwest Africa 998, Nakhla, and Governador Valadares. *Meteoritics and Planetary Science* **46**, 769–784.

Chiang E. and Youdin A.N. (2010) Forming Planetesimals in Solar and Extrasolar Nebulae. *Annual Reviews of Earth and Planetary Sciences* **38**, 493–522.

Ciesla F.J., Lauretta D.S., Cohen B.A., and Hood L.L. (2003) A nebular origin for chondritic fine-grained phyllosilicates. *Science* **299**, 549–552.

Clayton R.N. and Mayeda T.K. (1999) Oxygen isotope studies of carbonaceous chondrites. *Geochimica et Cosmochimica Acta* **63**, 2089–2104.

Clement B.M., Haggerty S. and Harris J. (2008) Magnetic inclusions in diamonds. *Earth and Planetary Science Letters* **267**, 333–340.

Condit R.H., Hobbins R.R. and Birchenall C.E. (1974) Self-diffusion of iron and sulfur in ferrous sulfide. *Oxidation of Metals* 8, 409–455.

Conroy M. and Armstrong J. (2005) A comparison of surface metrology techniques. *Journal of Physics: Conference Series* **13**, 458–465.

Converse D.R., Holland H.D. and Edmond J.M. (1984) Flow rates in the axial hot springs of the East Pacific Rise (21° N): implications for the heat budget and the formation of massive sulfide deposits. *Earth and Planetary Science Letters* **69**, 159–175.

Corlett M. (1968) Low-iron polymorphs in the pyrrhotite group. *Zeitschrift für Kristallographie* **126**, 124–134.

Craig J.R. (1973) Pyrite-pentlandite assemblages and other low temperature relations in the Fe-Ni-S system. *American Journal of Science* **273-A**, 496–510.

Cruz R., Gonzalez I. and Monroy M. (2005) Electrochemical characterization of pyrrhotite reactivity under simulated weathering conditions. *Applied Geochemistry* **20**, 109−121.

Cullity B.D. (1956) *Elements of X-ray diffraction*. Addison-Wesley Publishing, Boston, 514 p.

Dai Z.R. and Bradley J.P. (2001) Iron-nickel sulfides in anhydrous interplanetary dust particles. *Geochimica et Cosmochimica Acta* **65**, 3601–3612.

de Villiers, J.P.R. and Liles, D.C. (2010) The crystal-structure and vacancy distribution in 6C pyrrhotite. *American Mineralogist* **95**, 148–152.

de Villiers J.P.R., Liles D.C. and Becker M. (2009) The crystal structure of a naturally occurring 5C pyrrhotite from Sudbury, its chemistry, and vacancy distribution. *American Mineralogist* **94**, 1405−1405.

de Waal S.A. and Calk L.C. (1975) The sulfides in the garnet pyroxenite xenoliths from Salt Lake Crater, Oahu. *Journal of Petrology* **16**, 134–153.

de Wolf P.M., Janssen T. and Janner A. (1981) The superspace groups for incommensurate crystal structures with a one-dimensional modulation. *Acta Crystallographica* **A37**, 625–636.

Dekkers M.J. and Schoonen M.A.A. (1994) An electrokinetic study of synthetic greigite and pyrrhotite. *Geochimica et Cosmochimica Acta* **58**, 4147−4153.

Desborough G.A. and Carpenter R.H. (1965) Phase relations of pyrrhotite. *Economic Geology* **60**, 1431–1450.

Dódony I. (1997) Theoretical derivation and identification of possible two-layer lizardite polytypes. In *Modular Aspects in Mineralogy, EMU Notes in Mineralogy* **1**, 57–80 (ed. S. Merlino). Eötvös University Press, Budapest, 449 p.

Dódony I. and Pósfai M. (1990) Pyrrhotite superstructures; Part II, A TEM study of 4C and 5C structures. *European Journal of Mineralogy* **2**, 529–535.

Drits V. (1987) *Electron diffraction and high-resolution electron microscopy of mineral structures*. Springer-Verlag, Berlin, 304 p.

Eggler D.H. and Lorand J.P. (1993) Mantle sulfide geobarometry. *Geochimica et Cosmochimica Acta* **57**, 2213–2222.

Ekmekçi Z., Becker M., Tekes E.B. and Bradshaw D. (2010) The relationship between the electrochemical, mineralogical and flotation characteristics of pyrrhotite samples from different Ni Ores. *Journal of Electroanalytical Chemistry* **647**, 133–143.

Elliot A.D. (2010) Structure of pyrrhotite 5C (Fe_9S_{10}). *Acta Crystallographica B* **66**, 271–279.

Etschmann B., Pring A., Putnis A., Grguric B.A. and Studer A. (2004) A kinetic study of the exsolution of pentlandite $(Ni,Fe)_9S_8$ from the monosulfide solid solution (Fe,Ni)S. *American Mineralogist* **89**, 39–50.

Fleet M.E. (1978) The pyrrhotite-marcasite transformation. *Canadian Mineralogist* **16**, 31−35.

Fleet M.E. (2006) Phase equilibria at high temperatures. In *Sulfide Mineralogy and Geochemistry, Reviews in Mineralogy and Geochemistry* **61**, 365–405 (ed. D.J. Vaughan). Mineralogical Society of America, Chantilly, 714 p.

Fleet M.E. and Pan Y. (1994) Fractional crystallization of anhydrous sulfide liquid in the system Fe-Ni-Cu-S, with application to magmatic sulfide deposits. *Geochimica et Cosmochimica Acta* **58**, 3369–3377.

Francis C.A., Fleet M.E., Misra K. and Craig J.R. (1976) Orientation of exsolved pentlandite in natural and synthetic nickeliferous pyrrhotite. *American Mineralogist* **61**, 913–920.

Froese E. and Gunter A.E. (1976) A note on the pyrrhotite-sulfur vapor equilibrium. *Economic Geology* **71**, 1589–1594.

Frost B.R. (1991) Introduction to oxygen fugacity and its petrologic importance. *Reviews in Mineralogy and Geochemistry 25*, 1–9.

Fuchs L.H., Olsen E. and Jensen K.J. (1973) Mineralogy, mineral-chemistry, and composition of the Murchison (C2) meteorite. *Smithsonian Contributions to the Earth Sciences* **10**, 1-39.

Fuerstenau M.C., Jameson, G. and Yoon R.-H. (2007) *Froth flotation: a century of innovation*. Society for Mining, Metallurgy, and Exploration, Littleton (USA), 897 p.

Fujiwara K. (1957) On the period of out-of-step of ordered alloys with anti-phase domain structure. *Journal of the Physical Society of Japan* **12**, 7–13.

Geiger T. and Bischoff A. (1995) Formation of opaque mienrals in CK chondrites. *Planetary and Space Science* **43**, 486–498.

Georgopoulou Z.J., Fytas K., Soto H. and Evangelou B. (1996) Feasibility and cost of creating an iron-phosphate coating on pyrrhotite to prevent oxidation. *Environmental Geology* **28**, 61−69.

Gilder S.A., Egli R., Hochleitner R., Roud S.C., Volk M.W.R., Le Goff M. and de Wit M. (2011) Anatomy of a pressure-induced, ferromagnetic to paramagnetic transition in pyrrhotite: Implications for the formation pressure of diamonds. *Journal of Geophysical Research* **116**, B10101.

Goodenough J.B. (1962) Cation-cation three-membered ring formation. *Journal of Applied Physics* **33**, 1197−1199.

Gray N.F. (1997) Environmental impact and remediation of acid mine drainage: a management problem. *Environmental Geology* **30**, 62–71.

Gray N.F. and Delaney E. (2010) Measuring cummunity response of bentic macroinvertebrates in an erosional river impacted by acid mine drainage by use of a simple model. *Ecological Indicators* **10**, 668–675.

Grønvold F. and Stølen S. (1992) Thermodynamics of iron sulfides II. Heat capacity and thermodynamic properties of FeS and of $Fe_{0.875}S$ at temperatures from 298.15 K to 1000 K, of $Fe_{0.98}S$ from 298.15 K to 800 K, and of $Fe_{0.89}S$ from 298.15 K to about 650 K. Thermodynamics of formationa. *The Journal of Chemical Thermodynamics* **24**, 913–936.

Guinier A., Bokij G.B., Boll-Dornberger K., Cowley J.M., Durovic S., Jagodzinski H., Krishna P., de Wolff P.M., Zvyagin B.B., Cox D.E., Goodman P., Hahn Th., Kuchitsu K. and Abrahams S.C. (1984) Nomenclature of polytype structures. Report of the International Union of Crystallography ad hoc Committee on the Nomenclature of Disordered, Modulated and Polytype Structures. *Acta Crystallographica Section A* **40**, 399–404.

Gunsinger M.R., Ptacek C.J., Blowes D.W. and Jambor J.L. (2006) Evaluation of long-term sulfide oxidation processes within pyrrhotite-rich tailings, Lynn Lake, Manitoba. *Journal of Contaminant Hydrology* **83**, 149−170.

Guo W. and Eiler J.M. (2007) Temperatures of aqueous alteration and evidence for methane generation on the parent bodies of the CM chondrites. *Geochimica et Cosmochimica Acta* **71**, 5565–5575.

Guymont M. (1991) Stabilisation by entropy of incommensurate long-period ordered alloys. *Phase Transitions* **31**, 107–115.

Guymont M., Portier R. and Gratias D. (1980) Etude des phases ordonnées à longue période irrationnelle. Les alliages AuCu II et AuCu-Zn. *Acta Crystallographica Section A* **36**, 792–795.

Hall A.J. (1986) Pyrite-pyrrhotine redox reactions in nature. *Mineralogical Magazine* **50**, 223–229.

Hallberg K.B. (2010) New perspectives in acid mine drainage microbiology. *Hydrometallurgy* **104**, 448–453.

Hanowski N.P. and Brearley A.J. (2001) Aqueous alteration of chondrules in the CM carbonaceous chondrite, Allan Hills 81002: implications for parent body alteration. *Geochimica et Cosmochimica Acta* **65**, 495–518.

Harries D., Pollok K. and Langenhorst F. (2011) Translation interface modulation in NC-pyrrhotites: Direct imaging by TEM and a model toward understanding partially disordered structural states. *American Mineralogist* **96**, 716−731.

Hawley J.E. and Haw V.A. (1957) Intergrowths of pentlandite and pyrrhotite. *Economic Geology* **52**, 132–139.

Heaney P.J., Vicenzi E.P., Giannuzzi L.A. and Livi K.J.T. (2001) Focused ion beam milling: a method of site-specific sample extraction for microanalysis of Earth and planetary materials. *American Mineralogist* **86**, 1094–1099.

Herzig P.M. and Hannington M.D. (1995) Polymetallic massive sulfides at the modern seafloor: a review. *Ore Geology Reviews* **10**, 95–115.

Horng C.-S. and Roberts A.P. (2006) Authigenic or detrital origin of pyrrhotite in sediments?: Resolving a paleomagnetic conundrum. *Earth and Planetary Science Letters* **241**, 750–762.

Hudson-Edwards K.A., Jamieson H.E. and Lottermoser B.G. (2011) Mine wastes: past, present, future. *Elements* **7**, 375–380.

Hug S.J. and Leupin O. (2003) Iron-catalyzed oxidation of arsenic (III) by oxygen and by hydrogen peroxide: pH-dependent formation of oxidants in the Fenton reaction. *Environmental Science and Technology* **37**, 2734−2742.

Huss G.R., Rubin A.E. and Grossman J.N. (2006) Thermal metamorphism in chondrites. In *Meteorites and the Early Solar System II*, 567–586 (eds. D.S. Lauretta and H.Y. McSween Jr.).

University of Arizona Press, Tucson, 942 p.

Ikeda Y. (1992) An overview of the research consortium, "Antarctic carbonaceous chondrites with CI affinities, Yamato-86720, Yamato-82162, and Belgica-7904". *Proceedings of the NIPR Symposium on Antarctic Meteorites* **5**, 49–73.

Imlay J.A. (2003) Pathways of oxidative damage. *Annual Reviews of Microbiology* **57**, 395−418.

IUCr (International Union of Crystallography) (1992) Report of the Executive Committee for 1991. *Acta Crystallographica* **A48**, 922–946.

Izaola Z., Gonzalez S., Elcoro L., Perez-Mato J.M., Madariaga G. and Garcia A. (2007) Revision of pyrrhotite structures within a common superspace model. *Acta Crystallographica B* **63**, 693–702.

Jambor J.L., Blowes D.W. and Ritchie I.M. (eds.) (2003) *Environmental aspects of mine wastes. Short Course Handbook Vol. 31*. Mineralogical Association of Canada, Ottawa, 430 p.

Jamieson H.E. (2011) Geochemistry and mineralogy of solid mine waste: essential knowledge for predicting environmental impact. *Elements* **7**, 381–386.

Janzen M.P., Nicholson R.V. and Scharer J.M. (2000) Pyrrhotite reaction kinetics: Reaction rates for oxidation by oxygen, ferric iron, and for nonoxidative dissolution. *Geochimica et Cosmochimica Acta* **64**, 1511−1522.

Jehanno G. and Perio P. (1964) Étude radiocristallographique de AuCu II sur monocristaux. *Journal de Physique France* **25**, 966–974.

Jennings S.R., Dollhopf D.J. and Inskeep W.P. (2000) Acid production from sulfide minerals using hydrogen peroxide weathering. *Applied Geochemistry* **15**, 235−243.

Johnson C.A. and Prinz M. (1993) Carbonate compositions in CM and CI chondrites and implications for aqueous alteration. *Geochimica et Cosmochimica Acta* **57**, 2843–2852.

Johnson D.B. and Hallberg K.B. (2003) The microbiology of acidic mine waters. *Research in Microbiology* **154**, 466–473.

Johnson D.B. and Hallberg K.B. (2005) Acid mine drainage remediation options: a review. *Science of the Total Environment* **338**, 3–14.

Jones C.F., LeCount S., Smart R.S.C. and White T.J. (1992) Composotional and structural alteration of pyrrhotite surfaces in solution: XPS and XRD studies. *Applied Surface Science* **55**, 65−85.

Kalinkin A.M., Forsling W., Makarov D.V. and Makarov V.N. (2000) Surface oxidation of synthetic pyrrhotite during wetting-drying treatment. *Environmental Engineering Science* **17**, 329−335.

Kallemeyn G.W., Rubin A.E. and Wasson J.T. (1991) The compositional classification of chondrites: V. The Karoonda (CK) group of carbonaceous chondrites. *Geochimica et Cosmochimica Acta* **55**, 881–892.

Kaneda H., Takenouchi S. and Shoji T. (1986) Stability of pentlandite in the Fe-Ni-Co-S system. *Mineralium Deposita* **21**, 169–180.

Keil K., Stoeffler D., Love S.G. and Scott E.R.D. (1997) Constraints on the role of impact heating and melting in asteroids. *Meteoritics and Planetary Science* **32**, 349–363.

Kelly D.P. and Vaughan D.J. (1983). Pyrrhotite-pentlandite ore textures: a mechanistic approach. *Mineralogical Magazine* **47**, 453–463.

Kerridge J.F. (1976) Formation of iron sulphide in solar nebula. *Nature* **259**, 189–190.

Kerridge J.F., Macdougall J.D. and Marti K. (1979a) Clues to the origin of sulfide minerals in CI chondrites. *Earth and Planetary Science Letters* **43**, 359–367.

Kerridge J.F., MacDougall J.D. and Carlson J. (1979b) Iron-nickel sulfides in the Murchison meteorite and their relationship to phase Q1. *Earth and Planetary Science Letters* **43**, 1–4.

Kimura M., Grossman J.N. and Weisberg M.K. (2011) Fe-Ni metal and sulfide minerals in CM

chondrites: An indicator for thermal history. *Meteoritics and Planetary Science* **46**, 431–442.

Kissin S.A. and Scot S.D. (1982) Phase relations involving pyrrhotite below 350 °C. *Economic Geology* **77**, 1739–1754.

Kissin S.A. and Scott S.D. (1972) Phase relations of intermediate pyrrhotites. *Economic Geology* **67**, 1007–1007.

Kitajima F., Nakamura T., Takaoka N. and Murae T. (2002) Evaluating the thermal metamorphism of CM chondrites by using the pyrolytic behavior of carbonaceous macromolecular matter. *Geochimica et Cosmochimica Acta* 66, 163–172.

Koppenol W.H. (1993) The centennial of the Fenton reaction. *Free Radical Biology and Medicine* **15**, 645−651.

Kosyakov V.I., Sinyakova E.F. and Shestakov V.A. (2003) Dependence of sulfur fugacity on the composition of phase associations in the Fe-FeS-NiS-Ni system at 873 K. *Geochemistry International* **41**, 660–669.

Koto K., Morimoto N. and Gyobu A. (1975) The superstructure of the intermediate pyrrhotite. I. Partially disordered distribution of metal vacancy in the 6C type, $Fe_{11}S_{12}$. *Acta Crystallographica B* **31**, 2759–2764.

Koto K. and Kitamura M. (1981) The superstructure of the intermediate pyrrhotite. II. One-dimensional out-of-step vector of Fe vacancies in the incommensurate structure with compositional range from Fe_9S_{10} to $Fe_{11}S_{12}$. *Acta Crystallographica A* **37**, 301–308.

Krot A.N., Amelin Y., Bland P., Ciesla F.J., Connelly J., Davis A.M., Huss G.R., Hutcheon I.D., Makide K., Nagashima K., Nyquist L.E., Russell S.S., Scott E.R.D., Thrane K, Yurimot H. and Yin Q.-Z. (2009) Origin and chronology of chondritic components: A review. *Geochimica et Cosmochimica Acta* **73**, 4963–4997.

Kuban R.-J. (1985) Polytypes of the system $Fe_{1-x}S$. *Crystal Research and Technology* **20**, 1649–1656.

Kullerud G. (1963) Thermal stability of pentlandite. *Canadian Mineralogist* **7**, 353–366.

Lauretta D.S., Kremser D.T. and Fegley B. (1996) The rate of iron sulfide formation in the solar nebula. *Icarus* **122**, 288–315.

Lauretta D.S., Lodders K. and Fegley B. (1997) Experimental simulations of sulfide formation in the solar nebula. *Science* **277**, 358–360.

Lauretta D.S., Lodders K. and Fegley B. (1998) Kamacite sulfurization in the solar nebula. *Meteoritics and Planetary Science* **33**, 821–833.

Lee M.R., Bland P.A. and Graham G. (2003) Preparation of TEM samples by focused ion beam (FIB) techniques: applications to the study of clays and phyllosilicates in meteorites. *Mineralogical Magazine* **67**, 581–592.

Li F. and Franzen H.F. (1996) Ordering, incommensuration, and phase transitions in pyrrhotite. Part II: A high-temperature X-ray powder diffraction and thermomagnetic study. *Journal of Solid State Chemistry* **126**, 108–120.

Lianxing G. and Vokes F.M. (1996) Intergrowths of hexagonal and monoclinic pyrrhotites in some sulphide ores from Norway. *Mineralogical Magazine* **60**, 303–316.

Lipschutz M.E., Zolensky M.E. and Bell M.S. (1999) New petrographic and trace element data on thermally metamorphosed carbonaceous chondrites. *Antarctic Meteorite Research* **12**, 57–57.

Lorand J.-P., Chevrier V. and Sautter V. (2005) Sulfide mineralogy and redox conditions in some shergottites. *Meteoritics and Planetary Science* **40**, 1257–1272.

Losiak A. and Velbel M.A. (2011) Evaporite formation during weathering of Antarctic meteorites-A weathering census analysis based on the ANSMET database. *Meteoritics and Planetary Sciences* **46**, 443–459.

Lottermoser B.G. (2011) Recycling, reuse and rehabilitation of mine wastes. *Elements* **7**, 405–410.

Lowson R.T. (1982) Aqueous oxidation of pyrite by molecular oxygen. *Chemistry Reviews* **82**, 461−497.

Lusk J. and Bray D.M. (2002) Phase relations and the electrochemical determination of sulfur fugacity for selected reactions in the Cu-Fe-S and Fe-S systems at 1 bar and temperatures between 185 and 460 °C. *Chemical Geology* **192**, 227–248.

Maldonado E.M. and Brearley A.J. (2011) Exsolution textures of pyrrhotite and alteration of pyrrhotite and pentlandite in the CM2 carbonaceous chondrites Crescent, Mighei and ALH81002 (abstract #2271). *Proceedings*, *42nd Lunar and Planetary Science Conference.*

Marusak L.A. and Mulay L.N. (1980) Polytypism in the cation-deficient iron sulfide, Fe_9S_{10}, and the magnetokinetics of the diffusion process at temperatures about the antiferro- to ferrimagnetic (λ) phase transition. *Physical Review B* **21**, 238–244.

Mayeda T.K. and Clayton R.N. (1998) Oxygen isotope effects in serpentine dehydration (abstract #1405). *29th Lunar and Planetary Science Conference.* CD-ROM.

McSween Jr H.Y. (1979) Alteration in CM carbonaceous chondrites inferred from modal and chemical variations in matrix. *Geochimica et Cosmochimica Acta* **43**, 1761–1770.

Metzler K., Bischoff A. and Stöffler D. (1992) Accretionary dust mantles in CM chondrites: Evidence for solar nebula processes. *Geochimica et Cosmochimica Acta* **56**, 2873–2897.

Mikhlin Y.L., Tomashevich Y.V., Pashkov G.L., Okotrub A.V., Asanov I.P. and Mazalov L.N. (1998) Electronic structure of the non-equilibrium iron-deficient layer of hexagonal pyrrhotite. *Applied Surface Science* **125**, 73−84.

Mikhlin Y.L., Varnek V., Asanov I.P., Tomashevich Y.V., Okotrub A.V., Livshits A., Selyutin G. and Pashkov G.L. (2000) Reactivity of pyrrhotite (Fe_9S_{10}) surfaces: Spectroscopic studies. *Physical Chemistry Chemical Physics* **2**, 4393−4398.

Miller M.K. and Russell K.F. (2007) Atom probe specimen preparation with a dual beam SEM/FIB miller. *Ultramicroscopy* **107**, 761−766.

Misra K. and Fleet M.E. (1973) The chemical compositions of synthetic and natural pentlandite assemblages. *Economic Geology* **68**, 518–539.

Moncur M.C., Jambor J.L., Ptacek C.J. and Blowes D.W. (2009) Mine drainage from the weathering of sulfide minerals and magnetite. *Applied Geochemistry* **24**, 2362–2373.

Morimoto N. and Nakazawa H. (1968) Pyrrhotites: synthetics having two new superstructures. *Science* **161**, 577–579.

Morimoto N., Nakazawa H., Nishigucmi K. and Tokonami M. (1970) Pyrrhotites: Stoichiometric Compounds with Composition $Fe_{n-1}S_n$ ($n \geq 8$). *Science* **168**, 964–966.

Morimoto N., Gyobu A., Mukaiyama H. and Izawa E. (1975a) Crystallography and stability of pyrrhotites. *Economic Geology* **70**, 824–833.

Morimoto N., Gyobu A., Tsukuma K. and Koto K. (1975b) Superstructure and nonstoichiometry of intermediate pyrrhotite. *American Mineralogist* **60**, 240–248.

Mycroft J.R., Nesbitt H.W. and Pratt A.R. (1995) X-ray photoelectron and Auger electron spectroscopy of air-oxidized pyrrhotite: Distribution of oxidized species with depth. *Geochimica et Cosmochimica Acta* **59**, 721–733.

Nakamura T. (2005) Post-hydration thermal metamorphism of carbonaceous chondrites. *Journal of Mineralogical and Petrological Sciences* **100**, 260–272.

Nakamura T. (2006) Yamato 793321 CM chondrite: Dehydrated regolith material of a hydrous asteroid. *Earth and Planetary Science Letters* **242**, 26–38.

Nakato A., Nakamura T., Kitajima F. and Noguchi T. (2008) Evaluation of dehydration mechanism during heating of hydrous asteroids based on mineralogical and chemical analysis of naturally and experimentally heated CM chondrites. *Earth, Planets, and Space* **60**, 855–864.

Nakato A., Nakamura T., Noguchi T., Ahn I. and Lee J.I. (2011) The variety of thermal evolution of primitive hydrous asteroids recorded in dehydrated carbonaceous chondrites (abstract

#5416). *Meteoritics and Planetary Science* **46**, A175.

Nakazawa H. and Morimoto N. (1970) Pyrrhotite phase relations below 320 °C. *Proceedings of the Japan Academy* **46**, 678–683.

Nakazawa H., Morimoto N. and Watanabe E. (1975) Direct observation of metal vacancies by high-resolution electron microscopy. Part I: 4C type pyrrhotite (Fe_7S_8). *American Mineralogist* **60**, 359–366.

Naldrett A.J., Craig J.R., and Kullerud G. (1967) The central portion of the Fe-Ni-S system and its bearing on pentlandite exsolution in iron-nickel sulfide ores. *Economic Geology* **62**, 826–847.

Naraoka H., Mita H., Komiya M., Yoneda S., Kojima H. and Shimoyama A. (2004) A chemical sequence of macromolecular organic matter in the CM chondrites. *Meteoritics and Planetary Science* **39**, 401–406.

Nazarov M.A., Kurat G., Brandstaetter F., Ntaflos T., Chaussidon M. and Hoppe P. (2009) Phosphorus-bearing sulfides and their associations in CM chondrites. *Petrology* **17**, 101–123.

Nečas D. and Klapetek P. (2012) Gwyddion: an open-source software for SPM data analysis. *Central European Journal of Physics* **10**, 181–188.

Nesbitt H.W., Schaufuss A.G., Scaini M., Bancroft G.M. and Szargan R. (2001) XPS measurement of fivefold and sixfold coordinated sulfur in pyrrhotites and evidence for millerite and pyrrhotite surface species. *American Mineralogist* **86**, 318–326.

Nespolo M., Takeda H. and Ferraris G. (1997) Crystallography of mica polytypes. In *Modular Aspects in Mineralogy, EMU Notes in Mineralogy* **1**, 81–118 (ed. S. Merlino). Eötvös University Press, Budapest, 449 p.

Nicholson R.V. and Scharer J.M. (1994) Laboratory studies of pyrrhotite oxidation kinetics. In *Environmental Geochemistry of Sulfide Oxidation (ACS Symposium Series)* (eds. C. N. Alpers and D. W. Blowes), 14–30. American Chemical Society, Washington, 681 p.

Nicol M.J. and Scott P.D. (1979) The kinetics and mechanism of the non-oxidative dissolution of some iron sulphides in aqueous acidic solutions. *Journal of the South African Institute of Mining and Metallurgy* **79**, 298–305.

Nordstrom D.K. (2011) Mine waters: acidic to circumneutral. *Elements* **7**, 393–398.

Nouruzi-Khorasani A., Lunn M. A., Jones I. P., Dobson P. S., Williams D. J. and Astles M. G. (1990) Surface damage of CdTe by mechanical polishing investigated by cross-sectional TEM. *Journal of Crystal Growth* **102**, 1069–1073.

Novikov G.V., Egorov V.K., Popov V.I. and Sipavina L.V. (1977) Kinetics and mechanism of transformations in iron-rich pyrrhotites and in troilite-pyrrhotite metastable assemblages. *Physics and Chemistry of Minerals* 1, 1–14.

Ohmoto H. (1996) Formation of volcanogenic massive sulfide deposits: The Kuroko perspective. *Ore Geology Reviews* **10**, 135–177.

O'Shay T., Hossner L. R. and Dixon J. B. (1990) A modified hydrogen peroxide oxidation method for determination of potential acidity in pyritic overburden. *Journal of Environmental Quality* **19**, 778–782.

Paul R.L. and Lipschutz M.E. (1990) Consortium study of labile trace elements in some Antarctic carbonaceous chondrites: Antarctic and non-Antarctic meteorite comparisons. *Antarctic Meteorite Research* **3**, 80–95.

Perrin D.D. (1969) Dissociation contants of inorganic acids and bases in aqueous solution. *Pure and Applied Chemistry* **20**, 133–236.

Pierce L. and Buseck P.R. (1974) Electron imaging of pyrrhotite superstructures. *Science* **186**, 1209–1212.

Pósfai M. and Buseck P.R. (1997) Modular structures in sulphides: sphalerite/wurtzite-, pyrite/marcasite-, and pyrrhotite-type minerals. In *Modular Aspects in Mineralogy, EMU Notes in Mineralogy* **1**, 193–235 (ed. S. Merlino). Eötvös University Press, Budapest, 449 p.

Pósfai M. and Dódony I. (1990) Pyrrhotite superstructures; Part I, Fundamental structures of the NC (N = 2, 3, 4 and 5) type. *European Journal of Mineralogy* **2**, 525–525.

Pósfai M., Sharp T. G. and Kontny A. (2000) Pyrrhotite varieties from the 9.1 km deep borehole of the KTB project. *American Mineralogist* **85**, 1406–1415.

Powell A.V., Vaqueiro P., Knight K.S., Chapon L.C. and Sánchez R.D. (2004) Structure and magnetism in synthetic pyrrhotite Fe_7S_8: A powder neutron-diffraction study. *Physical Review B* **70**, 014415.

Pratt A.R., Muir I.J. and Nesbitt H.W. (1994) X-ray photoelectron and Auger electron spectroscopic studies of pyrrhotite and mechanism of air oxidation. *Geochimica et Cosmochimica Acta* **58**, 827–841.

Prichard H.M., Hutchinson D. and Fisher P.C. (2004) Petrology and crystallization history of multiphase sulfide droplets in a mafic dike from Uruguay: Implications for the origin of Cu-Ni-PGE sulfide deposits. *Economic Geology* **99**, 365–376.

Puretz J. and Swanson L.W. (1992) Focused ion beam deposition of Pt containing films. *Journal of Vacuum Science and Technology B* **10**, 2695–2699.

Putnis A. (1975) Observations on coexisting pyrrhotite phases by transmission electron microscopy. *Contributions to Mineralalogy and Petrolology* **52**, 307–313.

Raghavan V. (2004) Phase diagram evaluations: Fe-Ni-S (iron-nickel-sulfur). *Journal of Phase Equilibria and Diffusion* **25**, 373–381.

Ramdohr P. (1950) *Die Erzmineralien und ihre Verwachsungen*. Akademie-Verlag, Berlin, 827 p.

Rau H. (1976) Energetics of defect formation and interaction in pyrrhotite $Fe_{1-x}S$ and its homogeneity range. *Journal of Physics and Chemistry of Solids* **37**, 425–429.

Rickard D. and Luther G.W. III (2007) Chemistry of iron sulfides. *Chemical Reviews* **107**, 514–562.

Rochette P., Fillion G., Mattéi J.-L. and Dekkers M. J. (1990) Magnetic transition at 30-34 Kelvin in pyrrhotite: insight into a widespread occurrence of this mineral in rocks. *Earth Planetary Science Letters* **98**, 319–328.

Rubanov S. and Munroe P. R. (2004) FIB-induced damage in silicon. *Journal of Microscopy* **214**, 213-221.

Rubin A.E. (1997) Mineralogy of meteorite groups. *Meteoritics and Planetary Science* **32**, 231–247.

Rubin A.E. and Kallemeyn G.W. (1989) Carlisle Lakes and Allan Hills 85151: Members of a new chondrite grouplet. *Geochimica et Cosmochimica Acta* **53**, 3035–3044.

Rubin A.E., Trigo-Rodríguez J.M., Huber H. and Wasson J.T. (2007) Progressive aqueous alteration of CM carbonaceous chondrites. *Geochimica et Cosmochimica Acta* **71**, 2361–2382.

Sáez R., Moreno C., Gonzáles F. and Almodóvar G.R. (2011) Black shales and massive sulfide deposits: causal or casual relationships? Insights from Rammelsberg, Tharsis, and Draa Sfar. *Mineralium Deposita* **46**, 585–614.

Schippers A. and Kock D. (2007) Geomicrobiology of sulfidic mine dumps: a short review. *Advanced Materials Research* **37**, 71–73.

Schryvers D., Van Tendeloo G. and Amelinckx S. (1985) On the ordering mechanism of Ni_3Mo - A high resolution electron microscopy study. *Physica Status Solidi A* **87**, 401–415.

Schulze H., Bischoff A., Palme H., Spettel B., Dreibus G. and Otto J. (1994) Mineralogy and chemistry of Rumuruti: The first meteorite fall of the new R chondrite group. *Meteoritics* **29**, 275–286.

Schwarz E.J. and Vaughan D.J. (1972) Magnetic Phase Relations of Pyrrhotite. *Journal of Geomagnetism and Geoelectricity* **24**, 441–458.

Sharp W.E. (1966) Pyrrhotite: a common inclusion in South African diamonds. *Nature* **211**, 402–403.

Shaw C.S.J. (1997) Origin of sulfide blebs in variably metasomatized mantle xenoliths, quaternary west Eifel volcanic field, Germany. *Canadian Mineralogist* **35**, 1453–1463.

Shimoyama A., Komiya M., and Harada K. (1991) Release of organic compounds from some Antarctic CI and CM chondrites by laboratory heating. *Antarctic Meteorite Research* **4**, 247–260.

Stadelmann, P. (2008) JEMS: Java electron microscopy software. CIME-EPFL, Lausanne, Switzerland.

Steger H.F. (1982) Oxidation of sulfide minerals: VII. Effect of temperature and relative humidity on the oxidation of pyrrhotite. *Chemical Geolology* **35**, 281–295.

Sugaki A. and Kitakaze A. (1998) High form of pentlandite and its thermal stability. *American Mineralogist* **83**, 133–140.

Taylor L.A. and Liu Y. (2009) Sulfide inclusions in diamonds: not monosulfide solid solution. *Russian Geology and Geophysics* **50**, 1201–1211.

Thomas J.E., Jones C.F., Skinner W.M. and Smart R.S.C. (1998) The role of surface sulfur species in the inhibition of pyrrhotite dissolution in acid conditions. *Geochimica et Cosmochimica Acta* **62**, 1555–1565.

Thomas J.E., Skinner W.M. and Smart R.S.C. (2001) A mechanism to explain sudden changes in rates and products for pyrrhotite dissolution in acid solution. *Geochimica et Cosmochimica Acta* **65**, 1–12.

Tokonami M., Nishiguchi K. and Morimoto N. (1972) Crystal structure of a monoclinic pyrrhotite (Fe_7S_8). *American Mineralogist* **57**, 1066–1080.

Tomeoka K., Kojima H. and Yanai K. (1989a) Yamato-82162: A new kind of CI carbonaceous chondrite found in Antarctica. *Proceedings of the NIPR Symposium on Antarctic Meteorites* **2**, 36–54.

Tomeoka K., Kojima H., and Yanai K. (1989b) Yamato-86720: A CM carbonaceous chondrite having experienced extensive aqueous alteration and thermal metamorphism. *Proceedings of the NIPR Symposium on Antarctic Meteorites* **2**, 55–74.

Tonui E.K., Zolensky M.E. and Lipschutz M. (2002) Petrography, mineralogy and trace element chemistry of Yamato-86029 Yamato-793321 and Lewis Cliff 85332: Aqueous alteration and heating events. *Antarctic Meteorite Research* **15**, 38–58.

Tonui E.K., Zolensky M.E., Lipschutz M.E., Wang M.S. and Nakamura T. (2003) Yamato 86029: Aqueously altered and thermally metamorphosed CI-like chondrite with unusual textures. *Meteoritics and Planetary Science* **38**, 269–292.

Toulmin P. and Barton Jr. P.B. (1964) A thermodynamic study of pyrite and pyrrhotite. *Geochimica et Cosmochimica Acta* **28**, 641–671.

Treiman A.H. (2005) The nakhlite meteorites: augite-rich igneous rocks from Mars. *Chemie der Erde* **65**, 203–270.

Treiman A.H., Gleason J.D. and Bogard D.D. (2000) The SNC meteorites are from Mars. *Planetary and Space Science* **48**, 1213–1230.

Tsai H., Shieh Y. and Meyer H.O.A. (1979) Mineralogy and $^{34}S/^{32}S$ ratios of sulfides associated with kimberlite, xenoliths and diamonds. In *The Mantle Sample: Inclusion in Kimberlites and Other Volcanics*, 87–103 (eds. F. R. Boyd and H.O.A. Meyer), American Geophysical Union, Washington, 424 p.

van Dyck D., Broddin D., Mahy J. and Amelinckx S. (1987) Electron Diffraction of Translation Interface Modulated Structures. *Physica Status Solidi A* **103**, 357–373.

van Landuyt J. (1974) Shear structures and crystallographic shear propagation. *Journal de Physique* **35**, 53–63.

van Landuyt J., De Ridder R., Gevers R. and Amelinckx, S. (1970) Diffraction effects due to shear structures: A new method for determining the shear vector. *Materials Research Bulletin* **5**, 353-

362.

van Landuyt J., van Tendeloo G. and Amelinckx S. (1985) Electron microscopy and diffraction of modulated structures. *Pure and Applied Chemistry* **57**, 1373–1382.

van Smaalen (2004) An elementary introduction to superspace crystallography. *Zeitschrift für Kristallographie* **219**, 681–691.

van Tendeloo G., Van Landuyt J., Delavignette P. and Amelinckx S. (1974) Compositional changes associated with periodic antiphase boundaries in the initial stages of ordering in Ni_3Mo. *Physica Status Solidi A* **25**, 697–707.

Vaughan D.J. and Craig J.R. (1978) *Mineral chemistry of metal sulfides*. Cambridge University Press, Cambridge, 493 p.

Vaughan D.J., Schwarz E.J. and Owens D.R. (1971). Pyrrhotites from the Strathcona Mine, Sudbury, Canada; A thermomagnetic and mineralogical study. *Economic Geology* **66**, 1131–1144.

Veblen D.R. (1991) Polysomatism and polysomatic series: a review and applications. *American Mineralogist* **76**, 801–826.

Velbel M.A. (1988) The distribution and significance of evaporitic weathering products on antarctic meteorites. *Meteoritics* **23**, 151–159.

Volkert C.A. and Minor A.M. (2007) Focused ion beam microscopy and micromachining. *MRS Bulletin* **32**, 389–399.

Wang H. (2007) A review on process-related characteristics of pyrrhotite. *Mineral Processing and Extractive Metallurgy Review* **29**, 1–41.

Wang H. and Salveson I. (2005) A review on the mineral chemistry of the non-stoichiometric iron sulphide, $Fe_{1-x}S$ ($0 \leq x \leq 0.125$): polymorphs, phase relations and transitions, electronic and magnetic structures. *Phase Transitions* **78**, 547–567.

Wenk H.-R. (ed.) (1976) *Transmission electron microscopy in mineralogy*. Springer-Verlag, Berlin, 564 p.

Whitney J.A. (1984) Fugacities of sulfurous gases in pyrrhotite-bearing silicic magmas. *American Mineralogist* **69**, 68–78.

Williams D.B. and Carter C.B. (2009) *Transmission Electron Microscopy* (2nd Ed.). Springer, New York, 760 p.

Wittmann A., Swindle T.D., Cheek L.C., Frank E.A. and Kring D.A. (2010) Impact cratering on the H chondrite parent asteroid. *Journal of Geophysical Research* **115**, E07009.

Wojdyr M. (2010) Fityk: a general-purpose peak fitting program. *Journal of Applied Crystallography* **43**, 1126–1128.

Wozniakiewicz P.J., Ishii H.A., Kearsley A.T., Burchell M.J., Bland P.A., Bradley J.P., Dai Z., Teslich N., Collins G.S. and Cole M.J. (2011) Investigation of iron sulfide impact crater residues: A combined analysis by scanning and transmission electron microscopy. *Meteoritics and Planetary Science* **46**, 1007–1024.

Yamamoto A. and Nakazawa H. (1982) Modulated structure of the NC-type (N = 5.5) pyrrhotite, $Fe_{1-x}S$. *Acta Crystallographica Section A* **38**, 79–86.

Yamamoto K. and Nakamura N. (1990) REE characteristics of Yamato-82162 and -86720 meteorites and their inference to classification. *Antarctic Meteorite Research* **3**, 69–69.

Zega T.J., Nittler L.R., Busemann H., Hoppe P. and Stroud R.M. (2007) Coordinated isotopic and mineralogic analyses of planetary materials enabled by in situ lift-out with a focused ion beam scanning electron microscope. *Meteoritics and Planetary Science* **42**, 1373–1386.

Zolensky M.E. (1987) Tochilinite in C2 carbonaceous chondrites: a review with suggestions (abstract). *Proceedings, 18th Lunar and Planetary Science Conference*, 1132–1133.

Zolensky M.E. and Thomas K.L. (1995) Iron and iron-nickel sulfides in chondritic interplanetary dust particles. *Geochimica et Cosmochimica Acta* **59**, 4707–4712.

Zolensky M.E., Barrett R. A. and Prinz M. (1989) Petrography, mineralogy, and matrix composition of Yamato-82162, a new CI2 chondrite. *Proceedings, 20th Lunar and Planetary Science Conference*, 1253–1254.

Zolensky M.E., Prinz M., and Lipschutz M. (1991) Mineralogy and thermal history of Y-82162, Y-86720, and B-7904. *Proceeding, 16th Symposium on Antarctic Meteorites*. 195–196.

Zolensky M.E., Barrett R. and Browning L. (1993) Mineralogy and composition of matrix and chondrule rims in carbonaceous chondrites. *Geochimica et Cosmochimica Acta* **57**, 3123–3148.

Zolensky M.E., Mittlefehldt D.W., Lipschutz M.E., Wang M.-S., Clayton R. N., Mayeda T. K., Grady M.M., Pillinger C. and Barber D. (1997) CM chondrites exhibit the complete petrologic range from type 2 to 1. *Geochimica et Cosmochimica Acta* **61**, 5099–5115.

ERKLÄRUNG

Hiermit erkläre ich, dass ich die vorliegende Arbeit selbständig verfasst und keine anderen als die von mir angegebenen Quellen und Hilfsmittel verwendet habe.

Ferner erkläre ich, dass ich nicht anderweitig mit oder ohne Erfolg versucht habe, eine Dissertation einzureichen. Ich habe keine gleichartige Doktorprüfung an einer anderen Hochschule endgültig nicht bestanden.

Bayreuth, den 12. Januar 2012

Dennis Harries